Enhanced Buffer Gas Loading:
Cooling and Trapping of Atoms with Low Effective Magnetic Moments

A thesis presented

by

Robert Michniak

to

The Department of Physics

in partial fulfillment of the requirements

for the degree of

Doctor of Philosophy

in the subject of

Physics

Harvard University

Cambridge, Massachusetts

May 2004

To My Father

Thesis Advisor | Author

John Doyle | **Robert Michniak**

Enhanced Buffer Gas Loading:
Cooling and Trapping of Atoms with Low Effective Magnetic Moments

Abstract

A new technique for buffer gas loading is described. This technique greatly extends the range of atoms and molecules that may be magnetically trapped at low temperature. The advance is made possible by the rapid removal of the buffer gas on a time scale one hundred times greater than in previous buffer gas loading experiments. A new cryogenic valve is developed and employed. The following benchmarks were attained in our first experimental run; approximately 10^{12} atoms with effective magnetic moments $\mu_{eff} \gtrsim 3\mu_B$ were trapped and thermally isolated with near unit efficiency, ~ 10^{10} $\mu_{eff} = 2\mu_B$ atoms were trapped and thermally isolated, and ~ 10^9 $\mu_{eff} = 1\mu_B$ atoms were trapped, but without thermal isolation. For comparison, all previous buffer gas loading experiments that achieved thermal isolation after trapping were done with atoms having a magnetic moment of at least $6\mu_B$. In our second run of the experiment, better temperature management allowed us to increase the number of trapped and thermally isolated $\mu_{eff} = 2\mu_B$ atoms to ~10^{11} and trapped $\mu_{eff} = 1\mu_B$ atoms to ~ 10^{10}. The performance of the present apparatus is limited by the presence

of a desorbing helium film that compromises the vacuum in the cell after the bulk of the buffer gas is removed. Future improvements to address this problem are suggested that will likely allow for efficient trapping and thermal isolation of atoms and molecules with magnetic moments as low as $1\mu_B$. Analysis of the trapping and pumping dynamics is presented.

Contents

List of Figures

List of Tables

Acknowledgments

First and foremost I thank my (late) mother and father for love and support throughout my life. This thesis would certainly not have been possible without the encouragement they provided during my education. I would also like to express my gratitude to my Aunt, Dolores Allor for the generosity, love, and kindness she has always shown me.

At graduate school, I would first like to acknowledge my advisor, John Doyle for support and for creating an exciting and stimulating laboratory environment in which to work.

The quality of one's life in graduate school is determined in large part by the people we work with. I consider myself extremely fortunate for having met some extraordinary people in the basement of Lyman. I would first like to acknowledge the students in our group that graduated before me, particularly Dan McKinsey, Jonathan Weinstein, and Rob deCarvalho. I was lucky to have the opportunity to work closely with Dan during my early years of graduate school. He is an exceptional scientist, teacher, and person, and I have no doubt that he will make an excellent professor. I also am very glad to have shared an office for several years with Jonathan and Rob. I will always look back fondly on the many hours we spent discussing any number of random things (occasionally having to do with physics). I think we all contributed to making our office a less productive (but much more fun and interesting) place to work when we were all present.

I thank Bretislav Friedrich and Wieland Schollkopf for many interesting discussions of physics, history, politics, the Red Sox etc … and for generally making the lab a more pleasant place while they were there.

I would also like to thank Liang Yang for keeping us sane during countless brutal hours of magnet winding. I don't think that anyone else could have done this so well.

A large multi-faceted experiment is obviously a group effort. In graduate school, we do not often have the opportunity to choose the other people who participate in our experiments. In my case, I think this was for the best. I could not have asked for better people to work with. Jack Harris and Scott Nguyen worked on this project from its inception, and any success that we have had is certainly due (at the very least) in equal measure to their efforts.

Jack especially deserves much of the credit for the design of the original experimental apparatus, and for being an unending source of ideas, inspiration, and ingenuity.

As for Scott, his intelligence, hard work, and enthusiasm were largely responsible for the success of our experiment. Despite his occasional artwork at my expense and his sometimes despicable editing of Natalie Merchant photos, there is no one else I would rather have worked with.

I would also like to acknowledge Cindy Hancox as well as Rob (again) for allowing us to use the excellent software they developed for their experiment. This was

extremely helpful in our understanding and analysis of the data discussed in this thesis. Nathaniel Brahms, Joel Helton, and Andrew Jayich also contributed significantly to the construction of the experimental apparatus.

Without naming everyone, I also thank the many other students (past and present) in the group for making life in the lab interesting and enjoyable.

Finally, by far, the thing that I will value the most from my years in graduate school is the friendship of many wonderful people I met (or in some cases already knew). My years in Cambridge have been enriched for having known them. So finally, I would like to thank Mike, Marc, Cindy, Ila, Greg, Vernita, Mathew, Oksana, and many others for making life outside the lab so much nicer than it otherwise would have been.

Chapter 1
Introduction

This thesis will describe the development of a new technique that greatly extends the range of species amenable to magnetic trapping and study at low temperature. Buffer gas loading is the key method, and the advances described herein are in large measure due to the development of a method to rapidly remove the buffer gas and achieve thermal isolation of the trapped sample. This is done on a time scale one hundred times quicker than in previous buffer gas loading experiments. Because the initial lifetime of a trapped sample in the presence of the buffer gas falls precipitously with decreasing magnetic moment of the trapped species, the ability to more quickly remove the gas allows for much more efficient trapping and thermal isolation of weakly paramagnetic atoms or molecules[1].

Our "rapid pump-out" is accomplished by employing a newly developed fast actuating cryogenic valve. This valve connects the chamber in which the atoms are trapped to an auxiliary "pumping chamber." When the valve is opened, the buffer gas quickly rushes out of the "trapping chamber" leaving behind a magnetically trapped

[1] In all of the work described in this thesis, the particles trapped are chromium atoms. Nearly all of the principles of magnetic trapping and the issues involved with managing the buffer gas pertain equally well to other atoms and paramagnetic molecules as well. To avoid cumbersome language, we will usually use the term "atom" in general discussions of the issues involved in our technique with the understanding that the apparatus can be equally well used as a molecule trap.

sample. This method of buffer gas removal eases the requirements on the temperatures needed in this sort of experiment and thus allows for simpler cryogenic refrigeration to be used. Because this is the first in depth description of the new experiment, the reader will not always be spared the more mundane issues of cryogenic design and day to day operation of the apparatus. Hopefully, this will provide some useful introductory material to newer students in the field of low temperature experimental physics (without boring them too much).

Broadly speaking, this experiment has two goals. One, is to open up a new range of paramagnetic atoms and molecules to be explored using magnetic trapping, and two (more long term), to develop an apparatus suitable for producing extremely large samples of quantum degenerate gases (larger for example than is possible using laser cooling). We begin by briefly considering how such advances would be valuable to atomic physicists.

1.1 Importance of Cooling and Trapping (Historical Perspective)

During the 1960's, the field of atomic and molecular physics underwent a renaissance due in large part to the invention of the laser and it's subsequent use as a tool for spectroscopy. With the laser, physicists could probe matter with unprecedented precision and as a result gain valuable insights into the basic laws of physics. Atoms were a particularly convenient laboratory (simple enough to be characterized

in detail yet exhibiting a wide and rich range of phenomena) in which to study nature, and the laser became one of the most valuable tools in this laboratory.

In the last two decades, a new "Golden Age" of atomic physics has begun. We have gone from simply being passive observers of the atoms and molecules that we study to active participants exerting amazing control and influence over the quantum states of the species we explore and of their external degrees of freedom as well. The production of such novel states of matter as the BEC [1] [2] [3], fermi degenerate gases [4] [5] and, more recently, anti-Hydrogen [6] [7] allow scientists unique systems in which to explore the most basic laws of nature and offer new insights not possible with even the most careful study of more mundane "classical" systems. This new level of control over matter on extremely small size scales promises to lead to ground breaking advances in many practical areas such as computing, electronics, communications etc...

These new advances have been made possible largely through the development of techniques to cool and trap particles using electromagnetic fields. Like the laser before it, the particle trap has become a new tool that has revolutionized physics. By cooling and confining particles to a particular region of space, physicists are in a better position to both study and to control them. A number of different types of traps for various sorts of particles (ions, electrons, protons, positrons, anti-protons [8], neutrons [9], atoms, molecules etc... [10] [11] [12] [13]) have been developed over the past few decades allowing for a wealth of new experiments to be performed.

1.2 Magnetic Trapping

This thesis will focus on the techniques involved with the trapping of neutral particles. Neutral particles present in some ways a more difficult challenge than charged particles. Because neutral atoms or molecules have no net electric charge, they are less susceptible to the influence of electric fields in the lab. While dipole traps that exploit the polarizability of neutral particles have been used to trap atoms and molecules, they are typically quite shallow and generally must be loaded from some other sort of trap (after a great deal of cooling [14].) Fortunately, in addition to electric charge, nature provides another "handle" to grab onto for many neutral particles. Protons, neutrons, and electrons all have intrinsic magnetic moments. As a result, magnetic field gradients[2] can be used to exert forces on these particles. In the case of atoms and molecules, the overall magnetic moment of the particle is due to the combination of the intrinsic moments of the constituents as well as a contribution from the electrons' orbital angular momenta. In some cases, these combine to result in a magnetically "neutral" particle (one with no overall magnetic moment). Notable examples are the alkaline earths and the noble gases. Thankfully for the magnetic trapper, however, the vast majority of atoms on the periodic table (and a great number of molecules as well) have net magnetic moments on the order of $1\mu_B$ (the magnetic moment of the electron) or greater, making them suitable candidates for magnetic trapping. We'll see in a moment the consequences that the finite size of the magnetic

[2] Because magnetic monopoles do not exist in nature, a constant magnetic field does not exert a force on a magnetic particle.

Particle	Magnetic Moment
electron	$1\mu_B$
proton	$2.7928\mu_N$
neutron	$-1.9135\mu_N$

Table 1.1: Magnetic moments of the constituents of the atom.

field gradients that can practically be made in the lab have on the minimum magnetic moments required for efficient trapping.

1.3 Necessity for cooling

In order to successfully load particles into a magnetic trap, it is necessary to dissipate some of the kinetic energy (i.e. to cool the particles) while the particles are in the magnetic trapping potential. There are two reasons for this. First, the potential for a magnetic moment interacting with a magnetic field is conservative. The total energy of a particle in a magnetic trap is a constant of the motion. Any kinetic energy gained or lost as a particle enters the trapping region will be made up for as the particle leaves. In other words, a particle that rolls down into the trap will simply roll back out unless something is done to remove energy from the particle while it's in the trap.

The second reason is less fundamental and rather has to due with the size of the various magnetic moments that nature provides, and with the depth of the magnetic traps that can practically be made using available technology. The intrinsic magnetic moments of the basic constituents of the atom are listed in table 1.1.

moment	value	value in "Temperature Units"
μ_B	$9.27 \times 10^{-24} J/T$	$(0.67K/T) \cdot k_B$
μ_N	$5.05 \times 10^{-27} J/T$	$(0.35mK/T) \cdot k_B$

Table 1.2: Values of fundamental magnetic moments.

Here, μ_B is the Bohr magneton and μ_N the nuclear magneton. Their values are listed in table 1.2. Note, k_B is Boltzman's constant (equal to $1.381 \times 10^{-23} J/K$)

This last column is the most relevant for the magnetic trappist. In order for a magnetic field gradient to have a significant effect on the motion of a particle, the interaction energy between the magnetic moment and the ambient magnetic field must be comparable to or larger than the thermal kinetic energy of the particle. If this is not the case, then the thermal motion dominates, and the magnetic field is simply a small perturbation. If we are to have any hope of magnetically trapping a neutral particle, we must ensure that:

$$\mu \cdot B \gtrsim k_B \cdot T \tag{1.1}$$

Equation 1.1 may be regarded as the first "golden rule" of magnetic trapping. It is a necessary (although as we shall see not always sufficient) condition to satisfy for the production of a magnetically trapped sample. The deepest magnetic traps made today employ superconducting technology to achieve large fields. At present, standard superconducting technology limits the size of the magnetic fields possible in traps to $\sim$ 5 Tesla. While improvements in superconducting magnet technology may eventually raise this limit somewhat, it is unlikely to change significantly in the near future. To see what this technological constraint implies for the applicability

of magnetic trapping to different neutral species, we look at the last column of table 1.2.

First, we note that for atoms whose magnetic moment is solely due to the nucleus, trapping is a truly daunting task. These species must be cooled to temperatures on the order of a few milli-Kelvin or less in the presence of a several tesla deep trap in order to satisfy eq. 1.1. While this is possible (and indeed neutrons, for example, have been magnetically trapped [9]), the technical challenges are formidable. In this thesis, we restrict our attention to the more tractable problem of trapping paramagnetic atoms (those with an electron contribution to the magnetic moment). In order to trap particles with magnetic moments of $\sim 1\mu_B$ using magnetic fields on the order of a few tesla, the particles must first be cooled to temperatures of a few kelvin or less. For example, with a $1\mu_B$ species in a 5 T field, $\mu \cdot B/k_B = 3K$ indicating that to satisfy eq. 1.1, we need to achieve an initial temperature of $3K$ or lower. Given that most atomic and molecular sources produce particles at temperatures of several hundred Kelvin (or greater), a substantial amount of cooling must be done to arrive at temperatures low enough to make magnetic trapping possible.

At first, this task might not appear so challenging. Cryogenic refrigerators have been available for decades that can cool bulk matter to temperatures of $\sim 10mK$ and even lower [15]. There is a problem, however, with the simple direct application of cryogenic technology to the task of precooling a sample to be loaded into a magnetic trap; cold substances like to stick to cold surfaces. If one were to introduce a room

temperature gas of particles into a chamber kept at ~ $1K$ by some sort of cryogenic refrigerator, the result would not be a gas cooled to $1K$. Instead, the gas would freeze out (solidify) onto the chamber walls. The binding energy of particles to various surfaces will be discussed in more detail in ch. 6. In general, this binding energy varies greatly depending on the particle and surface under consideration. In most cases it is on the order of $50K$ to $150K$ (or higher) and thus much greater than what is needed for magnetic trapping[3]. This means that to cool a gas to sufficiently low temperature for magnetic trapping, the particles must be kept from contact with the walls of the chamber that they are trapped in.

1.4 Laser Cooling

One of the most successful and ubiquitous approaches to this task uses a clever application of light known as "laser cooling [12] [17]." In laser cooling, light that is off resonance from an atomic transition is shown upon an atomic source. If the light is tuned to a frequency below the natural atomic resonance, then the Doppler shift will cause fast (hot) atoms to preferentially absorb counter-propagating photons. Since the emission is random, the net effect is to reduce the forward momentum of a particle, and thus to cool it (see fig. 1.1).

---

[3] One noteable exception is the unusually low binding energy of atomic hyrdogen to helium surfaces. This binding energy is sufficiently low to allow hydrogen to be cooled through direct thermalization with a cold surface coated with helium, and has been used by the cryogenic MIT hydrogen experiment in the production of their cold trapped samples of atomic hydrogen [16].

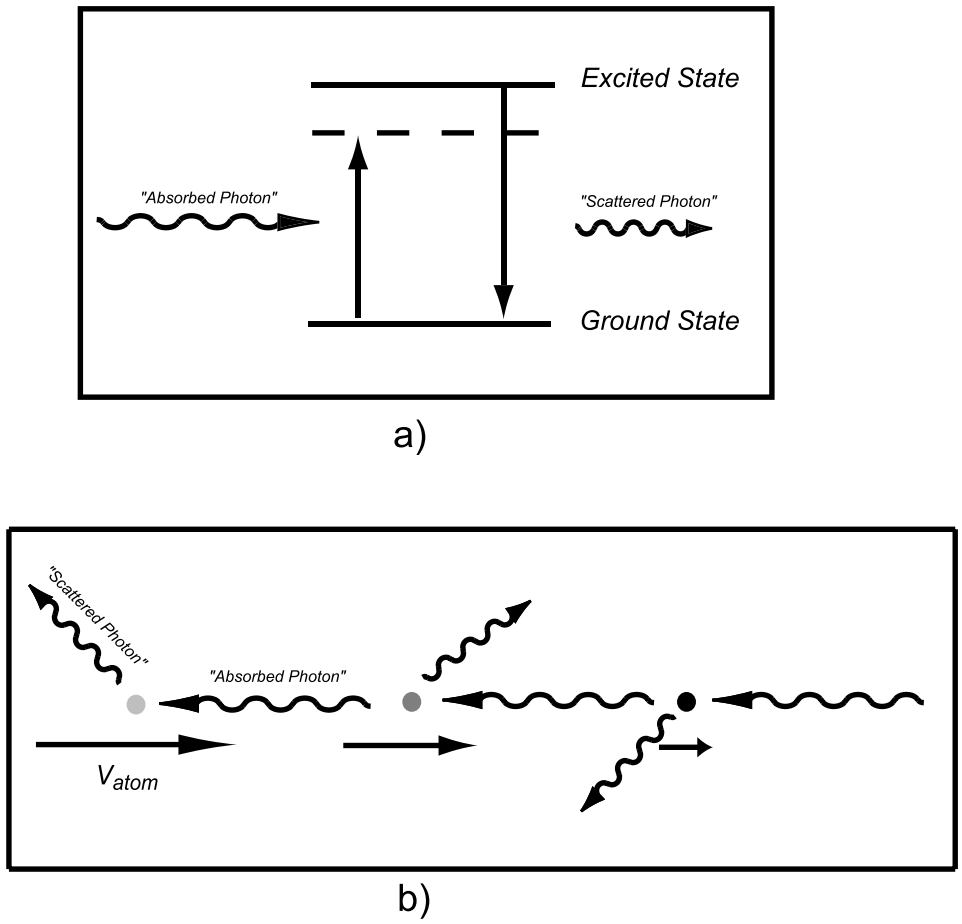

Figure 1.1: Schematic illustrating the basic concept of laser cooling. **a)** Light from the cooling beam is tuned slightly below the natural resonance of the atom to be cooled. As a result, the scattered photons are more energetic (and take away some of the kinetic energy of the atom). **b)** Through many cycles of absorption and (random) emmision, the atom's velocity is significantly reduced and the atom cooled.

Laser cooling has been used to load a number of species into magnetic traps, and has become one of the true "work horses" of low temperature atomic physics. There are, however, some limitations inherent in the laser cooling scheme that leads one to develop alternatives. Laser cooling is a technique that works best for species with simple level structures. Ideally, there would be just two levels, so as to guarantee that an atom once excited will decay back to the initial ground state (and thus be ready to absorb another photon and cool further). Real atoms are obviously more complex, and the possibility exists that once excited, the atom will decay to a state different than the initial state and far enough away in frequency that it will no longer readily absorb the laser light. This problem is shown schematically in fig 1.2.

Additional lasers may be used to "re-pump" the atoms into a state addressable by the cooling laser, however, this quickly becomes prohibitively complex for most atoms and nearly all molecules. For this reason, the atoms most successfully laser cooled have been those with the simplest level structures (notably, the alkali metals and metastable noble gases). In addition to the lack of generality, laser cooling is also limited in the size and density of the samples that it can create (partially due to technological limits on laser power and partially due to fundamental limits set by the absorption cross section of the atom for the light and other factors such as excited state collisions [18]). These considerations limit the size of samples cooled with lasers to orders of magnitude smaller than any fundamental limits associated with the magnetic traps. It is for this reason that while nearly all BEC experiments to date

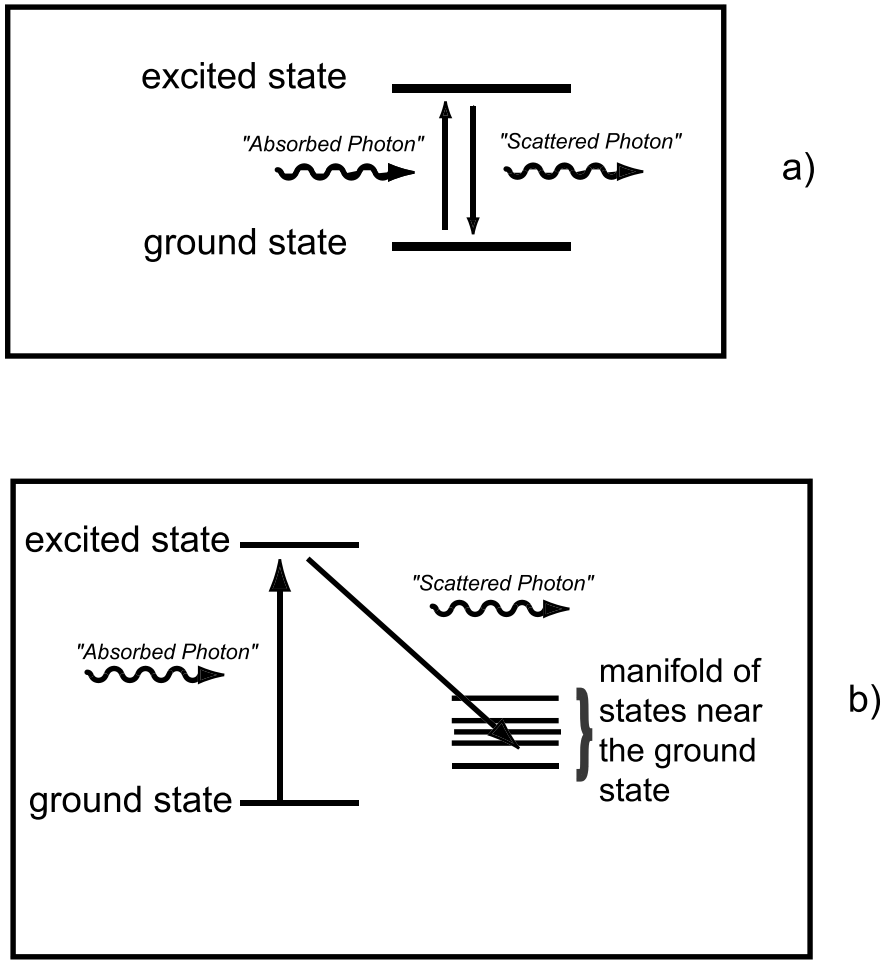

Figure 1.2: a) For laser cooling to work best, the species to be cooled would have only two energy levels ensuring that after absorbing a photon from the cooling beam, the particle would return to the ground state after emmision and be ready to absorb again. b) Real systems are more complex. The possibility exists that once an atom has adsorbed a photon, it will emit at a different frequency and end up in a state sufficiently far from resonance to be transparent to the cooling light.

use laser cooling as the first stage of trap loading, the experiment that produces the largest condensates (with more than 10^9 atoms), the MIT Hydrogen BEC experiment, does not [19].

Thus, while laser cooling has certainly been and will continue to be an important tool for the atomic physicist, it would be valuable to have at our disposal an alternative cooling technique, one that was both more generally applicable to a wider range of magnetically trappable species and that allowed for the production of larger trapped samples. Buffer gas cooling is such a technique.

1.5 Buffer Gas Cooling and Trapping

The idea of buffer gas cooling is to allow the species of interest to be cooled through elastic collisions with a cold gas inside of the trapping chamber. If an adequate density of the buffer gas can be maintained in the trapping chamber at the requisite low temperatures, then enough collisions between the atoms in the sample to be magnetically trapped and the gas will occur to sufficiently cool the atoms before they reach the walls of the trapping chamber (and are lost). The two isotopes of helium, ^3He and ^4He both have sufficiently high vapor pressures at low temperature to provide the required density of buffer gas (see fig. 1.3).

Buffer gas cooling is a very general cooling technique as it does not place any special constraints on the internal structure of the species to be cooled. All that is required is that there be elastic collisions between helium atoms and the species to be

cooled. In addition, there are no special limits on the size or density of the samples that can be cooled in this way[4], and thus buffer gas loading can be used to create very large trapped samples.

1.6 Removing the Buffer Gas

Once atoms have been cooled in a magnetic trap using a cryogenic buffer gas, it is desirable to remove the buffer gas, breaking thermal contact with the "hot" chamber walls. This is necessary for evaporative cooling, for example.

1.6.1 "Old" Method of Buffer Gas Removal

In the original demonstration of buffer gas cooling and trapping, the removal of the ^4He (^3He) buffer gas was accomplished by cooling the temperature of the chamber walls from $\sim$ $800mK$ ($250mK$) to $\lesssim$ $250mK$ ($80mK$). This cooling dramatically reduces the vapor pressure of the helium from a point where the density is sufficient for loading to a point where it no longer provides a significant heat link to the chamber. This technique of "freezing out" the buffer gas worked perfectly well in the first buffer gas loading experiments (the trapping of chromium and europium [20] [21]). There are, however, two undesirable features associated with this way of removing the buffer gas that lead us to develop an alternative approach.

---

[4] We should note a caveat to this statement which is that at very high buffer gas densities ($> 10^{18}cm^{-3}$ or so), the presence of the buffer gas can fascilitate the production of clusters through 3-body collisions.

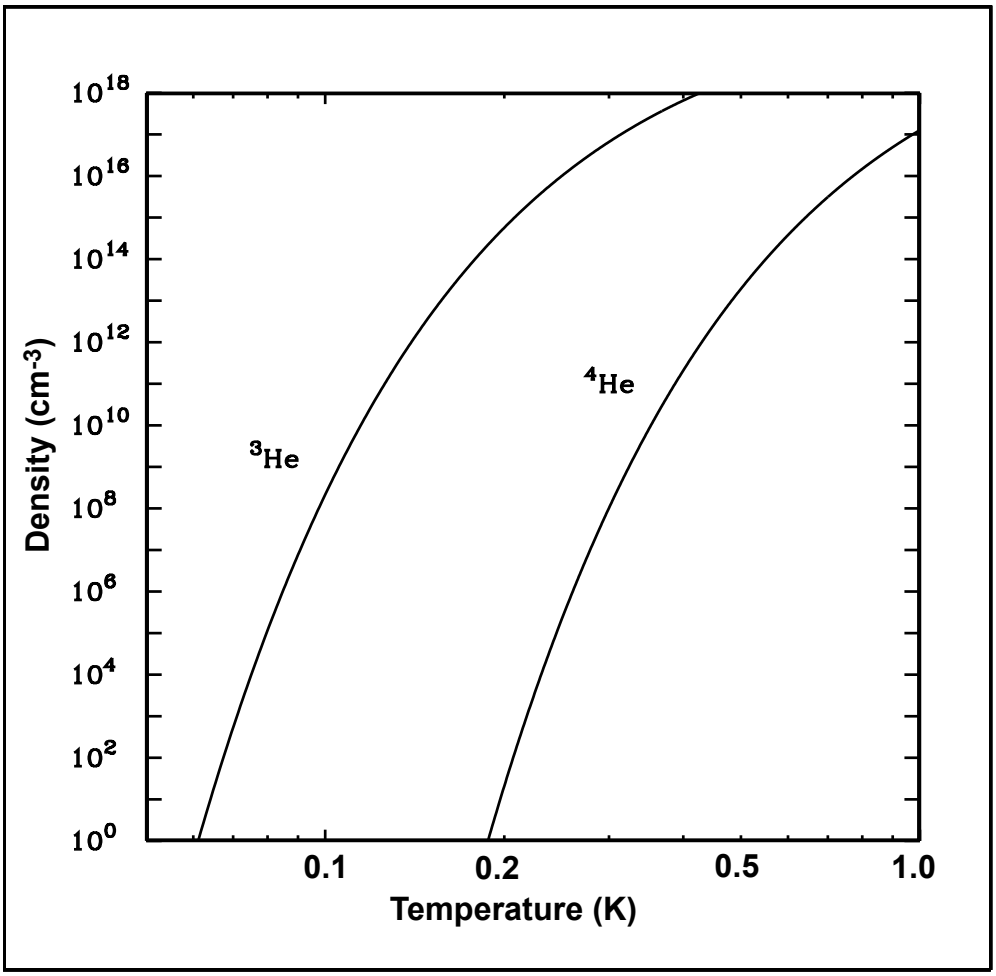

Figure 1.3: Vapor pressures of ^3He and ^4He as a function of temperature. For buffer gas loading, we typically require densities on the order of $n \sim 10^{16} cm^{-3}$ corresponding to temperatures of $\sim 250mK$ and $800mK$ for ^3He and ^4He respectively.

First, the extremely low temperatures required to freeze the gas to the walls of the trapping chamber require the use of a dilution refrigerator (a complex and expensive piece of cryogenics). The requirement to achieve a temperature lower than the magnetic trap depth (and so satisfy our golden rule, eq. 1.1) is a softer one, and if it were the only constraint, would allow the use of a simpler cryogenic refrigerator such as a pumped ^3He or even pumped ^4He system. Secondly, the "old" method of freezing the helium out to the chamber walls takes a relatively long time (several seconds). The evaporation rate (and thus the lifetime) of a trapped sample in the buffer gas is a strong function of the magnetic moment of the species. The greater the magnetic moment, the longer the lifetime. For atoms with large magnetic moments such as Cr and Eu ($6\mu_B$ and $7\mu_B$ respectively), the lifetime of the sample is much longer than a few seconds, allowing for the removal of the buffer gas while retaining most of the trapped sample. For atoms with smaller magnetic moments, however, the lifetime is much shorter (on the order of $\sim 50ms$ for $1\mu_B$ species as we shall see in the next chapter). For such low magnetic moment species, spending a few seconds to remove the buffer gas would result in essentially no atoms left after thermal isolation was achieved. To trap and thermally isolate atoms or molecules with small magnetic moments, the buffer gas must be removed much more rapidly.

1.6.2 "New" Method of Buffer Gas Removal

This thesis describes the next generation buffer gas loading method that accomplishes a much more rapid pump-out of the buffer gas. The key is a fast actuating large aperture cryogenic valve located on top of the trapping chamber. The experimental concept is shown in fig. 1.4. The experimental apparatus will be described in much more detail in chapters 3 and 4, but it is useful to describe the basic concept here. Our atoms are trapped in a cylindrical chamber ~ 3" ($7.6cm$) in diameter inside the bore of a superconducting magnet. To produce a trapped sample, the magnetic trap is energized and buffer gas introduced into the trapping chamber. At this point the valve is closed (to allow the buffer gas to accumulate). Inside of the trapping chamber is a solid precursor of the atom (or molecule) to be trapped. The sample is produced by illuminating the precursor with a very high intensity short duration laser pulse. This process of laser ablation is a very convenient way to introduce atoms into the trap as it allows the source to be placed directly inside of the trapping chamber. The atoms produced in this process are typically quite energetic (having energies of several eV corresponding to thermal kinetic energies of several thousand kelvin). After many collisions, they thermalize to a temperature close to that of the buffer gas and below the trap depth of the magnet.

At this point, the sample is trapped, but it is at a fixed temperature set by the temperature of the buffer gas (which in turn is fixed by the temperature of the walls of the trapping chamber). To break thermal isolation, we then open the valve on

top of the trapping chamber very rapidly (typically in $\lesssim 20ms$). The (non-magnetic) helium quickly rushes out of the chamber to an auxiliary chamber where it is pumped away using a charcoal sorption pump. The magnetic atoms are left behind leaving a trapped, thermally isolated sample.

This technique for faster buffer gas removal offers to greatly extend the range of species amenable to buffer gas trapping and will hopefully realize it's true promise as a "universal" trapping technique for paramagnetic particles. Table 1.3 [22] [23] shows the wide range of paramagnetic atoms on the periodic table with ground state magnetic moments $\geq 1\mu_B$.

Having given this brief introduction to the experimental idea, we will now delve into the details necessary in making this relatively simple idea into a reality. Chapter 2 will discuss some of the theory behind buffer gas loading and will describe a computer model used to simulate the dynamics of particles in a magnetic trap with buffer gas present. This model will provide insight into the tools needed to extend buffer gas loading to $1\mu_B$ species. Chapter 3 will then describe some of the development of these tools and early experiments to test the feasibility of our cryogenic valve, while ch. 4 will describe the integration of these various components into our full trapping apparatus. Chapter 5 will discuss the cool down of the apparatus and results of the first trapping run. Finally, in ch. 6, some preliminary results of the second run of the experiment will be presented. Possible improvements in the apparatus will also be discussed.

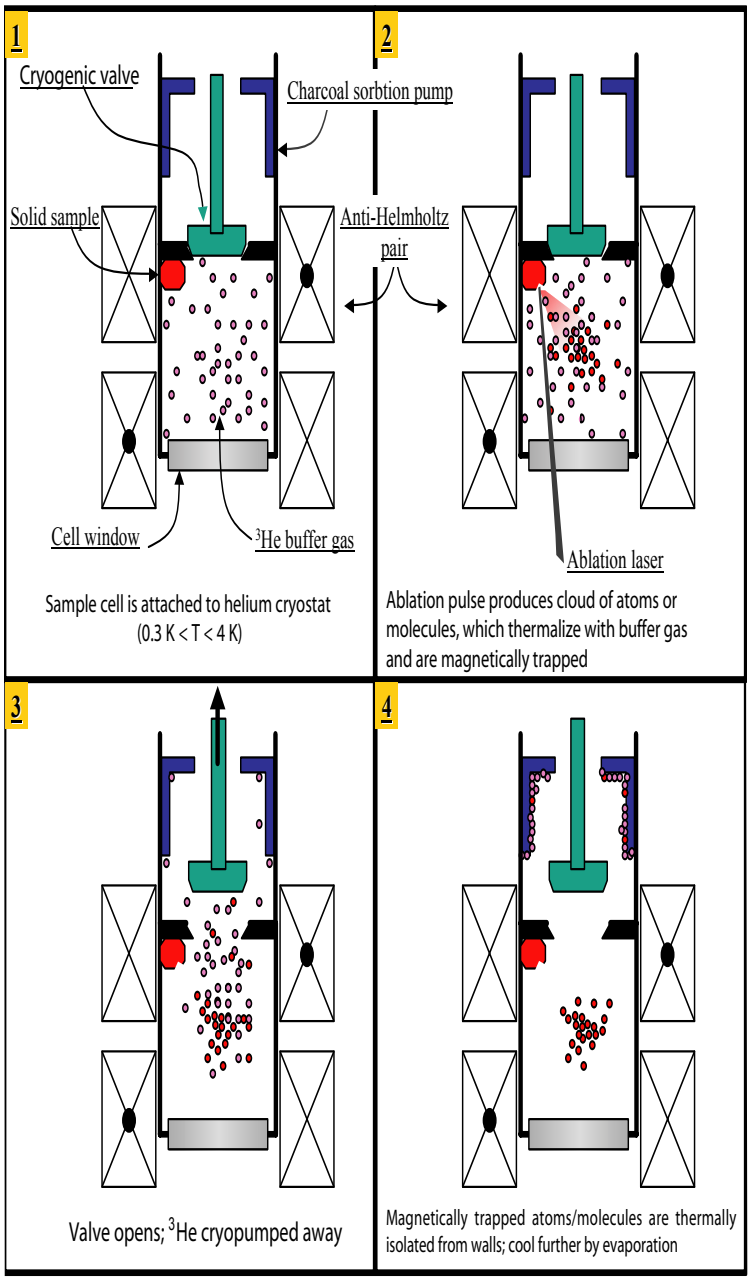

Figure 1.4: Schematic of the basic experimental concept.

State $^{2S+1}L_J$	$\boldsymbol{\mu}$ (in μ_B)	**Element**
$^2S_{1/2}$	1.001	H, Li, Na, K, Cu, Rb, Ag, Cs, Au, Fr
$^4S_{3/2}$	3.003	N, P, As, Sb, Bi
$^6S_{5/2}$	5.006	Mn, Re, Te
$^7S_3$	6.007	Mo, Cr
$^8S_{7/2}$	7.007	Eu
$^2P_{3/2}$	2.001	F, Cl, Br, I, At
$^3P_2$	3.002	O, S, Se, Te, Po
$^6D_{1/2}$	1.669	Nb
$^2D_{3/2}$	1.199	Sc, Y, La, Lu, Ac
$^3D_3$	4.002	Pt
$^9D_2$	5.303	Gd
$^5D_4$	6.005	Fe, Os
$^3F_2$	1.332	Ti, Zr, Hf
$^2F_{7/2}$	3.994	Tm
$^3F_4$	5.002	Ni
$^4F_{9/2}$	6.003	Co, Rh, Ir
$^5F_5$	7.005	Ru
$^1G_4$	3.782	Ce
$^6H_{5/2}$	3.782	Pm
$^3H_6$	6.983	Er
$^6H_{15/2}$	9.938	Tb
$^5I_4$	2.413	Nd
$^4I_{9/2}$	3.290	Pr
$^4I_{15/2}$	8.964	Ho
$^5I_8$	9.933	Dy

Table 1.3: Elements with magnetic moments greater than 1 Bohr Magneton

Chapter 2
Theoretical Considerations for Buffer Gas Loading

2.1 Need For Faster Pump-out

The extension of buffer gas loading to species with small magnetic moments ($1 - 2\mu_B$) requires a more rapid removal of the buffer gas than had been accomplished in previous experiments in which the buffer gas was removed by lowering the temperature of the trapping chamber enough to freeze the helium to the walls. This is evident from trapping data taken in the original buffer gas loading apparatus.

Figure 2.1 (taken from the thesis of Jonathan Weinstein [24]) shows the decay of a trapped Cr sample in a 2.2 Tesla magnetic trap. Cr has a relatively large magnetic moment ($6\mu_B$). As a result, the magnetic trapping potential is very deep for Cr ($\mu \cdot B = 8.8K$), and the lifetime of the sample in the buffer gas is sufficiently long to ensure that most of the atoms survive the several second removal of the buffer gas with most of the atoms remaining. The long time decay in fig. 2.1 is due to Cr - Cr dipolar relaxation (a trap loss process that will be discussed in ch. 5), and not to Cr - He collisions. After several seconds, the helium has been removed and an excellent vacuum achieved in the cell (allowing further experiments on a thermally isolated sample).

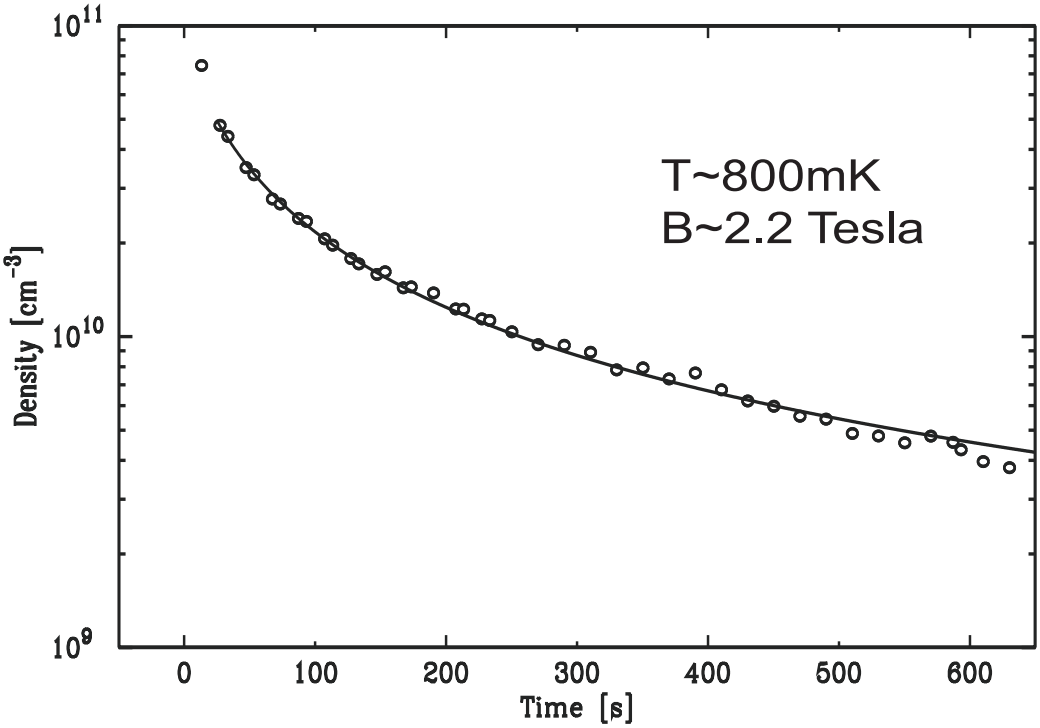

Figure 2.1: Decay of a sample of Cr ($6\mu_B$) atoms. For this trap depth and temperature, η ~11, leading to a sufficiently long lifetime in the buffer gas to allow for a slow (few seconds) pump-out. After several seconds, the helium has been almost completely removed, and an excellent vacuum achieved. The longtime decay is due to Cr - Cr dipolar relaxtion.

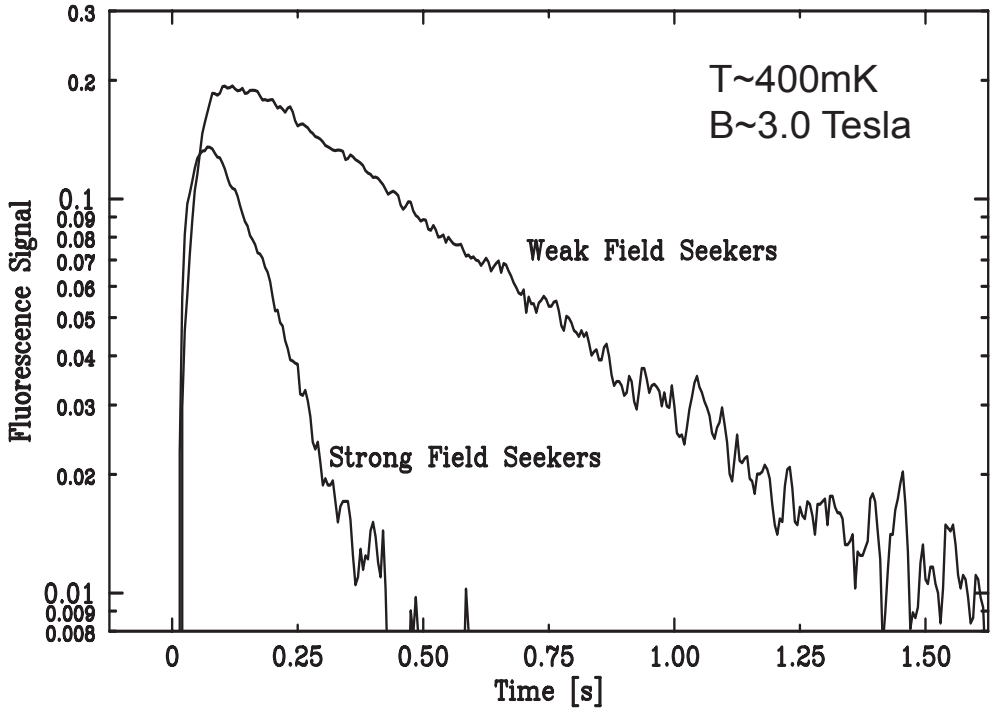

Figure 2.2: Decay of a sample of CaH ($1\mu_B$) molecules. For this trap depth and temperature, η ~5. The lifetime of the trapped weak field seeking state under these conditions is only a few hundred milliseconds. As a result, the buffer gas can not be removed to achieve vacuum and thermal isolation with any appreciable number of molecules remaining.

This is not the case for CaH. CaH has a magnetic moment of only $1\mu_B$. As a result, at the same field, the magnetic trapping potential for CaH is only one-sixth as deep as it would be for Cr. This results in a much shorter lifetime for the CaH sample in the buffer gas. In fact, as seen in fig. 2.2 (also taken from the thesis of Jonathan Weinstein), the CaH sample survives in the buffer gas for only a few hundred milliseconds. This time is much shorter than what is required to remove the buffer gas, and so thermal isolation can not be achieved with any significant number of CaH molecules remaining.

2.2 Simple Analytic Model for Trap Lifetime

We can gain a more quantitative understanding of the experimental conditions necessary to achieve thermal isolation with low magnetic moment atoms through a simple analytic model[5]. The lifetime of a sample of atoms in a buffer gas is a strong function of the magnetic trapping field and the temperature of the buffer gas. High magnetic fields and low temperatures lead to long trap lifetimes. These parameters can be combined to form a dimensionless quantity, η (eta) , that is very useful for characterizing the conditions for magnetic trapping. Eta is defined as follows:

$$\eta = \frac{\mu \cdot B_{trap}}{k_B \cdot T} \tag{2.1}$$

[5] The reader is cautioned that the model that we are about to develop, while leading to some useful insights, is incomplete (for reasons that will be discussed shortly) and a more rigourous numerical investigation of the trap lifetime will be described later in the chapter.

Here, B_{trap} is the difference between the magnetic field at the edge of the trap (typically determined by the position of the walls of the trapping chamber) and the magnetic field minimum in the trap. All of the work described in this thesis was done using an anti-Helmholtz magnetic trap. The anti-Helmholtz trap consists of two identical coaxial solenoids separated by some distance. The currents in the two solenoids are run in opposition. The result is a magnetic field that is zero at the center of the trap (between the two coils) and rises linearly in all directions away from the center. The geometry and field profile of this sort of magnetic trap will be discussed in detail in ch. 3.

To satisfy the first golden rule of trapping (eq. 1.1), we require that, $\eta \geq 1$. As noted in the Introduction, this is a necessary but not necessarily sufficient condition for magnetic trapping. We now proceed to investigate more carefully the requirements on eta. First, note that very generally the lifetime of the sample in the buffer gas can be expressed as:

$$\tau = \frac{N}{\dot{N}} \tag{2.2}$$

Where N is the number of atoms in the trapped sample and $\dot{N}$ the rate at which atoms are lost from the sample. If we assume that any atoms striking the surface of the trapping chamber are lost (an excellent approximation given the large sticking

probability of atoms to cold surfaces), $\dot{N}$ is just the flux of atoms to the chamber walls and is given by the familiar expression:

$$\dot{N} = \frac{\langle n_w \rangle \, vA}{4} \tag{2.3}$$

Where $\langle n_w \rangle$ is the density of the atomic sample (averaged over the chamber wall), v the atomic velocity, and A the surface area of the cell. Because the magnetic trapping potential has a minimum at the center of the trap, it is here that the density of the sample is greatest. We define n_0 as the density at the center of the trap. The density at any point in the trap is given by:

$$n(r) = n_0 \cdot e^{\frac{-U(r)}{k_B \cdot T}} = n_0 \cdot e^{\frac{-\mu \cdot B(r)}{k_B \cdot T}} \tag{2.4}$$

In the linear approximation, the magnitude of the magnetic field is given by:

$$|B| = |B_{trap}| \cdot \frac{\sqrt{r_w^2 + 4z^2}}{r_w} = |B_{trap}| \cdot \sqrt{1 + \frac{4z^2}{r_w^2}} \tag{2.5}$$

Where r_w is defined to be the radius of the cell. Note, in the anti-Helmholtz geometry, B_{trap} is the field at the wall of the cell at $z = 0$. At the cell wall, we have:

$$n(r = r_w) = n_0 \cdot \exp\left(-\eta \cdot \sqrt{1 + \frac{4z^2}{r_w^2}}\right) \tag{2.6}$$

This leads to:

$$\langle n_w \rangle \, A = n_0 \cdot \int_{z_{\min}}^{z_{\max}} 2\pi r_w \exp\left(-\eta \cdot \sqrt{1 + \frac{4z^2}{r_w^2}}\right) dz \equiv n_0 A_{eff} \tag{2.7}$$

Where A_{eff} is the "effective" surface area of the trap.

A plot of the ratio of the effective area to the real cell area is shown in fig. 2.3. Here we have assumed a cell radius of $3.56cm$ and length of $10cm$, equal to what is used in our experiment.

The mean thermal velocity of the atoms in the sample is:

$$v = \sqrt{\frac{3k_B T}{m}} \tag{2.8}$$

Combining eqs. 2.3, 2.7, and 2.8 leads to the following expression for the loss rate:

$$\dot{N} = \frac{n_0 A_{eff}}{4} \cdot \sqrt{\frac{3k_B T}{m}} \tag{2.9}$$

In discussions of magnetic traps, it is common to define an "effective" volume, V_{eff}:

$$V_{eff} = \frac{N}{n_0} \tag{2.10}$$

The effective volume is a useful quantity as it allows us to relate the total number of atoms in the trap to a single density (the peak density) rather than a distribution. Very loosely, it may be thought of as the volume in the cell containing "most" of the atoms in the sample.

For the anti-Helmholtz magnetic trap, the effective volume is related to eta through the following relation.

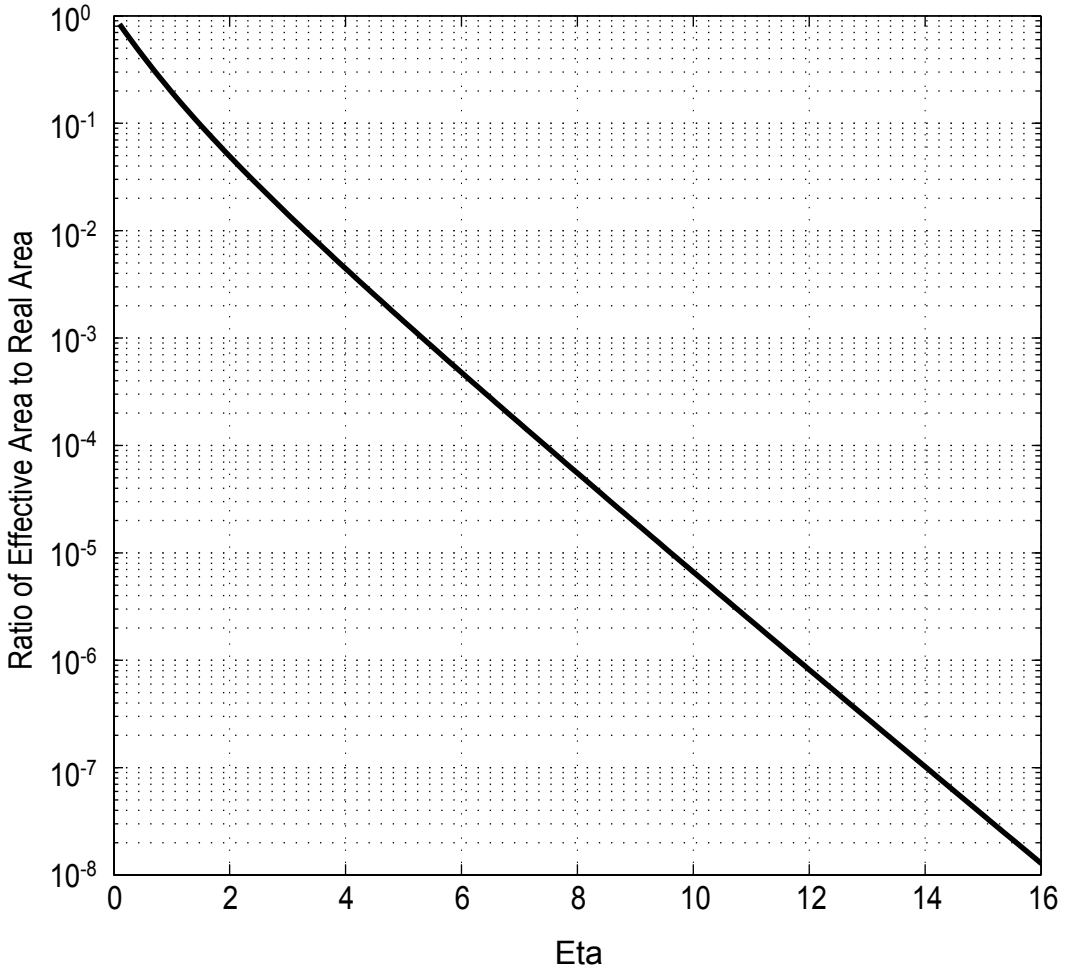

Figure 2.3: Ratio of the "effective" area of the cell (given by eq. 2.7) to the real (physical) surface area of the cell as a function of η.

$$V_{eff} = V_0 \cdot \eta^{-3} \tag{2.11}$$

Where V_0 is the real (physical) volume of the cell.

Combining eqs. 2.10 and 2.11 we have:

$$N = n_0 \cdot V_0 \cdot \eta^{-3} \tag{2.12}$$

Finally, combining equations 2.2, 2.9, and 2.12 gives for the trap lifetime:

$$\tau = \frac{4V_0}{A_{eff}} \cdot \frac{1}{\eta^3} \cdot \sqrt{\frac{m}{3k_B T}} \tag{2.13}$$

Where the effective area, A_{eff} is defined according to 2.7.

A plot of τ versus η for our cell geometry is shown in fig. 2.4. Here, we have assumed a cell temperature of $0.5K$ and a mass, m, equal to that of the Chromium atom.

This simple model is a useful starting point, but it is flawed in at least two respects. First, the approximations leading to eq. 2.13, are only valid in the limit of high eta ($\eta \gg 1$). At low eta, the density distribution of the atoms in the trap is significantly modified by the presence of the chamber walls (something not accounted for in eqs. 2.6 or 2.11). This is a particularly egregious problem since it is precisely the low η regime that we are interested (for working with low magnetic moment atoms).

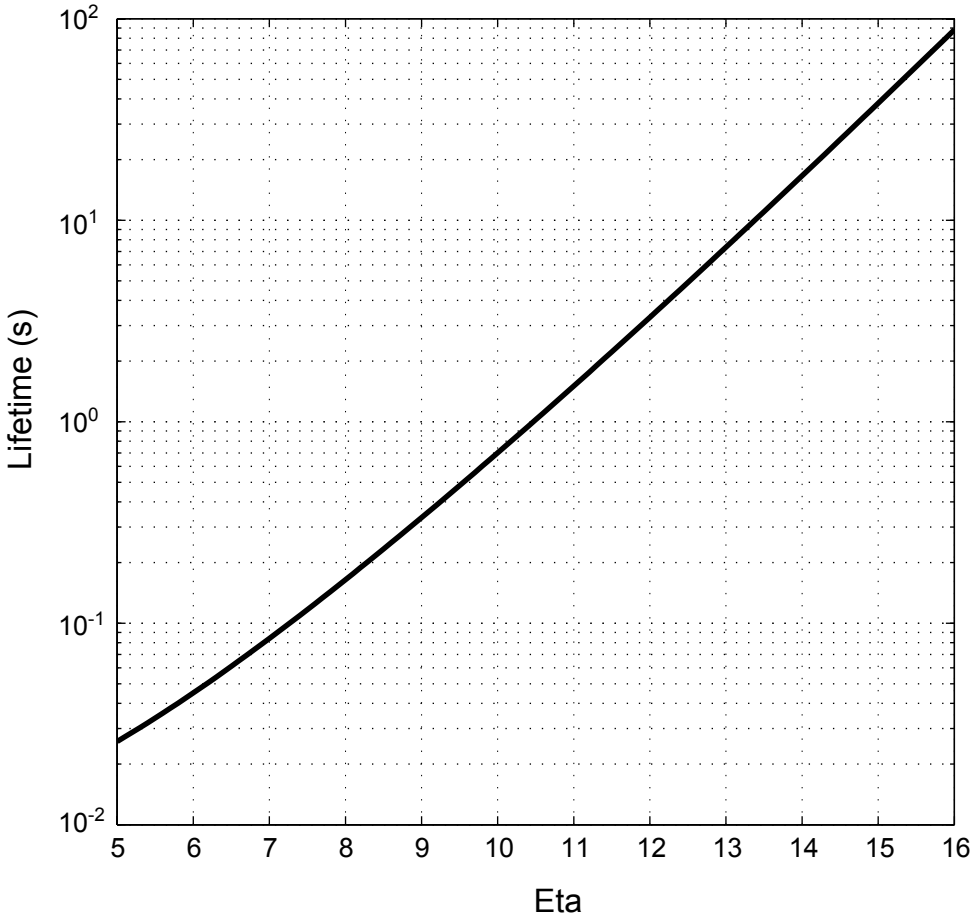

Figure 2.4: Trap lifetime predicted by eq. 2.13 vs. η.

2.3 Diffusion

A second deficiency is this model is that it completely neglects the effect of the buffer gas density on the lifetime of the sample. At high buffer gas densities, the need for the trapped atoms to diffuse through the buffer gas in order to reach the walls of the trapping chamber can lead to lifetimes much larger than predicted by eq. 2.13 (particularly if η is small). The exponential lifetime for diffusion (in the absence of a magnetic field) in a cylindrical geometry is worked out in many sources (see for example [25]) . The result is given below:

$$\tau = 2.1 n\sigma \cdot \sqrt{\frac{k_B T}{m'}} \cdot \left[\left(\frac{2.4}{r} \right)^2 + \left(\frac{\pi}{h} \right)^2 \right]^{-1} \tag{2.14}$$

Where τ is the diffusion time, T and n the buffer gas temperature and density, and σ the cross section for an elastic collision between a He buffer gas atom and the trapped particle. Here, m', is the reduced mass given by:

$$m' = \frac{m_X \cdot m_{He}}{m_X + m_{He}} \tag{2.15}$$

Where X denotes the trapped species. The radius and height of the cylinder are r and h respectively. Eq. 2.14 is plotted (again assuming $r = 3.56cm$ and $h = 10cm$) in fig. 2.5.

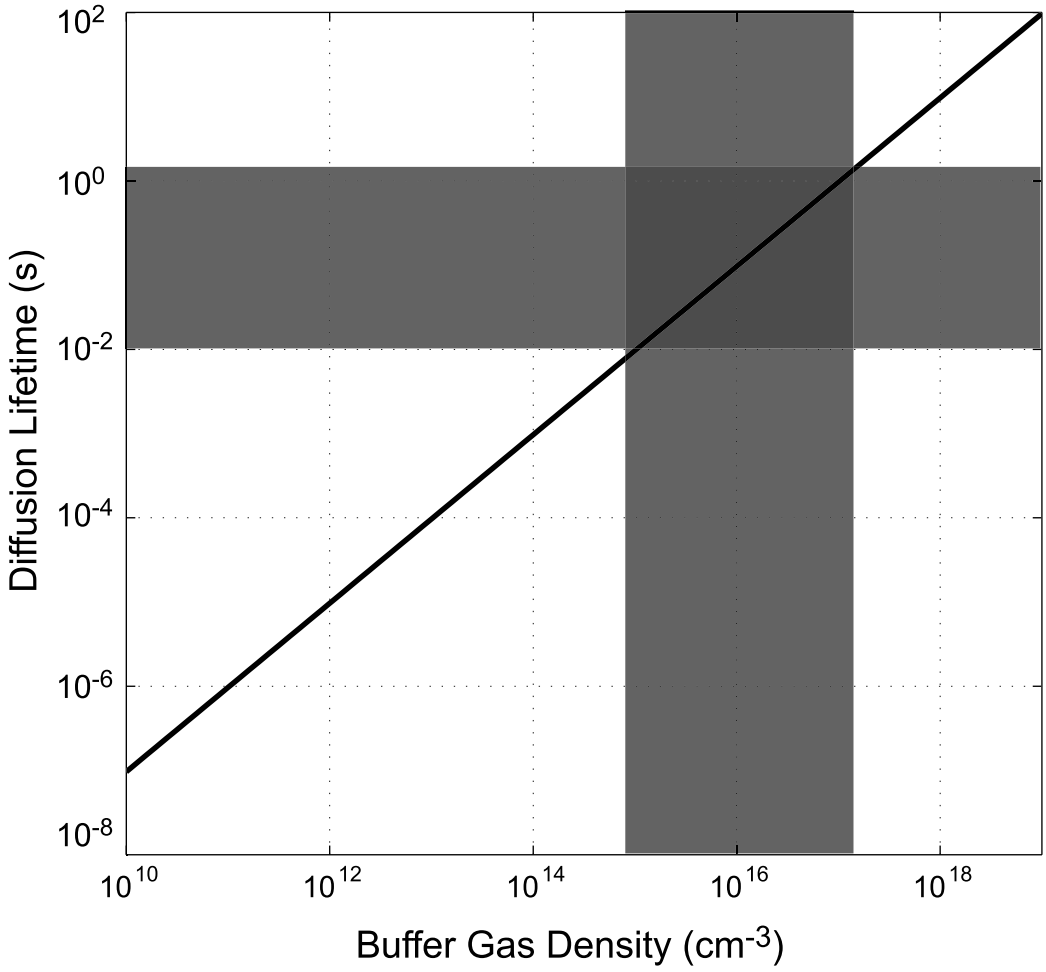

Figure 2.5: Diffusion lifetime vs. buffer gas density predicted by eq. 2.14 assuming a buffer gas temperature of $0.5K$. The shaded area indicates typical loading conditions in our experiments.

2.4 Mean Free Path and Helium Density Required for Loading

Typically, buffer gas loading experiments are done with initial densities in the range: n ~10^{15} to $10^{17} cm^{-3}$. This density is chosen to ensure that there be a sufficient number of collisions to allow the initially hot atoms to thermalize with the buffer gas before they reach the chamber walls (and are lost). Typically, ~100 collisions is sufficient[6]. To see how this number of collisions leads to the above mentioned densities, we first consider the distance a particle travels between collisions given on average by the mean free path, l as [26]:

$$l = \frac{\bar{v}}{\bar{V}} \cdot \frac{1}{n\sigma} \tag{2.16}$$

Here, $\bar{v}$ is the the mean velocity of the species to be trapped, and $\bar{V}$ is the mean relative velocity between the species to be trapped and the helium buffer gas atoms. In general,

$$\bar{V} \approx \sqrt{\bar{v}^2 + v_{He}^2} \tag{2.17}$$

Since the atoms begin quite hot, they initially are moving much faster than the helium atoms, and so, $\bar{V}$ and $\bar{v}$ are essentially the same. Thus, eq. 2.16 reduces to:

---

[6] This figure of 100 is meant only as an order of magnitude estimate on the number of collisions required for thermalization and should not be taken too literally. A more precise analysis (as is given in [4]) indicates that the temperature decreases exponentially to that of the buffer gas with a characteristic number of collisions (i.e. $1/e$) given by $(M_x + M_{He})^2/2M_X M_{He}$, where M_X is the mass of the atom and M_{He}, the helium mass. For example, if we are using a ^3He buffer gas (so that $M_{He} = 3$), then this number is ~10 for Cr ($M_X = 52$) and ~5 for Na ($M_X = 23$).

quantity	Before Thermalization	After Thermalization
$\bar{V}$	$\sim \bar{v}$	$\sim \sqrt{\frac{m_X}{m_{He}}}\bar{v}$
l	$\sim \frac{1}{n\sigma}$	$\sim \sqrt{\frac{m_{He}}{m_x}} \cdot \frac{1}{n\sigma}$

Table 2.1: Before and after thermalization

$$l \approx \frac{1}{n\sigma} \tag{2.18}$$

When, the atoms have thermalized, the helium is moving faster (because of its lower mass), and $\bar{V} \approx v_{He} = \sqrt{\frac{m_X}{m_{He}}}\bar{v}$. This gives for the mean free path after thermalization:

$$l \approx \sqrt{\frac{m_{He}}{m_x}} \cdot \frac{1}{n\sigma} \tag{2.19}$$

These differences between the "before thermalization" and "after thermalization" cases are summarized in table 2.1. For the purposes of estimating the density required for loading, we are interested in the first region (before thermalization has occurred). Initially, the particles are quite energetic, and there motion through the helium buffer gas is predominantly ballistic, so that the distance travelled after N collisions is $\sim N \cdot l$. To place a lower bound[7] on the minimum density required for loading, we will assume ballistic transport throughout the thermalization process. If

[7] This minimum required density is important since we are ultimately limited by the vapor pressure curves of helium as to how much buffer gas we can place in the cell. Ideally, we would load at as low a temperature possible (to get the maximum η). Eventually, however, the vapor pressure becomes prohibitively low to produce an adequate buffer gas density in the cell. Conversely, the buffer gas denisty can be made arbitratily low (simply by limiting the total quantity of He allowed into the cell).

we assume as before, that we require ~100 collisions for thermalization, then we have:

$$100 \cdot l < D \tag{2.20}$$

Where D is a typical cell dimension. If we take, for example, $D \sim 5cm$, then we need a collisional mean free path, $l \lesssim 0.5mm$. Assuming a typical elastic cross section[8] of $\sigma \sim 10^{-14}cm^2$ [27] [24], then eq. 2.18, implies that we need a buffer gas density $n \gtrsim 2 \cdot 10^{15}cm^{-3}$. In practice, the optimal loading density is found to be somewhat higher than this (closer to n ~$10^{16}cm^2$) probably due to local heating and hydrodynamic effects caused by the ablation plume.

To this point, we have discussed two different factors influencing the lifetime of a trapped sample. We have presented an analytic model (valid at high η) for the lifetime in the absence of a buffer gas, and we have given the diffusion lifetime (in the absence of a magnetic field) as a function of buffer gas density. We could go further and combine these effects to form a more complete picture of the dynamics valid for large η and high buffer gas density (see for example [24]), but we are still lacking a description valid for lower η's and low buffer gas densities. Such a description is needed because we are interested in working with lower magnetic moment species (low η's) and because during the course of the pump-out the buffer gas density is reduced to essentially zero. When the mean free path for a collision becomes com-

[8] It is worth mentioning here that the precise value of the collisional cross section σ is not particularly important. It is the mean free path that matters, and the buffer gas density can be adjusted accordingly (within the limits of the vapor pressure curves).

parable to and larger than the size of the trapping chamber, at $n \lesssim 10^{14} cm^{-3}$ for example, the motion of the atoms through the buffer gas is no longer diffusive.

There is one further significant deficiency in our model so far. Not only can the helium buffer gas extend the lifetime of the trapped sample (compared to what it would be if no buffer gas were present), it can reduce it as well. Collisions with helium atoms can promote atoms in the sample to energies above the depth of the magnetic trap. If the temperature of the buffer gas is low (compared to the trap depth), then the likelihood that a collision increases the energy of the trapped particle is small. For a relatively high density, however, the collision *rate* may be high enough to compensate for this low probability. As we shall see, the lifetime of the sample experiences a minimum in the intermediate density regime where the collision rate is still relatively high but where the mean free path is no longer short so that diffusion does not extend the trap lifetime.

2.5 Monte Carlo Simulation of Trajectories

In order to overcome the deficiencies of the simple analytic models described above, we developed a Monte Carlo computer simulation of the buffer gas loading process. The idea of the Monte Carlo model is to track the trajectories of an ensemble of atoms in the magnetic trap under various experimental conditions (trap depth, buffer gas temperature, buffer gas removal time etc...). From the results of these sim-

ulations, we can better understand the technical requirements we face in extending buffer gas loading and trapping to less magnetic species.

In these simulations, atoms are generated with some reasonable set of initial conditions. Typically, a random velocity is picked for each atom under the constraints of a Maxwell-Boltzman distribution at some specified temperature. The atoms' x, y, and z coordinates are typically generated so as to randomly distribute the sample throughout the trap volume[9]. The atoms' trajectories are then followed in the trap for some set amount of time or until they escape (i.e. the trajectory takes the atom outside the confines of the trapping chamber). In all of the simulations described in this thesis, the interaction between trapped atoms is neglected. This is a reasonable approximation since the low density of the atoms in the trap (in comparison to the initial helium density) implies that the atom-atom collision rate (both elastic and inelastic) will be much smaller than the atom-He collision rate. Even when the helium density is reduced and this condition no longer holds, the time scale for loss due to dipolar relaxation (the dominant inelastic trap loss mechanism) is long compared to any pump-out times that we will consider. In any case, it is the effect of the buffer gas (and buffer gas removal) on the trap lifetime that we are most concerned with and that we have some control over. As to the atom-atom interactions, we are stuck with whatever nature provides.

---

[9] Based on previous spectroscopic data, it seems a reasonable approximation to assume that the ablation pulse uniformly distributes the atoms throughout the trapping volume of the cell.

2.5.1 Simulation Description and Diagnostics

To begin, we describe some diagnostic results of the simulations. First, we consider the situation without any buffer gas at all. In this case, the particle trajectories are simply integrated in the potential of the magnetic trap [28]:

$$V_{trap} = -\mu \cdot B \tag{2.21}$$

In order to simplify (and speed up) the computer integration, we expand the magnetic field analytically keeping only the first order term. This is a very good approximation throughout most of our trap volume. In the case of the anti-Helmholtz trap, this gives for the field magnitude [11]:

$$|B| = \alpha\sqrt{x^2 + y^2 + 4z^2} \tag{2.22}$$

Where α characterizes the strength of the field[10].

We are generally concerned with the dynamics of the maximally trapped "weak field seeking" state in which the magnetic moment is counter-aligned with the field and has its maximum projection along the field axis. In this case, eq. 2.21, gives:

$$V_{trap} = |\mu| \cdot \alpha\sqrt{x^2 + y^2 + 4z^2} \tag{2.23}$$

This is the potential that is integrated to determine the trajectories of the atoms. For a conservative potential as the one above, the force on a particle is given by:

[10] Note that the field gradient in the z direction is twice that in x or y. This satisfies the Maxwell equation $\nabla \cdot B = 0$.

$$F = -m\nabla V_{trap} \tag{2.24}$$

In our case, this leads to:

$$F_x = -\mu\alpha \cdot \frac{x}{\sqrt{x^2+y^2+4z^2}}, \quad F_y = -\mu\alpha \cdot \frac{y}{\sqrt{x^2+y^2+4z^2}}, \tag{2.25}$$

$$Fz = -\mu\alpha \cdot \frac{4z}{\sqrt{x^2+y^2+4z^2}} \tag{2.26}$$

The numerical integration of the trajectories is done using an adaptive step size engine that employs the Runge-Kutta method [29]. Some results of these simulations are shown below. With no buffer gas present, the particles follow simple classical orbits in the trap. Because the trapping potential is conservative, the particle neither gains nor loses energy while in the trap. Thus, if the atom's initial energy is below the trap depth, it will remain in the trap forever (as in fig. 2.6) while if the particle has enough energy to escape, it will leave the trap (perhaps after a few orbits as seen in fig. 2.7). Under these simple conditions, the particles kinetic and potential energy simply oscillate between certain fixed values as the atom traverses its orbit in the trap.

This situation is changed when buffer gas is present. The atoms trajectory is altered from time to time through collisions with helium atoms as shown in fig. 2.8. While the total energy of the system is always conserved, the energy of the atom will in general be changed with each collision. We now describe how the effect of buffer

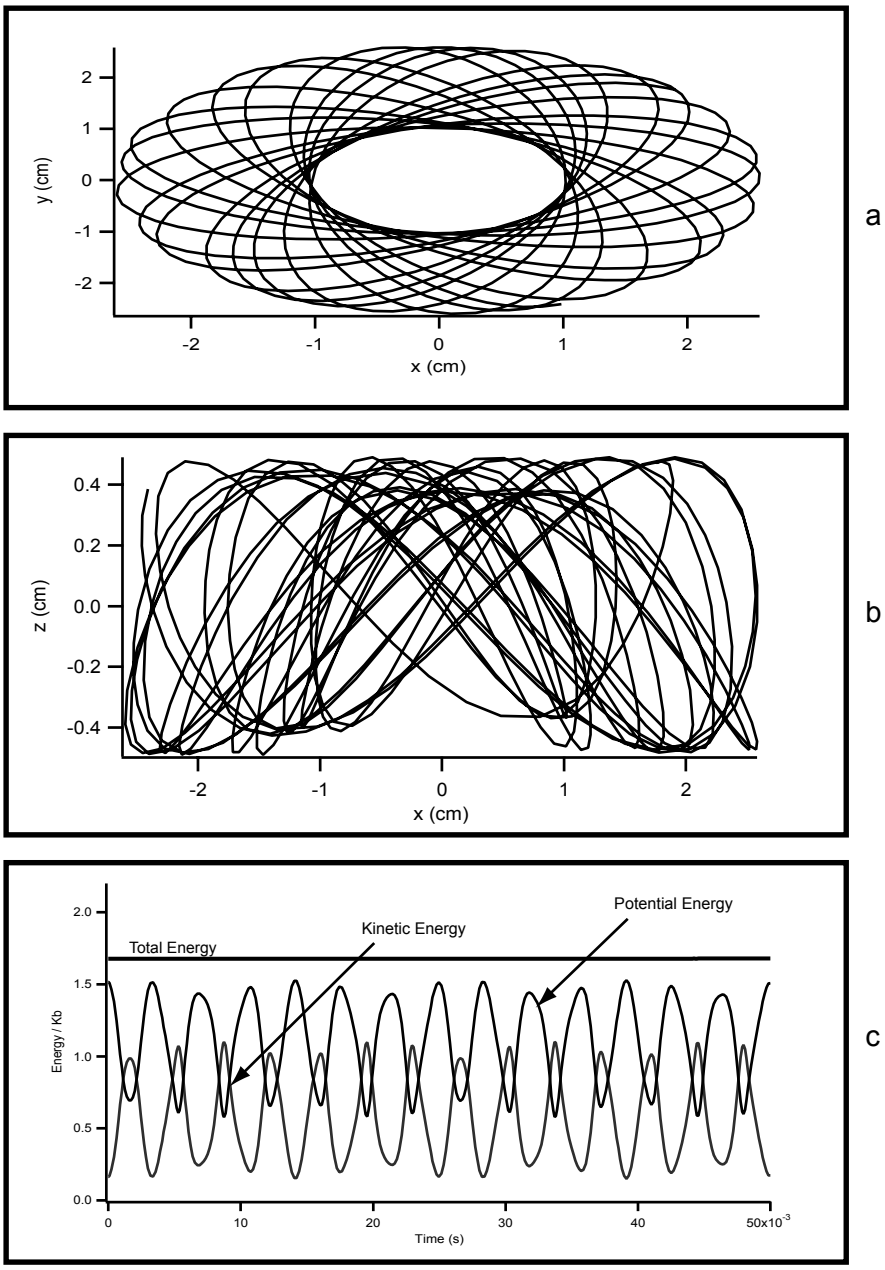

Figure 2.6: Simulation of a particle in a magnetic trap with no buffer gas present. **a)** particle position in the x, y plane. **b)** particle position in x, z plane. **c)** The initial energy of the particle (1.68 K) is below the trap depth (1.74 K). Because the potential is conservative, the particle's total energy is conserved, and the particle remains trapped forever.

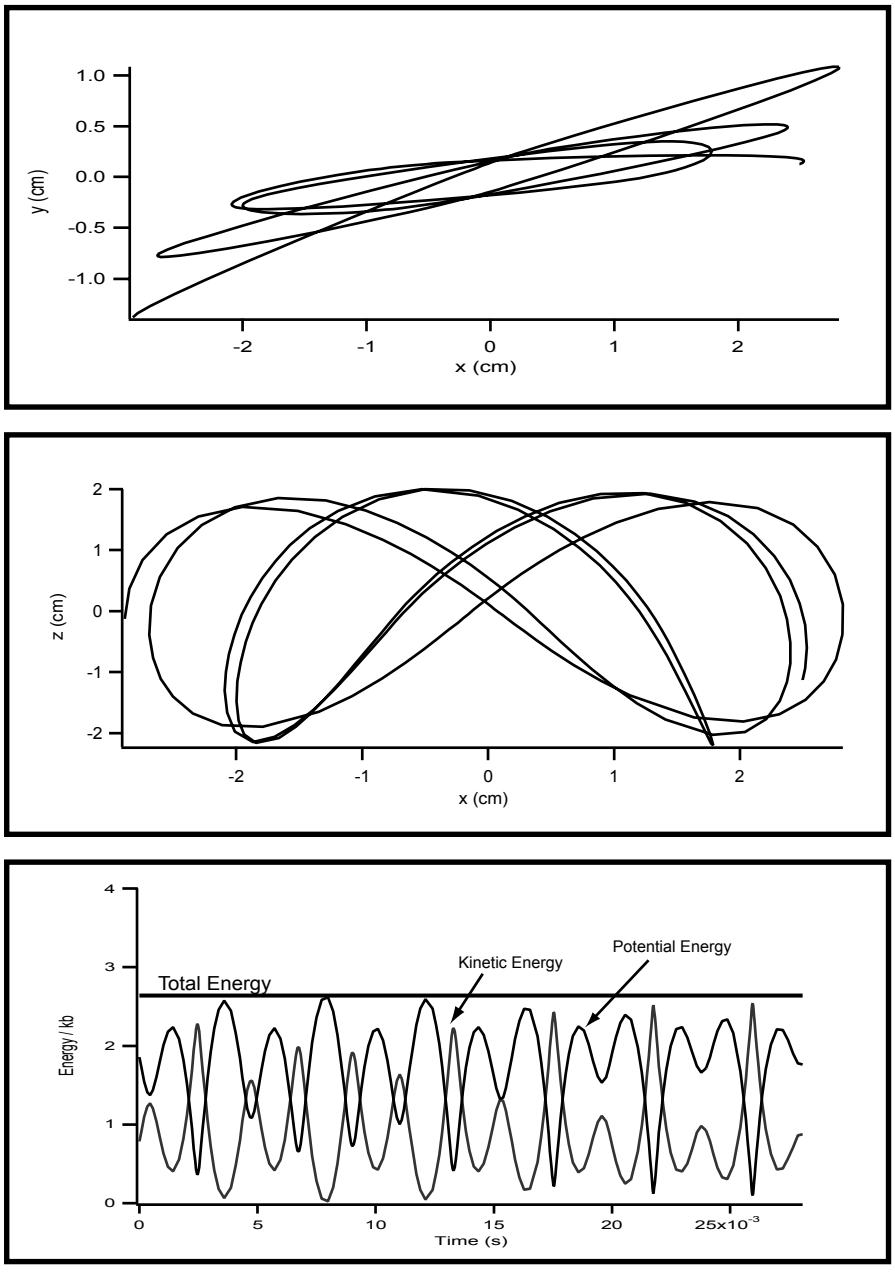

Figure 2.7: Simulation of a particle in a magnetic trap with no buffer gas present. **a)** particle position in the x, y plane. **b)** particle position in x, z plane. **c)** The initial energy of the particle (2.64 K) is greater than the trap depth (1.74 K). The particle leaves the trap after a few orbits.

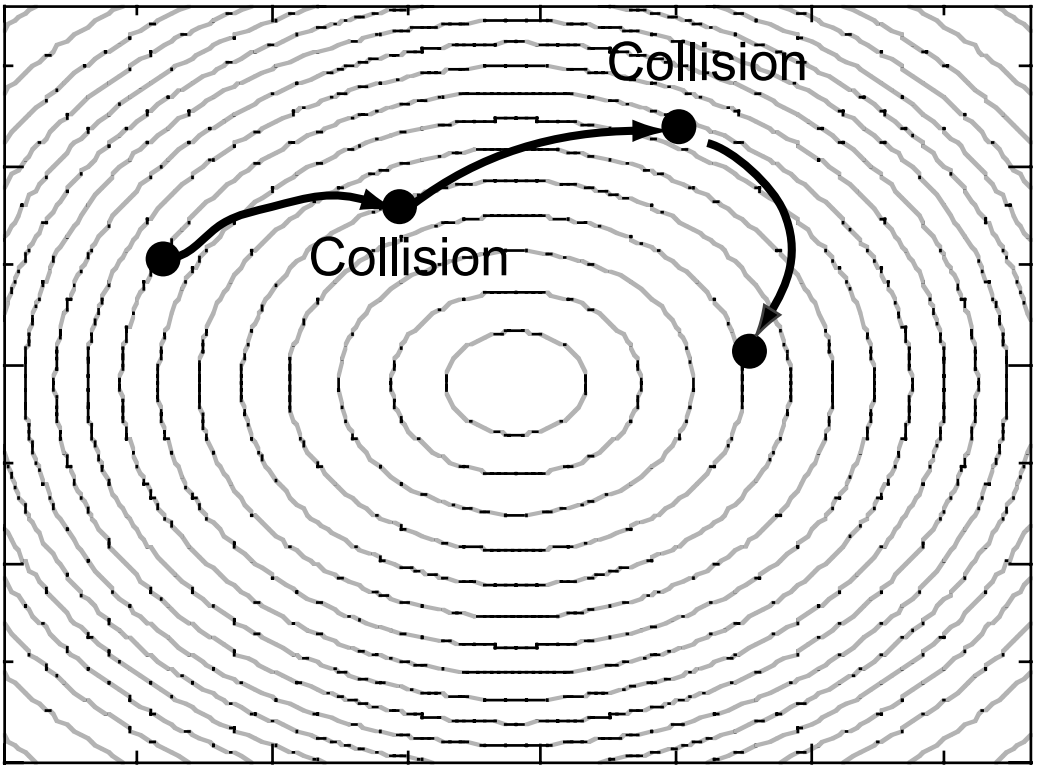

Figure 2.8: Illustration of the simulations that include collisions with He buffer gas atoms. The atoms trajectory is integrated in the magnetic trap (whose field contours are shown in grey), until the simulation determines that it is time for a collision at which point the particles trajectory is altered.

gas collisions is accounted for in our simulations. The time between collisions is calculated as follows:

2.5.2 Time Between Collisions:

As a first estimate, one might choose the time between collisions to be constant and equal to the mean time between collision given by [26].

$$\tau = \frac{1}{n\sigma\bar{V}} \tag{2.27}$$

where again, $\bar{V}$, is the mean relative velocity, $\bar{V} = \sqrt{v_X^2 + v_{He}^2}$

In reality, the time between collisions is not constant, but follows a distribution whose mean is given by eq. 2.27. To more accurately choose times between collisions, we first define a function $p(t)$ that is the probability that an atom survives a time t (measured from its last collision) without undergoing another collision. This function is plotted in fig. 2.9.

$$p(t) = e^{-t/\tau} \tag{2.28}$$

It can be shown [26] that eq. 2.28, implies that the probability of having a collision between times t, and $t+dt$, is independent of t and simply equal to $(1/\tau)\cdot dt$. We can define a new function, $P(t)$ that is the probability that a particle has a collision between times t and $t + dt$ after surviving a time t without suffering a collision.

$$P(t)dt = p(t) \cdot (1/\tau)dt = \frac{e^{-t/\tau}}{\tau} \cdot dt \tag{2.29}$$

We note that

$$\int_0^\infty P(t)dt = 1 \tag{2.30}$$

as required by normalization.

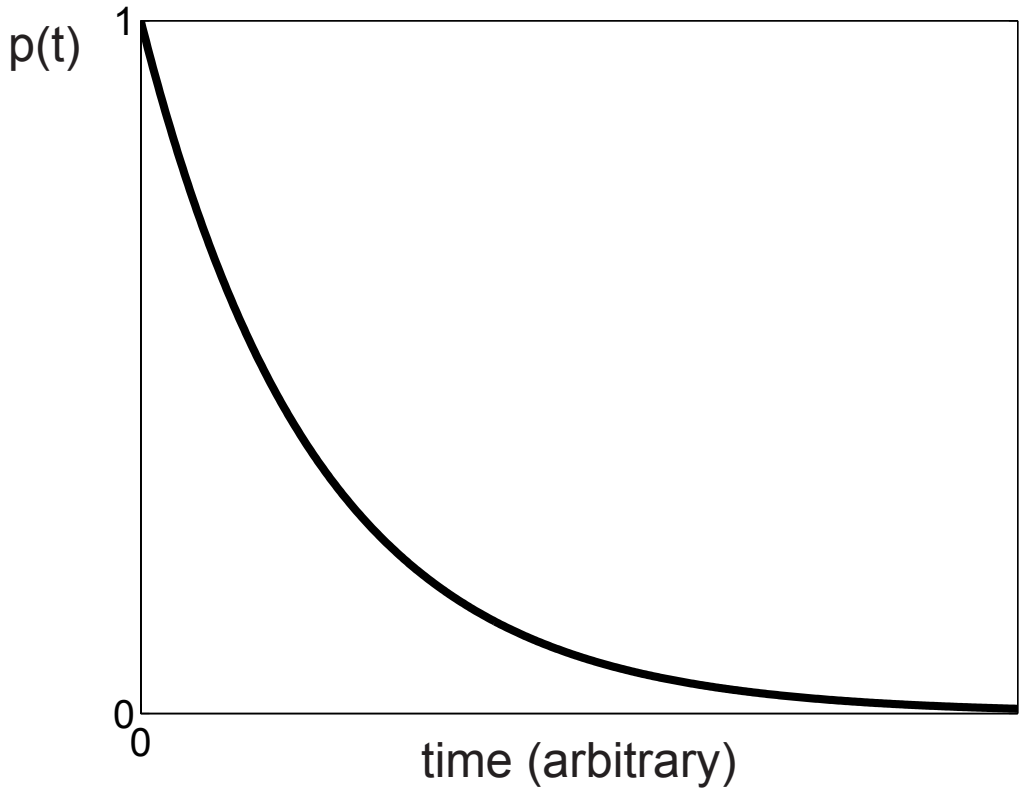

Figure 2.9: Probability that an atom survives a time, t (since its last collision) without suffering another collision.

A prescription for choosing collision times, t, should reproduce this probability distribution. The methods used to invert such probability distributions are well known (see for example [29]). First, we define a function, I, that is the indefinite integral of the probability distribution. This function is plotted in fig. 2.10.

$$I = \int_0^{t'} P(t)dt = 1 - e^{t'/\tau} \tag{2.31}$$

A random value for this function (uniformly distributed on the interval [0,1]) is chosen, and the corresponding collision time calculated according to:

$$t_{\text{col}} = \tau \cdot \ln(1 - Ran[0,1]) \tag{2.32}$$

Where $Ran[0,1]$ is the random number.

If a large number of collision times are calculated using the above formula, the distribution of eq. 2.29 should be produced.

2.5.3 Handling the Collision

Eq. 2.32 gives an expression for the time between collisions. Once the elapsed time before the next collision has expired, the computer routine handles the collision in the following way. First, to avoid confusion, note that the cross section σ that we are using is the cross section to randomize the velocity of the atom in the center of mass (CM) frame[11].

[11] Obviously, there are other cross sections that one may define (to randomize the velocity in the LAB frame for example as discussed in appendix B), and it is important that we understand the process involved when dealing with a particular value for the cross section. Our choice of defining

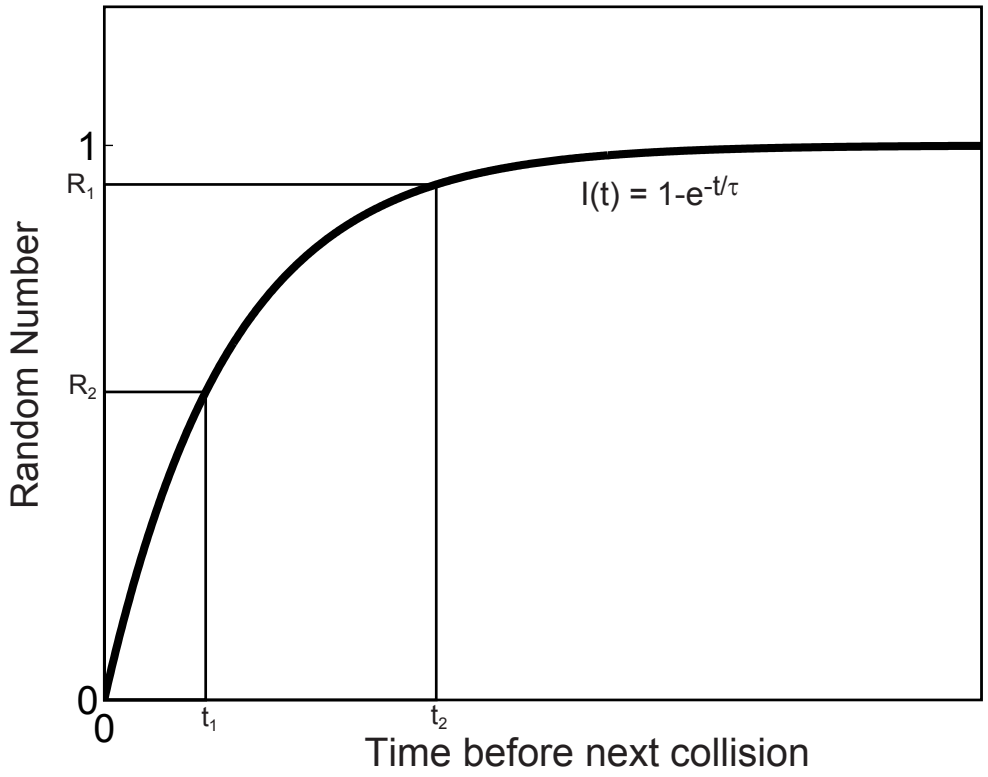

Figure 2.10: The collision times are generated by first generating a random number uniformly distributed on the interval between 0 and 1 (R_1 or R_2 for example), and then calculating the corresponding collision time (t_1 or t_2) according to eq. 2.32.

1) A Helium atom is "generated" with a random velocity, ($\overline{^{He}U}$ in fig. 2.11), consistent with a Maxwell-Boltzman distribution at the specified buffer gas temperature.

2) A series of dynamic transformations are done to compute the new velocity of the atom after the collision [30]. These transformations are shown schematically in fig. 2.11. First, we transform away the He velocity (i.e. we transform to a frame where the He particle is at rest). This allows us to deal with the relatively simple case of a particle colliding with a stationary target. We'll call this the "modified" LAB frame.

3) We now transform to the center of mass frame in this new system (leading to the velocities $\overline{^{X}V'}$ and $\overline{^{He}V'}$ in fig. 2.11).

4) By definition, the collision randomizes the particles velocity in the center of mass frame. Hence, we now choose a new random velocity $\overline{^{X}V'_{new}}$, (equal in magnitude to the old velocity) for the atom in the center of mass frame (see fig. 2.12).

5) We transform back to the modified LAB frame (leading to $\overline{^{X}V_{new}}$ in fig. 2.12).

6) Finally, we transform back the initial He velocity (thus returning to the initial (unmodified) LAB frame).

---

the elastic cross section, σ, as the cross section for randomizing the atom's velocity in the CM frame is in keeping with common convention and will be used throughout this thesis unless otherwise stated.

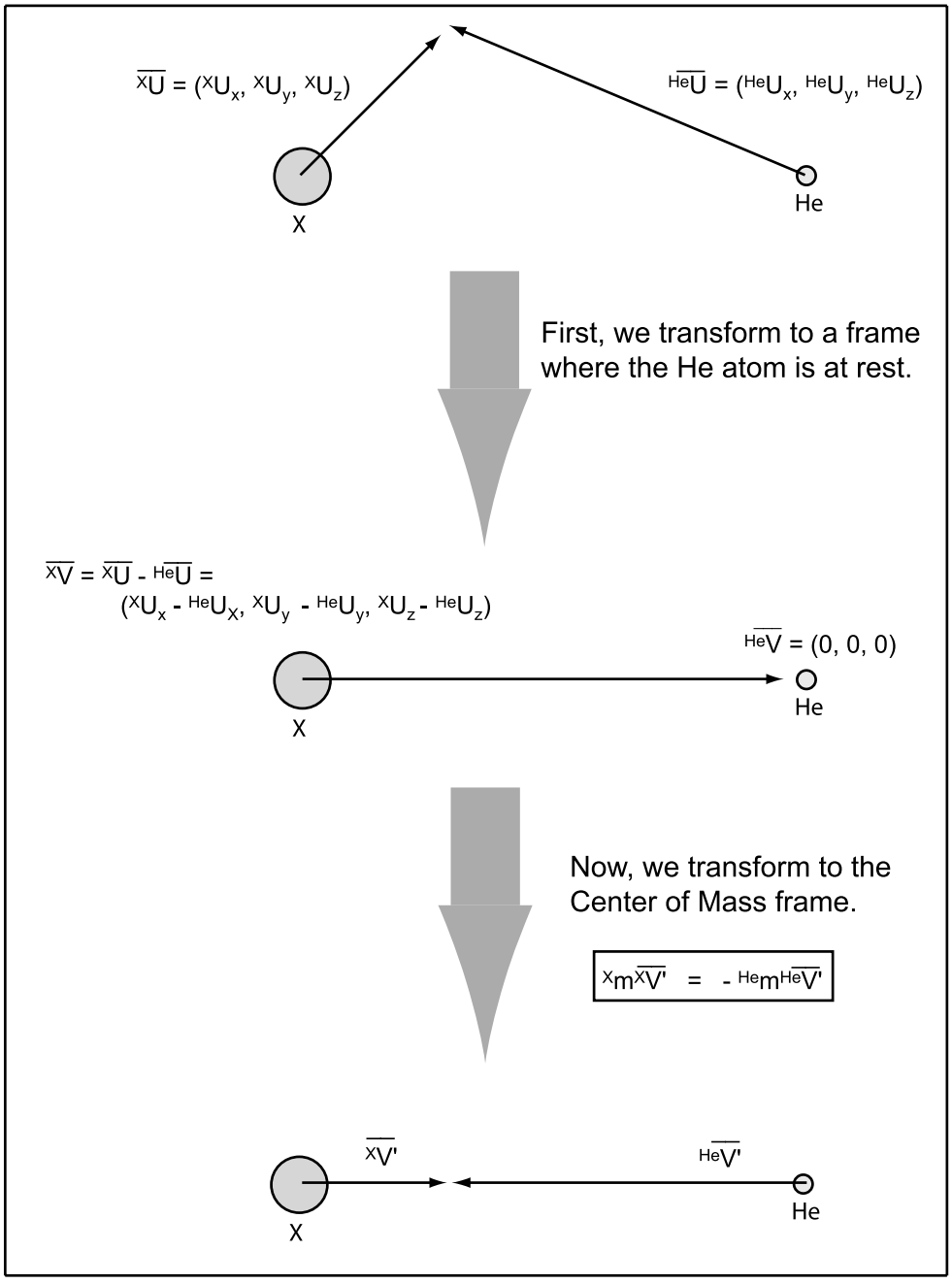

Figure 2.11: Illustration of the transformations in steps 2) and 3) for handling the collisions between the atoms in our trap and the He buffer gas atoms.

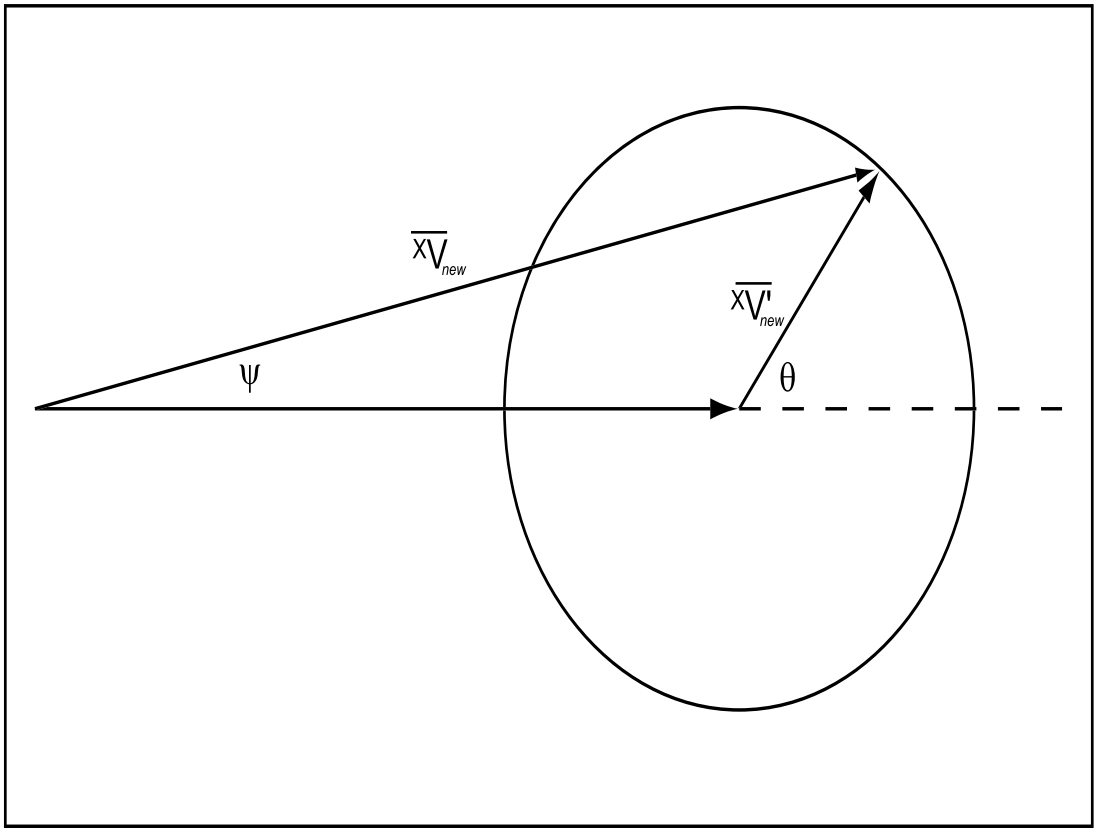

Figure 2.12: By definition, the elastic collision randomizes the velocity in the center of mass frame. Hence, the new velocity in the CM frame is chosen with magnitude equal to the old (and equal to the radius of the circle shown above) with a new random angle, θ. In this figure, ψ, is the scattering angle in the LAB frame. Because in general the He buffer gas atoms are light compared with the trapped particles, ψ will be a small angle, and it will take many collisions to randomize the velocity in the LAB frame (see appendix B).

7) The collision is now complete, and a new random number and corresponding time for the next collision are generated.

8) The particle trajectory in the trapping field is integrated until it is time for the next collision.

These steps are repeated to compute the particle's trajectory until the elapsed time for the simulation has expired (or the particle has left the trap).

Shown below (fig. 2.13) is an example of a single $1\mu_B$ atom's trajectory (in this case with $M_X = 23$ as for Na) in a buffer gas (of density $n = 10^{16} cm^{-3}$) in the presence of a $2.6T$ $(1.74K)$ deep trap. Also shown in this figure is the thermalization of the atom from an initial temperature of $10,000K$ to that of the buffer gas (at $1K$). According to this figure, after about $30\mu s$ or so, the atom is almost fully thermalized[12]. Approximately 40 collisions have occurred at this point. This is in good agreement with the ~5 collisions required for a "1/e" reduction in the temperature predicted in [23]. The last part of fig. 2.13 shows the fluctuations in the particles energy due to collisions with the buffer gas. The kinetic energy fluctuates "wildly" due to these collisions while the potential energy varies more

[12] In actual experiments, we might expect this thermalization time to be longer due to the local heating of the buffer gas from the ablation plume. In our simulations, we have assumed a fixed buffer gas temperature, and so neglected this effect. This approximation is reasonable since for our purposes, we can almost always regard the thermalization of the atomic sample as instantaneous (i.e faster than any other relevant timescale) and so the exact time required for thermalization (whether it be tens of microseconds or milli-seconds) is not particularly relevant. In fact, the early time dynamics of the ablation plume would be extremely difficult to model accurately at all. Suffice to say that experiments indicate that to a good approximation, the ablation plume uniformly distributes the sample throughout the chamber and this sample quickly thermalizes with the buffer gas (provided there is an adequate density of course). These are the initial conditions assumed for the bulk of the simulations that are described.

smoothly (since in the short mean free path regime, the magnetic field does not vary much from collision to collision).

Now that we have highlighted the basic elements of the simulation routines, we are ready to apply it to a careful investigation of the dynamics of the sample in the buffer gas. This will lead to a better understanding of the conditions necessary for extending the buffer gas loading technique to less magnetic atoms.

2.5.4 Lifetime of the Sample in the Buffer Gas (and the "Valley of Death")

To begin, we look at the decay of a sample of simulated atoms at various fixed (in time) buffer gas densities. One set of decay curves is shown in fig. 2.14. Here, the trapping field is $2.6T$ ($1.74K/\mu_B$), the buffer gas temperature, $0.5K$, and we consider a $1\mu_B$ species. It is assumed as usual, that the atomic sample begins uniformly distributed throughout the chamber. Each particle's velocity is chosen randomly from a Maxwell distribution at the temperature of the buffer gas. Figure 2.14 shows that there is a rapid initial loss of part of the sample. This is due to the escape of those atoms from the Maxwell distribution that began with energy greater than the trap depth. This loss is more pronounced at low buffer gas densities[13] (where the mean free path is long and thus it is unlikely that a collision with a helium atom will

[13] In the extreme case where the buffer gas density is zero, the part of the sample with intital energy greater than the trap depth is lost almost immediately (after at most a few orbits in the trap) while the remaining part (those atoms with energy lower than the trap depth) remain trapped forever (neglecting atom-atom interactions). This situation is approached for the low buffer gas densities in fig. 2.14.

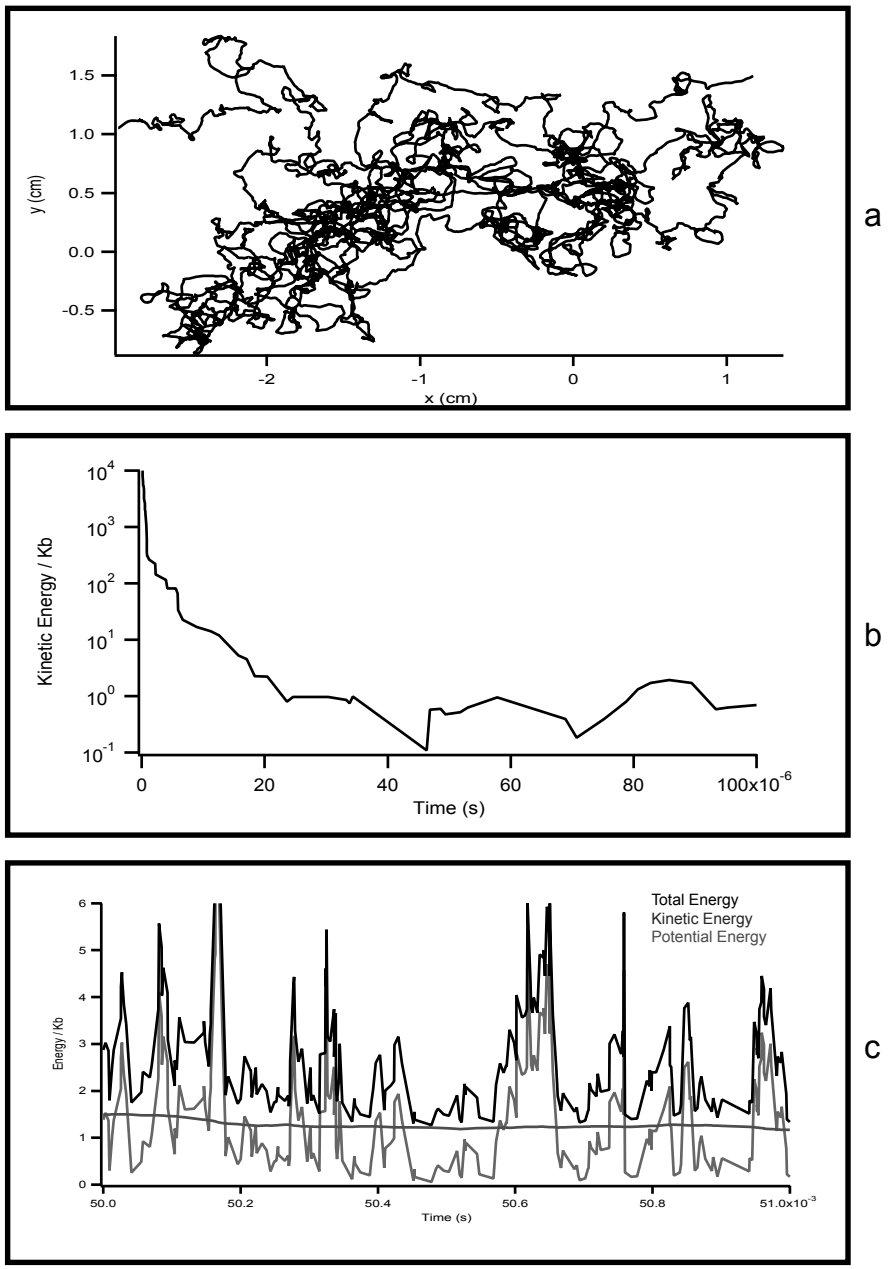

Figure 2.13: **a)** Trajectory of a particle in a buffer gas of density, $n = 10^{16} cm^{-3}$ (corresponding to a mean free path of $0.01 cm$) and temperature of $1.0 K$. **b)** Thermalization of the particle. The initial particle energy is $10,000 K$. After $\sim 30\ \mu s$, (and 40 collisions) the particle has come to about the same temperature as the buffer gas. **c)** Because collisions with the buffer gas may increase or decrease the energy of the trapped particle, the particle's total energy is no longer conserved.

save the particle before it leaves the trap). After this "purification" of the sample, there is further loss on a time scale that varies with different buffer gas densities.

In figure 2.15, we plot the (exponential) lifetime of the sample using the data from fig. 2.14 along with data from another set of simulations (where the trap depth is increased to $4.0T \longleftrightarrow 2.7K/\mu_B$). This figure provides a great deal of insight into the challenge we face in removing the buffer gas. As expected, at high buffer gas densities (where the mean free path is much shorter than any chamber dimension), the lifetime is long (due to diffusion) and increases with increasing buffer gas density. Likewise, at low buffer gas densities (where the mean free path is much longer than any chamber dimension), the lifetime is long and increases with decreasing buffer gas density as we move to better and better vacuum (and lower collision rates with the He atoms) in the chamber.

The requirement that we have adequate thermalization of the sample necessitates that we begin buffer gas loading at the relatively high densities on the right side of the graph in fig. 2.15. In order to achieve thermal isolation and a good vacuum, we must reduce the buffer gas density after loading until we are well into the region on the left side of this graph.

To do this, we must pass through a density region where the lifetime of the sample experiences a minima. This "valley of death" is one of the main obstacles that must be overcome if we are to save most of the atoms during the pump-out of the buffer gas. The reason for this minima in the lifetime has been discussed above.

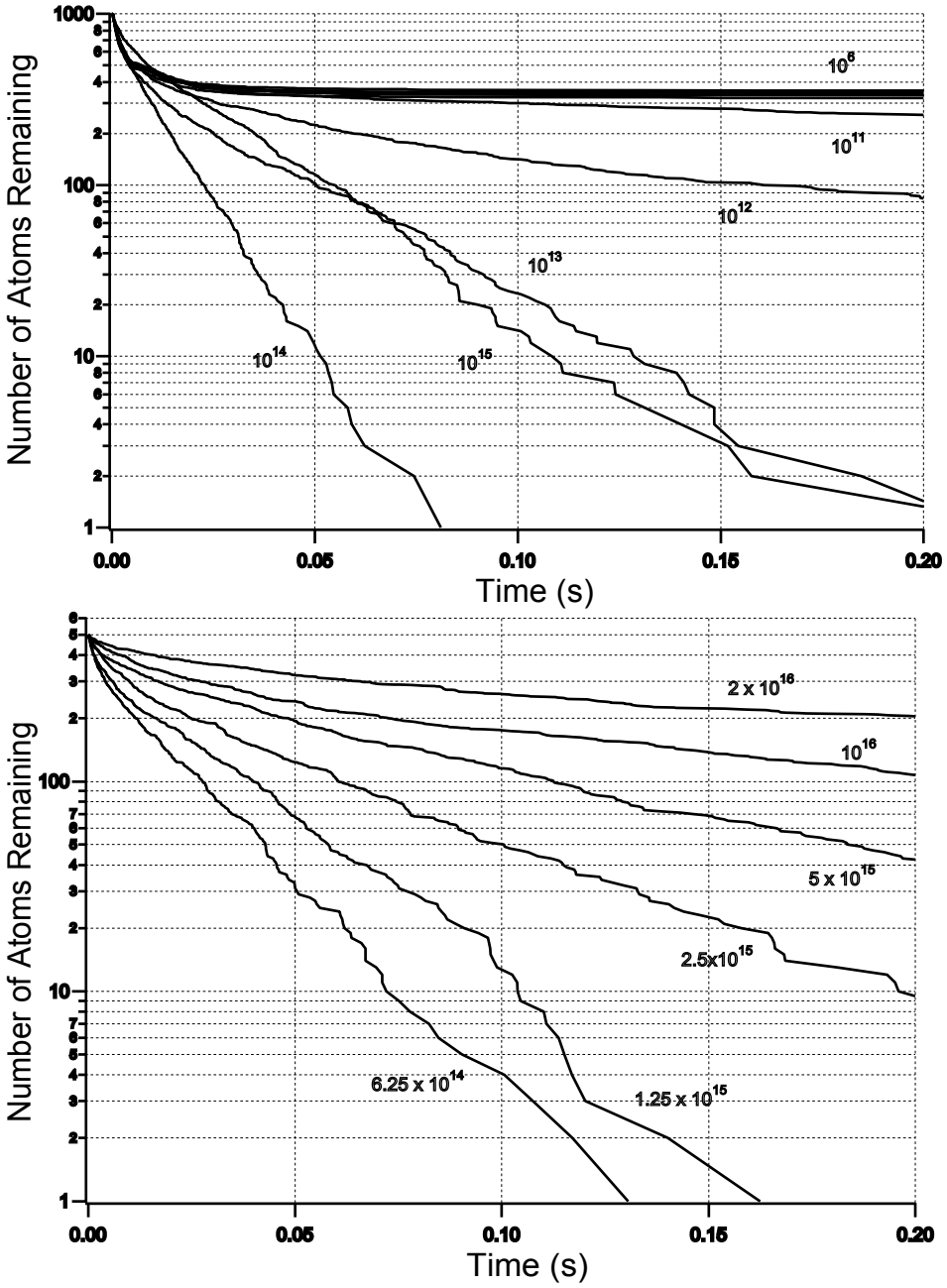

Figure 2.14: Decay of a sample in a buffer gas of various densities. For these simulations, the magnetic trapping field is $2.6T$ while the buffer gas temperature is set to $0.5K$. At high buffer gas densities, the trap lifetime increases with increasing buffer gas density (as expected from diffusion). Eventually, this rolls over, and at low buffer gas densities, the trap lifetime increases with decreasing density (as expected in a better and better vacuum). In between these two regimes, there is a minimum in the trap lifetime.

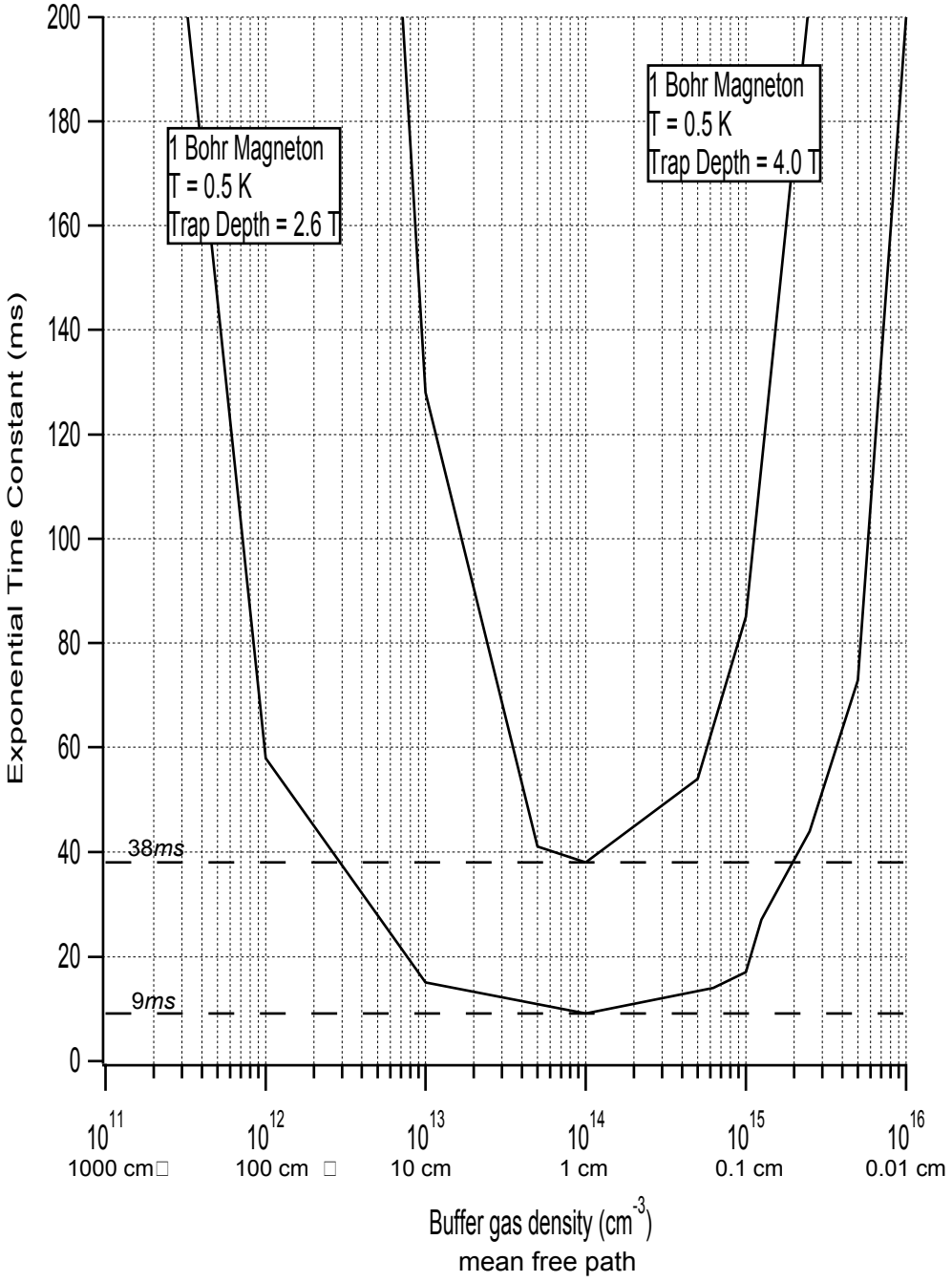

Figure 2.15: Lifetime as a function of buffer gas density for two different sets of simulations. Both deal with a $1\mu_B$ species in a buffer gas at $0.5K$. In one, the trap depth is $2.6T \longleftrightarrow \eta = 3.5$ and in the other, the trap depth is $4.0 \longleftrightarrow \eta = 5.4$. Notice the pronounced minimum in the lifetime in the intermediate mean free path regime (where the mean free path is comparable to our cell dimensions). This minimum lifetime in large part determines the slowest tolerable pump-out of the buffer gas.

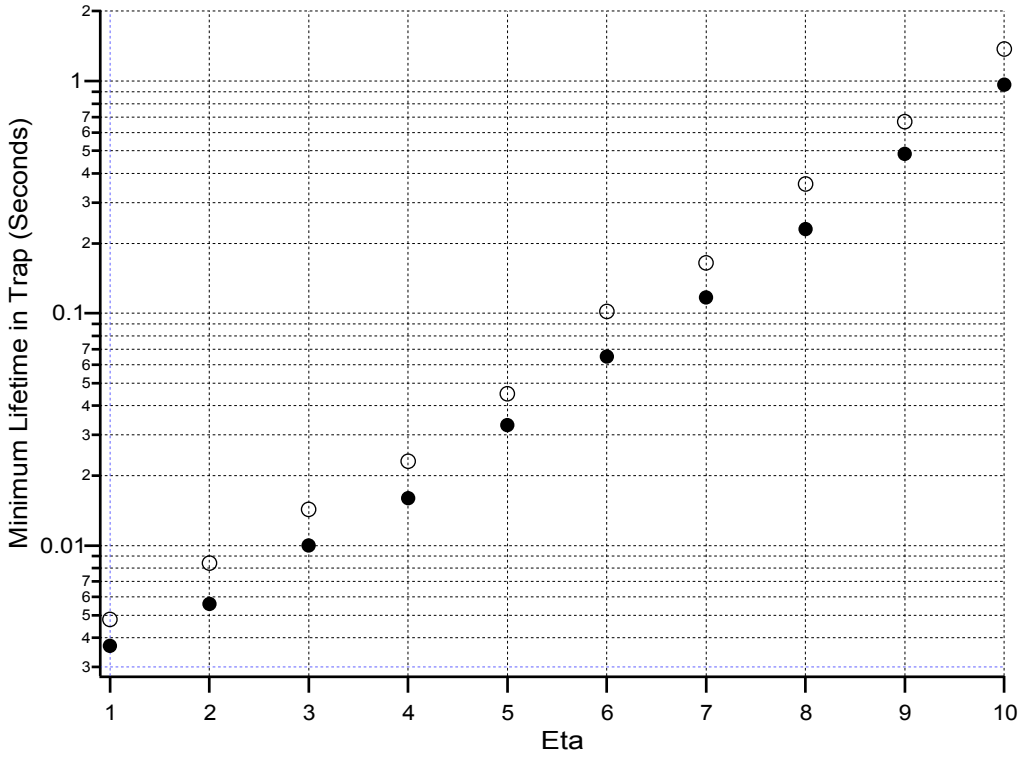

Figure 2.16: Plot of the minimum lifetime vs. eta of the trapped sample in the buffer gas at two temperatures, $0.2K$ (open circles) and $0.4K$ (solid circles).

It occurs in the intermediate density regime where the collision rate is high, but the mean free path still relatively long.

Clearly, if too much time is spent in this regime where the lifetime is close to it's minimum, then most of the atoms will be lost during the pump-out of the buffer gas (no matter how large the lifetime of the sample is at the initial loading density). It is this minimum lifetime, then, that in large part determines how fast the gas must be removed. A plot of this minimum lifetime as a function of eta is shown in fig. 2.16.

In all of the cases, the minimum occurs around a buffer gas density of $\sim 10^{14} cm^{-3}$ (corresponding to a mean free path of $0.1mm$).

2.5.5 Simulations Including Buffer gas Pump-out and the "Wind"

By looking at graphs like those in figures 2.15 and 2.16, we can get a pretty good idea for the speed necessary to remove the buffer gas under different magnetic field and temperature conditions. In order to make this more concrete, we now simulate the pump-out of the buffer gas by adding time dependence to the buffer gas density.

Before doing this, it is necessary to add one other feature to the simulation to account for the net motion of the helium out of the trapping chamber during the pump-out, an effect colloquially known as "the wind." During the pump-out, the helium buffer gas atoms acquire a drift velocity in the direction of the valve aperture roughly equal to the length of the cell, l, divided by the (exponential) pump out time, τ.

$$v_{drift} \approx l/\tau \tag{2.33}$$

To account for this, we add the drift velocity to the random thermal velocity of the He atoms generated during a collision. Physically, the effect of this wind is to restrict the fastest desirable removal time of the buffer gas. If there were no wind present (i.e. the density were somehow to magically decrease with no bulk motion of the gas), then it would be advantageous to remove the buffer gas as quickly as

possible. Because of the wind, however, if the drift velocity in eq. 2.33 is too high, then the atoms will be swept out of the trap along with the He[14].

How successful we are at retaining the atoms in the trapped sample through the buffer gas removal process will depend on many factors including temperature, trap depth, initial buffer gas density, pump-out time as well as cell size, aperture geometry etc... It would be hopeless to attempt a full exploration of this parameter space. Fortunately, we have past experiments to guide us somewhat, and available technology restricts the feasible values for many of these parameters. In our simulations we will focus our attention to the range of values (temperature and trap depth for example) that we have access to given present technological limits. We may be lead to push these limits somewhat in the design of the actual experiment, but we'll assume that we can't improve too greatly on existing cryogenic or superconducting technology. Also, we know from prior experiments that buffer gas loading requires initial densities of at least $n \gtrsim 10^{15} cm^{-3}$ for efficient thermalization. These considerations will be our guide in choosing the different experimental conditions that we simulate.

In fig. 2.17, we show a set of simulations of samples of $1\mu_B$ atoms in a $4T$ deep magnetic trap in the presence of a buffer gas at $0.5K$ (the resulting eta being, $\eta = 5.4$). Four series of simulations are shown with initial buffer gas densities ranging from $5 \times 10^{14} cm^{-3}$ to $5 \times 10^{15} cm^{-3}$. This example illustrates several points. First, as expected, we do better with a low initial buffer gas density (as this requires

[14] This is in fact essentially how a diffusion pump works (using He rather than oil).

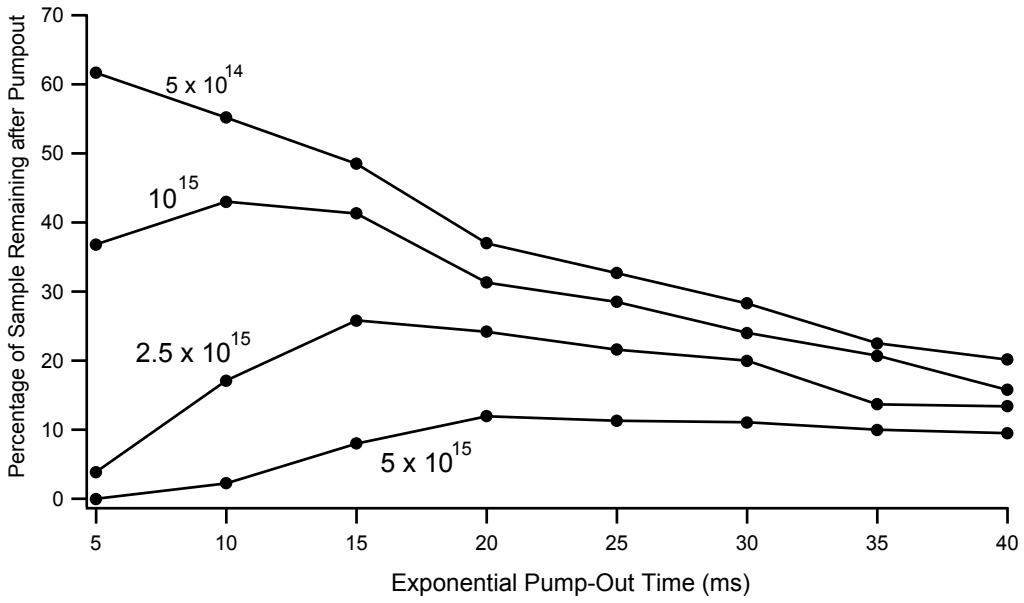

Figure 2.17: Results of some simulations on the effect of removing the buffer gas on a sample of trapped atoms. The trap depth used in these simulations was $4T$ while the temperature of the buffer gas was fixed at $0.5K$. A range of initial buffer gas densities (from $5 \times 10^{14} cm^{-3}$ to $5 \times 10^{15} cm^{-3}$) were chosen. As expected, more atoms are retained at low initial densities (since there is less buffer gas to remove). Also, the "wind" is more of an issue for the higher buffer gas densities (because the greater amount of He removed at higher densities leads to a greater drag force on the trapped sample).

less gas to be removed). We must keep in mind, however, that ultimately, the initial loading density is limited by the requirements for adequate thermalization of the sample produced in the ablation. Second, the effect of the "wind" in these simulations is manifest in the decline in the percentage of atoms retained for very short pump-out times. This loss is again worse for higher densities (and in fact not visible at all in these simulations for $n = 5 \times 10^{14} cm^{-3}$). This is reasonable given that a higher buffer gas density results in a greater net drag force on the trapped sample. Also, we note that for pump-out times such that $\tau \gtrsim 20ms$ the loss is no longer dominated by the wind. This is an important time scale to keep in mind for the valve aperture. We must avoid making the aperture too large (resulting in a pump-out time less than $20ms$ or so) so that the atoms are not swept out by the helium wind. The implication of this time scale on aperture geometry will be discussed in the following chapter.

In fig. 2.18, we show the results of some more simulations for $1\mu_B$ atoms at different trap depths ($3.5T$ to $4.5T$) and buffer gas temperatures ($0.3K$ to $0.5K$). In all cases, the initial buffer gas density is set to $n = 2.5 \times 10^{15} cm^{-3}$. These simulations further indicate the effect of the wind on the trapped sample (which greatly reduces the fraction of atoms surviving the pump out for $\tau \lesssim 10ms$). Also, the fraction of the sample that survives the pump-out is a very strong function of both the buffer gas temperature and the depth of the magnetic trap. At a temperature of $0.5K$ and trap depth of $3.5T$ ($\eta = 4.7$) for example, nearly the entire sample is lost no mat-

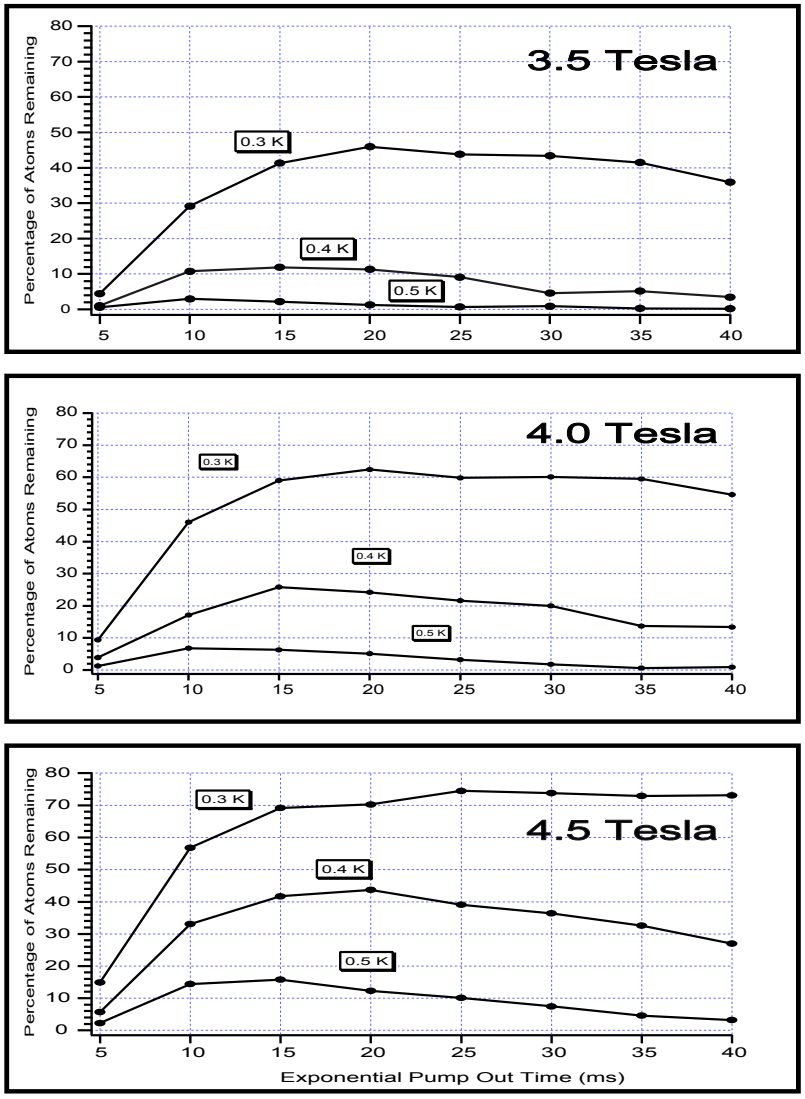

Figure 2.18: Results of further simulations of a sample of $1\mu_B$ atom during the pump-out of the buffer gas. In all of these simulations, the initial buffer gas density is $2.5 \times 10^{15} cm^{-3}$.

ter how quickly the buffer gas is removed. If the loading temperature is decreased to $0.3K$ while keeping the same trap depth (increasing our eta to, $\eta = 7.8$), the situation is greatly improved. Similar improvements result by raising the trap depth to $4.5T$.

This range of parameter ($0.3K \leq T \leq 0.5K$ and $3.5T \leq B_{trap} \leq 4.5T$) is very significant experimentally, for it spans what is easily achievable to what is quite difficult (though still possible) to achieve with present technology. A buffer gas temperature of $0.5K$ can be reached using a relatively simple ^3He refrigerator while to cool the trapping chamber to $0.3K$ would likely necessitate the use of a dilution refrigerator. Anti-Helmholtz magnets are routinely designed and built in our lab that can easily achieve fields of $3.5T$. While a depth of $4.5T$ in an anti-Helmholtz magnetic trap is possible, it would push the limits of what is possible using present (NbTi based) superconducting technology. So far, we have not worked with any traps of this depth in our lab. The intermediate range of these parameters might be termed "doable but challenging." A buffer gas temperature of $0.4K$ is possible using a ^3He refrigerator, but requires very careful management of the heat load on the experiment. A $4.0T$ deep trap is somewhat deeper than any previously used in our lab, but does not require any significant design change. These issues will be addressed at length in the next chapter.

Now, we focus our attention on the buffer gas removal time. According to the graphs in fig. 2.18, the fraction of the sample remaining is roughly independent of

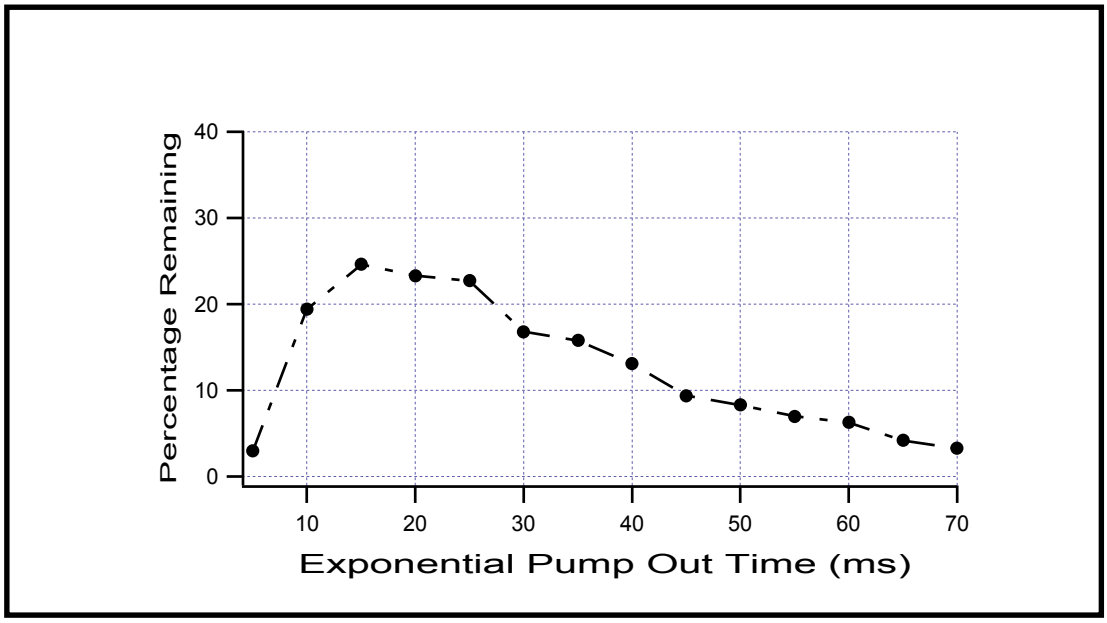

Figure 2.19: Simulations illustrating the need to quickly remove the buffer gas for $1\mu_B$ species. In these simulations, the trap depth is $4.0T$, the buffer gas temperature $0.4K$, and the buffer gas density $2.5 \times 10^{15} cm^{-3}$.

the pump-out time (apart from the wind) for $\tau \leq 40ms$. To see how leisurely we can be in our pump-out for $1\mu_B$ species, we simulate the effect of longer buffer gas removal ties.

In fig. 2.19, we show the results of another set of simulations where the magnetic trap depth and buffer gas temperature are fixed at the values $4.0T$ and $0.4K$ (where $\eta = 6.7$). Again, the effect of the wind is clearly pronounced and indicates that we should not attempt to remove the buffer gas on a time scale shorter than $20ms$ or so. If, however, we are too lackadaisical in the buffer gas removal, we suffer large atom loss as well. This is mostly due to the time spent in the "valley of death" region of fig. 2.15. According to fig. 2.19, we should aim for buffer gas removal times not

much longer than $50ms$ or so (note at this eta and temperature, the minimum lifetime according to fig. 2.16 is ~ $90ms$).

2.5.6 Conclusions from Simulation Studies

At this point, we have a pretty good handle on what is an acceptable (and experimentally accessible) range of parameters in the experiment to trap and efficiently thermally isolate $1\mu_B$ species. The results of these numerical simulations do not guarantee the success of the experiment, but they give us a good start on designing the apparatus. From the figures shown above (and many other sets of simulations) along with prior experimental experience, we conclude that we should aim for the following conditions in designing our experiment.

Buffer Gas Temperature ~$0.4K$
Magnetic Trap Depth ~$4.0T$
Buffer Gas Removal Time ~$50ms$

So far, we have restricted most of our attention to atoms with a magnetic moment of $1\mu_B$ in the spirit of extending buffer gas loading to low magnetic moment species. Just for a moment, it is interesting to stop and consider how a more rapid pump-out is particularly useful for working with more magnetic species (that don't necessarily require it). Fig. 2.20 shows the results of some simulations involving atoms with a magnetic moment of $3\mu_B$ (again with a trap depth of $4.0T$ and a buffer gas density of $2.5 \times 10^{15} cm^{-3}$). Because the magnetic moment is three times as great, roughly speaking, we expect to be able to load with a buffer gas at three times

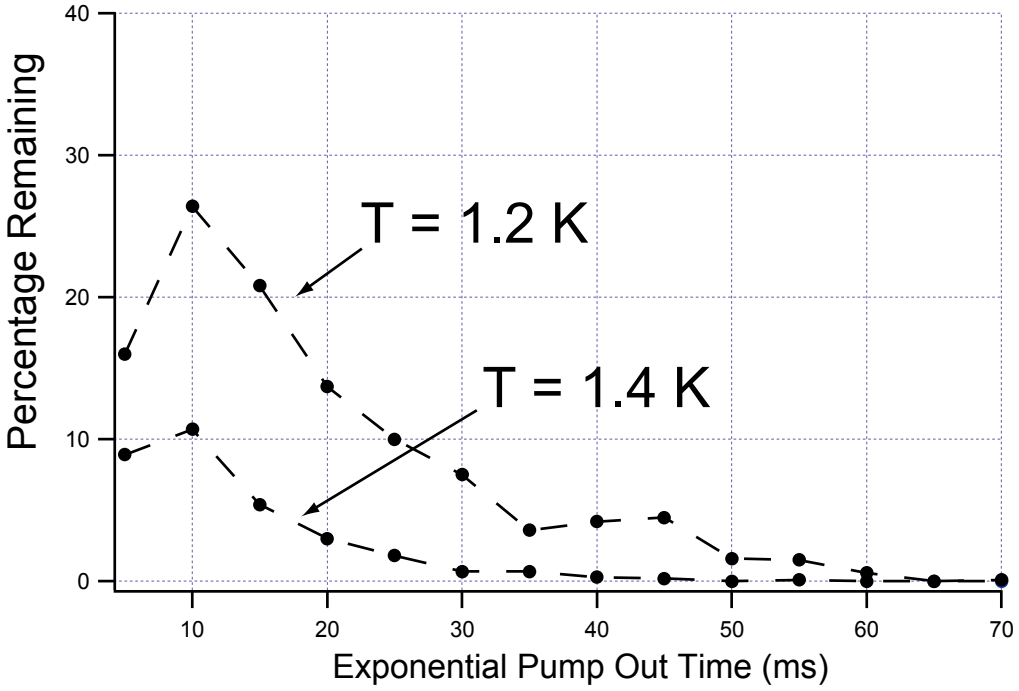

Figure 2.20: Simulations of $3\mu_B$ atoms. The magnetic trap depth is $4.0T$ and the buffer gas density $2.5 \times 10^{15} cm^{-3}$.

the temperature[15]. This is born out in fig. 2.20 which indicates that the buffer gas can be removed while retaining a substantial fraction of the trapped sample at temperature $\gtrsim 1.2K$. This temperature is technologically significant because it is accessible using a (very simple) pumped ^4He refrigerator. This implies that buffer gas loading experiments could be done on a large number of atoms (see table 1.3) in a very simple cryogenic apparatus.

[15] The elevated temperature does play a small role (even at the same η) in that it results in a slightly higher collision rate ($\propto \sqrt{T}$). This is a relatively minor effect compared to the strong dependency of trapping efficiency on η.

2.6 Helium Films

Before moving on to consider the experimental realization of the above parameters, we briefly mention one potential problem with our buffer gas removal scheme. So far, we have assumed that the He atoms in the buffer gas leave the chamber with some time constant that is set by the valve (determined by the aperture size and opening time). While this is true of the atoms in the gas phase in the volume of the chamber, there is another source of helium that we need to consider. When we introduce the buffer gas into the chamber, inevitably, some of the helium atoms go into forming a film on the walls of the trapping chamber. The amount of helium in this film depends on the chamber geometry as well as the material from which it is constructed. This latter is due to the variance in sticking affinity (i.e. binding energy) of He atoms to various substrates.

Once the atoms in the volume of the cell have been removed, the film will desorb with a time scale that is not set simply by the conductance of the valve aperture. Instead, the desorption time will be a function of temperature and binding energy. As the film thins during the desorption, the binding of the remaining portion of the film to the surface changes, resulting in a changing desorption time. Given that the initial layers of the film should be weakly bound (as they are relatively far from the substrate) and that the layers closest to the substrate are in general very tightly bound (as a result of the relatively high binding energy of He to most surfaces compared to our required temperatures [31]) we anticipate that there will be a regime where

the film desorbs on a time scale comparable to various time scales in the experiment. Whether or not this turns out to be an issue will depend on the buffer gas density that accumulates in the cell as a result of this desorption, and how long it takes the film to thin to the point where the desorption rate is negligible. A model for estimating the effect of the film on the buffer gas density in the trapping chamber is discussed in appendix A.

There are several possible remedies to this potential problem. For example, the cell temperature can be briefly elevated to facilitate the thin filming (a sort of "bake-out" procedure), or the cell surface properties may be modified so that the entire film readily desorbs on a time scale comparable to or faster than the pump-out of the volume. As it turns out, the film does indeed play a major (and detrimental role) in the buffer gas removal process. This will be discussed at length in ch. 5 along with a further discussion of the remedies. For now, we forge ahead and discuss some initial developments on the way to building the full experimental trapping apparatus.

Chapter 3
Preliminary Experimental Considerations

From the numerical simulations described in the previous chapter, we see that the ability to trap and achieve thermal isolation with weakly magnetic atoms (μ ~$1\mu_B$) is dependent upon our ability to achieve certain conditions in the magnetic trap. In these experiments, the most important parameters are the temperature of the buffer gas, T, the magnitude of the trapping field, B_{trap}, and the time constant for removing the buffer gas, τ. The number of atoms retained in the trap after the removal of the buffer gas is a complex function of these parameters. From the results of the last chapter, we anticipate that we will need a buffer gas temperature on the order of $\sim 400mK$, a magnetic trap depth of $\sim 4T$ and that we'll need to remove the buffer gas on a time scale of $\sim 50ms$. Each of these conditions has corresponding implications on the technology employed in the experiment. These technical requirements will now be discussed in detail.

3.1 Cryogenics

First we will address the requirement on the temperature of the buffer gas. As one might expect, low temperature physics experiments become more and more complex as the base temperature required in the experiment is lowered. Working at temperatures down to $77K$ (the boiling temperature of nitrogen at atmospheric pres-

sure), for example, is relatively straightforward. Such experiments can simply be immersed in a dewar (a type of cryogenic thermos bottle) of liquid nitrogen. Likewise, working at temperatures down to ~$4.2K$ (the boiling temperature of liquid helium at atmospheric pressure) can be accomplished through immersion in a liquid helium filled dewar (see for example, fig. 4.1). Because of its low latent heat of vaporization and its relatively high cost (~3 dollars per liter) more care must be taken to properly insulate this sort of experiment from the outside (room temperature) world.

3.1.1 General Considerations

Cooling an experiment to temperatures lower than $4.2K$ is done in several stages. Such experiments generally take place in a dewar filled with liquid He as well (to reduce the heat due to blackbody radiation from room temperature). An additional vacuum space (often referred to as the IVC for "Internal Vacuum Can") must be incorporated to isolate the experiment from the liquid to allow lower temperatures to be achieved. Inside of the IVC, some sort of cryogenic refrigerator (the details of which depend on the temperature required) provides further cooling of the experiment. The temperature that can be reached depends in general on the cooling power of the refrigerator (i.e. the rate at which energy is removed at a given temperature). This cooling power typically is a decreasing function of temperature. The "base" temperature is reached at the point where the cooling power exactly balances the heat load onto the sample. Inevitably, the experimental sample is in some

Temperature Needed	Refrigerator	Cost
$77K$	liquid Nitrogen	~ \$0.30 per liter
$4.2K$	liquid Helium	~ \$3.00 per liter
$4.2K$ to ~ $1K$	Pumped l^4He	~ \$10,000
~ $1K$ to ~$300mK$	Pumped l^3He	~ \$30,000
~ $1K$ to $\lesssim 10mK$	Dilution Refrigerator	~ \$200,000

Table 3.1: Various cryogenic refrigeration methods

way mechanically (and thus thermally) connected to the outside world, and so some heat load is unavoidable. To achieve the lowest temperatures possible, the cryogenic engineer attempts to minimize this heat load (through the use of low thermal conductivity materials, multiple vacuum spaces, shields against thermal radiation etc...). The lowest temperature required in the experiment determines the sort of refrigerator that one employs. Table 3.1 mentions a few of these refrigerators along with the base temperatures they can achieve and the approximate cost (as of 2004).

As mentioned above, working at temperatures down to $77K$ ($4.2K$) can be accomplished through immersion in liquid nitrogen (helium). Working at temperatures down to ~$1K$ can be accomplished by reducing the vapor pressure above a volume of liquid ^4He (evaporatively cooling the liquid). This is done by pumping on the volume containing the liquid. The same idea can be used to achieve temperatures down to ~$300mK$ using the rarer (and more expensive) isotope of helium, ^3He. This lower temperature is possible because ^3He has a lower boiling temperature than ^4He and also a much lower thermal conductivity at low temperatures resulting in a reduced heat load onto the liquid. Still lower temperatures are possible using a dilution refrigerator [15] albeit at a substantial price in complexity and cost.

The "old" method of buffer gas removal required the cooling of the chamber walls to temperature $\lesssim 200mK$ ($80mK$) to reduce the vapor pressure of the ^4He (^3He) buffer gas to a negligible value. As seen in the table, this necessitates the use of a dilution refrigerator. The "new" method of buffer gas removal eases the requirements on this temperature considerably. We expect (based on the results of the last chapter) to be able to trap and thermally isolate samples of atoms with magnetic moments $\gtrsim 3\mu_B$ in an experiment where the lowest temperature required is $\gtrsim 1.2K$. This temperature is attainable using simple pumped ^4He refrigeration. Getting to $400mK$ (to work with $1\mu_B$ species) requires a bit more effort and will require a pumped ^3He refrigerator. This is still a significant improvement in terms of cost and complexity compared to a dilution refrigerator. The new method of buffer gas removal not only greatly extends the range of atoms that may be worked with, it also substantially eases the requirements on the method of cryogenic refrigeration employed in the experiment.

3.1.2 ^{3}He Refrigeration

Because it is a key component in our experiment, the l^3He refrigerator, deserves a more thorough description. These types of refrigerators may be classified in two varieties, continuous and single shot [15]. As its name suggests, the continuously operating l^3He can maintain its base temperature indefinitely. This is accomplished by collecting and recondensing the ^3He as it evaporates.

Our experiment employs a single shot l^3He refrigerator [32]. This is a much simpler version as it avoids the necessity to recirculate the ^3He. The price paid for this simplicity is also apparent from the name. Base temperature can not be maintained indefinitely, rather from time to time the experiment must be halted to recondense the ^3He (which is generally collected on some sort of sorption pump as it evaporates). There is a finite amount of energy that the refrigerator can absorb before all the l^3He is evaporated. This is determined by the latent heat of evaporation of ^3He ($\sim 25J/mol$ at $\sim 0.4K$) [15] along with the total amount of liquid ^3He in the refrigerator. For every STP liter ($1/22.4$ moles) of ^3He in the refrigerator ($\sim 1.1J$ can be adsorbed). Our refrigerator contains a relatively large amount of ^3He (~ 30 STP liters) compared to most commercial l^3He refrigerators (which often contain ~ 6 STP liters). This allows the refrigerator to adsorb ~ 30 joules at a time. About 30% of this is "wasted" in cooling the l^3He from its condensation temperature to the base temperature of $\sim 350mK$. The amount of heat that can be absorbed before all of the ^3He is evaporated along with the heat load on the experiment determines the running time of the experiment. Quite favorable duty cycles (ratio of running time to regeneration time) can be achieved as long as the heat load is not too great. Typically, in our experiment, we can run for 1 or 2 days at a time before it is necessary to recondense the ^3He (a process often termed "regeneration")[16]. Regeneration can

[16] Even longer running times are possible in experiments that don't suffer from the relatively large heat loads present in our experiment. When it was originally tested, our refrigerator acheived a base temperature of ~$260mK$ with nothing attached to the ^3He pot and maintained this temperature for about two weeks!

be done relatively quickly (in ~ 1 hour or so). A schematic of the ^3He refrigerator used in our experiment is shown in fig. 3.1.

At room temperature, the ^3He gas is stored in a volume above the refrigerator (not shown). When the refrigerator is cooled down, the ^3He condenses onto a large sorption pump (top can in fig. 3.1). This sorption pump contains a large volume of activated charcoal which does the pumping. While charcoal may seem an unlikely substance to be used in a cryogenic experiment, it actually is quite an effective pump. The reason for this is that charcoal has an extremely high surface area to volume ration ($1g$ for example may have an effective surface area close to $1000m^2$). As a result, it has a high capacity for absorbing gases. The utility of charcoal as a pumping material will be considered in more detail when we discuss the removal of the buffer gas (also done through charcoal sorption pumping) in chapter 4.

Operating the refrigerator to attain temperatures of a few hundred milli-Kelvin requires that the ^3He desorb from the sorption pump and liquefy in the ^3He pot (bottom can in fig. 3.1). To desorb the helium from the charcoal, the temperature of the charcoal is raised to ~ $40K$. Liquefaction of the desorbing ^3He is accomplished by placing the gas in thermal contact with a cold surface. ^3He liquefies at ~ $3.5K$. The ^3He that desorbs from the sorption pump is cooled as it passes through a tube kept in good thermal contact with a can filled with ^4He. This ^4He is evaporatively cooled to temperatures as low as ~ $1K$ (hence the name of this stage, the "1 K pot"). In practice, the temperature of the 1 K pot is somewhat higher during regeneration

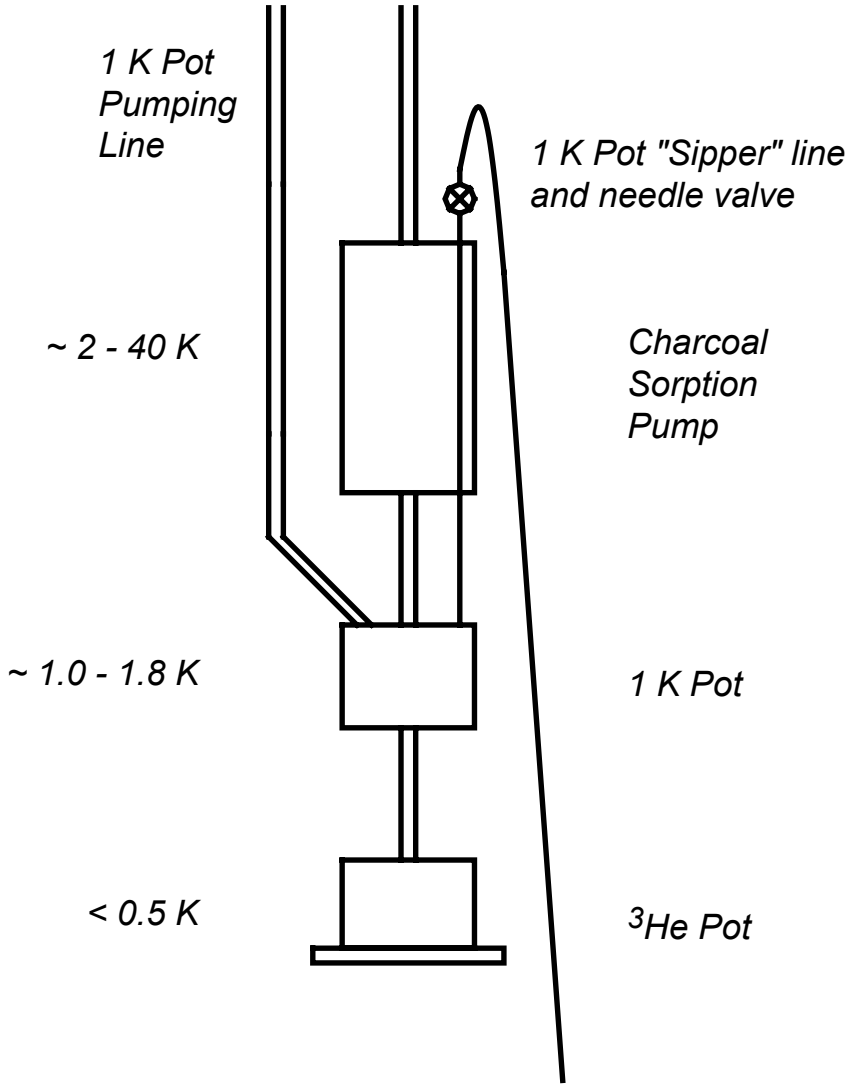

Figure 3.1: Schematic diagram of the "single shot" pumped l^3He refrigerator used in our experiment. Shown to the left are the typical temperatures of the various stages of the refrigerator.

due to the added heat load presented by the hot ^3He gas. Typically, our 1 K pot runs at ~ $1.6K$ or so during regeneration which is more than adequate to liquefy the ^3He.

Once the ^3He pot is filled with liquid, we are ready to begin operation of the refrigerator. The sorption pump is allowed to cool again (typically to $T \lesssim 5K$) at which point it becomes an excellent pump for ^3He (or any other gas for that matter) and begins to again collect the ^3He as it evaporates. The liquid ^3He in the pot then cools over time to the base temperature determined by the heat load and the cooling power of the refrigerator. This temperature is maintained until all the ^3He evaporates (at which point the cycle is repeated).

3.2 The Magnet

The second requirement for working with ~ $1\mu_B$ atoms is a trapping field on the order of ~4 Tesla. This is somewhat greater than what has been achieved in any previous magnetic trap in our group, and as a result required a bit of engineering [33].

3.2.1 Superconductivity

All of the magnets in our group employ superconducting technology to achieve their large trap depths. Materials that have the ability to superconduct do so only in a certain range of parameters. Specifically, the temperature, magnetic field, and electrical current in the material must be below certain "critical" values [34] . Above these values, the material no longer superconducts. Such a material is then said to

be in the "normal" state. The critical values for temperature, field, and current are not independent of one another. Rather, they form a three dimensional surface below which the material is in the superconducting state, and above which the material is normal. In general, as one of these parameters, T, B, or I increases, the critical values for the other two decrease.

3.2.2 NbTi versus Nb_3Sn

By far the most common superconductor used in magnets (and the one we have so far used exclusively) is an alloy of niobium and titanium[17] (NbTi). The prevalence of this alloy is due to its low cost and the ease with which it can be extruded to form long lengths of wire. The production of the NbTi wire is a truly remarkable process. This process is discussed in some detail in [34]. There are a number of more exotic superconducting materials that have superior characteristics but in general are not useful for magnets because the technology does not yet exist for cheaply manufacturing long lengths of wire from these materials. One exception deserves mention.

By far, the second most common material used in superconducting magnets is the compound Nb_3Sn. It has somewhat superior superconducting characteristics as compared to NbTi. Table 3.2 shows the critical values for temperature and field

[17] Typically the alloy is composed of 44% (by weight) titanium. This is to maximize the critical field (the quantity of most practical significance in the design of a magnet) at $4.2K$. It is interesting to note that the maximum in the critical temperature (~$10.1K$) does not accur for this content of titanium, rather at ~25% (by weight) titanium in the alloy [34].

Property	NbTi	Nb^3Sn
T_{c0}	$\sim 9.3K$	~ 18.5
B_{c0}	$\sim 15T$	$\sim 28T$
B_c at $4.2K$	$\sim 11T$	$\sim 20.5T$

Table 3.2: Properties of selected superconductors

(T_{c0} and B_{c0}) of these two superconductors when the other two parameters (field and current or temperature and current) are zero [34]. These represent the absolute maximum values that these parameters can take while maintaining superconductivity. Because our magnets are kept cold using liquid helium, it is of more interest what the critical values of field and current are at $4.2K$. The critical field (assuming I =0) is also given in table 3.2 for $T = 4.2K$. The actual maximum field that can be attained in a magnetic trap is less than the field given in table 3.2 and is determined by how much the critical field is lowered due to the current running through the magnet (see appendix D). Obviously the critical current and critical field for the magnet are intimately related since it is the current that generates the field. This field restricts the critical current and vice versa.

3.2.3 The Anti-Helmholtz trap

Solenoids made from NbTi (Nb^3Sn) are routinely able to achieve fields of ~ 9 Tesla (~ 15 Tesla) [35]. The fields of ~ 4 Tesla that are attained in our magnetic traps seem rather puny in comparison. In our traps, however, the goal is not to maximize the magnitude of the field, but rather to attain the largest depth (difference between minimum and maximum fields) and thereby exert the strongest confining

force possible on the magnetic atoms. The simplest way of attaining a large gradient is realized in the so called anti-Helmholtz trap [11]. This trap consists of two thin solenoids on the same axis separated by some distance (d in fig. 3.2).

The currents in these two solenoids are equal and run in opposite directions. The resulting field is zero at the center of the trap (defined to be on axis in the mid plane between the coils) and increases (roughly) linearly in r and z [11]. Because the currents are run in opposition, the field from the two coils tend to cancel each other over a large volume of the trap. As a result, attaining a given field magnitude requires a greater current than in the case of a pure solenoid. The greater current results in a lower critical field. This is the primary reason that the field magnitude in the high gradient configuration is lower than for a solenoid. It should be noted that this is solely a result of the limits due to the superconductors and does not apply to magnets wound with non-superconducting wire.

The field for the magnetic trap in our experiment is plotted in fig 3.2. Note that the field gradient in the axial (z) direction is twice that in the radial (r) direction (a consequence of Maxwell's equations which require $\nabla \cdot B = 0$). The maximum (critical) current to which the magnet may be energized is limited by the point in the coils where the magnetic field is at a maximum[18]. The maximum trap depth is determined by the value of the magnetic field at the wall of the trapping chamber when

[18] As the saying goes, "the chain is only as strong as the weakest link." Our whole magnet must be superconducting and so regardless of what the average field in the magnet is, it is only the field maximum that matters in determining the critical current.

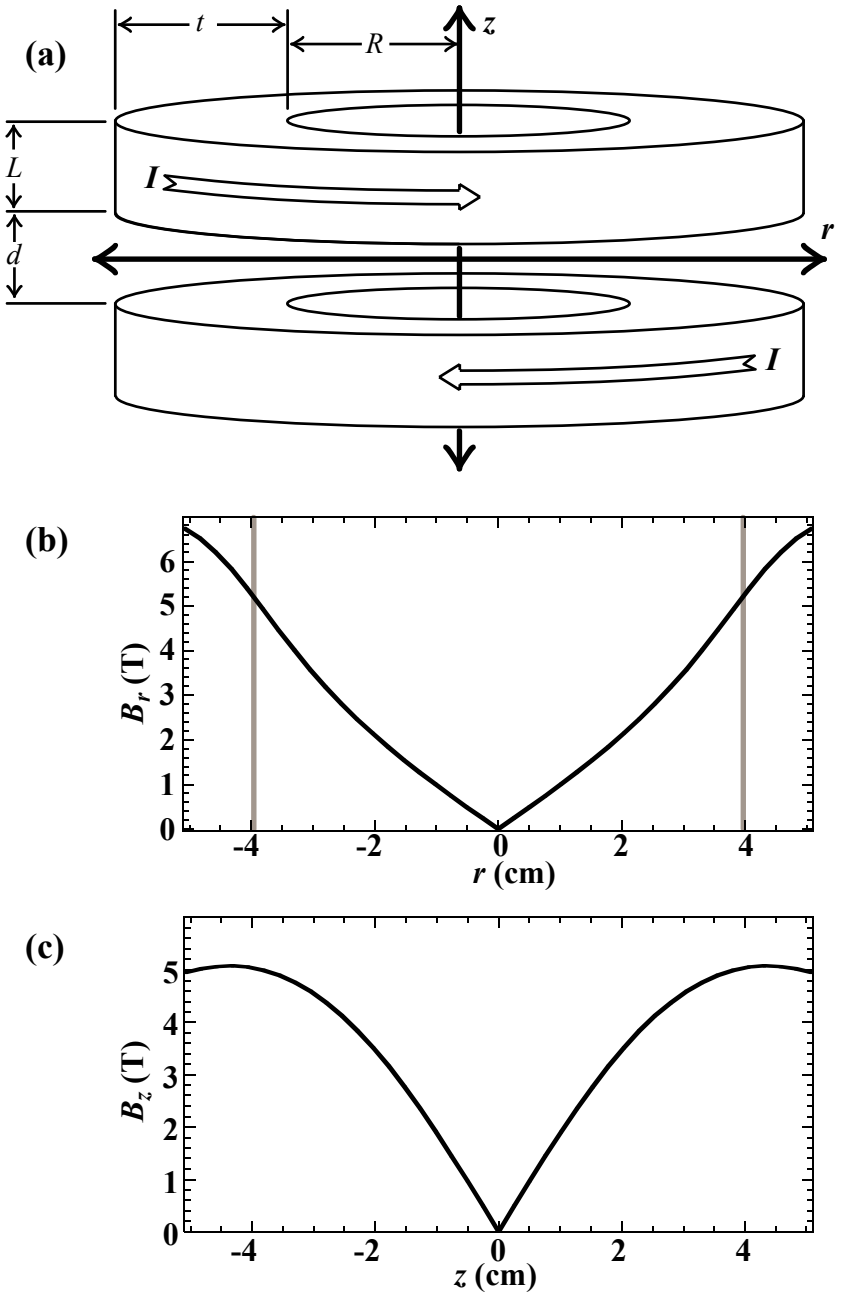

Figure 3.2: **a)** geometry of our anti-Helmholtz magnet. **b), c)** The maximum field in this magnet as a function of r and z. Note, the maximum field at the wall of the magnet bore (indicated in grey) is $\sim 4.7T$. The actual trap depth in the experiment, however, is limited to the field at the wall of the cell inside of the magnet. This maximum field is $\sim 4T$.

the magnet is energized to its critical current[19]. Since this trap depth is dependent on the actual position of the chamber in the magnet bore, it is not an intrinsic property of the magnet. Figure 3.2 shows that the maximum achievable field at the bore of our magnet is ~4.7 Tesla. If the magnet bore served as the trapping chamber as well, then this would also be the trap depth. Unfortunately, the requirement that we keep the chamber at low temperature ($\sim 400mK$) means that there must be a separate vacuum space to isolate the "hot" ($\sim 4.2K$) magnet bore from the trapping chamber. In our experiment, the gap (between chamber wall and magnet bore) chosen to safely insure that the cell not touch the magnet restricts the maximum trap depth to $\sim 4T$.

3.2.4 Magnet Support Structure

The trap depth of our magnets is a complicated function of the geometry of the coils, and any optimization procedure is fairly involved. In addition, there is a second factor to consider that has a profound impact upon the design of the magnet. When current is run through the coils in opposite directions, there is a repulsive force tending to push the coils apart. Due to the high current densities possible in superconducting magnets, this force can be quite large. The magnet we designed

[19] In practice, the critical current may be limited to a value below the predicted "short-sample" critical current of the wire from which the magnet was wound. This is due to local heating that can result from motion of the wire under the large magnetic forces present in the coil. Frictional or eddy current heating from this motion may drive part of the magnet into the normal state. Once in the normal state, this section of the magnet generates additional (resistive) heat. If this heat is not dissipated (and that part of the magnet returned to the superconducting state), it can cause more of the magnet to go normal resulting in an avalanche process known as a "quench" [34]. In well manufactured magnets, this is not an issue, and the short sample critical current can be reached. Sometimes this requires that the magnet be "trained" (quenched a few times) to remove weak points in the coil.

Material	Yield Strength (Ksi)
Al (6061)	30
Brass	18-45
Copper (OFE)	10-53
Stainless Steel (304)	35
Stainless Steel (316)	35
Ti ASTM Grade 2 (pure)	40
Ti ASTM Grade 6 (6-4)	120
Ti ASTM Grade 5 (5-2.5)	110

Table 3.3: Yield strengths of selected metals

for our experiment has a repulsive force between the coils of ~32 tons when the coils are fully energized. A great deal of care must be taken in the manufacture of these magnets to ensure that they can handle this force. The form to support the coils in our magnets are machined from a high strength titanium alloy. The most common alloy of titanium is 6-4 Ti (containing 6% by weight aluminum and 4% by weight vanadium). This alloy is strong and relatively easily machined. Unfortunately, it superconducts at $4.2K$ [36] leading to unpredictable modifications in the field [24] and thus making it unsuitable to be used in our magnets. Instead, we use the more difficult to acquire 5-2.5 Ti (containing 5% by weight aluminum and 2.5% by weight tin) which does not superconduct at $4.2K$. The strength of this alloy is compared to that of other common materials in table 3.3 [37].

The characteristics of the magnet used in our experiment are contrasted with those of the previous generation magnetic trap (used in experiments to trap Cr [38]) in table 3.4. Note, the last column of table 3.4 gives the value for the maximum field at the bore of the magnet.

	$\mathbf{L(mm)}$	$\mathbf{d(mm)}$	$\mathbf{t(mm)}$	$\mathbf{R(mm)}$	$\mathbf{I_c(A)}$	$\mathbf{F(N)}$	$\mathbf{B_{max}(T)}$
"old" magnet	50.67	20.1	31.6	41.4	79	2.3×10^5	4.4
"new" magnet	61.0	15.2	35.6	42.2	99	3.1×10^5	4.7

Table 3.4: Comparison of "old" and "new" magnets.

In addition to the greater field produced in this magnet, the support structure is quite different. The previous magnet relied on the inner wall of the magnet bore for support against the repulsive force between the coils. A series of plates on the outside of the magnet provide additional support (see fig. 3.3). Our new magnet is supported by a thick titanium sheath surrounding the coils on the outside. A set of titanium pegs lock this sheath to two titanium annuli sandwiching the coil as shown in fig. 3.4.

This sort of construction results in a heavier and bulkier magnet, but it has the advantage that the inner wall of the bore no longer needs to be load bearing. As a result, it can be made quite thin ($0.065" = 0.165cm$ in our magnet compared to $0.125" = 0.3175cm$ in the "old" magnet). This further increases the field at the magnet bore (and thus the trap depth). This gain is relatively modest (accounting for about half of the $\sim 0.3T$ increase in the field at the bore of our magnet versus the "old" magnet), but given the strong dependence of loading efficiency on field, every little bit helps.

In addition, the bore of the magnet itself was designed to be a vacuum space (removing the necessity of inserting a separate vacuum space inside). This was intended to allow us to place the trapping cell closer to the magnet bore resulting in

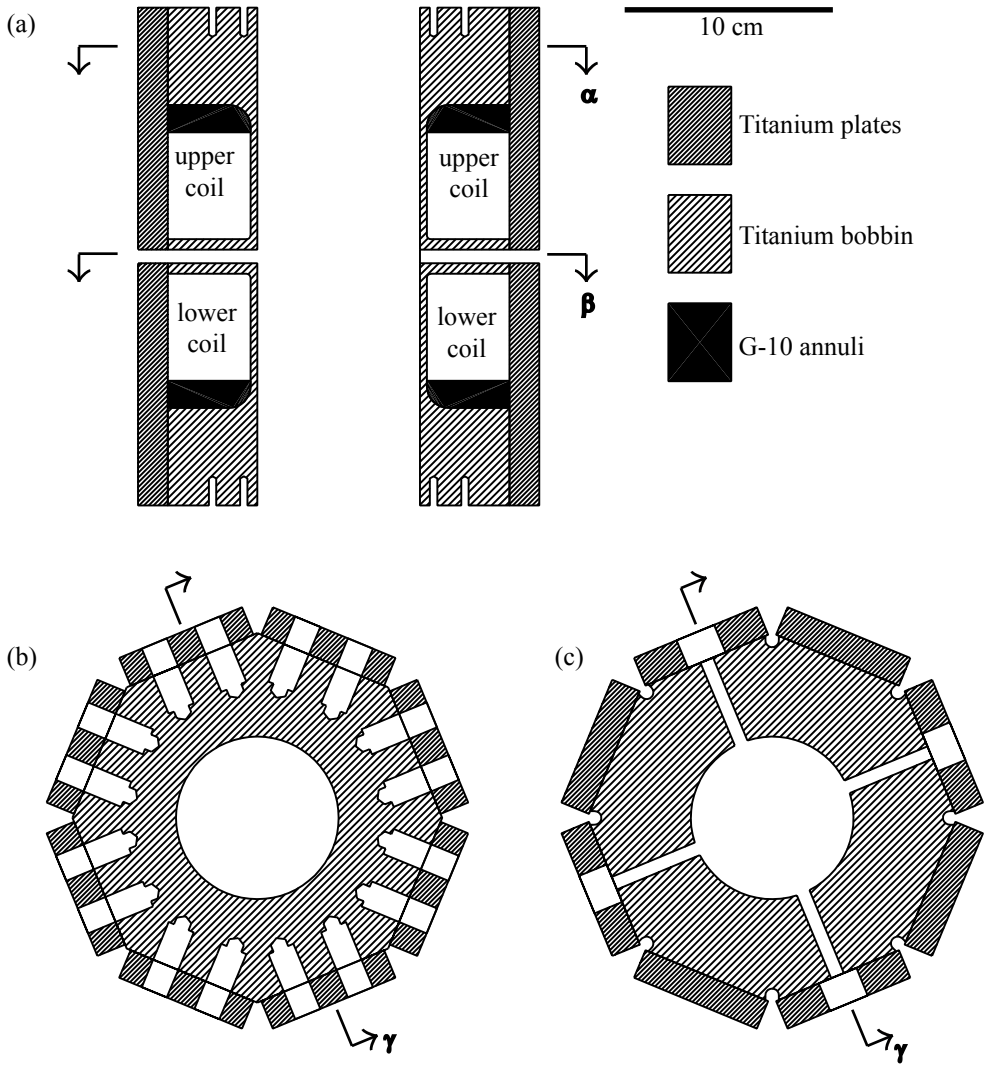

Figure 3.3: Support structure for the "old" magnet **a)** Cross sectional view (along γ). The magnet coils are wound directly on the magnet bore [35]. Eight titanium plates provide additional support against the repulsive inter-coil forces present when the magnet is energized. **b)** Cross sectional view along α showing the peg holes used to attach the plates to the magnet form. The pegs themselves are omitted for clarity. **c)** Cross sectional view taken along β (the midplane of the magnet) showing the part of the magnet form that separates the two coils. The midplane spacer includes four holes to allow side optical access to the magnet bore. So far, these have not been utilized.

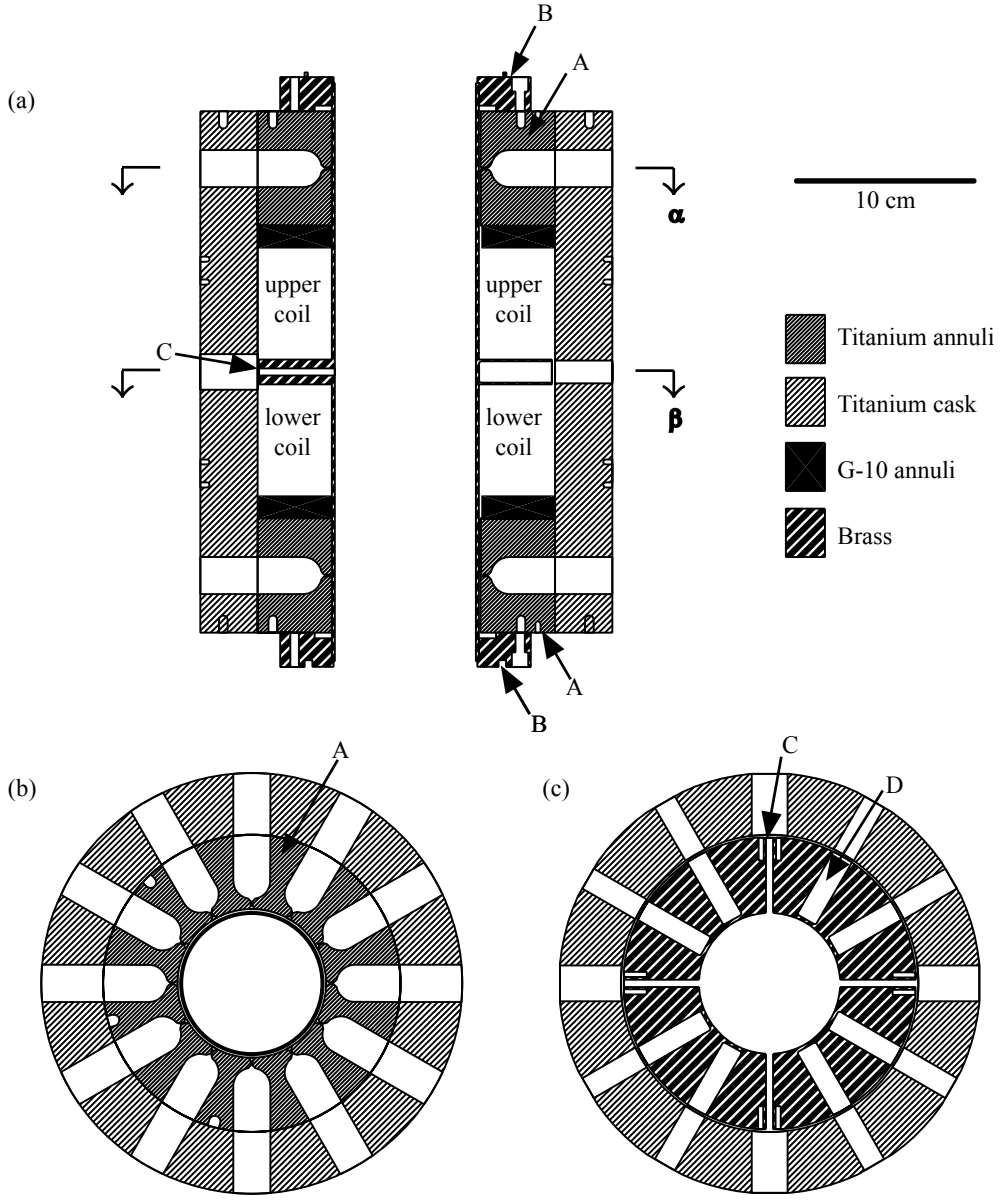

Figure 3.4: Support structure for our "new" magnet. **a)** The titanium annuli "A" and the G-10 annuli are slid over the brass bobin and then captured by brazing the brass vacuum flanges "B" to the bobbin. **b)** Cross sectional view taken along α showing the twelve $20.6mm$ diameter holes in the titanium annuli and cask to accomodate the load-bearing pegs. For clarity, the pegs are omitted. **c)** Cross sectional view taken along β, the midplane of the magnet showing the part of the brass bobin that separates the two coils. One of the four optical ports is indicated by "C". One of eight addition radial ports is indicated by "D". These ports do not penetrate the bore of the magnet.

still greater fields. Unfortunately, during tests of the magnet, a leak opened in the brass bobbin preventing it's use in this respect, and requiring that we place part of the IVC in the bore after all (a decision that was agonized over for several months as we attempted unsuccessfully to repair the leak).

Another feature incorporated into our magnet is the addition of eight "general purpose" radial access ports in the mid-plane of the magnet (see fig. 3.4). These ports allow us, for example, to place additional small solenoids into the magnet to modify the field profile. They were not used in any of the work described in this thesis.

3.2.5 Magnet Heaters

One other important new feature of our magnet is the presence of resistive heater wire wound on the inner and outer diameters of both superconducting coils. These wires can be used to drive the superconducting coils into the normal state, thereby removing any trapped fluxes from the coil. Trapped fluxes in the magnet can seriously degrade the quality of the magnetic trap especially at low fields ($\lesssim$ 40 gauss), and thus limit the amount of evaporative cooling that may be done on a trapped sample through magnet ramping. The presence of these trapped fluxes limited the evaporative cooling of Cr to $\sim 1mK$ [38] and their elimination would greatly facilitate further cooling toward quantum degeneracy. Figure 3.5 demonstrates the ability of the heaters to remove the trapped fluxes in our magnet. The remnant field after ramp-

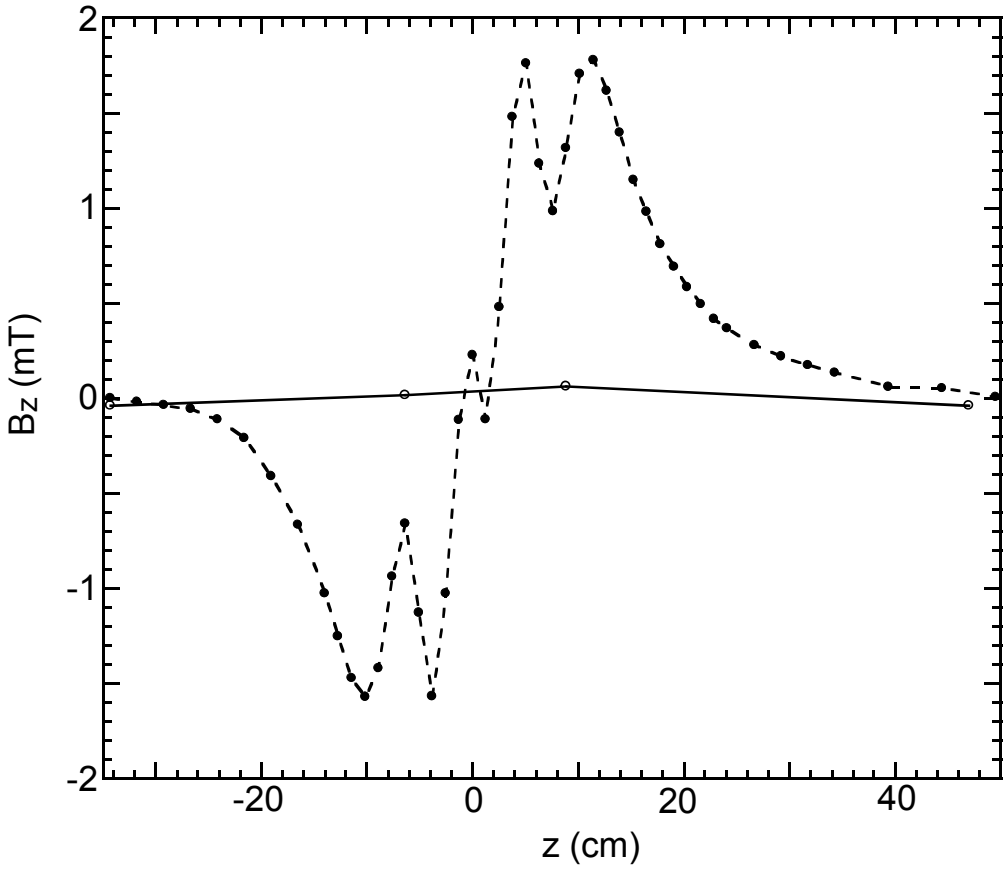

Figure 3.5: Solid points: Remnant field measured along the z-axis after ramping the magnet from 98 to 0 amps. Open points: Field after the magnet was driven normal using the heaters on the coils.

ing the magnet from near full current (98 amps) to 0 amps is shown both before and after the heaters were used to drive the coils normal.

3.3 The Valve

The last of the requirements listed at the beginning of this chapter is the ability to remove the buffer gas with a time constant of $\sim 50ms$. This is much too short to

be accomplished using the old technique of cooling the walls of the trapping chamber with a dilution refrigerator. That method of removing the buffer gas takes several seconds, a time unacceptably long for working with low magnetic moment atoms. As a result, we needed to implement a fundamentally new method for removing the buffer gas to achieve short pump-out times.

In the new experiment, a valve is present on top of the trapping chamber. When the buffer gas is introduced into the cell, the valve is closed. When it is time to remove the buffer gas, the valve rapidly opens, and the helium rushes out to an auxiliary chamber on top of the trapping cell where it is sorption pumped away using a large volume of activated charcoal (similar to the charcoal in our ^3He refrigerator). If this valve is opened fast enough, and the aperture is large enough, then very short pump out times can be achieved.

3.3.1 Pump-out Time

Now, a large aperture, fast actuating valve that makes a good seal at sub-Kelvin temperatures is not a commercial item. To convince ourselves that such a device was possible, we built a prototype. First, we calculate how large the valve aperture needs to be to achieve pump-out times on the order of $50ms$. We begin with the standard expression for the throughput, Q, of a gas [39]

$$Q = \frac{dP}{dt} \cdot V = C \cdot P \tag{3.1}$$

Where, V is the volume of the chamber being evacuated, P the pressure in the chamber, and C the conductance of the aperture connected to the chamber.

As seen from eq 3.1, the pressure and (hence the density) decreases exponentially with time with a time constant, $\tau = V/C$.

$$P = P_0 e^{-t/\tau} \tag{3.2}$$

$$n = n_0 e^{-t/\tau} \tag{3.3}$$

$$\tau = V/C \tag{3.4}$$

The conductance of the aperture depends on its size. The larger the aperture, the greater the conductance (and the faster the gas is removed from the chamber). Again, we make a distinction depending on the size of the collisional mean free path of the gas particles compared to the size of the aperture. In the "viscous" regime, the mean free path is short compared to the aperture size. In the "molecular" regime, the mean free path is long compared to the aperture size. The conductance of an aperture is different for these two regimes. The formulas for the conductances in both cases are given below [39]. In general, the conductance is larger in the viscous regime by some factor of order unity compared to what it is in the molecular regime. In the intermediate regime (where the mean free path and aperture size are comparable), the conductance is somewhere between the two.

$$C_{viscous} = \frac{9.13A}{1-(P_2/P_1)} \left(\frac{P_2}{P_1}\right)^{1/\gamma} \sqrt{\frac{2\gamma}{\gamma-1}\left(\frac{T}{M}\right)\left(1-\left(\frac{P_2}{P_1}\right)^{\frac{\gamma-1}{\gamma}}\right)} \tag{3.5}$$

Here, P_1, and P_2, are the pressures on either side of the aperture ($P_2 < P_1$), T the temperature (in Kelvin) of the gas, M the (molar) mass of the gas, and A the area of the aperture (in cm^2). Here, γ is the ratio of the specific heat at constant pressure to the specific heat at constant volume ($5/3$ for helium). As it stands, eq 3.5 is not quite right. There is a certain ratio of P_2/P_1 for which the conductance is a maximum[20]. For P_2/P_1 above this value, the conductance is correctly given by eq. 3.5. For P_2/P_1 below this value, the conductance is that given by eq. 3.5 with P_2/P_1 set equal to the critical value. For helium, the critical value is ~ 0.49. Since in our experiment, the pressure in the region above the trapping chamber is expected to be extremely low, we are in this regime. After plugging this in along with the molar mass of ^3He (3), eq. 3.5 reduces to something fairly simple.

$$C_{viscous} = 3.8A\sqrt{T} \tag{3.6}$$

With A in cm^2, T in Kelvin, and $C_{viscous}$ in liters/s.

For molecular flow with ^3He, the conductance is given by [39]:

$$C_{molecular} = 2.10A\sqrt{T} \tag{3.7}$$

We see from eqs. 3.6 and 3.7 that the conductance depends (weakly) on temperature as well as aperture size. Values for the pump-out times at a temperature

[20] At this point, the velocity of the gas flowing out of the aperture is equal to the speed of sound in the gas and can not be increased further.

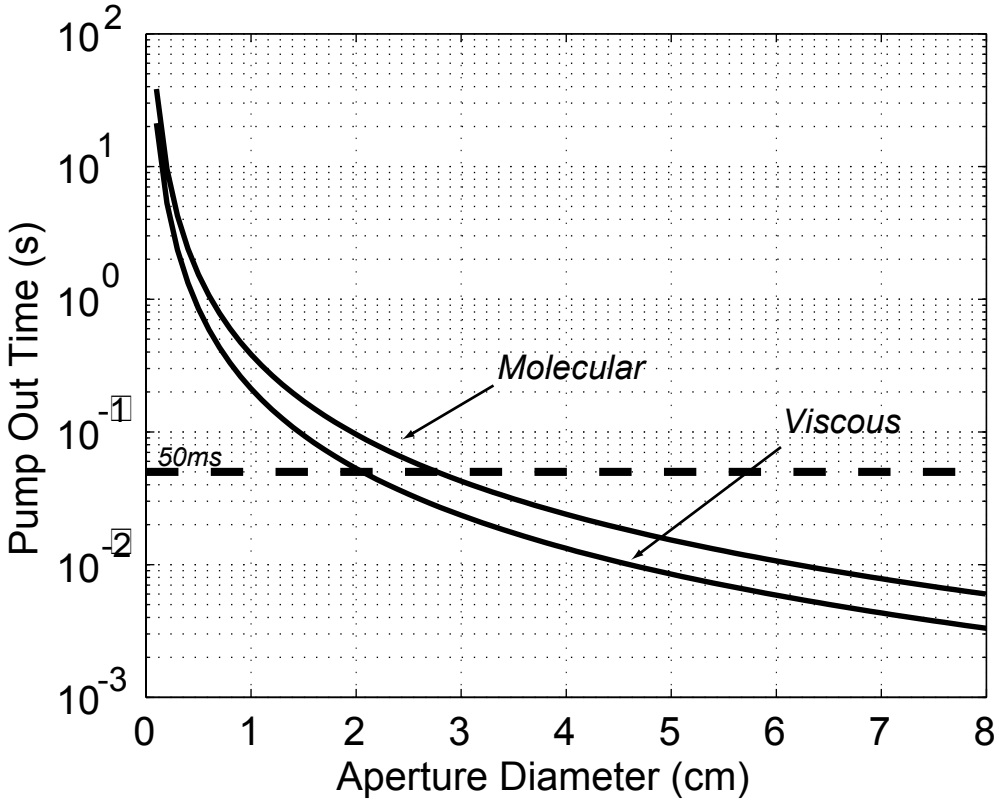

Figure 3.6: Pump-out time vs. aperture diameter for both the molecular and viscous regimes. Here, we have assumed a temperature of $400mK$ and a cell volume of $400cm^3$.

of $400mK$ versus aperture diameter are plotted for both the viscous and molecular regimes in fig. 3.6.

3.3.2 Valve tester

From fig. 3.7, we see that in order to achieve pump-out times of $\sim 50ms$, we need to have an aperture with diameter $\sim 2-3cm$. With this in mind, we built a prototype of our valve to test sealing quality and actuation time. There are a number of

methods typically used to open and close room temperature valves (springs, electro-magnets, air pressure etc...). Our situation is complicated by the fact that the valve has to open (very rapidly) and close in a cryogenic environment. For the best chance of success and to simplify the design as much as possible (in cryogenics, often two ways of saying the same thing!) we decided to put the actuation mechanism at room temperature. The prototype is shown schematically in fig. 3.7.

The idea is quite straightforward. On top of the dewar, at room temperature, is a pneumatic cylinder. Inside of this cylinder is a piston. Connected to the piston is a shaft that runs down the neck of the dewar to the valve "boot". This boot mates with a brass ring to form a seal. The pneumatic cylinder can be pressurized both on top and bottom of the piston. In order to close the valve, we simply put more pressure on top so that there is a net force downward causing the boot to press against the brass sealing surface. To open the valve, we do the opposite. We make the pressure on top less than the pressure on the bottom of the cylinder so that there is a net force upward. Because the valve must open very rapidly, the top pressure must be reduced quickly. This is accomplished by connecting a large (3/4" diameter) aperture solenoid valve to the top of the pneumatic cylinder. This solenoid valve can be opened quickly to rapidly reduce the pressure on top of the cylinder to normal atmosphere. Whatever excess pressure is behind the piston will drive the valve open.

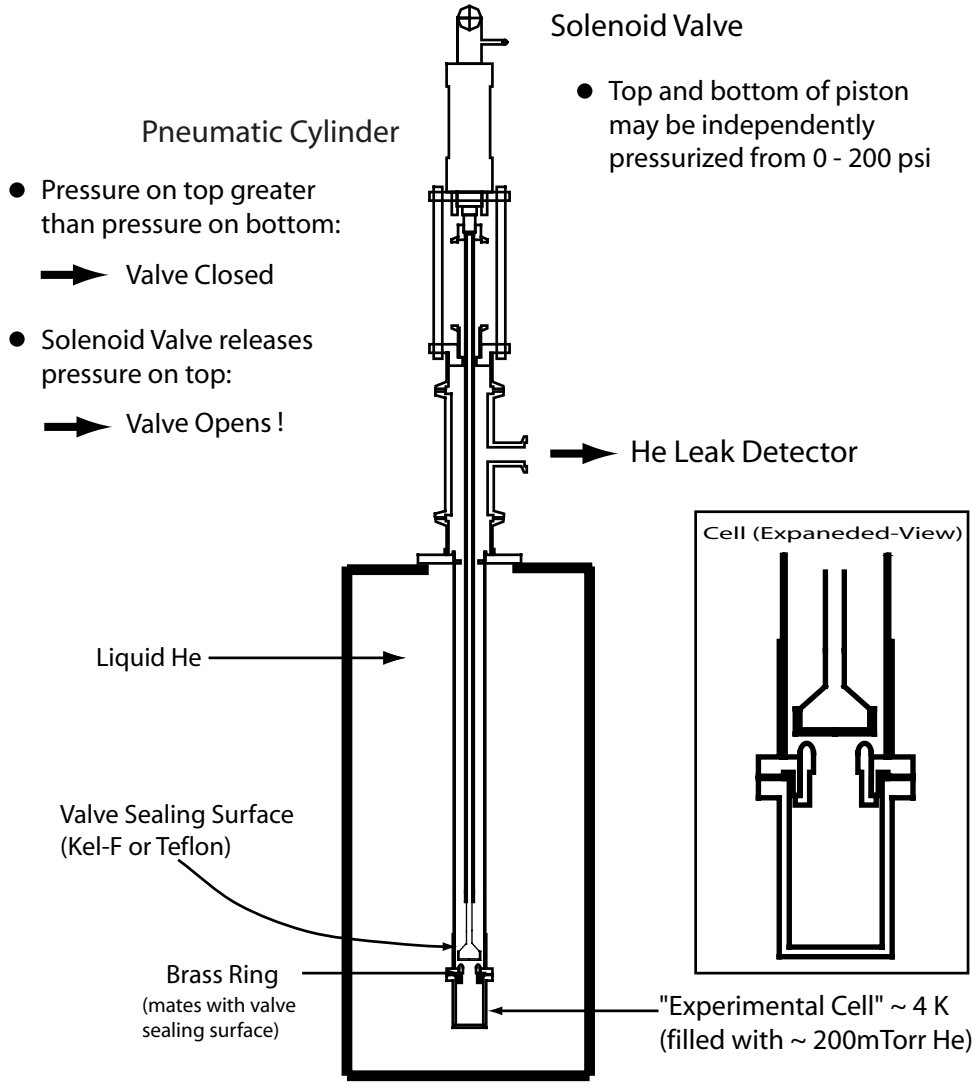

Figure 3.7: Valve testing apparatus. Helium is introduced into the "experimental cell" with the valve closed, and the leak rate monitored using a He mass spectrometer leak detector. Note, this figure is only meant as a schematic. Several details such as baffles, cell fill line, etc... have been omitted for clarity.

3.3.3 Thermal Considerations and Buckling Force

Now, apart from the issues of actuation speed and sealing quality, there is another important design consideration for our valve. In the actual experiment, the valve boot connects directly to the top of the trapping chamber (when the valve is closed). This is the part of the experiment that we want to keep as cold as possible (to maximize η when the buffer gas is in the cell). The other end of the shaft is connected to the room temperature piston. As a result, there may be a considerable heat load onto the chamber resulting in an elevated temperature. To mitigate this problem, we must "heat sink" the valve shaft at various colder parts of the experiment (at $4.2K$ for example) before the shaft reaches the cell. In addition, we must carefully consider the size and material used in the valve shaft. Ideally, the shaft would have a small cross sectional area to minimize the heat flow down it. This consideration must be balanced against the fact that considerable closing pressure may be needed to make an adequate seal, and as a result the shaft must be strong enough so as not to buckle under this force.

For a long, slender, tube, the maximum force that can be applied to the tube (before the tube buckles) is given by the well known Euler formula [40]:

$$F_{\max} = \frac{4\pi^2 EI}{L^2} \tag{3.8}$$

Where, E is the elastic modulus of the tube material, and I and L are the tube's moment of inertia and length.

The moment of inertia of a tube is:

$$I = \frac{\pi}{4}(R_1^4 - R_2^4) \tag{3.9}$$

Where, R_1, and R_2, are the tubes outer and inner radii respectively. For a thin walled tube, we may approximate the moment of inertia as:

$$I \approx \pi t R^3 \tag{3.10}$$

Where t is the thickness of the tube. Plugging this in to eq. 3.8 gives for the buckling force:

$$F_{\max} = \frac{4\pi^3 E t R^3}{L^2} \tag{3.11}$$

We see that the force that a tube may tolerate is strongly dependent on the radius of the tube (and less so on the thickness).

Now, consider the heat conducted down the tube. In general for an object with one end at temperature T_2 and the other at T_1 (with $T_2 > T_1$), the heat conducted (in one dimension) is given by [41]:

$$\dot{Q} = \frac{A}{L}\int_{T_1}^{T_2} k(T)dT \tag{3.12}$$

Where A and L are the cross sectional area and length of the object and $k(T)$ the thermal conductivity of the material (which in general is temperature dependent). For a tube, the area is given by:

$$A = \pi(R_1^2 - R_2^2) \tag{3.13}$$

If our tube is thin, we may approximate this as:

$$A \approx 2\pi Rt \tag{3.14}$$

Plugging this in to eq. 3.12 gives:

$$\dot{Q}_{tube} = \frac{2\pi Rt}{L} \int_{T_1}^{T_2} k(T) dT \tag{3.15}$$

According to eqs 3.11 and 3.15, the maximum force that we may apply before buckling the tube goes like the third power of the tube radius whereas the heat conducted down the tube is proportional to only the first power of the tube radius. Clearly, to maximize strength while minimizing heat flow, we want a thin walled, relatively wide tube (unfortunately, there is not much we can do about the shaft length, L, since the experiment height is set by other considerations).

Also, in designing the shaft, we must carefully consider the material to use. Because, it must function in a cryogenic environment (and remain non-brittle and retain fracture toughness) while possessing strength, we are lead to choose a metal. Many common metals (copper, aluminum, brass etc...) would be suitably strong, but possess relatively high thermal conductivities (see tables 3.5 [37] and 3.6 [15] [41]). Stainless steel (alloy 304 or 316 for example) turns out to be a very good choice. It is strong, has very poor thermal conductivity for a metal, and has been extensively used

metal	*Elastic Modulus* [$\times 10^9 N/m^2$]
Cu	~108
Al	~69
Brass	~110
Stainless Steel (316)	~200

Table 3.5: Elastic moduli for various metals

metal	$\int_{0K}^{77K} k(T)dT$ [W/cm]	$\int_{0K}^{4K} k(T)dT$ [W/cm]
Cu (RRR=100)	1000	10
Cu (RRR=20)	600	2.0
Al	220	0.4
Brass	20	0.07
Stainless Steel (316)	3.2	0.003

Table 3.6: Thermal conductivity integrals for various metals

in cryogenic applications. In our prototype (and in the actual experimental apparatus as well), the valve shaft is made from stainless steel tubing ($1/2" = 1.27cm$ in diameter with $0.049" = 0.124cm$ thick walls).

Now, let's plug in some numbers. First, we'll consider buckling strength. In our experiment, the valve shaft needs to be $\sim 1.5m$ long. If we plug this into eq. 3.11 along with our other tube parameters, we have:

$$F_{\max} = \frac{4\pi^3 \cdot (200 \times 10^9 N/m^2) \cdot (0.00124m) \cdot (0.00635m)^3}{(1.5m)^2} \cong 3500N \cong 800lbs \tag{3.16}$$

This is probably an overly optimistic estimate, for it assumes an ideal tube (free from defects, perfectly straight, etc...). None the less, given that the forces required to seal our valve are on the order of $\sim 100lbs$ (see the next section), we are confident that our tube will be up to the task. Again, notice, the strong dependence on radius.

If the tube were 1/4" in diameter rather than 1/2", the maximum acceptable force would be reduced nearly an order of magnitude (putting us dangerously close to the buckling regime) while we would only reduce the heat load a factor of two (see eq. 3.15).

Let's look at this heat load more carefully. Plugging in the values for our tube into eq. 3.15 gives:

$$\dot{Q} = \frac{2\pi \cdot (0.00635m) \cdot (0.00124m)}{1.5m} \int_{T_1}^{T_2} k(T)dT \tag{3.17}$$

$$\dot{Q} = 3.3 \times 10^{-5} m \cdot \int_{T_1}^{T_2} k(T)dT \tag{3.18}$$

Consider two cases. First, let's assume that we have heat sunk our shaft well at $4.2K$. Then, the value of the thermal conductivity integral (assuming $T_1 = 0$) in eq. 3.17 is ~$1.2W/m$. This gives a heat load of, $\dot{Q} = 4 \times 10^{-5} W = 40\mu W$ onto the cell. This is a reasonably small amount of heat considering that the cooling power of our refrigerator at $400mK$ is ~$700\mu W$ (see appendix C), and would lead to a negligible temperature rise in our cell. Assuming we only heat sink the shaft at $77K$ before it reaches the cell, the integrated thermal conductivity is ~$3200W/m$ resulting in a heat load of $100mW$. This is an unacceptable amount of heat and would make it impossible to maintain a suitably cold cell with the valve closed. Clearly, effective heat sinking of the shaft is vital!

3.3.4 Valve Sealing Quality

To test the low temperature sealing quality of the valve, we immersed the prototype in a dewar filled with liquid helium. During the tests, a certain quantity of helium gas (typically $\sim 200mTorr \longleftrightarrow n = 5 \times 10^{17}/cm^3$ at $4.2K$) was placed into the brass chamber (see fig. 3.7) with the valve closed. The flow of helium out of the chamber (i.e. the leak) was monitored using a helium mass spectrometer leak detector. A perfect valve would allow no helium to pass when closed. Fortunately, we don't need a perfect valve in our experiment. We simply need the valve to provide a sufficient seal to allow an adequate density of buffer gas to accumulate in the trapping chamber and to maintain that density long enough to fire the ablation laser to produce the trapped sample. The method of buffer gas introduction (discussed in detail in ch. 4) requires that we heat the cell somewhat. Typically, we allow the cell to cool for several minutes before ablating. It also takes a few minutes to build up the buffer gas density in the cell. This sets the time scale for how long the buffer gas must be retained in the cell.

Not surprisingly, the leak rate is found to depend on the amount of pressure used to close the valve. In general, the more closing pressure used, the better the seal. This must be balanced against the greater mechanical strain on the cell and the shaft buckling issue discussed above. Two materials for the valve boot were tested, Kel-F and teflon. These were chosen because they remain somewhat elastic at low temperature and are often used in commercial cryogenic valves. The teflon boot

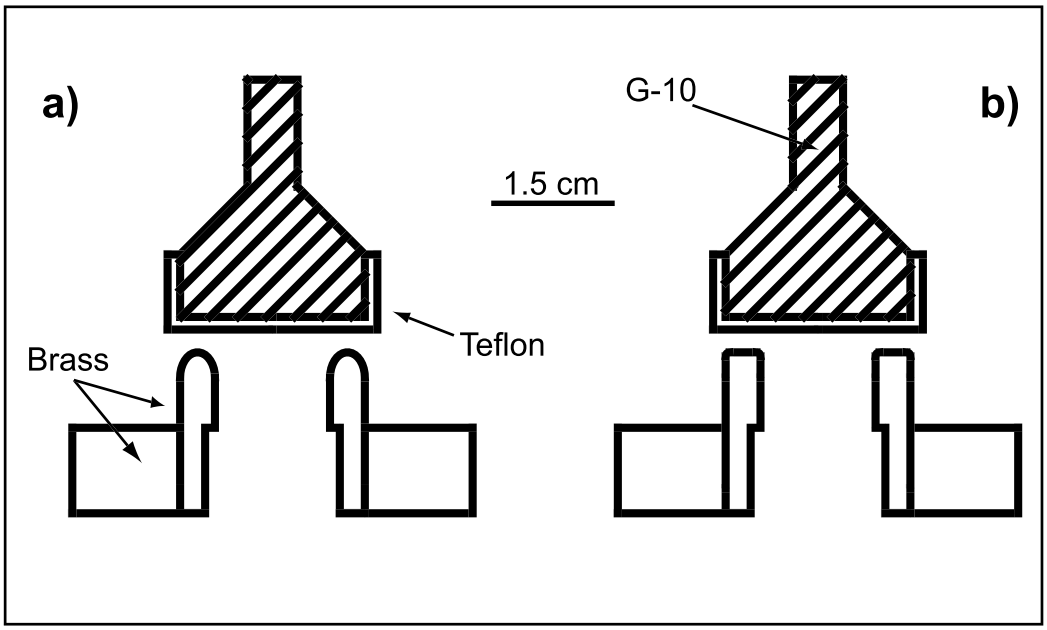

Figure 3.8: Sealing surface geometries used in valve tests. **a) "**Rounded Ring" **b)** "Flat Ring"

performed marginally better than the Kel-F, and was used for most of the tests. The sealing quality is also expected to depend on the geometry of the ring that the boot presses against. A sharp "knife edge" sort of sealing surface, (as used for example in ConFlat seals) might result in a good initial seal, but could damage the soft boot making subsequent seals less reliable. The valve must perform adequately under many (~1000 or so) cycles since it can not be serviced once the experiment has been cooled down. Conversely, while a wide flat surface would be gentler on the valve boot, it might not result in a sufficient pressure to form an adequate seal. With this in mind, two different ring geometries (shown in fig 3.8) were tested. In one of these geometries, the ring was formed from a rounded piece of brass (radius of curvature $\sim 0.2cm$). In the other, the brass ring was flat (and $\sim 0.4cm$ thick).

In figs. 3.9 and 3.10, we plot the buffer gas hold time (adjusted for the conditions in the actual experiment) for various closing pressures based on the measured leak through the valve for the two ring geometries. These tests were done with the valve at ~ $4.2K$ (with the apparatus in liquid helium)[21]. The hold time was calculated by first determining the conductance of the closed valve (zero for a perfect seal) and extrapolating to $400mK$ (recall $C \propto \sqrt{T}$) and assuming a cell volume of $400cm^3$.

The quality of the seal made with the "rounded" ring was found to degrade after cycling the valve a number of times. This may be due to some deformation of the teflon by the brass as discussed above. The tests with the "flat" ring showed no degradation in sealing quality with multiple cycles. As a result of these tests, we conclude that a teflon boot sealing against a flat surface with ~ 50 psi of closing pressure will provide a seal more than adequate for the experiment. Given that the area of the piston in the pneumatic cylinder is ~ $2in^2$ the resulting *force* is ~ 100 pounds ($445N$).

3.3.5 Valve Actuation Speed

While the sealing quality depends on the closing pressure (i.e. the pressure difference between the top and bottom of the piston), the opening speed is determined

[21] The sealing quality of the valve depends on temperature and drops precipitously when the valve is cooled (due to the increased brittleness of the materials involved). In room temperature tests of the valve, it was easily possible to create seals with no measureable leaks at all. We also tested the valve at ~$77K$ (through immersion of the apparatus in liquid nitrogen) and found the sealing quality to be indistinguishable from that at $4K$ indicating that whatever material alterations occur upon cooling the valve that lead to the reduced sealing quality have happened by the time the valve has reached liquid nitrogen temperatures, and we would expect no further degradation (from cooling to $400mK$ for example).

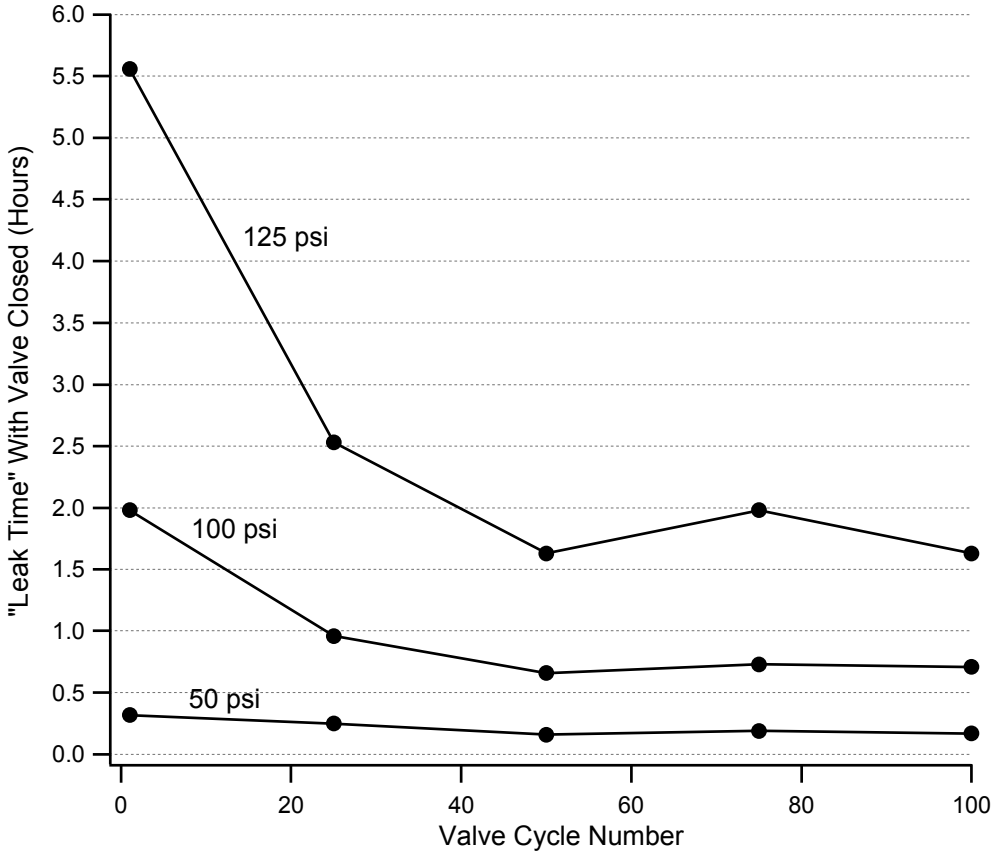

Figure 3.9: Valve test with a teflon boot and "rounded" brass ring. Three differential closing pressures were tested (50 psi, 100 psi, and 125 psi).

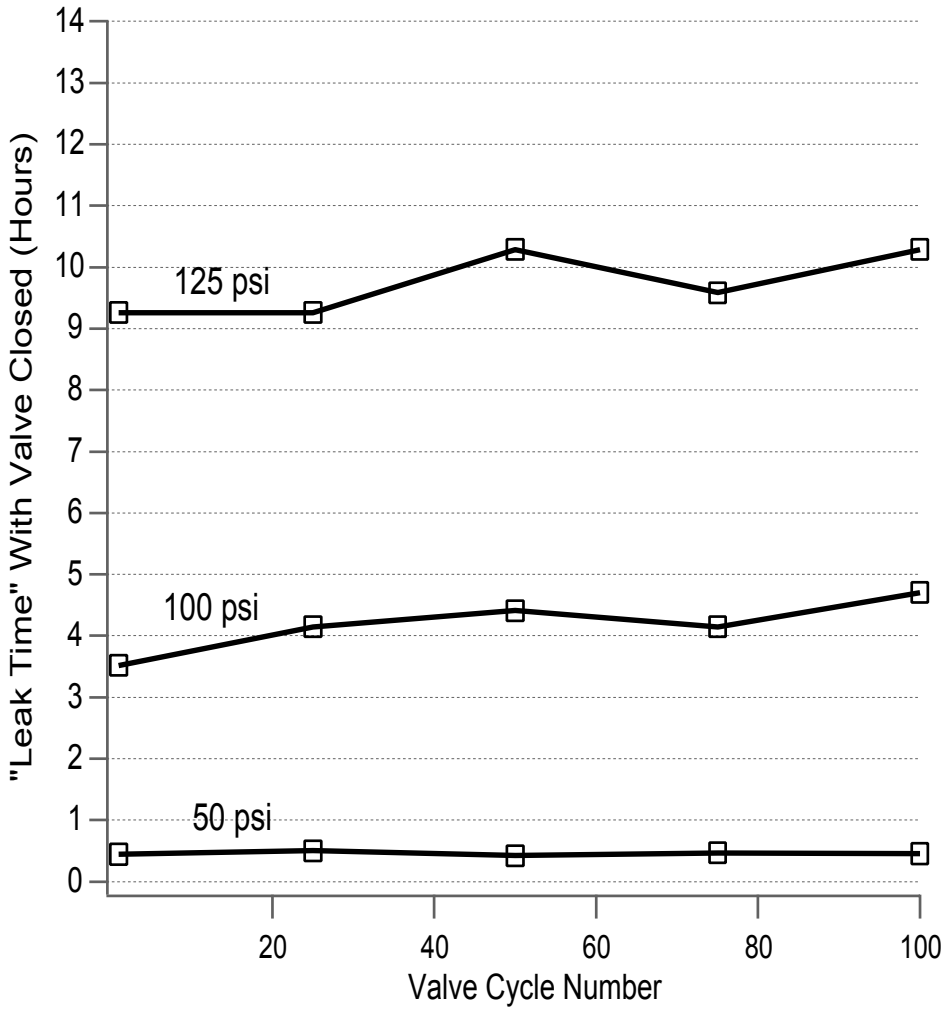

Figure 3.10: Valve test with "flat" brass ring

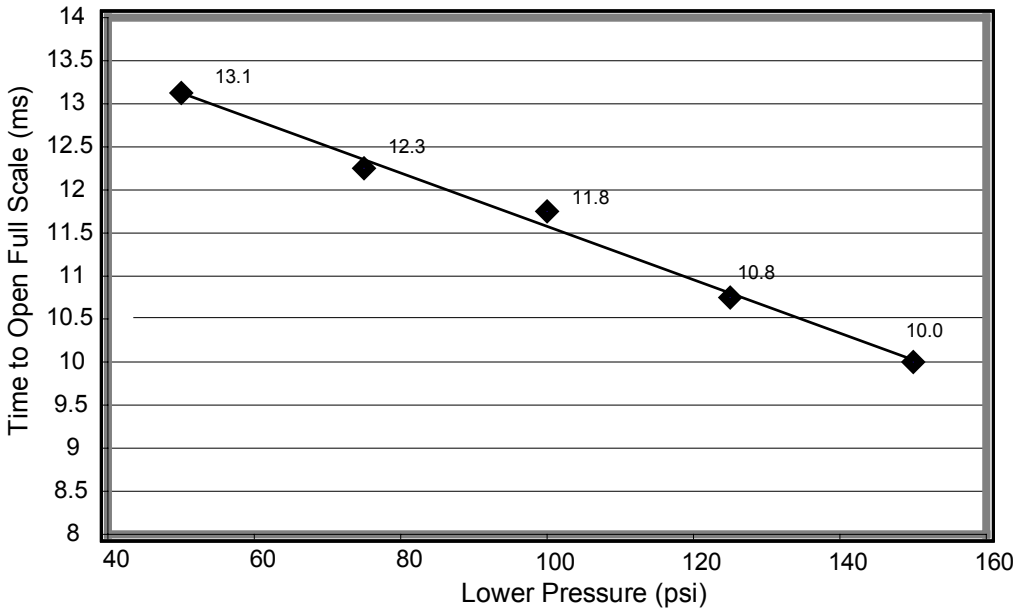

Figure 3.11: Valve actuation speed vs. the pressure behind the piston. Note, the valve moves a total distance of $\sim 3cm$.

primarily by just the pressure on the bottom. This is because the pressure on top is removed very quickly when the solenoid valve opens leaving only the residual pressure behind the piston. This bottom pressure then drives the piston up (opening the valve). By monitoring the position of the piston (using a HeNe laser and photodiode) we were able to measure the opening speed of the valve at various pressures. It was found that the valve could be opened in less than $20ms$ using fairly moderate pressures ($\lesssim 50psi$). Given that we would like the aperture conductance to result in a time constant of $\tau \sim 50ms$ to empty the cell volume of gas, this actuation speed is more than adequate.

Chapter 4
The Experimental Apparatus

The previous chapter described some of the major pieces of the experiment (refrigerator, magnet, and valve). It is not enough that these components function properly on their own. One of the challenges of this experiment is the integration of these systems into a successful trapping apparatus. The full apparatus is the subject of this chapter.

4.1 The Cryogenic Dewar

Our atoms are trapped using a buffer gas cooled to cryogenic temperatures by the ^3He refrigerator. This refrigerator must be insulated from room temperature black body radiation if it is to function. The superconducting magnet must be kept at $\sim 4K$ to operate properly. As a result, the experimental apparatus resides in a dewar filled with liquid helium. A dewar is a familiar item in cryogenic experiments. It consists of several layers to isolate the coldest part of the experiment from the outside environment. Our dewar is shown schematically in fig. 4.1.

This dewar is a commercial item [42] that contains a $\sim 140 l He$ bath space. As noted in ch. 3, liquid helium is fairly expensive, and its consumption represents a significant operating expense during the course of an experimental run (which typically lasts several months). As a result, cryogenic dewars are designed to conserve liquid

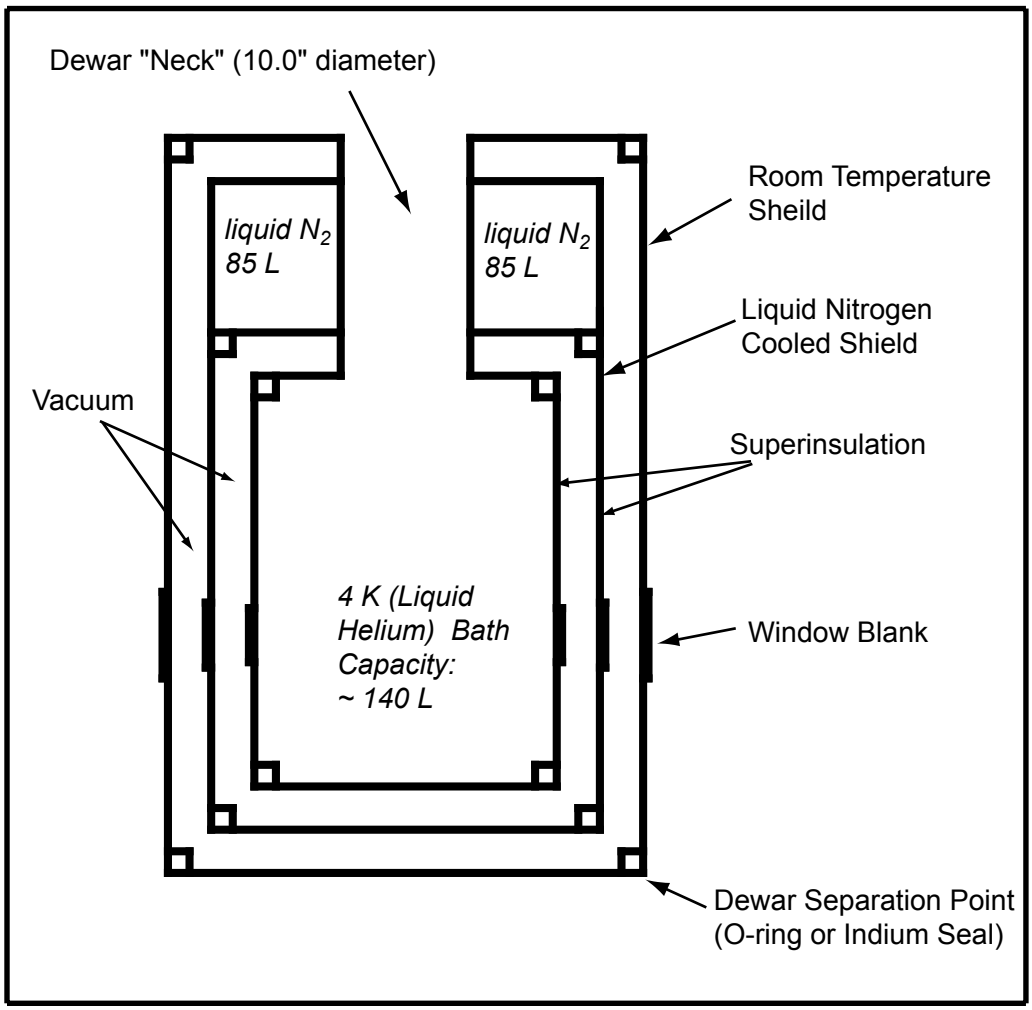

Figure 4.1: Schematic view of the cryogenic dewar used in our experiment. Not shown are the window ports in the bottom of the dewar which were added separately.

helium as much as possible. The dewar contains a vacuum space (generally known as the OVC for Outer Vacuum Can) between the room temperature part and the 4 K bath space. The purpose of this vacuum is to reduce the heat load on the liquid helium due to conduction or convection of gas in the space between room temperature and the bath. To combat the third form of heat transport, radiation, the dewar contains a liquid nitrogen cooled shield between room temperature and the $4K$ bath space in the OVC as shown in fig. 4.1. Because the heat load due to thermal radiation is proportional to the forth power of the temperature of the radiating surface [43], reducing that temperature a factor of three (from $300K$ to $100K$ for example) reduces the radiated power a factor of 81. To further reduce this heat load, both the $4K$ bath and liquid nitrogen cooled shield are wrapped with low emissivity super-insulation (aluminized mylar).

Unfortunately, in even the best designed dewar, some boil-off of both the liquid helium and liquid nitrogen is unavoidable, and so the dewar requires constant "feeding." In a test run, our dewar was cooled down by itself (without the experiment inside) to measure the hold time of the various cryogens and to ensure that the various vacuum tight seals were indeed vacuum tight. During this cool down, a thermometer was placed on the bottom of the liquid nitrogen cooled shield. It was determined that the hold time for both the helium and the nitrogen in the dewar was greater than a week, and no leaks were found. The bottom of the liquid nitrogen cooled shield remained at $\sim 90K$. This (along with the super-insulation) reduces the

radiative heat load to an insignificant level. In these respects, the dewar performed quite well.

The hold time of the dewar drops considerably with the experiment inside. This is due to the additional heat load on the liquid helium presented by the various metal feedthroughs (pumping lines, magnet leads, support rods, valve shaft, etc...) running down into the 4 K bath space. While the experiment is running, we typically transfer about $50L$ of helium every day. Occasionally we might go a day without transferring, but there is another motivation to transfer often. The higher the liquid level in the bath, the colder the top of the IVC is. A cold IVC results in a lower operating temperature for the 1 K pot which in turn leads to a (slightly) lower base temperature for the cell. A high liquid level in the bath may mean the difference between a base loading temperature for the cell of $550mK$ and a temperature of $600mK$. As we shall see, this small difference in temperature can have a large impact on trapping efficiency.

The dewar along with the support structure from which it hangs is shown in fig. 4.2. For mechanical stability, the support structure is both anchored to the floor and braced to two walls using I-beams (not shown) rigidly connected. Also shown in fig. 4.2 is the optics table that is home to the laser systems in our experiment. The laser systems and associated optics will be discussed later in this chapter.

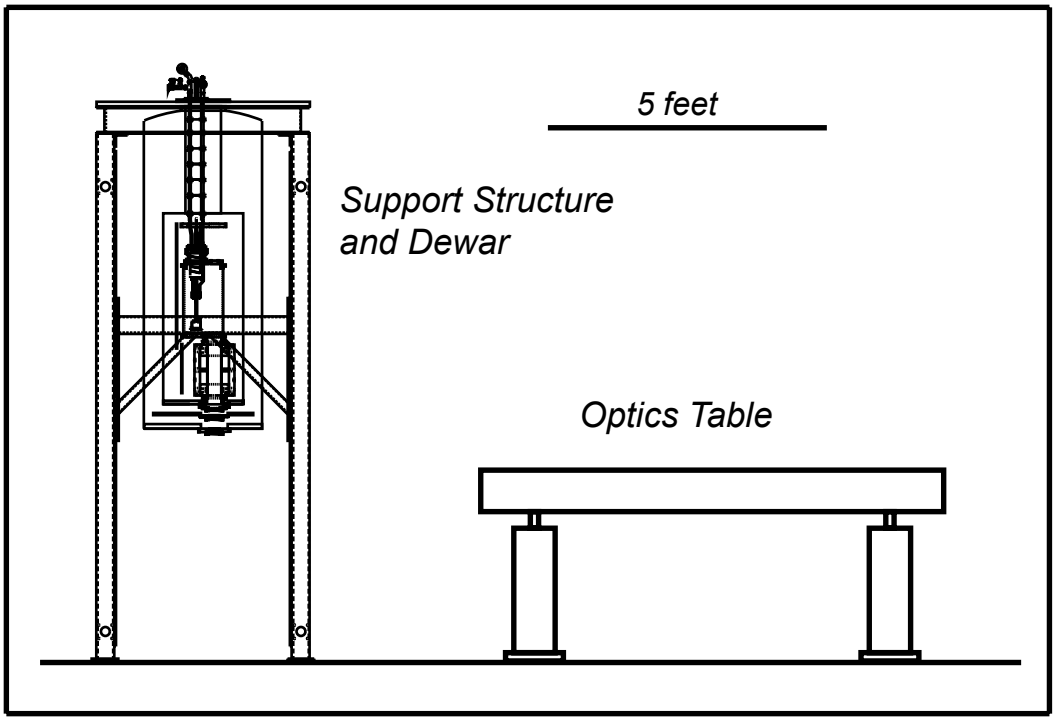

Figure 4.2: Experiment layout showing the (~10 feet tall) support structure for the dewar and the optics table on which the two laser systems (ablation and probe) reside. The beams from these lasers are directed from the optics table upward into the experiment using mirrors on a smaller optics breadboard mounted to the bottom of the dewar (not shown).

4.2 Geometry of the Experiment

Previous buffer gas loading experiments were performed in a geometry such that the cell, refrigerator, and magnet all shared the same central axis. This "on-axis" approach is shown schematically in fig. 4.3.

This geometry is both natural and convenient. Our experiment, however, is complicated by the necessity for a feed through running down the dewar from room temperature to the top of the cell (to accommodate the valve shaft). No such feed through was needed in any of the previous buffer gas loading experiments. In order to incorporate such a feature while maintaining the "on-axis" geometry would require that the various components of the refrigerator (sorb, 1 K pot, ^3He pot) be made annular to allow the shaft to run through them. While this is in principle possible (and was even discussed with various refrigerator vendors), it would represent a substantial increase in cost and complexity. Instead, we decided to adopt an unprecedented "off-axis" geometry shown schematically in fig. 4.4.

In this approach, the ^3He refrigerator runs along side the axis of the magnet, cell, and valve shaft, and is not rigidly connected to any of these. The cell is thermally connected to the refrigerator through flexible copper braid. Despite its awkwardness, this sort of design has several advantages. It has the virtue of modularity in that it separates the mechanical support of the cell and magnet from the thermal connection to the refrigerator. No heavy masses or rigid structures need be connected to the (rather delicate) ^3He pot. This is especially important in our ex-

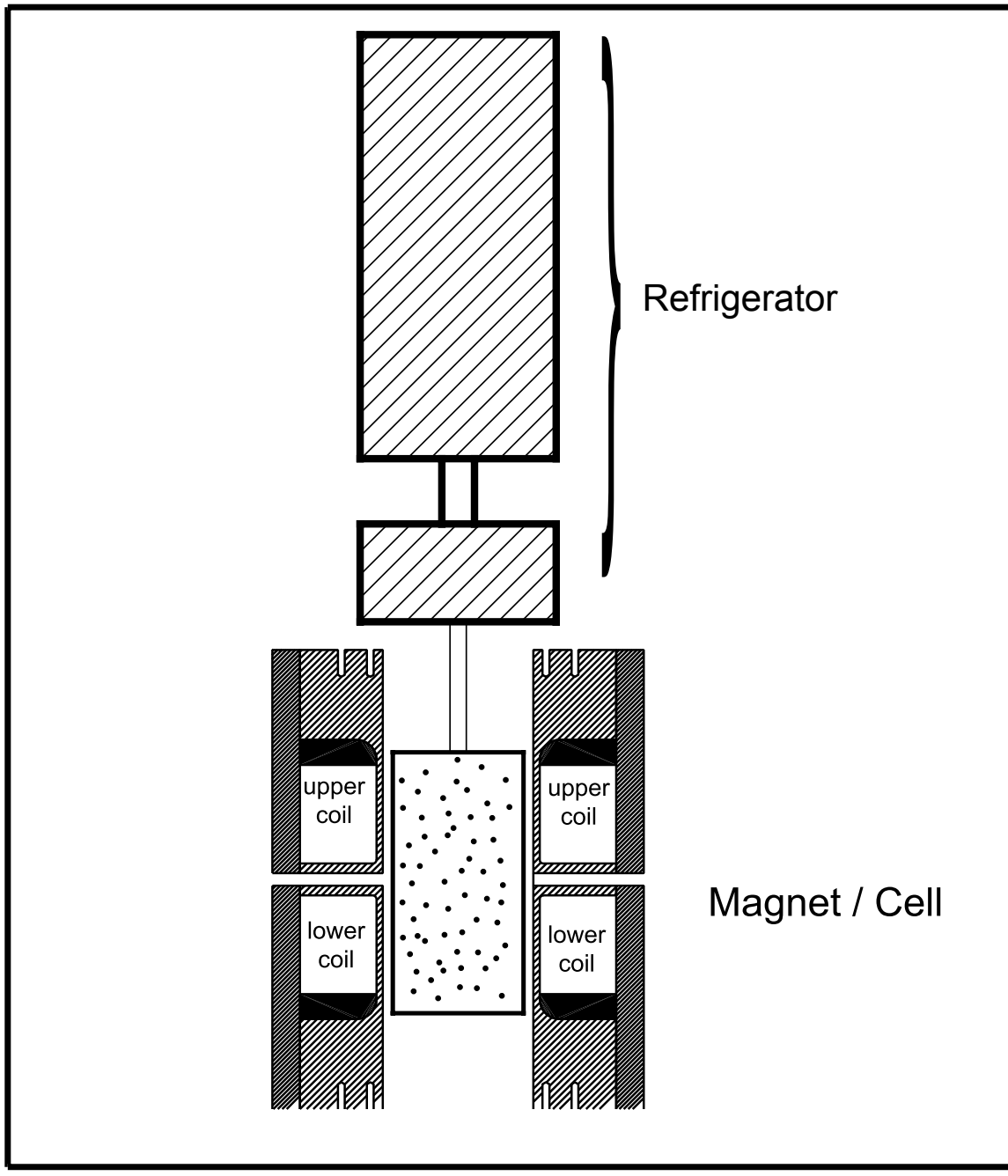

Figure 4.3: Typical geometry for a cryogenic experiment. The key components all share the same central axis.

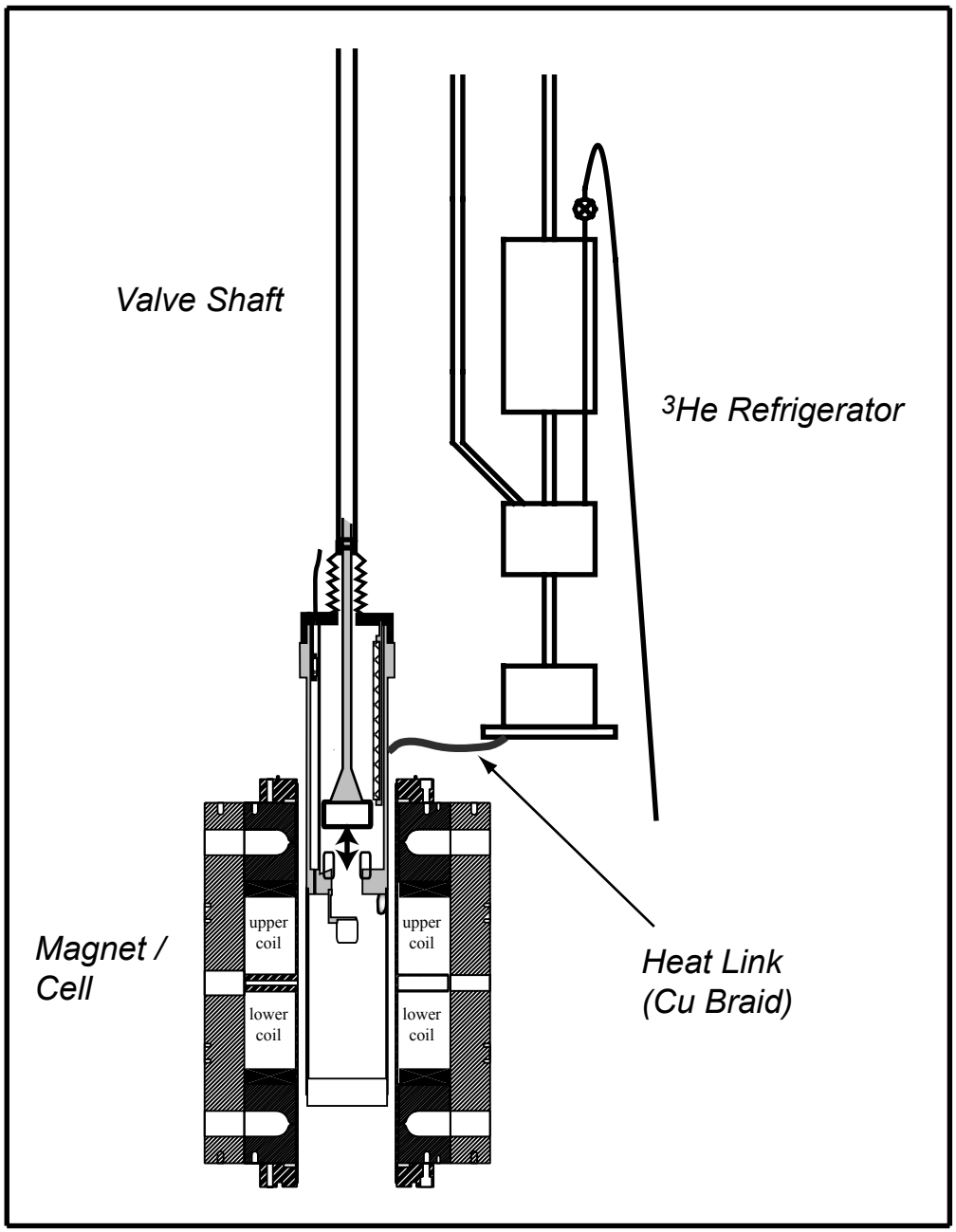

Figure 4.4: In our experiment, the key components do not share the same central axis. This complication is due to the presence of the valve shaft running from room temperature down to the top of the cell.

periment because of the additional (and variable) force provided by the valve boot on top of the cell. Results of test experiments (presented in the previous chapter) indicate that a good seal requires that ~ 100 pounds of force be applied to the valve seat. This force is suddenly released when the valve opens. It is best dealt with separately through a dedicated support structure that doesn't transmit stresses elsewhere. A photograph showing the position of the cell in relation to the ^3He refrigerator (without the magnet present) is shown in fig. 4.5.

An added benefit of this approach is the option to replace the refrigerator without disturbing the cell. For example, if it is found that a dilution refrigerator is necessary to get the cell cold enough to trap $1\mu_B$ particles, or if we decide to work with higher magnetic moment species that don't require the low temperatures possible with a ^3He refrigerator, we can replace it (and free the ^3He for use in a different experiment). A more detailed view of the apparatus is shown in fig. 4.6.

4.3 The Cell

Atoms are trapped in a cell that resides in the bore of the superconducting magnet. While the idea of the cell is relatively simple, in practice it is a complex and delicate piece of the experiment. The cell consists of two parts, the "trapping chamber" and the "pumping chamber." These two parts are connected through the valve aperture (when the valve is open) or isolated (when the valve is closed). The trap-

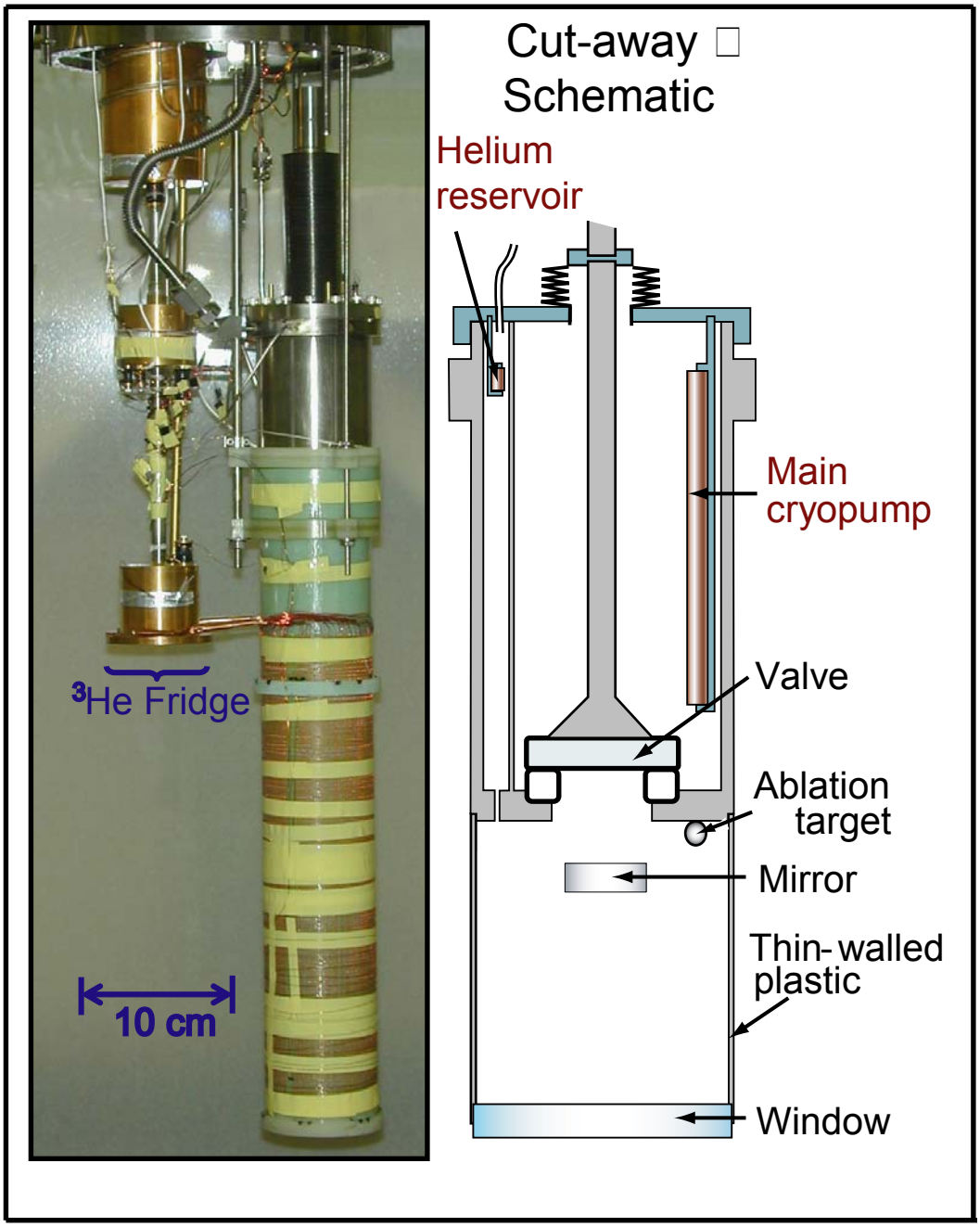

Figure 4.5: Photo and schematic of the cell and the ^3He refrigerator in our experiment.

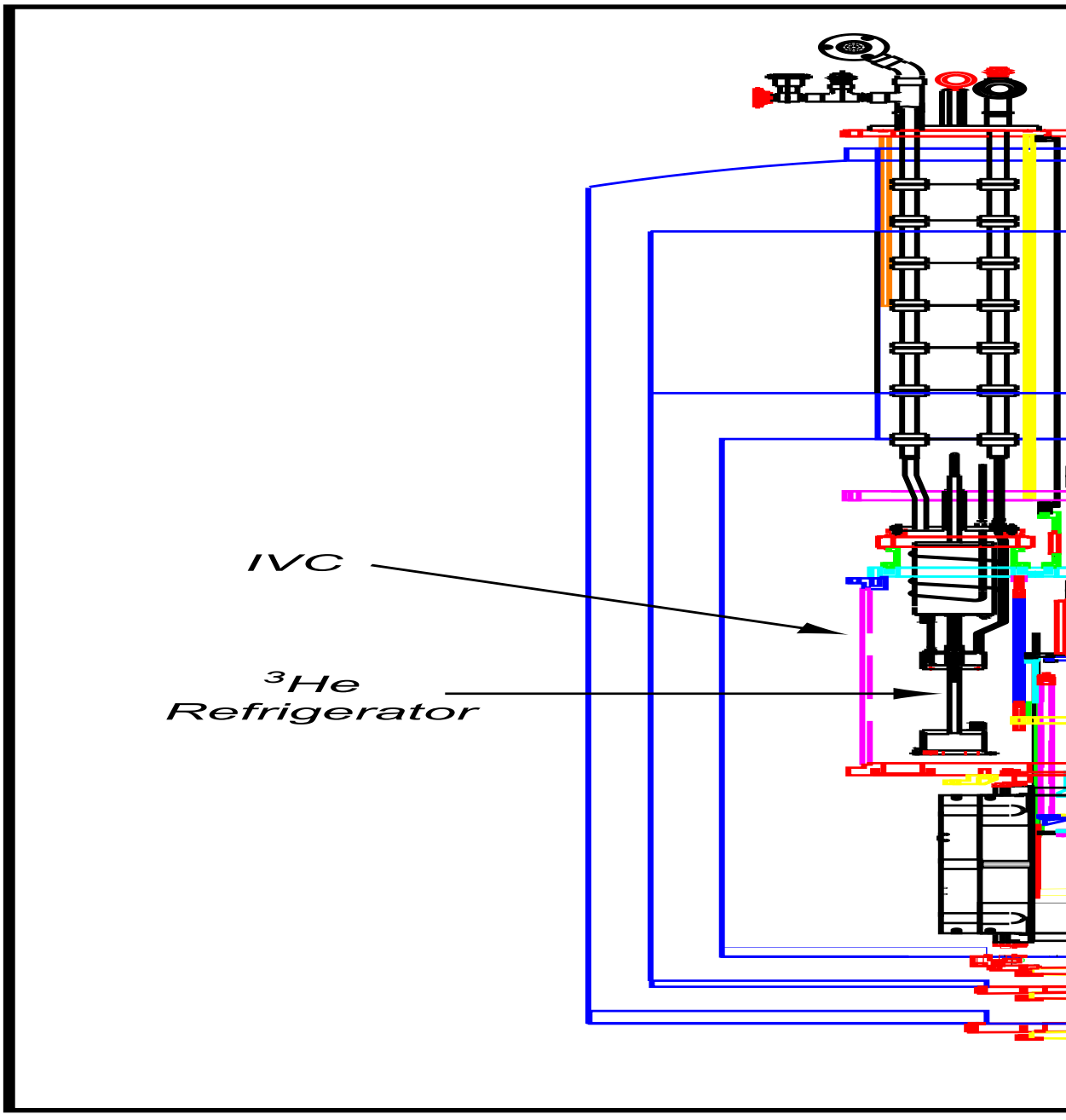

Figure 4.6: Detailed experimental view showing magnet, cell, refrigerator, etc... inside of the dewar

ping chamber contains the experimental samples and is filled with buffer gas before ablation. It is located so that the center coincides (roughly) with the center of the magnetic trap. It also contains a mirror that reflects a probe beam for spectroscopic detection of the trapped sample. The pumping chamber contains a large volume of activated charcoal with sufficient capacity to hold the buffer gas removed from the trapping chamber while maintaining vacuum in the cell. The cell is shown schematically in fig. 4.7. Now, we will discuss in more detail some of its key elements.

4.3.1 Sorption Pump

The pump in the pumping chamber consists of a cylindrical piece of G-10 that is approximately 11" ($28cm$) long and 2" ($5.1cm$) in diameter. About 100 thin (0.010" in diameter) copper wires are embedded in an epoxy layer on top of the G-10 cylinder. These wires run longitudinally down the cylinder and are electrically insulated from one another. Their purpose is to compensate for the poor thermal conductivity of the G-10 and maintain a fairly uniform temperature down the length of the sorption pump. This is too prevent any "hot spots" that might desorb helium and degrade the vacuum. G-10 is used because it is insulating and thus avoids eddy current heating when the magnetic field is ramped up or down. Eddy currents are a concern in all aspects of the cell design and leads us to minimize the use of metal in the cell as much as possible. Approximately 10 grams of activated charcoal are epoxied (using Stycast 2850 [44]) to the G-10 cylinder on the inside and outside to

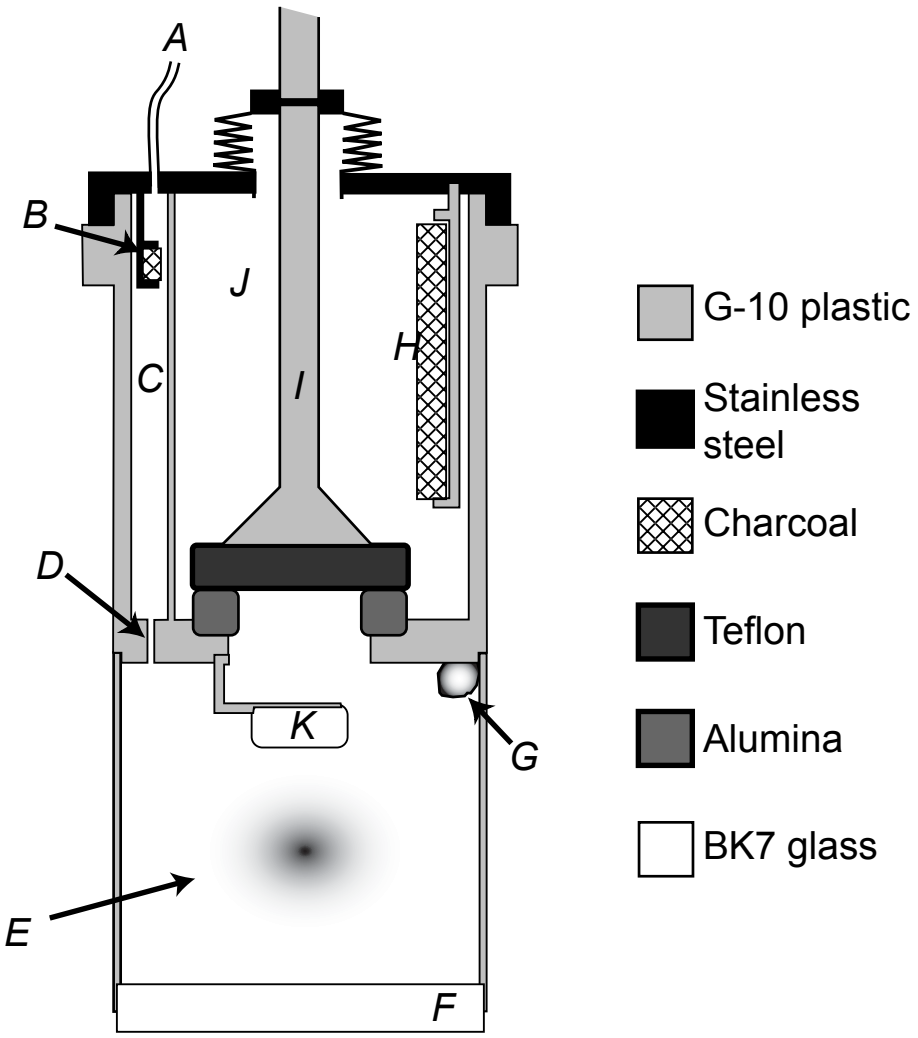

Figure 4.7: Schematic cross-section of the cell with the valve closed. A: Fill line; B: Fill line sorb; C: "Waiting Room"; D: High-impedance pin-hole; E: Trapped sample; F: Window; G: Ablation Target (Cr or Mn); H: Large sorb; I: Valve shaft; J: "Pumping Chamber"

complete the sorption pump. A thermometer and heater allow us to monitor and change the temperature of the sorb (to drive the helium off, for example).

At this point, it is worthwhile to discuss in a bit more detail some of the properties of charcoal that make it useful in our experiment. Why is it that this rather dirty substance that most people associate with grilling hamburgers turns out to be such an effective material for pumping helium (or other gases) from a vacuum chamber? One's first instinct might be to assume that the surface of the charcoal is particularly "sticky" to helium atoms. This in fact is not the case. The binding energy of helium to charcoal (due to the van der Waals interaction) is about $140K$ [45] [31]. This is neither particularly high nor low compared to other substances. It is, however, quite high compared to the $\lesssim 1K$ temperature of the helium gas that we are trying to remove. As a result, at least one monolayer of helium can be very tightly bound to the surface of the charcoal. This is true of most other materials as well (so long as the binding energy of helium to the surface is not unusually low). What makes charcoal special is it's enormous surface area to volume ratio. A single gram of activated charcoal, for example, may present an effective surface area of up to $1000m^2$ [39]. For common varieties of charcoal, this implies a ratio of microscopic to macroscopic surface area of close to 1000. As a result, a single monolayer on such a surface can contain an extremely larger number of atoms. The surface density of helium in a film is $\sim 10^{15}cm^{-2}$ [45]. As a result, a single monolayer of helium sticking to just one gram of activated charcoal may contain as many as 10^{22} atoms. Given that there

are ~ $10g$ of charcoal in the sorb, the total capacity should be on the order of 10^{23} helium atoms. In any given trapping run, we need to fill our ~ $0.4L$ cell volume with a density of ~ $10^{16}cm^{-3}$. If we over fill the cell a bit, we might end up depositing ~ 10^{19} helium atoms on the sorb each time we open the valve. Using these values, we would estimate that the capacity of the sorb is sufficient for ~ 10,000 trapping cycles. In reality, the capacity depends on details of the sorb preparation and may be less than this estimate would indicate. For example, the epoxy may "clog" some of the pours in the charcoal, reducing the useful volume. Even if the capacity is an order of magnitude less than what was estimated above, the sorb would still be good for ~ 1000 cycles.

What about pumping speed, i.e., how quickly the charcoal can remove the helium? Clearly, we need the pumping speed to be comparable to or greater than the conductance of the valve else it will limit the rate at which the buffer gas is removed. Due to it's importance in cryogenic refrigeration and vacuum technology, there has been extensive study of pumping speeds of various types of charcoal, and of how this pumping speed changes as a function of coverage[46] [47] [48] [45]. Because, of the large variation in performance depending on the type and preparation of the charcoal, the pump was over-engineered so there would be little danger that it would prove to be the bottleneck in our buffer gas removal scheme.

A typical value for the pumping speed of charcoal is $\sim 5L/(s \cdot cm^2)$ [46]. In other words, a pump exposing $1cm^2$ of charcoal will have a pumping speed of

approximately 5 Liters per second. Here, the relevant surface area is the apparent (macroscopic) surface area of the charcoal (not the much larger microscopic surface area relevant for determining the charcoal's capacity). This is a relatively high pumping speed. Consider what we need in the experiment. The volume of the trapping chamber in the cell is $\sim 400cm^3 = 0.4L$. We would like to pump this volume out in $\sim 50ms$ (and in fact we could not go faster than this regardless of the amount of charcoal in the pump due to the limit set by the conductance of the valve aperture). The pumping speed required is then on the order of $\sim 0.4L/0.050s = 8L/s$. This can be achieved with only $(8L/s)/(5L/(s \cdot cm^2)) = 1.6cm^2$ of charcoal. In fact the exposed surface area of our pump is $\sim 900cm^2$.

4.3.2 Valve Shaft and Boot

Because the cell must be a separate vacuum space from the rest of the experiment, the shaft for the valve can not run unbroken from the top of the dewar directly to the valve boot. Instead, the shaft is composed of two parts. Most of the length consists of a stainless steal tube ($1/2$" in diameter with 0.049" thick walls as used in the valve testing apparatus) running from the room temperature pneumatic cylinder to the top of the cell. The rest of the shaft is made from a solid G-10 rod ($1/2$" in diameter). This portion of the shaft is inside the pumping chamber of the cell and ends in the valve boot. These two parts are joined at a vacuum tight flexible metal bellows at the top of the cell.

The valve boot consists of a piece of teflon epoxied to a G-10 body. This boot is identical to the one tested in the prototype. The valve seat, however, is not identical. The use of metal must be avoided in this part of the experiment because of the large magnetic field present when the trap is energized. This prevents us from duplicating the brass ring used in the prototype. Instead, the boot is made from polished alumina (in the "flat" geometry that was found optimal in the valve tests).

4.3.3 Thermal Considerations

In order to most efficiently trap low magnetic moment species, we would like to keep the cell as cold as possible. The ^3He pot of the refrigerator is connected only to part of the cell through the copper braid. To keep the entire cell as cold as possible, it would be desirable to construct the body of the cell from a material with high thermal conductivity (thus minimizing temperature gradients). Unfortunately, the best common materials for thermal conductivity are metals (OFE copper for example). As noted above, the use of large quantities of metal must be avoided because of the issue of eddy current heating.

Note, eddy currents would not be a problem (even with the large magnetic fields present in the cell) if it weren't necessary to change the magnetic field during the course of the experiment. The field does need to be changed, however, both to form the trap and to do evaporative cooling of the sample once it has been trapped. The first issue is not prohibitive. Ramping the magnet up slowly would minimize

eddy current heating and allow the use of a metal cell if desired. In fact, other buffer gas loading experiments have used all metal cells [21] [20]. Efficient evaporative cooling, however, requires that the magnet be ramped down rapidly (in comparison to the trap lifetime). Such a rapid change in field would result in prohibitively large heating if an all metal cell were used.

As a result, the bulk of the cell is constructed from the insulating material G-10. Despite its many favorable properties for use in cryogenic experiments, G-10 suffers from exceedingly poor thermal conductivity (more than 1000 times worse than OFE copper at $1K$ [41]). As a result, something must be done to increase the thermal conductivity along the length of the cell to maintain a constant (and low) temperature throughout the cell. There are two approaches that have been used to bolster the thermal conductivity in cells constructed from G-10. One method is to employ a double walled design for the cell. In such a cell, there is an additional G-10 cylinder concentric with and surrounding the inner wall. In between the inner and outer walls, there is a small amount of space (colloquially known as the cell "jacket"). This space is filled with superfluid liquid helium. Superfluid He at ~$2.2K$ (the so called lambda point) has an extremely high thermal conductivity (better even than OFE copper) [15]. The thermal conductivity at typical operating temperatures for our experiments ($\sim 0.5K$) is somewhat lower, but still sufficiently high to maintain a uniform temperature throughout the cell [49]. This approach is used in the MIT hy-

drogen experiment [19] and has been used in the Cr evaporative cooling experiments in our lab [38].

In this experiment, we use a different approach (see [24]) which has already been alluded to earlier in the discussion of the charcoal sorption pump. The cell has ~ 100 thin OFE copper wires (0.010" in diameter) running down its length. These wires are epoxied (using Stycast 1266 [50]) to the body of the cell. Kevlar string is wrapped around and epoxied to the cell body to provide additional protection against the wires peeling off. The copper wires provide sufficient thermal conductivity along the length of the cell to maintain a uniform temperature (to better than ~$10mK$ as measured by two thermometers on top and bottom of the trapping chamber). Because the wires are not electrically connected, there are no large closed loops for eddy currents to flow, and heating when the magnet is ramped up or down is insignificant. In fact, the cell temperature actually decreases when the magnet is ramped down probably due to nuclear demagnetization of some materials in the cell body.

4.3.4 Cell Fill Line

Filling the cell with helium buffer gas is in principle a straight forward process. A small (lecture bottle) cylinder at room temperature contains the ^3He. Connected to this cylinder is a line that runs to a clean gas handling system also at room temperature. This room temperature gas handling system has two lines that run into the dewar. One of these lines (composed mostly of $1/4$" stainless steal tubing) goes to

the top of the cell and is used to pump out the cell volume. The other line is connected to the cell waiting room shown in fig. 4.7. It is through this line that the buffer gas is introduced.

The reason that this line is not connected directly to the trapping chamber is a little subtle, but it is vital to our rapid pump-out scheme. Chapter 3, discussed the size of the valve aperture needed to give a sufficiently rapid evacuation of the buffer gas. Now, after the majority of the gas is removed, any contiguous small volumes will leak gas into the trapping chamber degrading the vacuum in the cell for a period of time determined by the impedance of the line that connects this volume to the trapping chamber. If this impedance is high (as with a long thin fill line for example), then the time constant for removing the gas from the line will be unacceptably long and defeat the rapid pump out scheme provided by the valve. To get an idea for how this might be a problem, consider the following.

In the molecular flow regime, the conductance of a long tube is given by [39]:

$$C = 3810\sqrt{\frac{T}{M}}\frac{D^3}{L} \tag{4.1}$$

Where T and M are the temperature (in Kelvin) and molar mass of the gas, D and L are the tube's diameter and length (in cm), and C is the conductance (in cm^3/s). Recall from ch. 2 that the pump-out time of a volume is given by:

$$\tau = V/C \tag{4.2}$$

The volume of a tube is simply:

$$V = \frac{\pi}{4} D^2 L \tag{4.3}$$

Combining eqs 4.1, 4.2, and 4.3 gives:

$$\tau_{tube} = 2.06 \times 10^{-4} \sqrt{\frac{M}{T}} \frac{L^2}{D} \tag{4.4}$$

Plugging in a molar mass of 3 (for ^3He), and assuming a temperature of $0.5K$ gives a formula for the conductance that depends only on the tube geometry:

$$\tau_{tube} = 5.05 \times 10^{-4} \frac{L^2}{D} \tag{4.5}$$

Now, let's say that we have a fill line attached to our cell that is ~ 2′ (61 cm) long and has an inner diameter of $0.1cm$. This length is rather conservative given that the fill line must extend all the way to the room temperature gas handling system, but let's say we've placed a cryogenic valve somewhere along the path of the fill line to reduce the length of the volume that we need to pump out. Even with such a reduction in length, the pump-out time for such a volume is ~ $20s$ which is much too long a time to wait to achieve vacuum in the cell.

As a result of this consideration, we introduce buffer gas into the cell in a two stage process. First, helium is placed onto the cell fill line sorb (see fig. 4.7) from the room temperature gas handling system. This is done with the fill line sorb cold ($\lesssim 5K$) so that the helium is bound tightly to the charcoal. Typically, several torr liters (1 torr liter = 3×10^{19} atoms) of helium is put onto the sorb. This is an ample quantity for many cell fillings, and is done relatively infrequently (about once a week or so while running the experiment).

Once the sorb is filled, the room temperature part of the gas handling system is pumped out and closed off to the dewar. At this point, we are ready to introduce the buffer gas into the trapping chamber. To do this, a voltage pulse is applied to a ($\sim 150\Omega$) resistive heater on the cell fill line sorb. Typically, $\sim 10V$ is applied for $1s$ (corresponding to $\sim 0.7J$ of energy). This heats the sorb from $\sim 1K$ to $\sim 10K$. As a result of the elevated temperature, enough helium desorbs to fill the waiting room with a density of $\sim 10^{18} cm^{-3}$ of ^3He. Note, this is a much higher density than what is needed in the cell (typically $\sim 10^{16}\, cm^{-3}$). The buffer gas then begins to leak into the trapping chamber through a high impedance pinhole. The cell fill line sorb remains relatively hot for several minutes. The (1/e) to fill the trapping chamber through the pinhole was engineered to be ~30 minutes (corresponding to a pinhole conductance on the order of $\sim 2 \times 10^{-4} L/s$). Because the cell waiting room is initially filled to a high density with helium, we don't need to wait a full 1/e time to fill the trapping chamber. After about two minutes or so, enough helium

has accumulated in the trapping chamber to yield the requisite density for trapping. After about five minutes, the cell file line sorb is cold again ($\lesssim 2K$ as seen in fig. 5.3) and the residual helium in the waiting room returns to the sorb creating a good vacuum in the waiting room. The cell fill line sorb is trying to pump-out the trapping volume as well, but it is doing so through the extremely high impedance provided by the pinhole (with the ~30 minute 1/e time). As a result, the buffer gas density in the trapping chamber remains relatively constant for an extended period.

At this point, the cell is full of buffer gas and the waiting room is adequately pumped out so as to avoid the problem of buffer gas "trickle" discussed above. To reiterate, the key to this whole procedure is in the large impedance provided by the pinhole between the waiting room and the cell trapping volume. The cell can be filled relatively quickly because the waiting room contains a high density of helium. The pinhole, however, prevents the fill line sorb from rapidly pumping out the trapping volume as it does with the waiting room (note the 1/e time above). We can now ablate at our leisure (so long as we don't wait more than an hour or so!). In practice we often wait ten to fifteen minutes to allow the cell to cool from the slight temperature increase that results from the heating of the fill line sorb.

4.4 Laser and Optics Setup

Having discussed the major cryogenic elements, we now briefly turn to the laser system and associated optics in the experiment. The optics setup in our experiment

is quite similar to that of the previous Cr trapping experiments [24] [51]. While our laser cooling colleagues can justifiably point out the complexity of our cryogenic setup compared to their room temperature vacuum systems, they are no doubt envious of our relatively barren optics table. There are two relatively simple laser systems used in the experiment, one to produce that atoms and one to detect them.

The trapped atoms are produced through laser ablation of a solid precursor in the trapping chamber. The ablation is done using a Q-switched Nd:Yag laser [52]. The fundamental output of the YAG laser is at $1064nm$. We use the frequency doubled $532nm$ (green) light output of the laser for safety and ease of alignment. The YAG laser is capable of outputting quite energetic pulses (on the order of $100mJ$ and greater). This high energy is much greater than what is typically used in the experiment. The optimal pulse energy is found empirically. In general, the more energy used, the more atoms produced in the ablation (though we see saturation around $\sim 10mJ$). Greater pulse energy also results in more heating of the cell (and thus a higher buffer gas temperature) and can result in lower trapping efficiency. Typically, ~ 1 or $2mJ$ pulses are optimal. The pulse duration is $\sim 5ns$ and may be regarded as instantaneous when compared with any other time scale in the experiment.

For spectroscopic detection of the Cr, we use a diode laser [53]. This laser produces up to $\sim 1mW$ of light at $\sim 425.55nm$. It can be scanned rapidly (up to $\sim 1kHz$) over a range of $\gtrsim 10\ GHz$. It allows us to address the ${}^7S_3 \rightarrow {}^7P_4$ transition

(but not the ${}^7S_3 \rightarrow {}^7P_3$ or ${}^7S_3 \rightarrow {}^7P_2$) in Cr. The layout of the optics is shown in fig. 4.8.

The probe beam is split in two using a beam splitter mounted to the small optics breadboard on the dewar. One part of the probe beam is sent directly to the "Reference" PMT. The other part is sent through the atomic sample and is retroreflected from the mirror in the cell. The reflected beam then lands on the "Signal" PMT. We denote the intensities of these two signals as I_{ref} and I_{sig}. To compute the optical density of the sample, we use the divide signal: $D = I_{sig}/I_{ref}$ to remove noise associated with fluctuations in the laser. When atoms are present in the cell, we denote the divide signal as D_{atoms}. When we are taking a baseline with no atoms present, we denote the divide signal as $D_{b.l.}$. The transmission of light, T, through the cell is simply $D_{atoms}/D_{b.l.}$[22]. The optical density and transmission are related through:

$$T = e^{-OD} \tag{4.6}$$

Thus, we have for the optical density of the sample,

$$OD = -\ln\left(\frac{D_{atoms}}{D_{b.l.}}\right) \tag{4.7}$$

[22] We assume that contributions from various noise sources, shot noise, cell vibrations etc... are small.

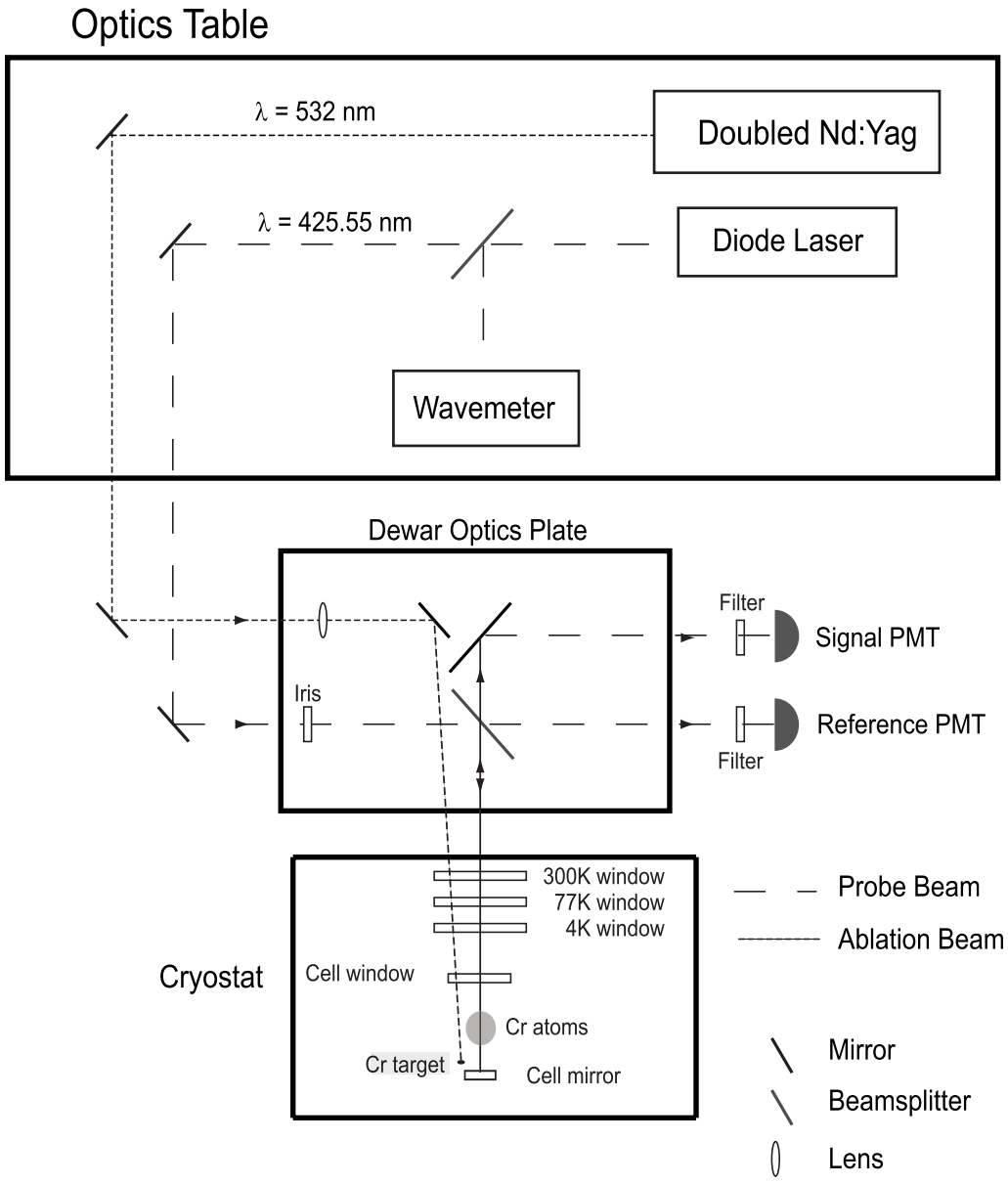

Figure 4.8: Optics setup in the experiment. Various beam shaping optics have been omitted for clarity.

Chapter 5
1st Experimental Run: Cool down and Results

5.1 Recap of Requirements

In the preceding chapters, we discussed the theoretical issue involved with extending buffer gas loading to lower magnetic moment species as well as preliminary experimental work to address these issues. Numerical simulations described in ch. 2 indicated that to efficiently trap and thermally isolate atoms with magnetic moments down to $1\mu_B$, the buffer gas temperature should be $\lesssim 400mK$, the magnetic trap depth on the order of 4 Tesla, and the buffer gas removal time $\sim 50ms$. Chapter 3 discussed the ^3He refrigerator, the new deep anti-Helmholtz magnetic trap, and the development of a large fast actuating cryogenic valve that allow us to satisfy these requirements. In 4 it was discussed how these elements were brought together to form a complete trapping apparatus. We now describe the operation and performance of this apparatus in the first run of the experiment.

5.2 What Atom to Trap?

We want to choose an atom that gives the best hope of success at demonstrating trapping and that allows us to work out the inevitable bugs in the machine. With this

in mind, we chose chromium (Cr) for the first run. Chromium has many favorable properties, some of which are listed below:

1) It has a large ($6\mu_B$) magnetic moment which makes for (relatively) easy trapping.

2) We know from prior experience that it can be produced efficiently through laser ablation (~ 10^{13} atoms per pulse).

3) It is a common metal that is stable in air in its bulk form and can easily be incorporated into the cell.

4) The dominate isotope, ^{52}Cr has no nuclear spin and as a result, no hyperfine structure. This makes the spectroscopy straightforward. In addition, there is a convenient strong optical dipole transition in the visible (at ~$425nm$) for doing absorption spectroscopy.

5) We have worked with Cr extensively in the past in the lab.

5.3 Goals of 1st Experimental Run

We hoped to accomplish a number of specific goals during the inaugural run of the experiment. First, we wanted to perform a sort of proof of principle demonstration of the experimental concept. In other words, to show that this new method for removing the buffer gas is an effective means for quickly achieving thermal isolation of a trapped sample without losing too great a number of atoms in the process.

Besides the number of atoms that could be trapped with this approach, we were also concerned with the ultimate quality of the vacuum achieved after pump-out of the buffer gas. To do evaporative cooling and reach quantum degeneracy requires that the sample be thermally isolated from the walls of the trapping chamber. In addition, any loss due to residual gas in the chamber (even if it is does not heat the sample) must not limit the lifetime of the sample to a time less than what is required to achieve quantum degeneracy (on the order of $\sim 100s$ say in a typical evaporative cooling experiment).

To be able to trap and thermally isolate a large number of Cr atoms with this apparatus would by itself represent a significant technological advance in the field of buffer gas cooling, for it would obviate the need for a dilution refrigerator to remove the buffer gas. Our goal, however, is not simply to ease the requirements on the cryogenic refrigeration needed in this sort of experiment, but also to extend the technique to lower magnetic moment species. In the first run of the experiment, we did not place any low magnetic moment atoms into the cell. Instead, we could simulate what it would be like to work with lower magnetic moment species by simply loading Cr at different initial magnetic trap depths. Recall that the interaction potential for a magnetic dipole in a field is given by:

$$V = -\mu \cdot B \tag{5.1}$$

For the purpose of magnetic trapping, it is only the product of the magnetic moment and the magnetic field that is important. For example, working with Cr at a magnetic trap depth one half of the maximum achievable trap depth is entirely equivalent to working with a $3\mu_B$ species at the maximum trap depth. Likewise, by energizing the magnet to only one-third of the maximum, we can simulate working with $2\mu_B$ species and so on. It is in this sense that we use the qualifier "effective" in front of magnetic moment (and also to appease the nit-pickers who point out that the only thing we trap in this 1st run is a $6\mu_B$ atom).

5.4 Cool Down of the Experiment

We now discuss the final assembly and cool down of the experiment for the first trapping run. Because many aspects of the cool down are generic and apply equally well to any run of the experiment, we will keep the discussion general. In any large scale experiment, there is a laundry list of items to check before operation of the experiment may commence. Given the long turn around time to assemble, cool down, warm up, and disassemble, a cryogenic experiment, it is especially important that care be taken in every aspect of the assembly. In addition, because of the effects of thermal contraction and other material property changes that result from cooling to cryogenic temperatures, there are a number of tests to perform at each stage of the cool down[23].

[23] Sadly, a seal that is vacuum tight at room temperature need not be at 4 K!.

5.4.1 Room Temperature Valve Test

In addition to the many electrical tests, thermometry tests, leak tests etc... common to most cryogenic experiments, we test the quality of the valve seal both before and during the cool down. We do this in much the same way as we tested the valve prototype. A certain amount of helium gas (usually ^4He to be economical) is introduced into the cell through the gas handling system with the valve closed. The leak rate through the valve is monitored by pumping on the other side of the valve with a helium (mass spectrometer) leak detector (see fig 5.1).

Several room temperature tests of the valve seal are done during the assembly of the experiment. These multiple tests are performed because the cell is moved around by small amounts during the assembly, and we want to see if this has any effect on the sealing quality. The seal is tested after the installation of the cell, after the magnet is put up (the large mass of which causes the cell to shift slightly), and after final assembly is complete. Generally, the sealing quality remains fairly constant during the assembly procedure. In all of the valve tests, we operate with ~95 Psi on top of the piston and 30 Psi behind the piston. These are the same pressures used during the experiment and result in a net closing pressure of ~80 Psi (95 Psi - 30 Psi + atmospheric pressure).

The performance of the valve in the experiment is somewhat worse than in the valve prototype. At room temperature, we typically measure a conductance for the closed valve on the order of $\sim 10^{-5} L/s$. This results in a (1/e) time constant

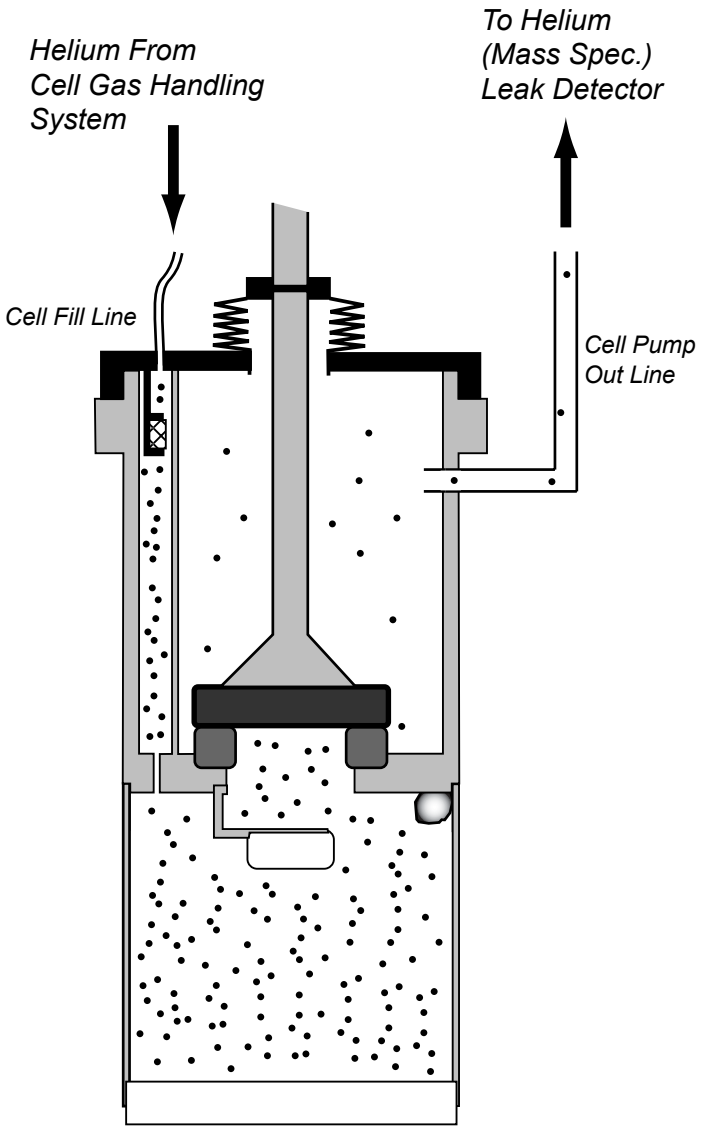

Figure 5.1: Schematic illustrating procedure for testing the quality of the valve seal in the experiment. Buffer gas is introduced to the trapping chamber of the cell through the cell fill line with the valve closed. Any helium that leaks through the valve is detectected using a helium (mass spectrometer) leak detector connected to the pumping port on top of the cell.

for emptying our ($\sim 0.4L$) cell volume of $\sim 40,000s$. In comparison, the room temperature tests of the valve prototype showed no (measurable) leak at all at room temperature. The reason for this poorer seal remains to be determined. Perhaps the longer length of the shaft in the experiment results in a less ideal "seating" of the valve boot on the sealing surface, or perhaps the surface quality of the teflon boot and alumina surface are not quite as good as that of the teflon and brass that were used in the prototype. Fortunately, as we noted earlier, the actual performance requirements on our valve are rather modest, and the leak rates that we observe while troublesome (in that they may indicate some design flaw) are not prohibitive.

5.4.2 Cooling to 77 K

It is common practice in cooling down a large liquid helium based cryogenic experiment to first pre-cool the apparatus using liquid nitrogen. This is done because nitrogen is relatively cheap compared to helium (recall table 3.1) and has a much greater cooling power [15]. Cooling the experiment to $\sim 77K$ is also convenient as it allows us to perform a number of tests at an intermediate temperature before the experiment is cooled to its lowest temperature. To cool to $77K$, liquid nitrogen is transferred into the $4K$ bath space. Before doing this, we typically blow helium gas through the bath space for several hours to ensure that it is dry. This is to avoid condensation of water vapor or other impurities as the experiment cools. We transfer liquid nitrogen slowly, taking about 12 hours (or more) so as to avoid excessive ther-

mal shock to the various dissimilar materials in the experiment. Differential thermal contraction is unavoidable during the cool down. If, however, parts of the experiment cool more rapidly than others, this effect may be exacerbated causing leaks to form. We have diode thermometers [54] on many parts of the apparatus (the bottom of the $77K$ shield, two on the magnet, one on top of the IVC, in addition to various cell and fridge thermometers) that allow us to measure the temperature of these components during the cool down. Typically, we try to ensure that no part of the experiment is cooling faster than ~$1K$ per minute.

Because the IVC is under vacuum, the cell and refrigerator inside are only in weak thermal contact to the bath space. As a result, they cool quite slowly. To facilitate the cooling of these components at a reasonable rate, we typically put ^3He exchange gas (~ 0.5 torr) into the IVC to create better thermal contact. We can also use this exchange gas to check for leaks from the IVC into the cell. Once the cell and refrigerator have reached ~ $77K$ and leak checks have been performed, we pump the exchange gas out of the IVC. At this point, the quality of the valve seal is again tested. The presence of the large sorption pump in the cell prevents further valve testing in this manner at $4K$, so this is the last indication of the valve performance apart from running the actual experiment[24]. The results of the $77K$ valve leak check typically yield a value for the conductance of a few times $10^{-4}L/s$.

[24] Recall, that in tests with the prototype, the performance of the valve at $77K$ was indistinguishable from that at $4K$.

Comparing this with the room temperature results, we see that the sealing quality degrades considerably during the cool down. This is not unexpected given the increased brittleness of materials when they are cold (and indeed, we saw the same trend in the tests with the valve prototype). It does, however, put us into somewhat dangerous territory as regards our ability to hold onto the buffer gas during the initial phase of trapping. This problem is made worse by the large impedance of the pinhole (recall $C \sim 2 \times 10^{-4} L/s$) that separates the cell waiting room from the trapping chamber. Obviously, the rate that buffer gas enters the cell (through the pinhole) must be greater than the rate it exits (through the leaky valve). Working in our favor is the fact that during the introduction of buffer gas into the cell, the pressure in the waiting room is much higher (typically by a factor of 100 or so) than what is required in the trapping chamber. If the impedances of the pinhole and leaky valve were comparable, then this would result in a flux into the cell about 100 times greater than the flux out. Fortunately, the valve seal is adequate for the experiment. This sealing issue is sill troublesome, however, and warrants further investigation. Work is currently underway to attempt to improve upon the sealing quality so that it is not an issue in future experiments.

5.4.3 Cooling to 4.2 Kelvin

With the experiment pre-cooled and the $77K$ tests performed, it is ready to cool further using liquid helium. This requires first removing any excess liquid nitrogen

from the bath space. If we are feeling particularly efficient, we collect this nitrogen and use it as we fill the $77K$ shield reservoir. Before transferring liquid, we again flush the bath space with dry helium gas for several hours to make sure that we have really gotten rid of all the residual liquid nitrogen. As before, we transfer liquid into the bath slowly to avoid thermal shocks. During this time, the IVC remains under vacuum. Periodically, we pump on the IVC with the helium leak detector to check for leaks from the bath into the IVC. Even with a slow (~ 5 hour) transfer of helium, leaks periodically opened and closed in the IVC during the first cool down. These leaks seemed largest when the transfer of each dewar began (note: three 100 liter dewars were used during the cool downs to 4 K). Perhaps this is due to the increased pressure in the bath space during the early part of the transfer. These leaks were initially noticed by monitoring the temperature of the various components of the cell in the IVC which were observed to cool at an accelerated rate at certain times (due presumably to the presence of the "exchange gas" in the IVC resulting from the leak). Opening the IVC to the gas handling system and leak detector revealed a pressure in the IVC of $\sim 4mTorr$ when these leaks were noticed, and a leak rate on the order of $\sim 10^{-6}$ to $10^{-5} mbar \cdot L/s$. The leaks generally closed when the transfer of each dewar was complete. By pumping on the IVC, we could quickly remove the residual helium gas in the IVC (and in so doing observed that the cell cooling proceeded at its initial rate before the leaks were observed). The source of these leaks remains a mystery. There are ~ 20 indium seals of various sizes on our IVC which have

been thermally cycled several times (during test cooldowns) and which are subject to stresses resulting from the differential thermal contractions (during the cooldown). Similar behaviour has been observed during the cooldown of the apparatus used in the neutron lifetime measurement experiment. During the second experimental run, we tried to be gentler on the apparatus during the cooldown. Cooling to 4 K was done about three times more slowly (taking ~15 hours). It is interesting to note that no leaks were observed at any time during this slower cooldown.

While transferring liquid helium into the bath space, we also transfer liquid nitrogen into the $77K$ shield reservoir. Once the bath space is filled, (^3He) exchange gas is again put into the IVC to cool the refrigerator and cell. At this point, we generally have the valve closed so that the shaft isn't thermally "floating." This ensures that the shaft and valve boot cool along with the rest of the cell. Typically it takes ~12 hours for the cell to cool to $\sim 4K$.

5.4.4 Running the ^{3}He Refrigerator

Once the cell is at $\sim 4K$, the ^3He refrigerator can be run for the first time. We begin by operating the $1K$ pot. This is done simply by opening the needle valve to allow liquid helium into the pot (which is collected from the main bath space through the 1K pot sipper line) while pumping on the pot to evaporatively cool the liquid inside. Once liquid has accumulated in the pot, the temperature drops quickly to $\sim 1.0K$ or so. At this point, we are ready to condense the ^3He into the ^3He pot.

As described in ch. 3, this is done by heating the charcoal sorption pump in the refrigerator to $\sim 40K$ while maintaining the temperature of the $1K$ pot at $\lesssim 2.0K$ so that the ^3He is able to condense. Typically, the sorb is kept at $\sim 40K$ for about 30 minutes to ensure that all of the ^3He is condensed. Once this is done, heating the sorb is ceased, and the sorb allowed to cool. At this point, the charcoal begins to pump on the ^3He pot. The refrigerator is now running and continues to operate until all of the ^3He has evaporated (at which point it must be recondensed).

During the first cool down of any run of the experiment, much of the ^3He is expended in cooling the cell to its base temperature. From this point on, regeneration can be done rather infrequently (once every one or two days typically). The base temperature of the cell is different depending on whether the valve is opened or closed (due to the heat load presented by the shaft). In the first run of the experiment, the base temperature with the valve closed was $\sim\mathbf{550mK}$ and with the valve opened $\sim\mathbf{420mK}$[25]. Both of these numbers are important and have a large effect on the trapping efficiency. Because the valve must be closed to introduce the buffer gas, it is the higher temperature that largely determines the efficiency of the first stage of trapping. Because of the film issue (alluded to in ch. 2) the temperature of the cell with the valve open is also significant (more on this shortly).

---

[25] The base temperature of the ^3He pot during the first experimental run was $\sim 350mK$. The discrepency between this temperature and the higher temperature of the cell indicates that we have not done an optimal job of heat sinking the cell to the refridgerator. In addition, the relatively large temperature difference ($\sim 130mK$) with the valve open versus the valve closed could be alleviated through better heat sinking of the valve shaft. Both of these issues will be addressed (with differing levels of success) in the next chapter that describes some of the result from the second cool down.

5.4.5 Day to Day Operation ("Feeding" the dewar)

An unhappy fact of life working on a cryogenic experiment is that the cryogens evaporate over time and thus must be continually replenished in order to keep the experiment cold. Typically, during operation of the experiment, we transfer $\sim 50L$ of liquid helium a day. This is to maintain the liquid level in the bath as well as to keep the top of the IVC (and thus the $1K$ pot and cell) as cold as possible. Although the liquid nitrogen boil-off rate is substantially lower than that of the helium, we generally transfer a small amount of liquid nitrogen into the $77K$ shield reservoir while we transfer helium. This doesn't take much additional time, and it ensures that the $77K$ shield reservoir is slightly overpressured during helium transfers. This is convenient, because during helium transfers, the $77K$ shield reservoir (which is in weak thermal contact with the bath space) actually cools slightly. The overpressure that results from transferring nitrogen at this time ensures that the $77K$ shield reservoir does not begin to suck in air from the outside (possibly resulting in a dangerous plugging of the reservoir fill line!).

We should also note here, that during liquid helium transfers, the photo-multiplier tubes are removed from the room. This precaution is taken because helium can be quite bad for the PMT's. Helium gas can diffuse through the glass window on front of the phototube resulting in a degraded vacuum in the tube. This leads to a phenomena known as after-pulsing and general degraded performance of the PMT's over time.

5.4.6 Additional Steps and Checks before Trapping

Once the experiment is cold, there are a few additional tasks to complete before trapping atoms. We generally test the magnet by energizing it to 50 or 60 amps (recall that the maximum rated current is about 100 amps) to ensure that it hasn't been damaged somehow during the cool down. While we're at it, we measure the magnetic field profile outside the dewar to double check that we have properly wired our magnet in the anti-Helmholtz configuration[26]. If all of this looks good, the optics setup is completed. This involves mounting the small optics breadboard on the bottom of the dewar and aligning the lasers.

The probe beam is positioned so that it retroreflects from the mirror in the cell. Proper overlap of the incident and reflected beam is necessary for analysis of the atomic spectra. As much as possible, the beam is positioned so that it passes through the center of the magnetic trap. This can only be done roughly at this point. Fine tuning of the position is done later (by actually observing the spectra). The YAG (ablation) beam is focused on one of the Cr samples in the cell. As the exact position of the focus can have an effect on the ablation yield, this YAG position may be optimized later to produce the largest number of atoms possible per pulse.

[26] Because each of the coils in the magnet is independently wired, we have the option of running the magnet in either Helmholtz or anti-Helmholtz mode.

5.5 Experimental Procedure

The procedure for producing a trapped sample of atoms has already been described briefly in the introduction (recall fig. 1.4) and parts of the last chapter. A flowchart of this procedure is shown in fig. 5.2. We will now discuss in more details the steps involved.

1) The fill line sorb is filled with ^3He buffer gas from the room temperature gas handling system. This is done infrequently. Typically, ~ 10 Torr·Liters of helium ($\sim 3 \times 10^{20} atoms$) is placed onto the fill line sorb. This is enough for several dozen atom trapping cycles.

2) Buffer gas is introduced into the cell with the valve closed. This is done by heating the sorb in the fill line. To do this, a voltage (typically $\sim 6 - 14V$) is applied for 1 second to the heater on the sorb. The resistance of this heater is $\sim 150\Omega$, and so the energy delivered per heat pulse is on the order of a joule or so. The heat pulse causes the temperature of the sorb (monitored with a silicon diode thermometer) to rise from $\gtrsim 1K$ to $7 - 12K$ depending on the size of the pulse. Because of this elevated temperature, some of the helium bound to the sorb desorbs, filling the waiting room with buffer gas (probably to a density on the order of $10^{18} cm^{-3}$, though we don't measure this directly).

Buffer gas enters the cell trapping chamber through the pinhole at the base of the waiting room. As noted in ch. 4, the conductance of this pinhole is quite small (recall $C \sim 2 \times 10^{-4} L/s$). Given the volume of the cell ($\sim 400 mL$), the resulting

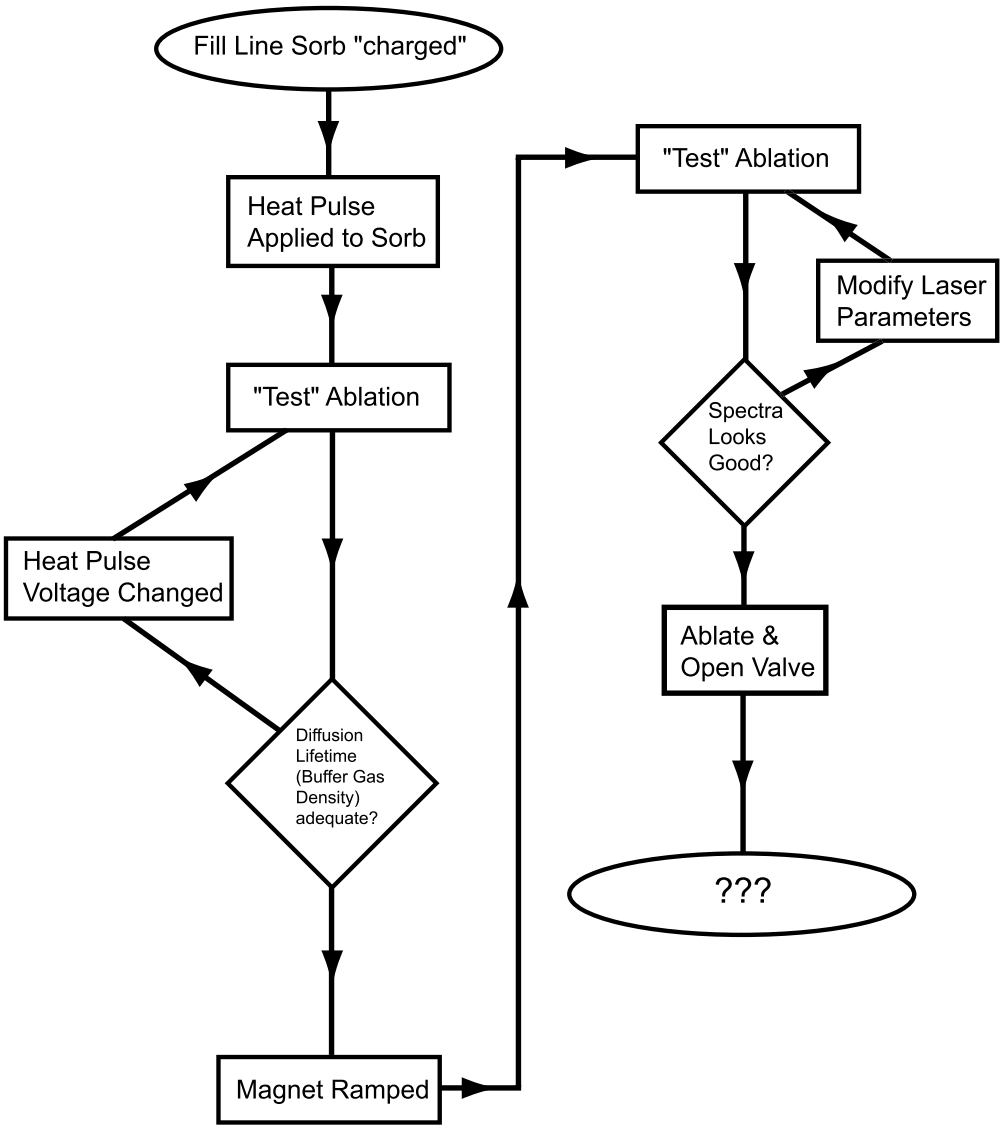

Figure 5.2: Flow chart describing the procedure for producing a trapped sample of atoms.

1/e time to fill (or empty) this volume is approximately half an hour. It doesn't take this long to fill the cell with buffer gas because the density required in the cell is only $n \sim 10^{15} cm^{-3}$ to $10^{16} cm^{-3}$. In practice, we find that after approximately 2 minutes, enough buffer gas has accumulated in the trapping chamber to provide adequate thermalization of the ablated sample. After the initial temperature rise due to the heat pulse, the cell fill line sorb begins to cool over the course of several minutes. A plot of the sorb temperature as a function of time for a typical heat pulse is shown in fig. 5.3.

As the fill line cools, it begins to pump-out the waiting room. Typically, we allow the cell to cool for $\sim 10\,\mathrm{min}$ before attempting to produce a trapped sample. By this point, the fill line temperature is generally below $2K$, and the waiting room should be under excellent vacuum. This rather long waiting period is quite conservative as regards the pressure in the waiting room, but is has the added benefit of allowing the cell body to cool as well, resulting in a higher η and increased trapping efficiency.

3) Once the trapping chamber is filled with buffer gas, the atoms to be trapped are introduced via laser ablation of one of the Cr targets in the cell. Typically, about 1 or $2mJ$ pulses are delivered resulting in the production of ~10^{13} Cr atoms. This energy is not limited by the YAG laser, but rather by the desire to minimize the heating of the cell that results from the energy deposited by the ablation pulse. Ablation is first done with the magnet off. This allows us to easily measure the

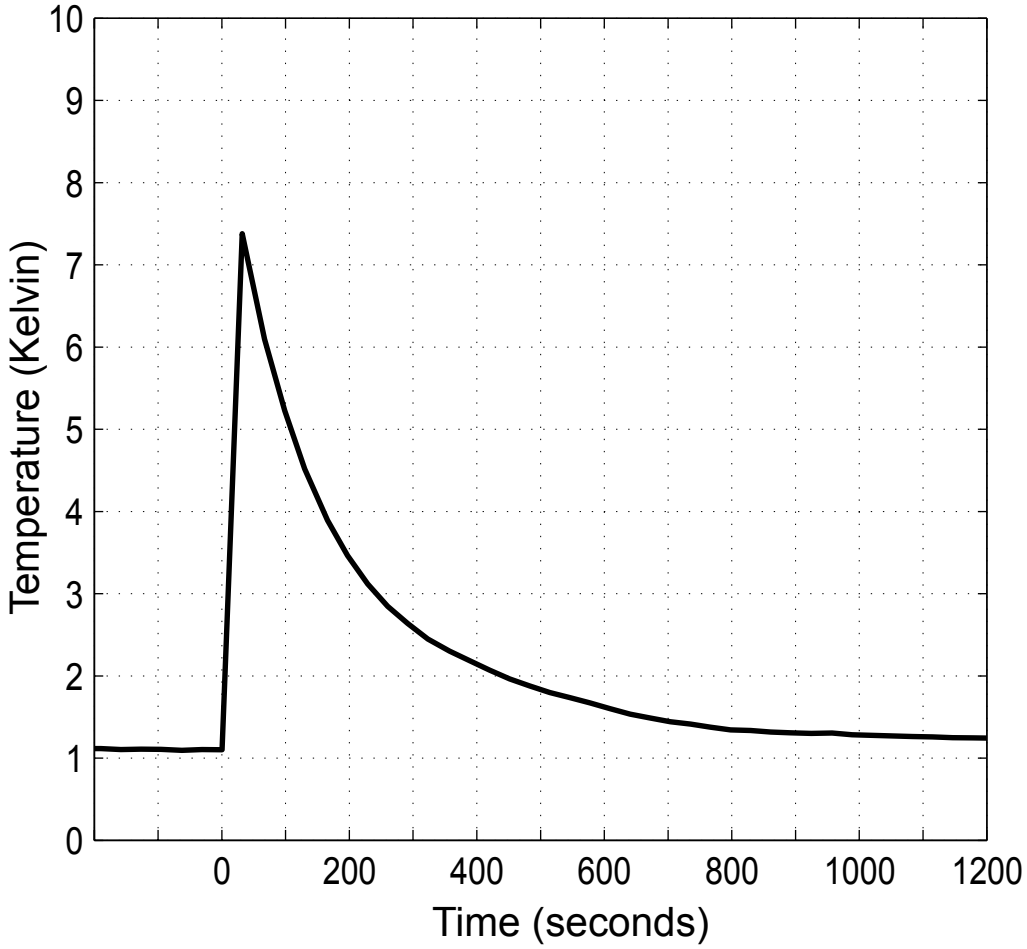

Figure 5.3: Fill line sorb temperature as a function of time after a $6V$, 1 second heat pulse is applied at $t = 0$.

diffusion lifetime of the sample in the buffer gas from which we can extract the density (see fig. 2.5). If the buffer gas density is too low (high), the heat pulse voltage is adjusted to desorb more (fewer) He atoms from the sorb. In between ablations, the valve is opened and closed again to remove any lingering buffer gas from the trapping chamber. The atoms are probed using absorption spectroscopy on the ${}^7S_3 \rightarrow {}^7P_4$ (at $\sim 425.55nm$) addressable by our diode laser. The spectroscopy of Cr is discussed at length in [24].

4) Once the correct heat pulse voltage has been determined[27], the valve is cycled again and the magnet ramped to the desired trap depth (50 amps $\longleftrightarrow \sim 2$ Tesla for example). With the trap on, another heat pulse is applied to fill the trapping chamber with buffer gas.

5) Before opening the valve, we generally do one additional "test" ablation. This allows us to adjust the parameters of the laser scan as desired (and to verify that there still is enough buffer gas). Spectroscopic data is taken in two modes which we term "scanning" and "parked." In the laser "scanning" mode, the laser frequency is swept back and forth over the atomic resonance. This mode is useful for determining the temperature of the trapped sample (by fitting the spectral features to a Maxwell-Boltzman distribution accounting for the Zeeman broadening due to the magnetic field [24] [51]). In "parked" mode, the laser frequency is fixed at a particular value close to the peak of $\Delta m = +1$ transition. The $\Delta m = +1$ transition is used to

[27] Because with each cycle of the experiment, some of the helium is removed from the fill line sorb, the voltage required to generate the appropriate buffer gas density tends to slowly rise until eventually the sorb must be refilled.

avoid optical pumping the atoms into a lower m_J state (which would be less trapped). This results in a better signal to noise ratio (because time is not "wasted" observing frequency intervals where the absorption signal is weak) with which to measure the decay of the sample. Typical spectra taken in these two modes are shown in figs. 5.4 and 5.5.

6) If everything looks good so far, then we are ready for the valve to be opened. After the "test" ablation, we wait several minutes to allow the cell to cool before ablating again. Also, immediately prior to ablating, we generally reduce the closing pressure of the valve from ~ 95 Psi to ~ 30 Psi (reducing the differential closing pressure from ~ 80 Psi to ~ 15 Psi). This is done to minimize the mechanical shock and vibration on the cell when the valve opens[28]. We then ablate, and after some time (which ranges from nearly zero to about twenty seconds) open the valve. The helium rushes out of the trapping chamber through the valve aperture into the pumping chamber never to be seen (we hope) again. The time between ablation and valve opening is chosen to maximize the number of atoms trapped. There are two competing effects that determine the optimal waiting time. The temperature of the cell rises somewhat due to the ablation. The longer we wait after this, the lower the cell temperature (and thus the temperature of the trapped sample). A lower temperature results in a higher efficiency for retaining what's left of the trapped sample when the valve is opened. The longer we wait, however, the fewer atoms that

[28] The reason that we don't just use this smaller closing pressure throughout is that it does not result in a very good seal. We find that with the lower pressure, we lose the buffer gas in about a minute or so, and thus we must take care not to waste time between lowering the pressure and opening the valve.

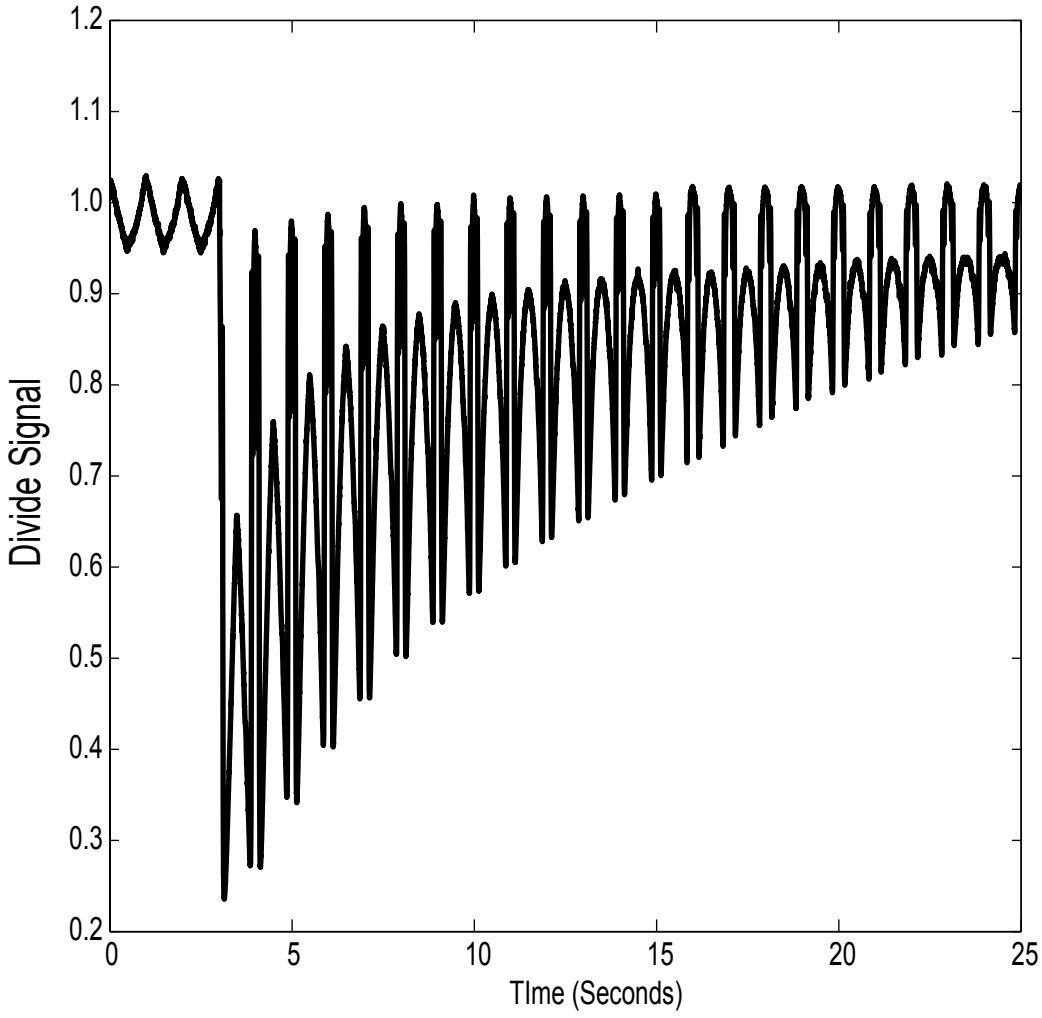

Figure 5.4: Example of a spectra taken with the laser in "scanning" mode. In this case, the laser scans $\sim 10Ghz$ at a rate of $1Hz$. The y-axis shows the result of dividing the output of the "Signal" PMT and the "Reference" PMT.

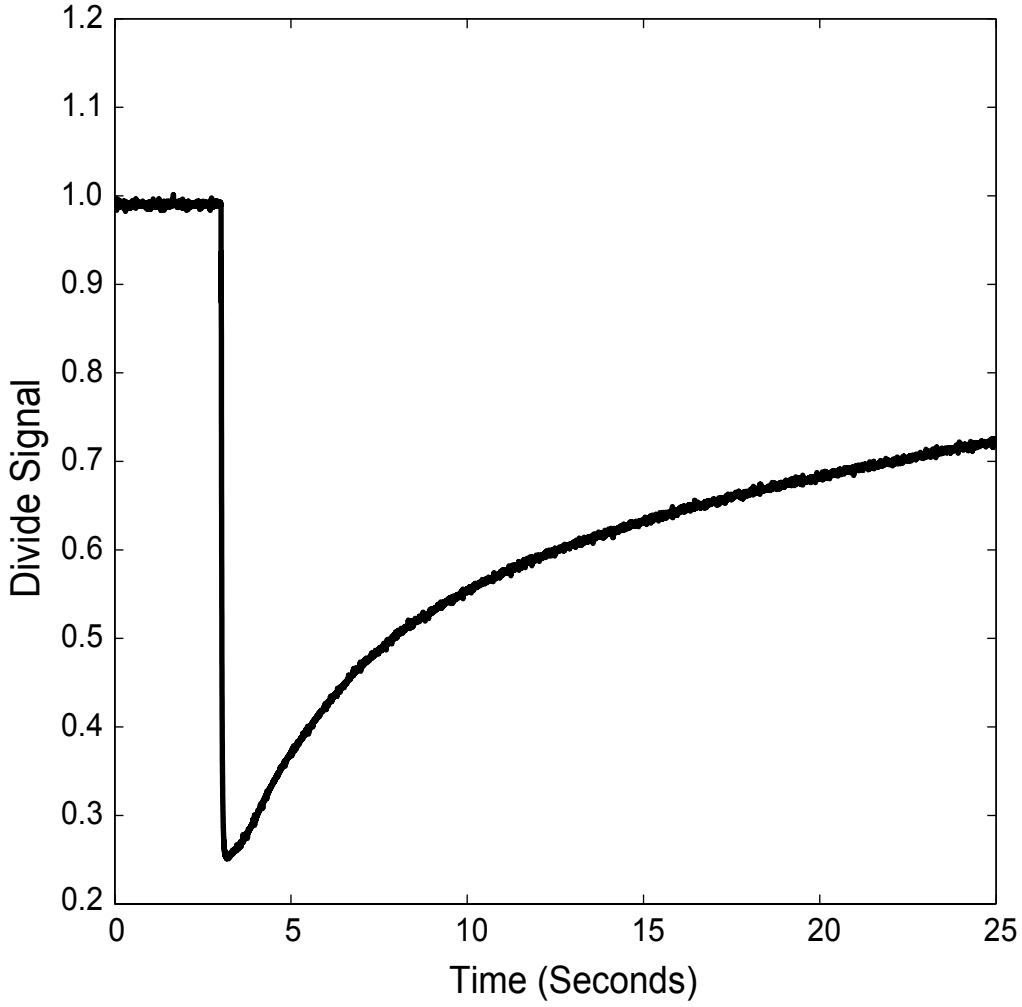

Figure 5.5: Example of atomic decay with taken with the laser "parked" on the $\Delta m = +1$ transition.

are left in the sample at the moment the valve is opened. Data from a typical trapping run with valve opening is shown in fig. 5.6.

This shows that we accomplished our initial goal. Trapping is indeed possible with this new apparatus, and the rapid buffer gas removal process is not too violent to significantly disturb the trapped sample. Now, we turn to the various other goals mentioned at the beginning of the chapter. First, we address the quality of the vacuum in the cell after the valve has opened and the buffer gas nominally been removed.

5.6 Quality of the Vacuum after Pump-out:

There are no gauges in the trapping chamber of the cell to measure the pressure directly. We do, however, have a very sensitive probe of the density of residual buffer gas in the cell, the trapped atomic sample itself. The diffusion lifetime of the sample is used to measure (and adjust) the initial buffer gas density during trap loading. Likewise, by monitoring the loss of atoms from the trap once the valve is open, we can determine how good the vacuum is. Helium atoms that survive the initial pump-out will from time to time collide with atoms in the trapped sample. During these collisions, energy may be imparted to the atoms in the trapped sample. During one or more collisions, an atom in the sample may acquire enough energy to leave the trap. If it does, then it is likely that this atom will escape in roughly one trap oscillation period unless it should undergo a "saving" collision with another

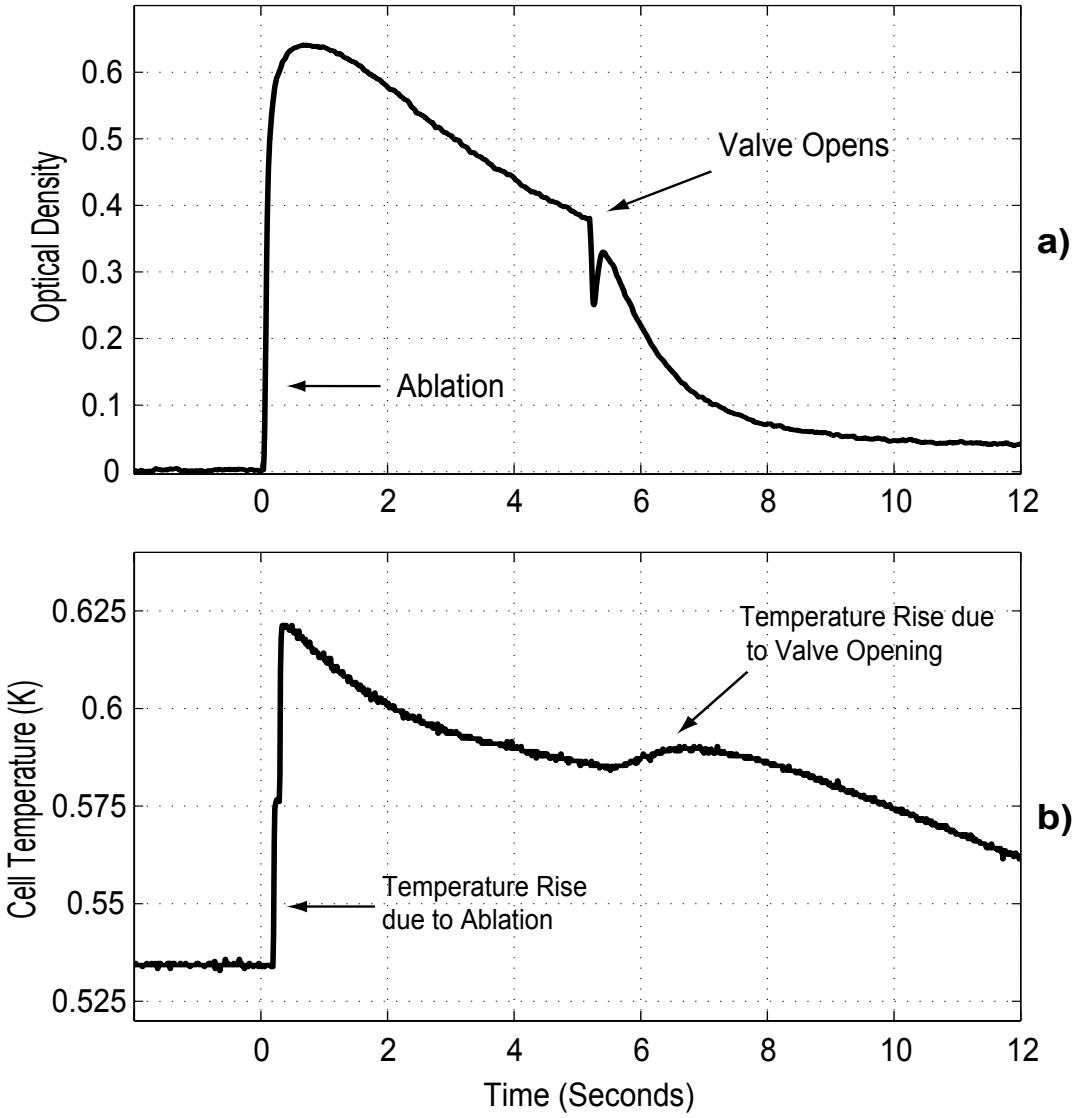

Figure 5.6: Example of data from a typical trapping run. The magnet current is 36 amps. This corresponds to a trap depth of $5.64K$ for Cr. The effective magnetic moment at this current is $2.2\mu_B$. **a)** Optical density as a function of time. The atoms are produced through ablation at time $t = 0$. The valve opens at $t \sim 5s$. **b)** Cell temperature as a function of time. There is an initial rise in the cell temperature due to the energy deposited by the ablation pulse. There is also a small amount of heating associated with the valve opening.

atom (Cr or He) that lowers its energy back below the trap depth. This is unlikely since the relatively small density of the trapped sample and background helium gas place us in the long mean free path regime for a collision.

5.6.1 Inelastic Processes in the Trap

Several physical processes can lead to atom loss in the sample besides collisions with He atoms. There are a number of inelastic collisional processes such as spin exchange [55] [56] [57], 3-body recombination [58] [59], majoranna losses [60] etc... that can remove atoms from the trap. For the moment, we can neglect most of these. Spin exchange does occur with Cr, but the rate constant is so high that the sample very quickly "purifies" to the maximally trapped "stretch" state (with $m_J = +3$) which does not undergo further spin exchange. Three body recombination should not be significant at our operating densities, and we see no signs of such effects. Majoranna loss (which result when atoms undergo spin flips in low field regions where the Larmor precession frequency is low compared to the rate the field is changing) is also not expected to be significant, and again our observations are consistent with this.

5.6.2 Dipolar Relaxation

There is one other inelastic process, however, that is important, namely dipolar relaxation [61] [58] [57]. Dipolar relaxation results from the exchange of angular momentum between the internal spin degree of freedom of the atom and the atom's

external orbital angular momentum in the trap that occurs during the interaction of two Cr atoms. For atoms in the maximally trapped ($m_J = +3$) state, one (or both) atoms are left in a less trapped state. Classically, you might think of this as one atom "tipping" the spin of the other as it passes closely by in the magnetic trap. Because the "weak field seeking" atoms are trapped, dipolar relaxation is an exothermic process that does not shut off as the temperature of the sample is lowered. It is the dominant intrinsic loss mechanism in our magnetic trapping experiment, so much so that the terms inelastic and dipolar loss are used synonymously in this thesis unless specifically stated otherwise.

To accurately estimate the amount of background gas left in the cell, atom loss due to collisions with the He atoms must be differentiated from loss due to dipolar relaxation. Fortunately, this can be done because the rates for these two loss processes have different density dependences. By observing (and fitting) the time profile of the decay, it is possible to separate the two effects.

5.6.3 1-Body versus 2-Body Loss

Collisions with background He atoms are in a class of "1-body" loss processes. Even though the collision involves two atoms, the process is termed 1-body because it involves only one Cr atom. Dipolar relaxation on the other hand results from the interaction of two Cr atoms and thus is termed a "2-body" collisional process. Consider how the rates of these reactions depend on density.

For 1-body loss, the rate of atom loss is simply proportional to the number of atoms present in the sample i.e.,

$$\dot{N} \propto N \tag{5.2}$$

or equivalently,

$$\dot{n} \propto n \tag{5.3}$$

Where n is the density of the sample.

The resulting density decay is:

$$n(t) = n_0 e^{-t/\tau} \tag{5.4}$$

Where n_0 is the initial density and τ is the (1-body) lifetime of the sample.

In the case of dipolar relaxation, because two Cr atoms are needed to take part in the collision, the rate goes as the density squared[29]:

$$\dot{n} = -\Gamma_2 n^2 \tag{5.5}$$

Where Γ_2 denotes the two body rate constant. This equation can be solved to give the decay profile. The result is:

[29] In general, for a "x-body loss process", we have $\dot{n} = -\Gamma_x n^x$ where x is the number of Cr atoms that participate in the collsion.

Collision Process	**Type**	**Dependence on n**	**Decay Form**
Cr - He (elastic)	1-body	$\dot{n} \propto n$	$n(t) = n_0 e^{-t/\tau}$
Cr - Cr (inelastic)	2-body	$\dot{n} \propto n^2$	$n(t) = n_0(1 + t\Gamma_2 n_0)^{-1}$

Table 5.1: Loss processes in trap

$$n(t) = \frac{n_0}{(1 + t\Gamma_2 n_0)} \tag{5.6}$$

These results are summarized in table 5.1

Now that we have a way of distinguishing these two loss processes, we can look at the data to see how big a role 1- body loss is playing in the decay of our sample and thus determine whether background gas is an issue in the experiment. Figure 5.7 shows the decay of a trapped sample in the presence of a 1.95 Tesla trapping field (with the magnet energized to 50 amps). This corresponds to a trap depth for Cr of $7.84K$, and an effective magnetic moment of $3\mu_B$ for the atom.

The density decay in this sample fits very well to a 2-body decay curve. The best 1-body fit is shown as well in fig. 5.7. and shows very poor agreement with the data. From this, we might be led to conclude that there is no significant density of background gas to cause trouble in the cell. This conclusion would be premature, however. The magnetic trap when this data was taken was quite deep. The depth of the trap is large compared to the temperature of the Helium buffer gas ($\sim 600mK$). As a result, it is unlikely that a single collision between an He atom and a Cr atom will impart enough energy to the Cr to remove it from the trap.

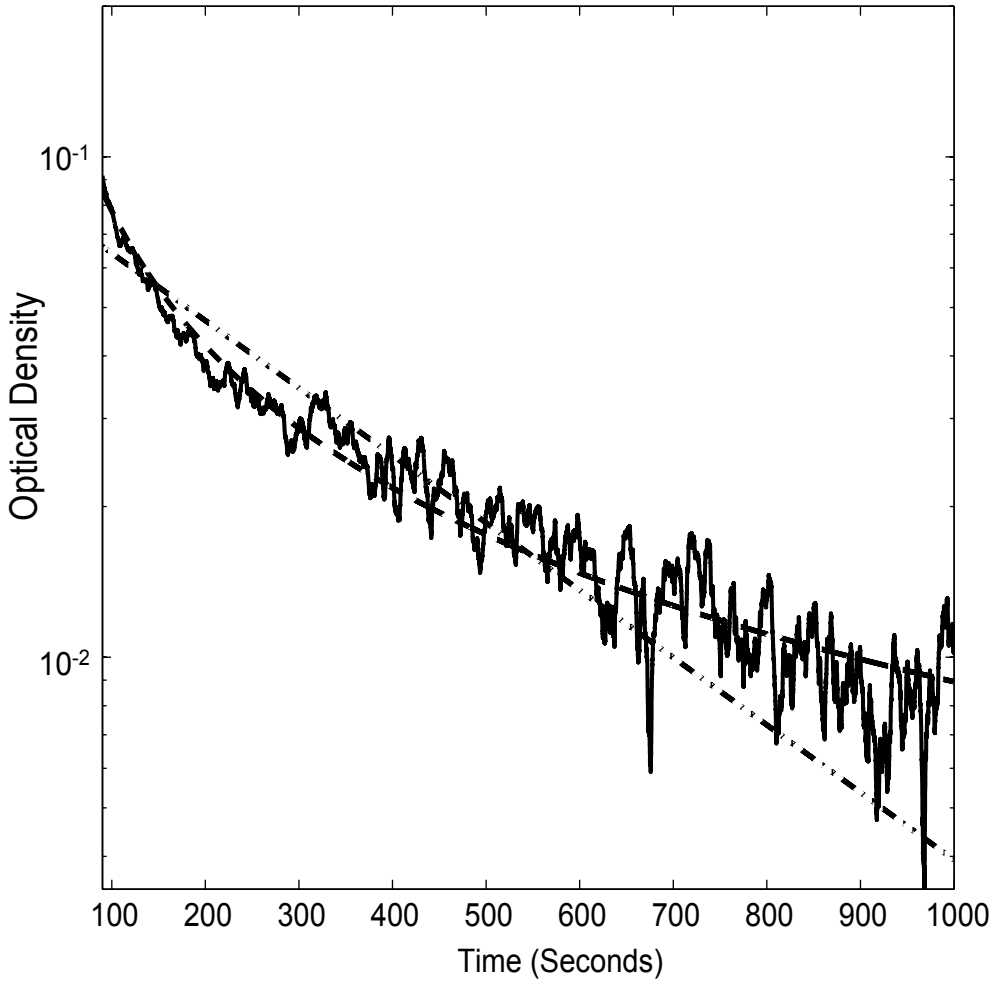

Figure 5.7: Optical denisty vs. time at 50 amps with a 1-body (straight dashed line) and 2-body fit to the decay.

Normally, even if the helium atoms did not directly knock atoms out of the trapped sample, they would heat or cool the sample. In the absence of a buffer gas, there is a natural balance between heating of the sample (due to dipolar relaxation which preferentially removes low energy atoms in the high density region near the center of the trap) and cooling of the sample (due to evaporation of atoms over the trap edge which preferentially removes "hot" energetic atoms) that sets an equilibrium temperature for the sample. Coincidentally, at this trap depth, this temperature happens to be very close to $600mK$ [24] [51]. This coincidence means that we would not expect to see a significant temperature change (either heating or cooling) due to any background helium in the cell. The atomic sample in this deep trap is fairly robust against collisions with helium. Figure 5.8 shows a spectra taken at 50 amps (with the laser in "scanning" mode) along with a fit to the temperature.

We know that our vacuum is not "too bad[30]", but can conclude little more without lowering the depth of the trap to make the sample more sensitive to collisions with background helium atoms. The more shallow the magnetic trap, the easier it is for a helium atom to knock an atom out of the trapped sample. Also, at a new trap depth, we expect the equilibrium temperature of the atoms to be different, and thus would be in a position to determine whether the sample was truly thermally isolated from the chamber walls.

[30] Our simulations suggest that the data indicates a background helium density no greater than $\sim 10^{12} cm^{-3}$.

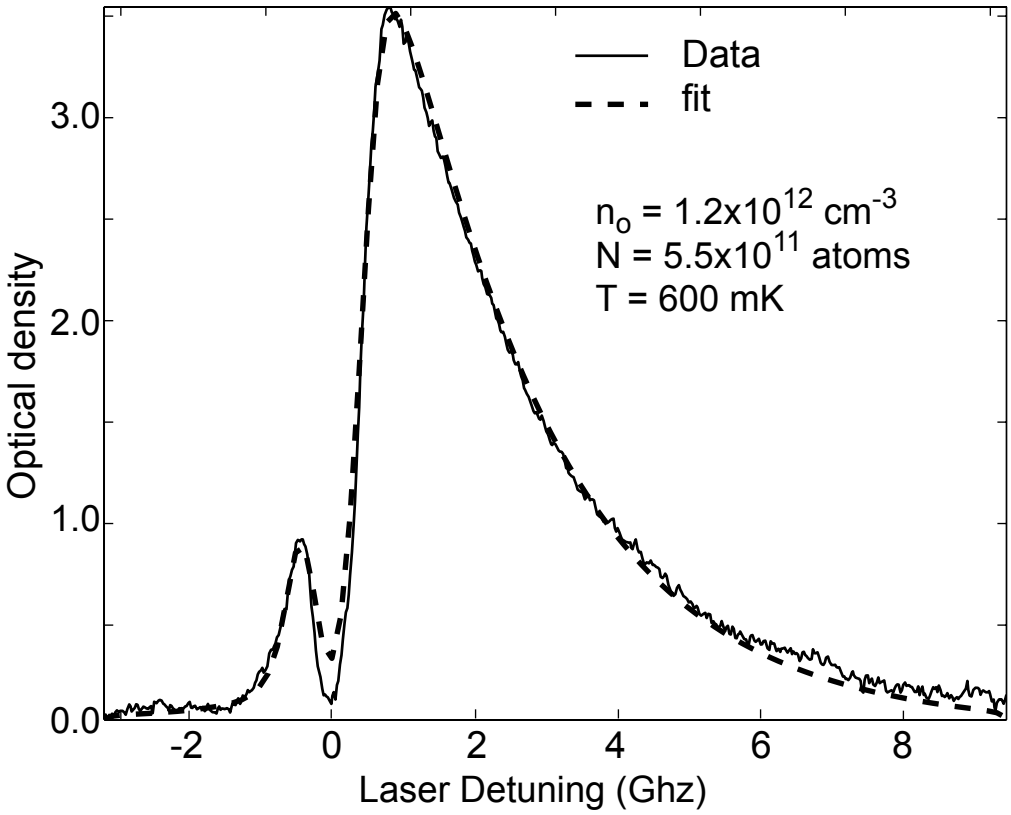

Figure 5.8: Spectra taken with the magnet at 50 amps. A fit is shown indicating atom number, peak density, and temerature. Note, the $600mK$ atom temperature coincidentally coincides with the buffer gas temperature as well as the equilibrium temperature for this field expected from the balance of heating (due to dipolar relaxation) and cooling (due to evaporation. As a result, it is not clear whether the sample is in thermal isolation from the chamber walls.

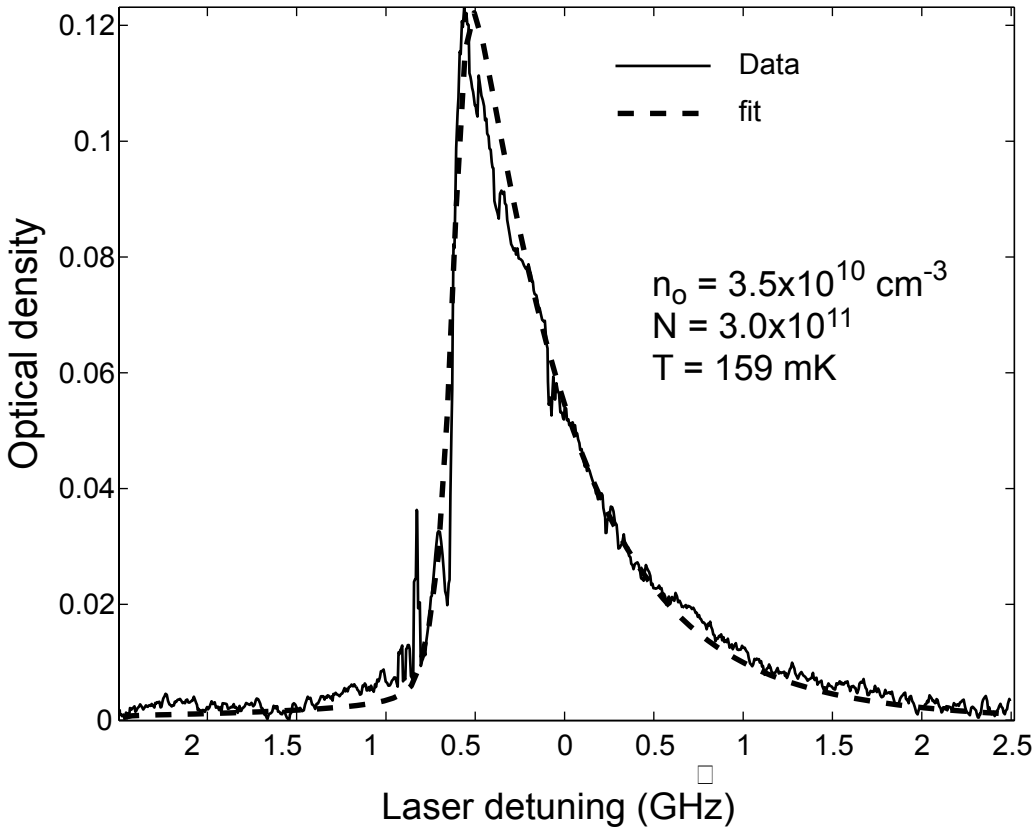

Figure 5.9: Atomic spectra taken at 5 amps along with a fit indicating number, N, peak density, n_0, and temperature, T.

Our procedure for lowering the trap depth is as follows. We begin with the trap relatively deep (say 50 amp $\longleftrightarrow 7.84K$). We put in the buffer gas, ablate, and open the valve as usual. After a few seconds the magnet is ramped down to the desired current. Typically, the current is ramped down exponentially with a time constant of ~ 5 seconds. In fig. 5.9 we show a spectra taken in "scanning" mode after ramping the magnet to 5 Amps (trap depth = $0.78K$).

As indicated in the figure, the temperature of the atomic sample is ~$160mK$ which is in good agreement with the expected equilibrium temperature for this trap depth and is substantially different from the temperature of the buffer gas. This is good evidence that the buffer gas density is sufficiently low so that the sample is thermally isolated from the chamber walls. Even if the buffer gas density is too low to provide a thermal link between the sample and the chamber, it may be high enough to result in a large 1-body loss rate at lower trap depths. To check for this, we lower the trap still further to a current of 1 amp (trap depth = $157mK$). At this point, a single collision with a helium atom has a significant probability of removing an atom in the sample from the trap. Figure 5.10 shows a spectra taken on the sample with the magnet current at 1 Amp (trap depth = $157mK$). The temperature of the sample is found to be ~$47mK$ again in good agreement with the expected equilibrium temperature. Figure 5.11 shows the long time decay of the sample (with the laser "parked") along with a 1-body fit to this data.

In contrast to the 50 Amp data, here, we do indeed see evidence for residual helium in the cell. The data fits well to the expected form with a 1-body time constant of approximately 40 seconds.

We are in a regime where the vacuum in the chamber after pump-out is good enough to allow for trapping and thermal isolation of a sample, and it is good enough for holding a cold sample for a long period of time in a deep trap, but it is not quite as good as we would like. In the absence of background gas, the sample would last

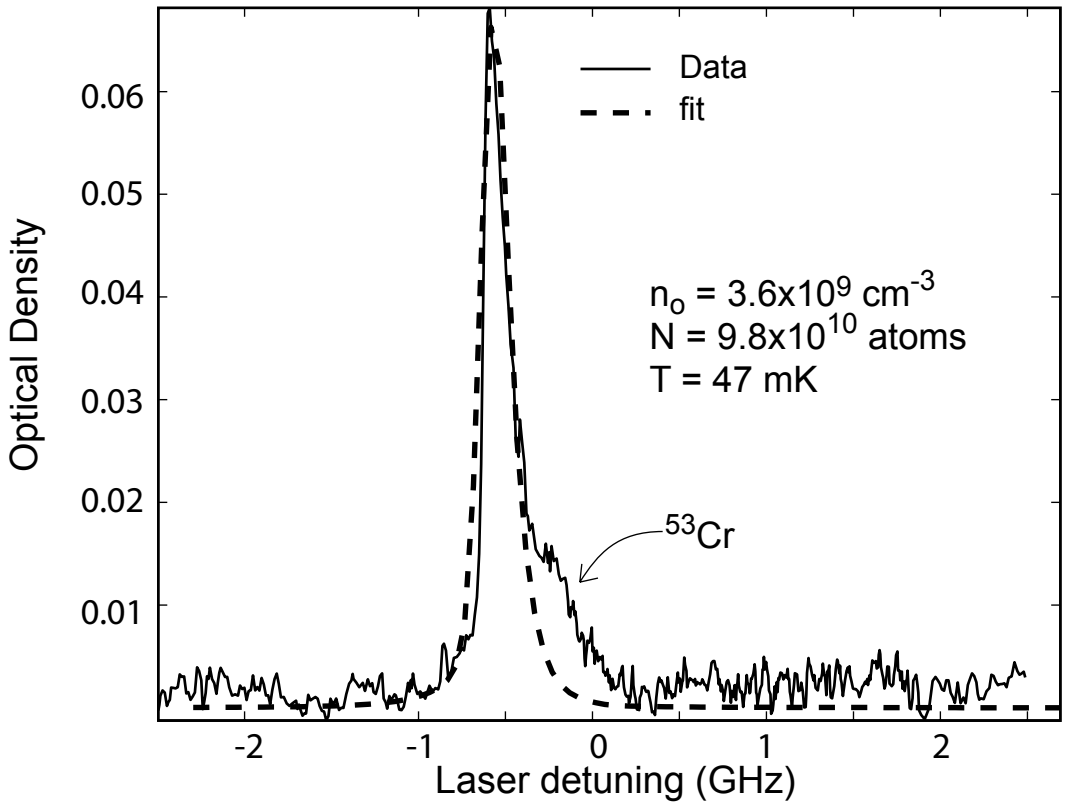

Figure 5.10: Atomic spectra taken at 1 amp along with a fit indicating number, peak density, and temperature.

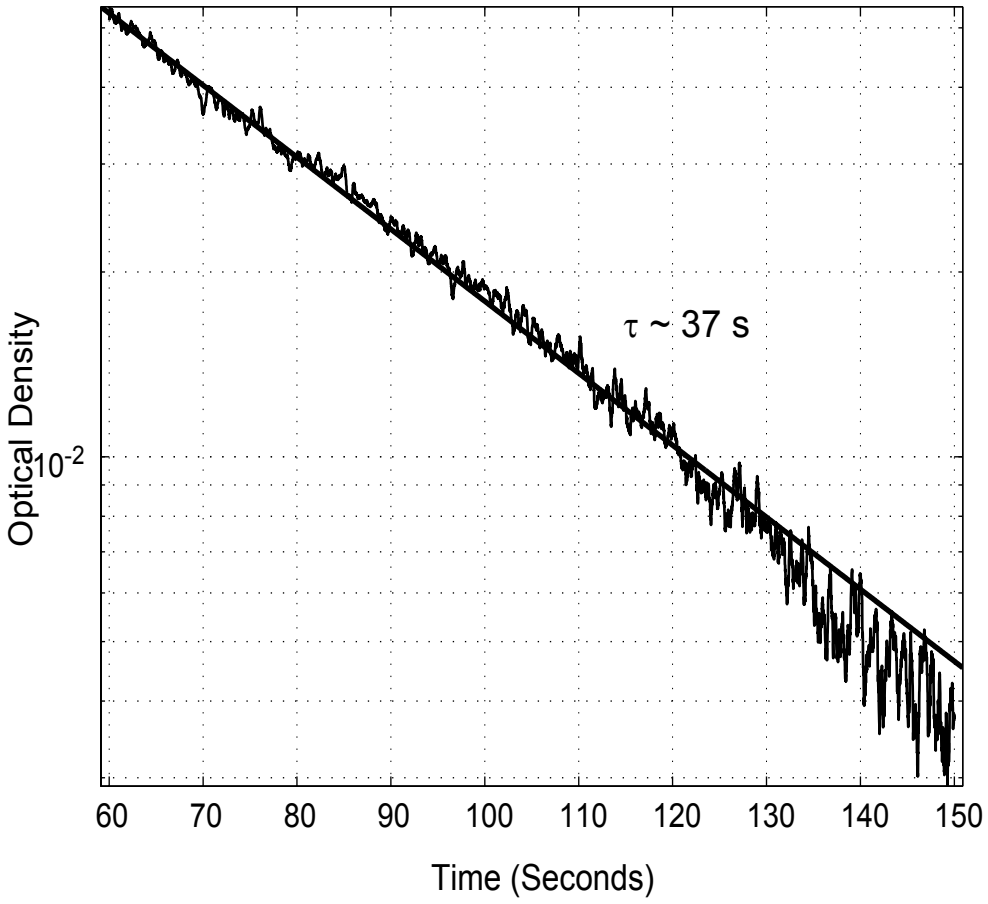

Figure 5.11: 1-body decay after evaporatively cooling to 1 amp. The 1-body time constant is, $\tau \sim 37s$.

for several hundred seconds or more (this limit being due to dipolar relaxation). We would like to improve the vacuum to a point where 1-body loss does not limit the trap lifetime. To do this, we must first determine the source of the helium in the cell after the pump-out. Unless the large sorb in the cell pumping chamber is close to saturation (unlikely given the large capacity of this sorb), it should not be limiting the quality of the vacuum.

The culprit here is the helium film on the wall of the trapping chamber. This was discussed as a potential problem in ch. 2, and indeed it is (we'll discuss specific evidence for this shortly). Once the bulk of the buffer gas has been pumped out of the trapping chamber, the film desorbing from the walls provides a flux of atoms into the chamber. Appendix A describes a model used to estimate the effect of the desorbing film on the density of buffer gas in the trapping chamber. Here we present some of the results of this model. Figure 5.12 shows how we might expect the buffer gas density in the chamber to be altered as a function of time with the film present compared to the situation where there is no film at all.

According to fig. 5.12, with the film present in the cell, the buffer gas density falls rapidly when the valve opens, but then this fall slows due to the desorption of the film. Fortunately, there are ways of solving this problem. Ideally, we would eliminate the film entirely so that only the helium in the gas phase in the trapping volume needed to be removed. This may be possible in the future by suitable altering the surface properties of the cell (making the walls less sticky to He for example).

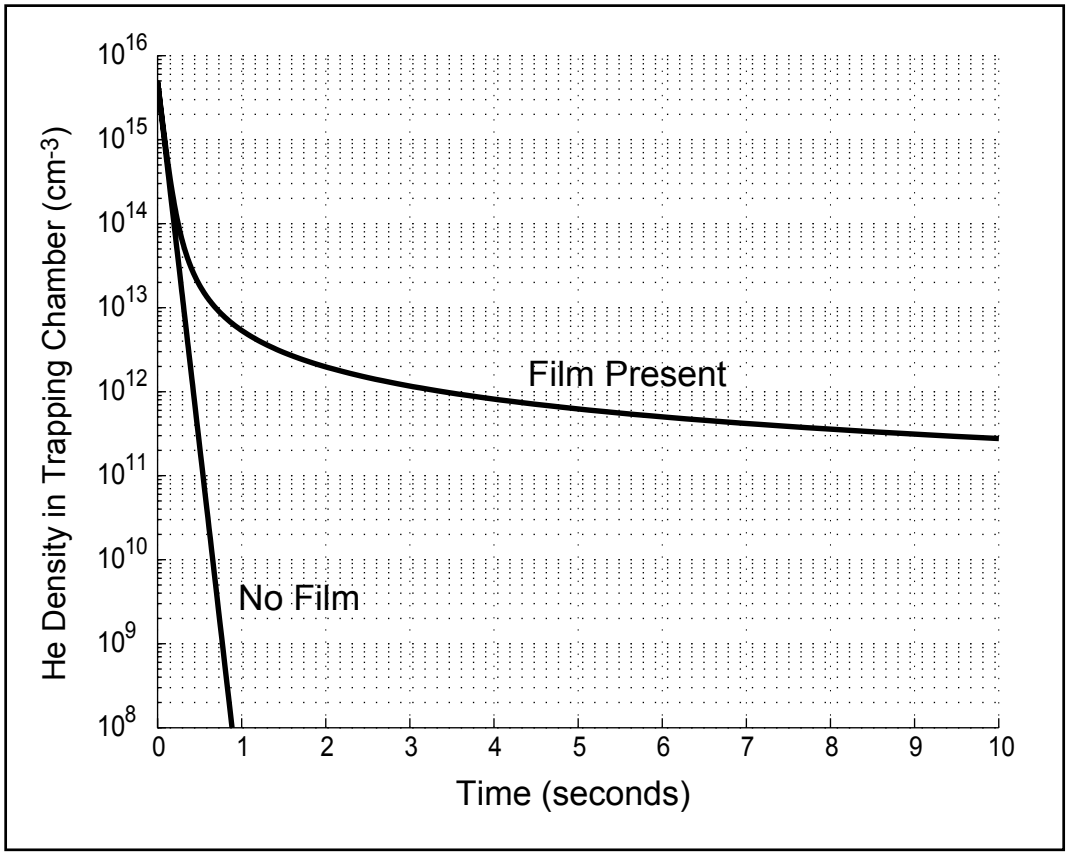

Figure 5.12: Predicted buffer gas density in the chamber assuming that a film is coating the chamber walls. Here, the initial buffer gas density is taken to be $5\times10^{15}cm^{-3}$, the temperature, $0.5K$, and we assume a film binding energy of $100K$ (see appendix A). Also shown is the expected buffer gas density in the absence of the film (which simply falls exponentially with a time constant $\sim 50ms$ set by the valve aperture).

This will be discussed a bit more later in this chapter and in the next. For now, we focus on a more experimentally accessible solution in this run.

5.7 The "Cryo-Bakeout"

As discussed in ch. 2, the film desorption rate depends on many factors including, the temperature of the film, T, the film thickness, t, the binding energy, E_B, of the film to the substrate, the binding energy of the film to He, E_B^{He} and the vapor pressure, P, above the film. The top most layers of the film are far enough from the substrate that the desorption time is essentially determined by the binding energy of helium to itself (i.e. by E_B^{He}). This binding energy is quite low (on the order of $4K$). As a result, when the valve is opened, we expect that part of the film desorbs very rapidly (see eq. 6.1 and table 6.2 in ch. 6). Conversely, the binding energy of helium to the substrate, E_B, is quite large (on the order of $100K$ [31]), and the bottom layers are thus very strongly bound. In fact, the bottom layer will not desorb on any time scale relevant to the experiment (unless we can retain our atoms for the age of the universe or so!). The problem is that in between, inevitably, there is a region where the film desorbs on a time scale that is harmful to the experiment. As the film thins, the desorption time drops (as the binding energy goes from E_B^{He} to E_B). Eventually, the desorption rate is small enough that the film thickness is essentially fixed. As a result, the desorption rate is essentially fixed as well. It is our poor fortune that this ultimate rate results in a buffer gas density intolerably high for the experiment

(An optimist might say we're lucky to have as good a vacuum as we do with the film present!). This point is illustrated in fig. 5.13 which shows results for the film model for a fixed temperature ($0.5K$) assuming different binding energies between the film and substrate.

We see from fig. 5.13, that the density of buffer gas in the chamber as a result of the film is only a weak function of the binding energy. The exception is if the binding energy is so low that even the most tightly bound (first) monolayer readily desorbs. This is true for the $5K$ binding energy shown in fig. 5.13.

To deal with the problem that the film presents, we exploit the fact that the desorption rate is a strong function of temperature (see appendix A). The greater the temperature, the greater the desorption rate for a given film thickness. Fixing the cell temperature at a higher value isn't very useful (and in fact the lower resulting η would be harmful). The reason this doesn't help is that at a higher temperature, the film does indeed desorb more readily at first, but eventually the desorption rate is nearly the same as at a lower cell temperature. Again, this final desorption rate is set simply by the condition that the rate be low enough that the film thickness doesn't change. Whatever desorption rate results in a negligible change in film thickness is the final desorption at which the film stagnates regardless of the temperature. What is different is the ultimate thickness of the film at this point. The higher temperature film will be thinner (and thus more tightly bound). The higher temperature

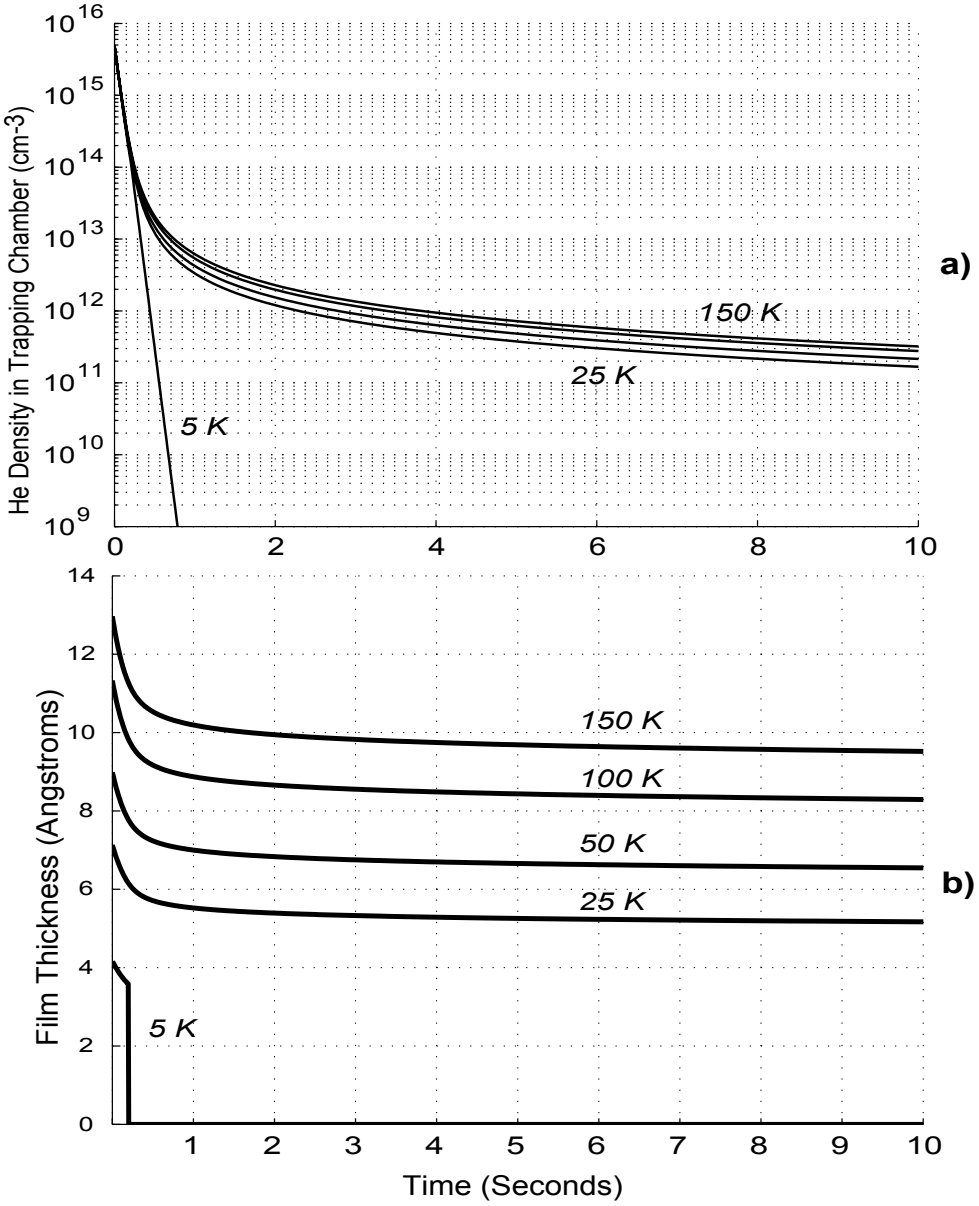

Figure 5.13: **a)** Density in the trapping chamber for different binding energies $(5 - 150K)$ of the film to the substrate. Here, we assume a fixed cell temperature of $0.5K$. **b)** Corresponding film thickness as a function of time. Note, the top graph is a semilog plot whereas the bottom is not.

and the tighter binding nearly offset one another. This concept is illustrated in the simulations of the film behavior shown in fig. 5.14.

While simply raising the cell temperature would be foolish, what can help, is to first raise the temperature (to thin the film) and then to reduce the temperature to lower the final desorption rate. This is analogous to the bakeout of a room temperature vacuum system to expedite the removal of impurities (condensed water for example) from the system. Because the bakeout is done at temperatures on the order of $\lesssim 1K$, we call it a "cryo-bakeout." To see how big an effect this can have on the ultimate desorption rate, we show some results from further simulations in which the temperature of the film changes with time.

Figure 5.15 shows that dramatic changes in the ultimate buffer gas density can be made with relatively small changes in the temperature. Qualitatively this can be understood as follows. Once the valve has opened and the vapor pressure above the film drops, the two most important quantities in characterizing the film are the temperature and the thickness. Raising the temperature, quickly thins the film. As noted above, this does not immediately help. The desorption rate increases temporarily as the film thins, but again settles to a constant value (once the film is no longer thinning). The film is now thinner than it would be at a lower temperature when the constant desorption rate condition is met. Thus, when we cool the film back to the initial temperature, the desorption rate drops to a value much lower than what it would be otherwise. The film is still present, but it is "frozen out" on the

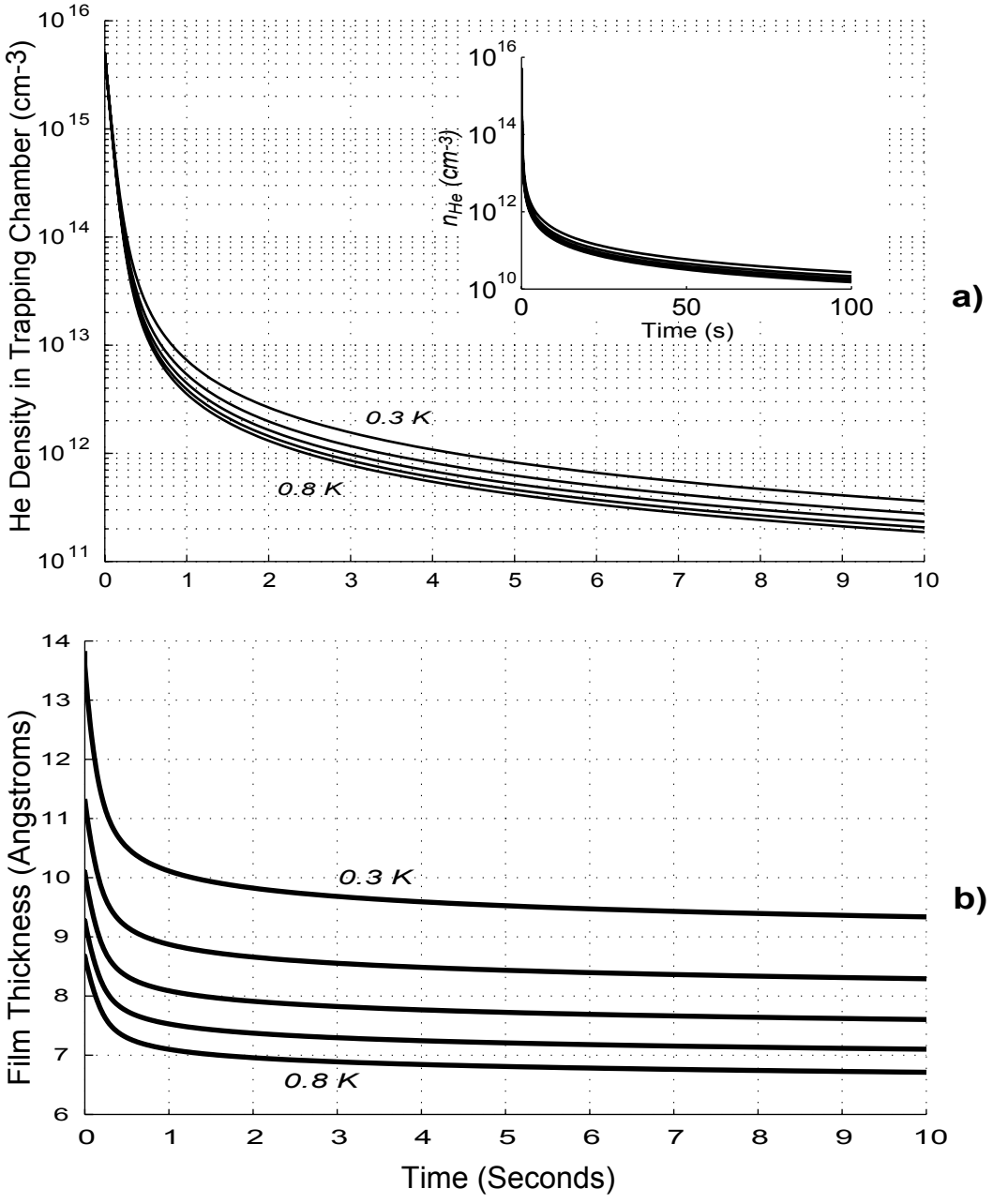

Figure 5.14: Behaviour of the film for different temperatures (assuming a binding energy, E_B, of $100K$). **a)** Buffer gas density in the trapping chamber. **b)** Film thickness

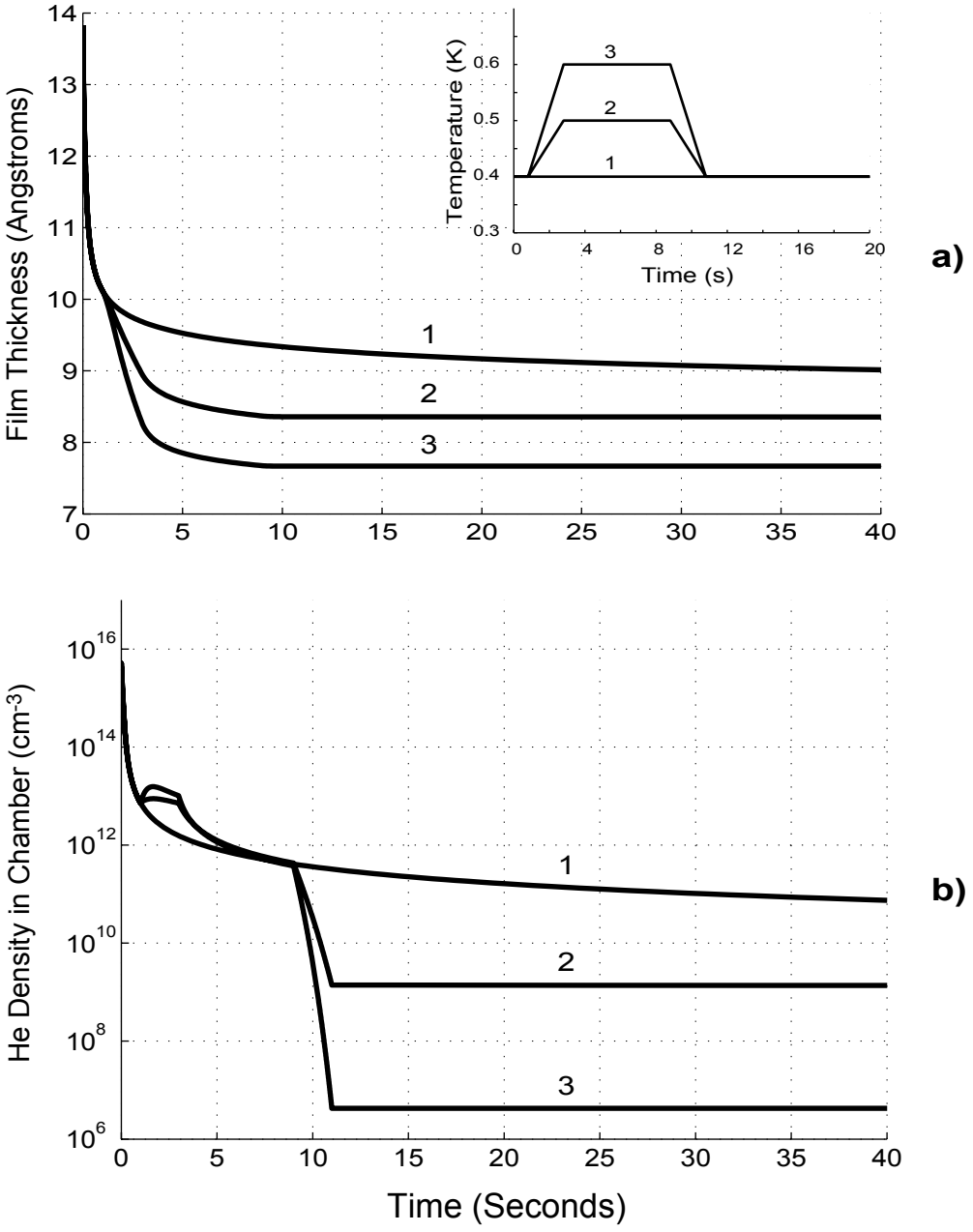

Figure 5.15: Simulations of the film illustrating the idea behind the "cryo-bakeout." **a)** Film thickness as a function of time in the chamber without the bakeout and with two different bakeout procedures (2 & 3 shown in the inset). The temperature in bakeout 2 (3) is initially $400mK$, and is raised to $500mK$ ($600mK$) linearly during a period of 2 seconds, held contant for 6 seconds and then linearly reduced back to $400mK$ during a period of 2 seconds. **b)** Buffer gas density as a function of time.

chamber walls. To some extent, this temperature changes occurs naturally when the valve opens. The base temperature with the valve closed ($\sim 550mK$) is higher than with the valve open ($\sim 420mK$) because of the increased heat load through the shaft. When the valve opens, the cell cools. Ideally, we would cool the cell even further at this point to freeze out the film. We do the next best thing which is to artificially raise the temperature of the cell and then allow the cell to cool.

Experimentally, the cryo-bakeout procedure is as follows. We begin with the magnetic trap relatively deep (typically 50 amps $\longleftrightarrow 7.84K$). We introduce buffer gas, ablate, and open the valve as per the normal recipe. Now, we wait a while (typically several seconds) and then raise the temperature of the cell (still with the trap deep). This is done using a resistive heater wrapped around the cell body. After some time, the cell is allowed to cool. At this point, we hope that we have burned through some of the film and thus improved our vacuum. To test this, we again ramp our magnet down to 1 Amp (trap depth ~ $160mK$) and monitor the decay of the sample.

The optimal bakeout procedure to follow as far as temperature and duration is determined experimentally. As usual, there are trade-offs that guide us. The more severe the bakeout, the better the resulting vacuum. At the same time, the elevated cell temperature leads to increased atom loss from the trap. In practice, we aim for the most aggressive bakeout that the atomic sample can tolerate without significant

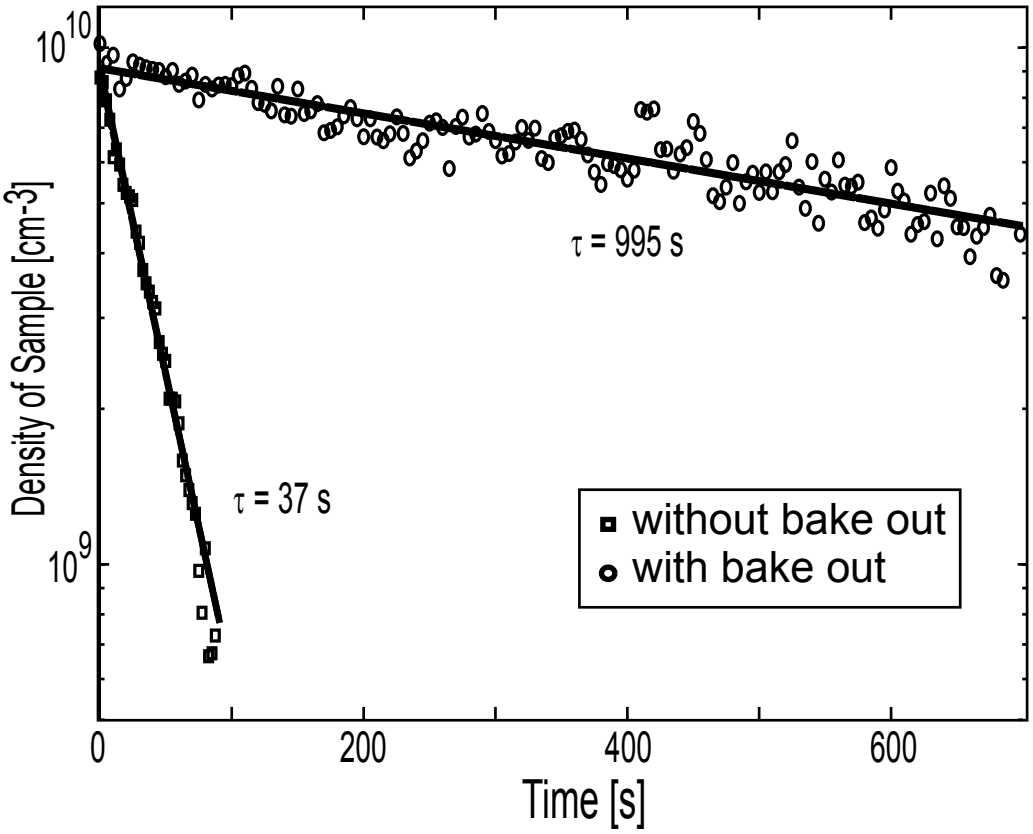

Figure 5.16: Density of sample with and without the "cryo-bakeout." This data shows the decay of the sample after the trap has been ramped down from 50 amps (trap depth = $7.84K$) to 1 amp (trap depth = $160mK$).

loss. Typically, this corresponds to heating the cell to ~ $650mK$ and holding it there for ~30 seconds. The results are shown in fig. 5.16.

As seen from the long lifetime shown in fig. 5.16, this sort of bakeout can be a very effective way to dramatically improve the vacuum in the cell[31]. A 1000 second lifetime is more than adequate for our purposes. In fact, at this point, we can not say conclusively that this lifetime is limited by collisions with helium atoms

[31] It also is good evidence that it is indeed the film that is causing our problems with the vacuum.

(as opposed to majoranna loss or dipolar relaxation for example). The downside of the cryo-bakeout is that it requires raising the cell temperature which has detrimental effects on the lifetime of the sample during the bakeout and is prohibitive at lower magnetic moments. We will have more to say about the helium film later.

5.8 Trapping Efficiency versus μ_{eff}

At this point, we have accomplished the first two goals mentioned at the beginning of the chapter. We have demonstrated the ability to trap atoms in this new apparatus, and we have shown that a good vacuum (both sufficient for thermally isolation and such that it does not limit the lifetime of the sample) can be achieved using the "cryo-bakeout."

Now, we turn to the last of our main goals, namely to see how far down we can push the effective magnetic moment of the atom, μ_{eff}, while still efficiently trapping and thermally isolating the sample. So far, most of the data has been taken with the magnetic trap initially energized to 50 Amps. Given that the maximum operating current is 100 Amps, this means that we are effectively able to trap and thermally isolate $3\mu_B$ species, already a significant advance in buffer gas loading. Now, we describe a more detailed investigation, systematically changing the initial current to simulate loading different magnetic moment species into the trap. We are interested primarily in the efficiency at retaining atoms in the trap once the buffer gas has been removed (at least enough for thermal isolation to be achieved).

As an example, we show in fig. 5.17 data taken at 40 amps (corresponding to $\mu_{eff} = 2.5\mu_B$). At ~ 100 seconds in this data set, a heat pulse is applied to drive the atoms out of the cell. This allows us to get a baseline signal with the cell empty, and thus determine how many atoms were present in the cell before the heat pulse. Figure 5.18 shows similar data taken at 35 amps ($\mu_{eff} \sim 2.1\mu_B$).

This data, shows that there is a sudden loss in atoms when the valve opens (as the bulk of the buffer gas leaves) and then a slower (several second) decay. This slow decay is consistent with the expected desorption time for the film (and is further evidence that the film is indeed the problem). The number of atoms left in the trap once the film has thinned sufficiently (for thermal isolation to be achieved) is calculated from the final optical density of the sample. A plot of this final number versus μ_{eff} is shown in fig. 5.19. For consistency, we plot the number for each data set at 10 seconds after the valve opens. By this time, atom loss due to the film has ceased.

According to fig. 5.19, the efficiency above $\mu_{eff} \sim 3\mu_B$ is quite high. We see almost no loss of atoms from the trap either after opening the valve or after thermal isolation has been achieved. The total number of atoms left in the trap is limited solely by the number produced in the maximally trapped weak field seeking state (~ 10^{12})[32]. Below $\mu_{eff} \sim 3\mu_B$, this efficiency drops precipitously (mostly as a result of the film desorption). Still, a relatively large number ($\gtrsim 10^9$) of atoms with

[32] About 10^{13} atoms are produced per ablation pulse. These are approximately evenly distributed throughout the seven m_j states ($m_j = +3, +2, ... -2, -3$) in Cr, and thus we expect a little more than 10^{12} to be in the maximally trapped ($m_j = +3$) state.

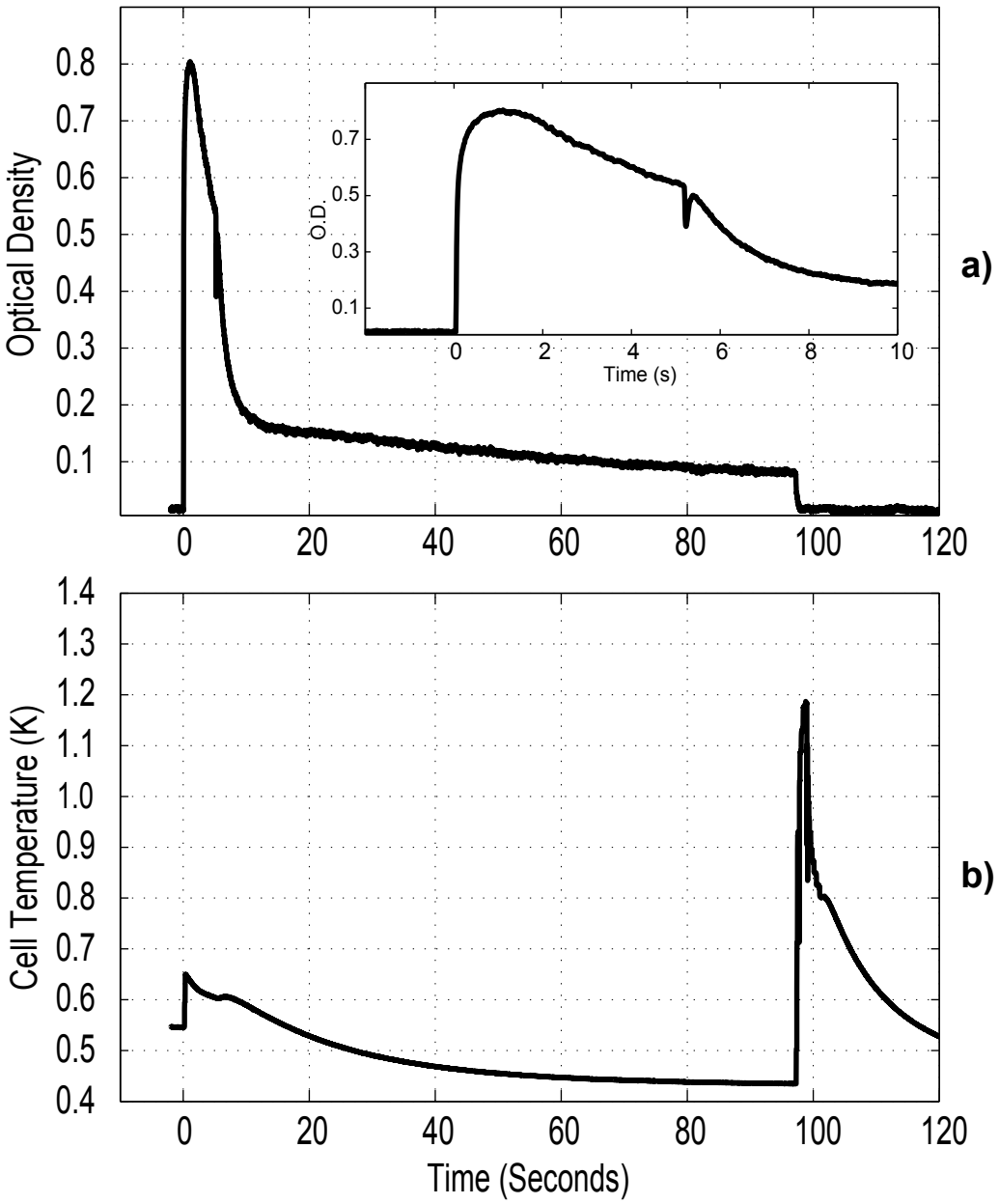

Figure 5.17: **a)** Decay of atoms from the trap at 40 amps. Ablation occurs at time $t = 0$. The valve opens at time $t \sim 5s$. **b)** Cell temperature. The base temperature of the cell is initially $\sim 550mK$ and rises to $\sim 650mK$ after the ablation pulse. At the moment the valve opens, the temperature is $\sim 600mK$. At t $\sim 100s$ a large heat pulse is applied to the cell to drive any remaining atoms from the trap. This allows us to establish a baseline signal with the cell empty which is needed for calculating the atom number in the trap.

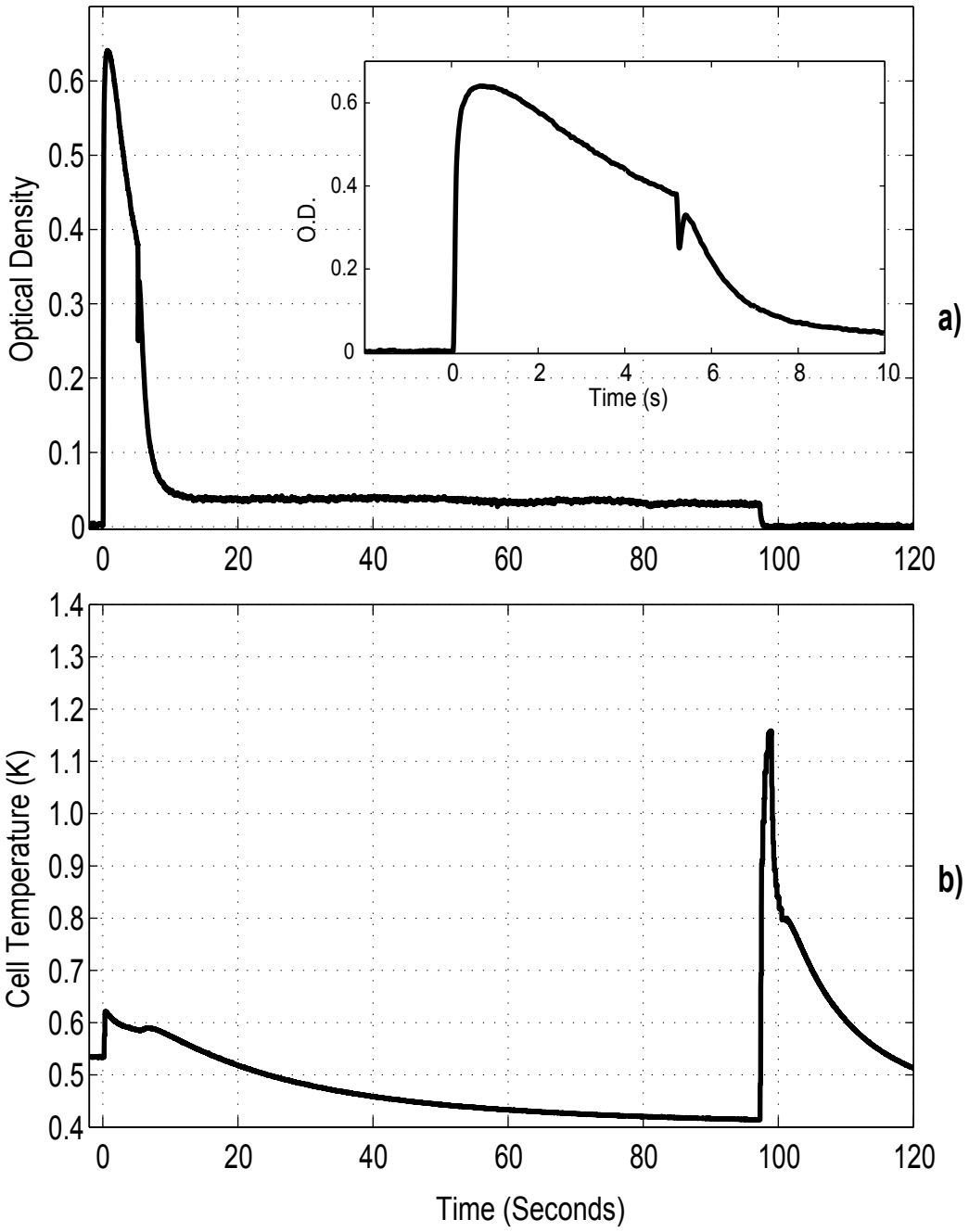

Figure 5.18: **a)** Decay of atoms from the trap at 35 amps. **b)** Cell temperature.

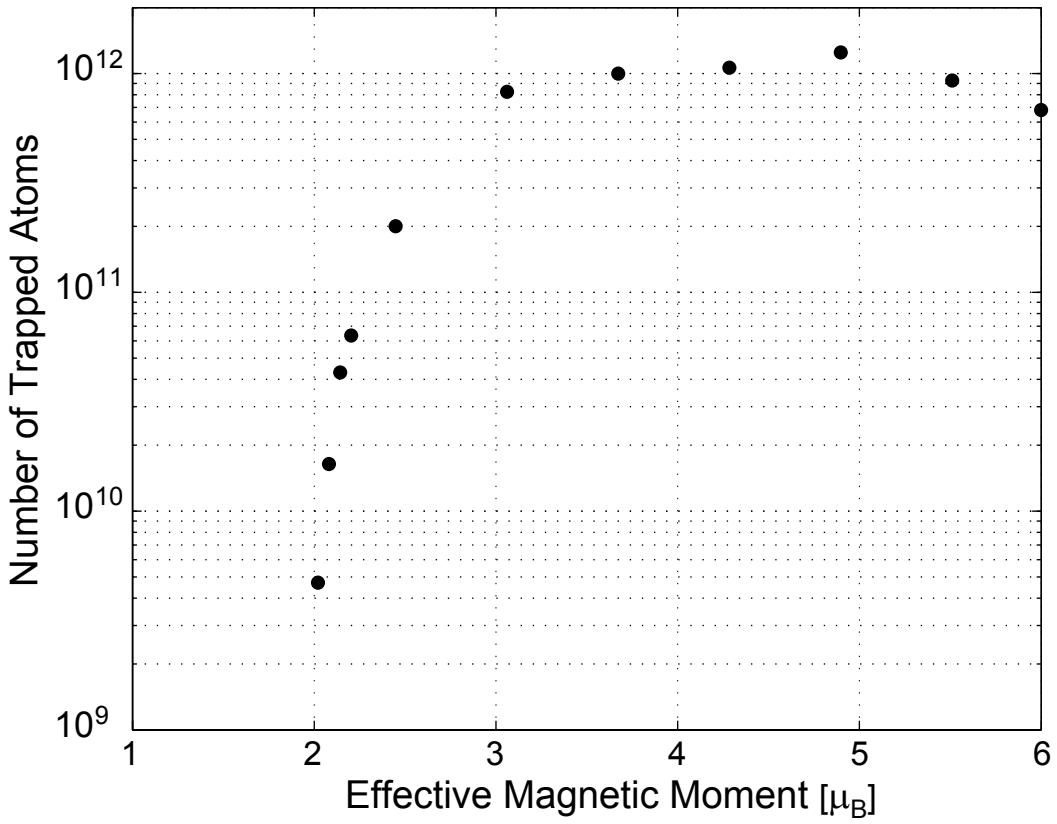

Figure 5.19: Number of atoms left in trap after thermal isolation vs. effective magnetic moment.

effective magnetic moments down to $2\mu_B$ can be trapped and thermally isolated. This represents a substantial improvement in buffer gas loading, but it is somewhat short of our goal of pushing the limits to $1\mu_B$. To do better, we need some way of dealing with the film problem[33].

Now, assuming that it were possible to deal with the film more effectively (more on this later), it is useful to consider how well we would be doing in the present apparatus if the film were not present. This can be done crudely by noting that the time scale to pump the atoms out of the cell volume ($\sim 100ms$) is significantly different than the time scale over which the film thins (~ 2 seconds). By looking at intermediate times (long compared to the cell emptying time, but short compared to the film desorption time), we have a good indication of what the atom number left in the trap would be if only the buffer gas atoms in the gas phase in the cell had to be removed. With this in mind, we pick $300ms$, and plot the number of atoms left in the trap at this time in fig. 5.20 (along with the data from fig. 5.19).

Figure 5.20 gives us cause for more optimism. It seems that if the film were not present, the efficiency would improve dramatically (allowing us to trap and isolate $\sim 10^{10}$ atoms at $1\mu_B$). Further improvements on this number could be made by lowering the initial loading temperature (see ch. 6) and/or by improving the yield

[33] The cryo-bakeout can't be accomplished quickly enough to avoid excessive atom loss for low magnetic moment species.

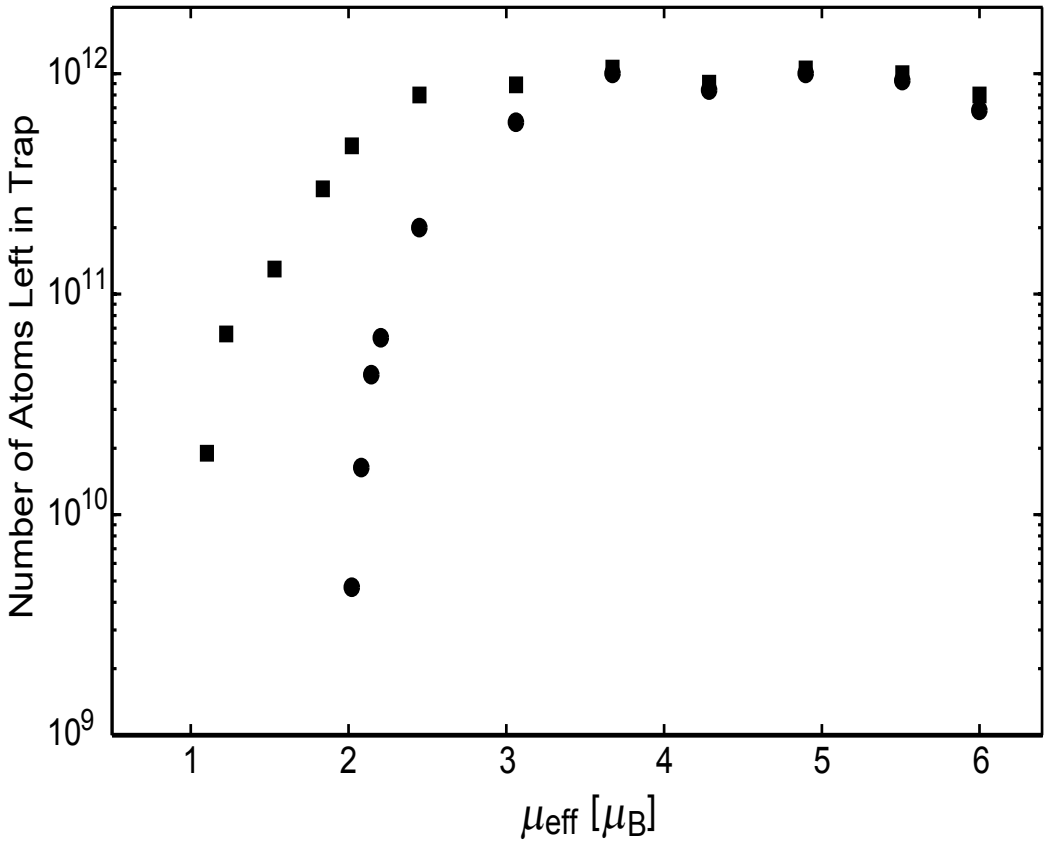

Figure 5.20: Number of atoms left in trap at $300ms$ (solid squares) and $10s$ (solid circles) after the valve opens. The number at $300ms$ is an indication of how many atoms we might expect to retain after thermal isolation if there were no film present in the cell.

from the ablation[34]. Now, getting rid of the film is easier said than done, but there are some promising schemes that which we'll consider in the next chapter.

It is interesting to compare the data shown in fig. 5.20 with our simulations. Figure 5.21 shows the results of simulations of trapped samples using the experimental conditions corresponding to the data points in fig. 5.20. The buffer gas density as a function of time is calculated using the measured cell temperature incorporating the effect of the film as per the model described in appendix A. One thousand atoms are simulated for each point. One hundred percent trapping efficiency is normalized to 1.25×10^{12} atoms. The simulations show reasonable qualitative agreement with the data. The simulations appear to somewhat overestimate the loss at early times while underestimating the loss during the film desorption. These effects cancel to some degree resulting in an "accidental" agreement between the $10s$ data and simulations which should not be taken to seriously. Given the strong dependence (both of the simulations and the data) on the buffer gas temperature, density, and the magnetic moment of the trapped species, the qualitative agreement between theory and data seems quite good.

[34] It is known for example (from experiments in our group) that the ablation yield for sodium can be as high as 10^{15} atoms (two orders of magnitude larger than for Cr) per pulse at the pulse energies that we operate at . The reason for this improved efficiency are not understood completely at this time. There does seem to be a general trend that the yield is higher for species with lower boiling boints ($T_b^{Na} = 1156K, T_b^{Cr} = 2945K$).

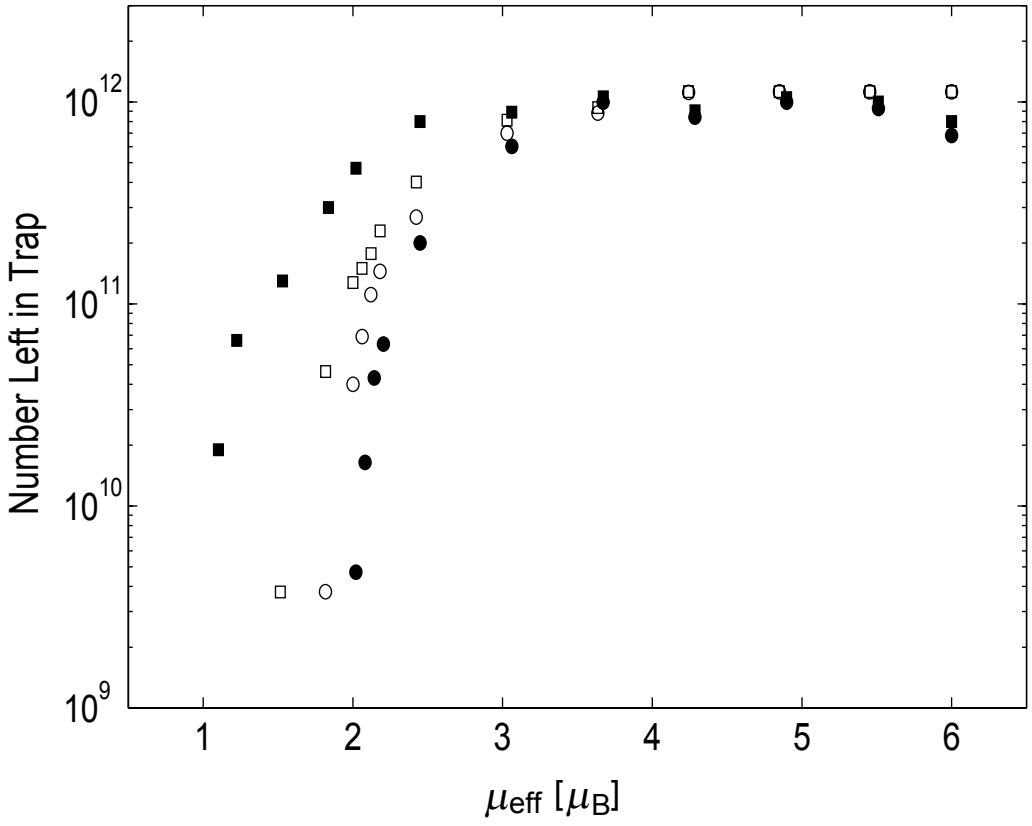

Figure 5.21: Comparison of simulations (described in ch. 2) to the data. Open circles (squares) show the simulation predictions of the number of atoms left in the trap at $10s$ ($300ms$). Solid circles and squares show the data from fig. 5.20.

5.9 Trapping Efficiency versus Temperature

We have explored the trapping efficiency as a function of magnetic moment, now we consider the effect of buffer gas temperature. This was not one of the major goals discussed at the beginning of the chapter. In practice, we'll almost always want to operate at as low a base temperature as possible to maximize η. Still, it is useful to investigate how changes in temperature effect the performance of the apparatus so as to better understand the trap loss dynamics during the removal of the buffer gas and more significantly because such a study can give an initial indication of what sort of improvement we might make in latter generations of the experiment by lowering the cell temperature.

Figure 5.22, shows the number of atoms left in the trap (again at 10 seconds after valve opening) for different buffer gas temperatures. In the data shown, the magnet was energized to 70 amps ($\mu_{eff} = 4.2$). The temperature of the buffer gas was controlled manually using the heater wrapped around the cell body.

Figure 5.22 indicates that the loading efficiency for $\sim 4\mu_B$ species is good up to $\sim 900mK$ and drops sharply above $\sim 1.1K$. By $1.2K$, only $\sim 10^9$ atoms are left in the trap (which is about the limit of our detection ability). In figure 5.23, we show the maximum buffer gas temperature possible to retain $\sim 10^9$ atoms in the trap after thermal isolation has been achieved. This represents a sort of maximum useful temperature for operating the apparatus. The number 10^9 is somewhat arbitrary, but as seen from figs. 5.19 and 5.22, the loading efficiency is a sharp function of

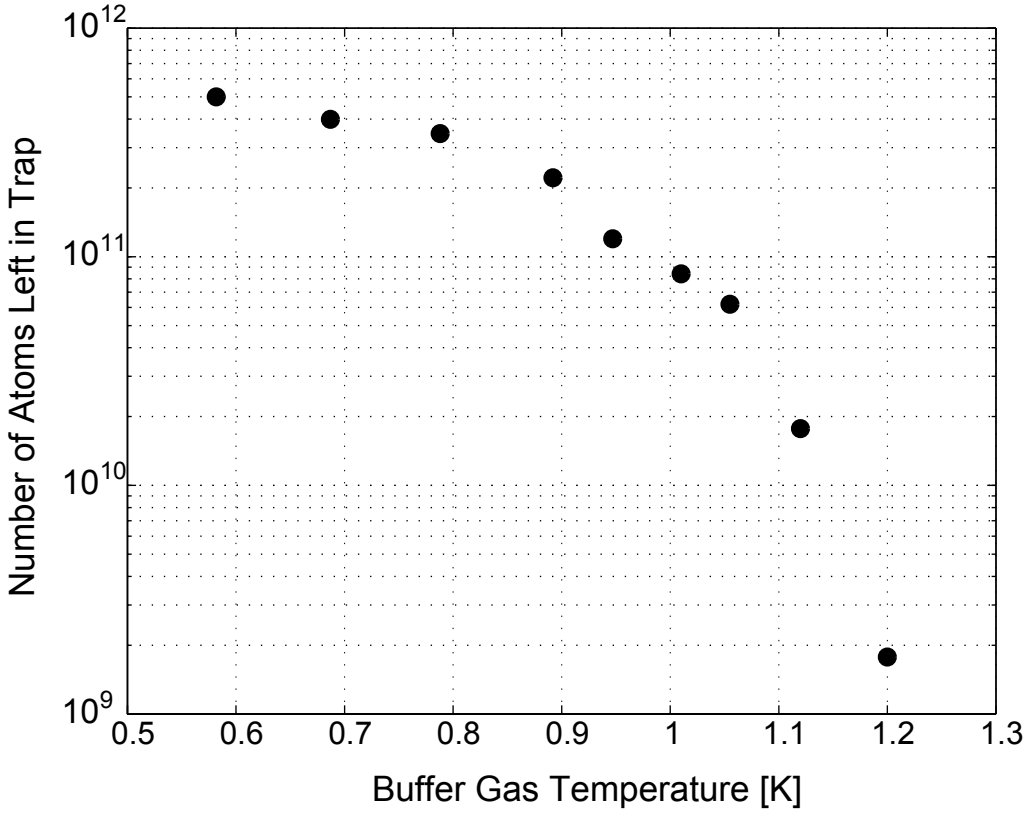

Figure 5.22: Number of atoms left in the trap after thermal isolation vs. buffer gas temperature. The data shown was taken with the magnetic trap energized to 70 amps (2.34 Tesla) corresponding to working with a species with an effective magnetic moment of $4.2\mu_B$.

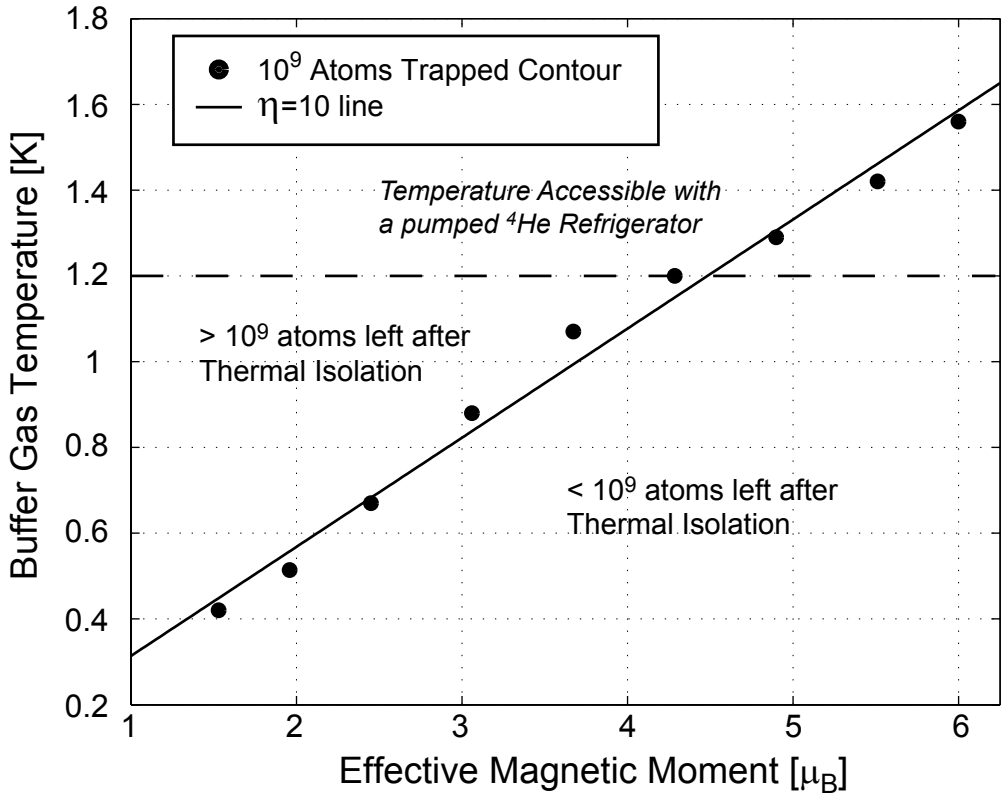

Figure 5.23: Minimum buffer gas loading temperature vs. μ_{eff}. The line indicates a ratio of trap depth to temperature for $\eta = 10$. The dashed horizontal line indicates a temperature region accessible by a pumped ^4He refrigerator.

both temperature and magnetic moment at this point, and so contours for other atom numbers (say for 10^8 or 10^7) would likely be quite similar.

There are a few useful pieces of information to draw from this plot. First, it is interesting that the data fits well to a straight. This indicates (not unexpectedly) that one parameter, η can be used to gauge the performance of the apparatus. From the data, we see that $\eta \gtrsim 10$ is required to efficiently trap with the present apparatus. This value for η is somewhat higher than we would like (as a result of the film issue).

Second, from extrapolation, it seems that we could reasonably expect to trap and thermally isolate the sample (even in the presence of the film) if the initial loading temperature were lowered to $\sim 330mK$. This may be possible using our ^3He refrigerator through better heat management, and it would be easy to accomplish using a dilution refrigerator.

Also significant from a cryogenic point of view is the ability to efficiently trap at temperatures above 1.4 K (for atoms with magnetic moments $\gtrsim 5\mu_B$). This temperature range is easily accessible using a pumped ^4He refrigerator and implies that trapping of high magnetic moment atoms could be done in an extremely simple cryogenic system.

5.10 ^{4}He loading

At this point, we have discussed most of the useful data taken in the first run of the experiment. Before moving on, we briefly describe the results of some other experiments that were performed which may be of interest. So far, all of the data presented was taken using ^3He as a buffer gas. ^3He was used because it has a higher vapor pressure than ^4He, and so trap loading can be done at a lower temperature (see fig 1.3). Also, we were somewhat concerned that the superfluidity of ^4He at these temperatures might result in a leakier valve or otherwise adversely effect the performance of the cell. For completeness, ^4He loading was attempted. Somewhat

surprisingly, we were able to load with equivalent success as with ^3He. Trapping data taken using ^4He is shown in fig. 5.24.

The reason that this is a bit surprising is that according to the vapor pressure curves shown in fig. 1.3, we should not have an adequate density of helium in the cell at the loading temperature ($\sim 600mK$) to ensure sufficient thermalization of the ablated sample. There is some uncertainty in the validity of those curves (which were not measured, but rather extrapolated from higher temperature data). Perhaps these curves are a bit off. This wouldn't be too surprising given the strong dependence of the density on temperature at these temperatures. This might be useful in some other buffer gas loading experiment (Note, for example, ^4He is completely non-magnetic whereas ^3He has a small magnetic moment due to the nuclear spin), but is of little consequence in our experiment.

5.11 Coating the Cell with H_2

As alluded to earlier, in principle, it would be possible to eliminate the film problem entirely if the cell were coated with a substance particularly non-sticky to helium. Put more concretely, we would like a substrate such that the binding energy of helium to that substrate is low enough that the film readily desorbs once the valve is open (on a time scale comparable to or shorter than the pump-out time of the cell volume). For a wide range of binding energies, the film behavior is essentially the same. So long as the binding energy of the most tightly bound (first) monolayer

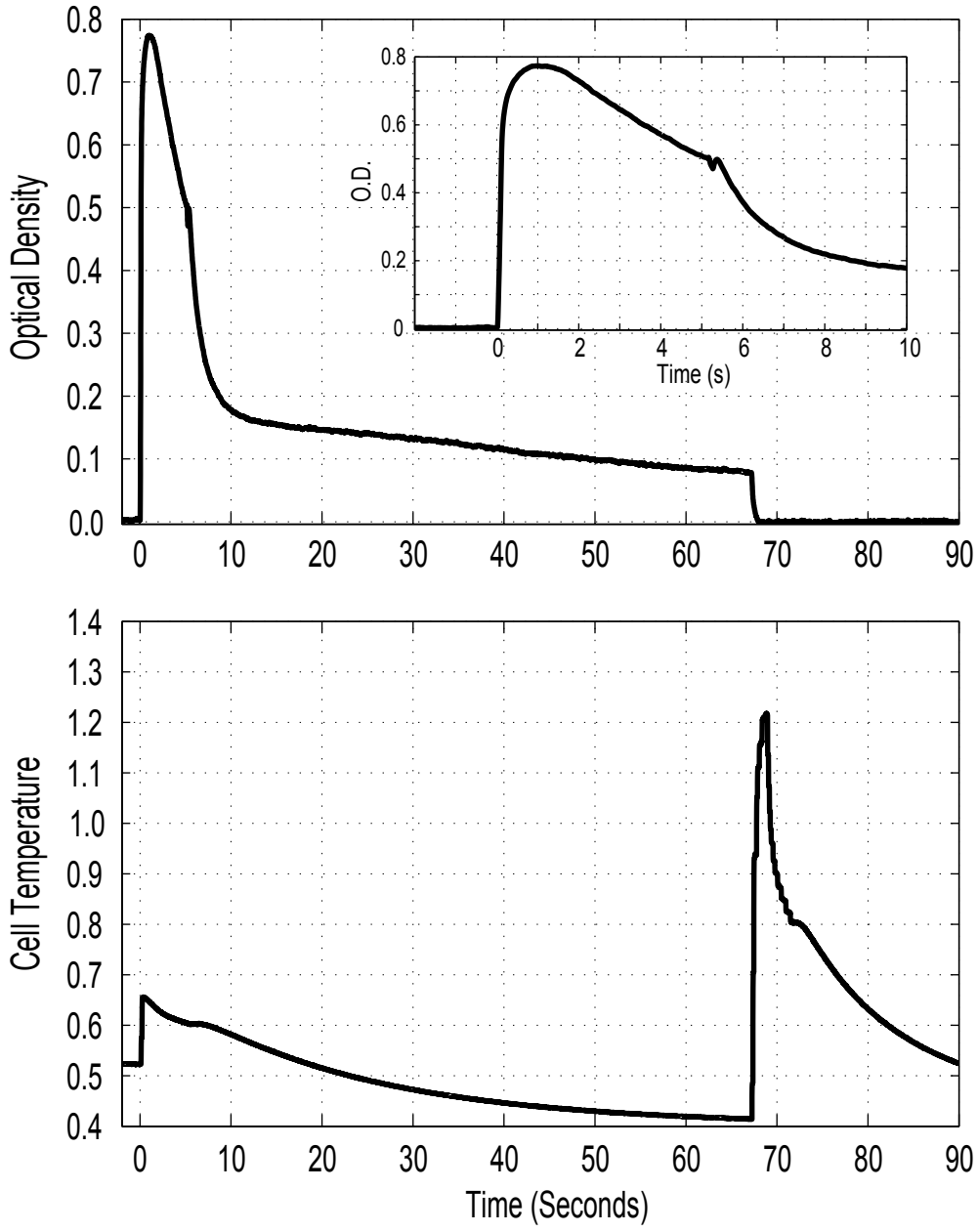

Figure 5.24: Buffer gas loading using ^4He. The magnetic trap is energized to 40 amps as in fig. 5.17. **a)** Decay of atoms from the trap. **b)** Cell temperature.

is high enough to result in a desorption time long compared to the time scale of the experiment, then it doesn't matter specifically what it is (recall fig. 5.13). If this is the case, then the film will be a problem, whether the residence time of the first monolayer is the age of the universe, or just one minute. Recalling an earlier discussion, we note that the most weakly bound monolayers will desorb very quickly. If the last monolayer is tightly bound, then at some point, the desorption rate of the film will pass through a harmful region.

What we need, is to find a substrate such that the residence time of even the most tightly bound monolayer is short. This is definitely not the case with G-10 (or any other common material that a cell might be constructed from). There are, however, a number of substrates (notably the alkali metals) that are suitable. This will be discussed at greater length in ch. 6. Unfortunately, we are not in a convenient position to alter the surface properties of the cell with the experiment running. It is possible, however, to introduce various gases into the cell with the experiment cold. By doing this, we have the option of coating the cell wall with a limited number of materials. Of all the gases that we might introduce into the cell, the one that helium has the lowest binding energy to (besides itself) is molecular hydrogen. There is a fair amount of uncertainty in the exact value for the binding energy of ^3He to solid hydrogen. The tabulated values range from $\sim 10 - 20K$ [31]. This leads to a range in desorption times (according to eq. 6.1) of $5 \times 10^{-5}s$ to $2 \times 10^5 s$. There is even further uncertainty in the prefactor τ_0 in eq 6.1. If the binding energy of ^3He to

H_2 is on the low end of the tabulated values, then there is a chance that a hydrogen coating could be beneficial.

Getting a uniform coating of hydrogen onto the cell wall is not easy. Care must be taken not to cool the cell too quickly (to avoid forming hydrogen "icicles" etc...). The cell temperature must also be kept very uniform to prevent the film from preferentially adhering to one (colder) portion of the cell. For our procedure, we attempted to mimic that of the Silvera experiment [62]. Our situation is further complicated by the presence of the sorbs in the cell. Charcoal is an even more effective cryo-pump for hydrogen than it is for helium. As a result, these sorbs must be kept warm ($\gtrsim 80K$) to prevent the hydrogen from sticking to them.

There are two possible paths for putting hydrogen into the cell. One possibility is to introduce the hydrogen through the cell fill line with the valve closed. This path has the advantage of avoiding the large sorb in the pumping chamber of the cell. The disadvantage of this approach is that the gas must pass through a very high impedance line (including the pinhole at the entrance to the trapping volume), and thus there is a significant danger of plugging the line with solid hydrogen. Alternatively, gas can be introduced through the cell pump-out line. This line has a much higher conductance (and therefore lower chance of plugging) but the large sorb in the pumping chamber is in the way. In practice, it proved impossible to keep this sorb hot enough while maintaining the cell temperature low enough to solidify the hydrogen ($T \lesssim 14K$). We did try both approaches, however. To go via the pump-out line, H_2 was "blasted"

down the line in the hopes that some would make it past the large sorb to land on the cell trapping chamber. Unfortunately, neither approach was successful in improving the performance of the apparatus. There are several possible reasons for this.

1) We were not able to get enough hydrogen into the trapping chamber to form a film (possibly due to the presence of the charcoal sorbs).

2) The quality of the hydrogen film was poor.

3) The binding energy of ^3He to H_2 is not sufficiently low to result in the rapid desorption of the film.

4) Some combination of these is at fault.

In any case, the hydrogen coating was not successful, and we leave it to a future run to try coating the cell with more promising substances.

Chapter 6
Further Results and Conclusions

6.1 Second Run of the Experiment

There are two major improvements to the apparatus that would allow us to trap and thermally isolate less magnetic atoms. One is to lower the temperature of the buffer gas (see fig. 5.23) and the second is to deal with the film more effectively. Both of these were addressed in the second run of the experiment. The setup for the second experimental run was virtually identical to that of the first. In fact, the same experimental cell was used again[35]. At the time of the writing of this thesis, the second run of the experiment is underway, and some preliminary results will be given here.

6.2 Temperature Management During 2nd Run

Our ^3He refrigerator is capable of achieving a base temperature of $\sim 260mK$ with no additional experimental heat load. This is a far cry from the $\gtrsim 550mK$ loading temperature during the first run of the experiment. Some heat load is unavoidable, but we should be able to do better than this. The two main areas for

[35] Because our cell is constructed from G-10 and most of the joints are permanent (having been made with epoxy) the cell is not very modular. It is possible, however, to insert new samples into the cell by carefully sawing off the cell bottom (including window joint), placing new samples into the cell, and then epoxying on a new cell bottom.

improvement are in the heat sinking of the valve shaft and in the thermal link between the cell and the ^3He pot. There was an $\sim 130mK$ difference between the base temperature of the cell with the valve closed ($T \sim 550mK$) compared to the base temperature with the valve open ($T \sim 430mK$) during the first experimental run. By more effectively dealing with heat conducted down the valve shaft, we would expect to reduce this temperature difference. In addition, the base temperature of the ^3He pot during the experiment was $\sim 350mK$. The fact that the cell is considerably warmer than this suggests that we did not do an adequate job of thermally connecting the cell the the refrigerator.

Making an effective heat link between two parts of a cryogenic apparatus is a bit of an art [15] [63]. It involves choosing the proper materials for the heat link (considerations include high thermal conductivity, flexibility, mass etc...) as well as properly connecting this link to the desired pieces to reduce thermal contact resistances. Because the valve shaft must move up and down (as the valve opens and closes), it is necessary that the heat link for the shaft have some flexibility. In the first run of the experiment, the valve shaft was connect to the top of the IVC (on the inside) using flexible copper braid. The length of the braid used was $\sim 5in$ ($12.7cm$) and the diameter was $\sim 0.06in$ ($0.16cm$). During the second run of the experiment, the braid thickness was increased to $\sim 0.2in$ ($0.51cm$).

To connect the cell to the ^3He pot, copper braid was also used. During the first run, the ~100 Cu wires running longitudinally down the cell body were collected

	1st Run	**2nd Run**
Cell (Valve Closed)	$\sim 550mK$	$\sim 480mK$
Cell (Valve Open)	$\sim 420mK$	$\sim 400mK$
^3He Pot	$\sim 350mK$	$\sim 330mK$

Table 6.1: Cell and fridge temperatures

and assembled into two groups which where joined to two copper braids (through a crimp joint) that ran to the ^3He pot where they were bolted on using #4 bolts. The thermal conductivity of this link was much lower than what was expected from the copper used suggesting that the weak link was in the contacts. For the second run, an intermediate plate (OFE copper, gold plated) was added to the bottom of the ^3He pot. This plate allowed us to use larger bolts (#8's versus #4's) to connect the heat link to the ^3He pot (allowing more pressure to be applied in the connection). In addition, a large copper braid (composed of several hundred $0.010mil$ diameter OFE copper wires [32]) with an overall diameter ~$0.4in$ ($1.0cm$) was wrapped around the cell body and attached using epoxy (stycast 2850).

This joint was not ideal, and for future cell designs, it would be advantageous to consider methods to more effectively connect the various heat links to the cell (in such a way that a large contact area was available and a large pressure could be applied). What we did during the second run was a best effort with the constraint of the current experimental geometry and cell design. As a result of these changes, the base temperature of the cell during the second run was ~ $400mK$ ($480mK$) with the valve open (closed) and the base temperature of the ^3He pot was ~ $330mK$. These results are contrasted with the first run in table 6.1.

Apparently, we did a somewhat better job of heat sinking the valve shaft while not making much improvement at all in the heat link between the cell and the ^3He pot. A rebuilding of the cell is probably necessary to more effectively make this heat link. Never-the-less, the marginal improvement in the base temperature of the cell with the valve closed does result in some improvements in the number of atoms trapped. Figure 6.1 shows data taken during the second run (again using Cr) where the initial trapping field is changed to vary the effective magnetic moment of the atom as before. The number left in the trap at $300ms$ and $10s$ is shown and compared to similar data from the first run (see fig. 5.20).

6.3 Managing the Film

As alluded to earlier, the best way to deal with the film would be to eliminate it as a problem entirely by coating the cell with a substrate that He has a low binding energy to. Appendix A describes a detailed model for estimating the effect of the film on the buffer gas density in the cell after the valve opens based on the temperature of the film, binding energy, film thickness, etc... Here we present a brief estimate on how low a binding energy we require in order for the film to desorb rapidly (compared to the pump-out time of the cell volume) once the valve opens.

The characteristic time for an atom to desorb from the film is given by [39]:

$$t_d = \tau_0 \exp(E_b/T) \tag{6.1}$$

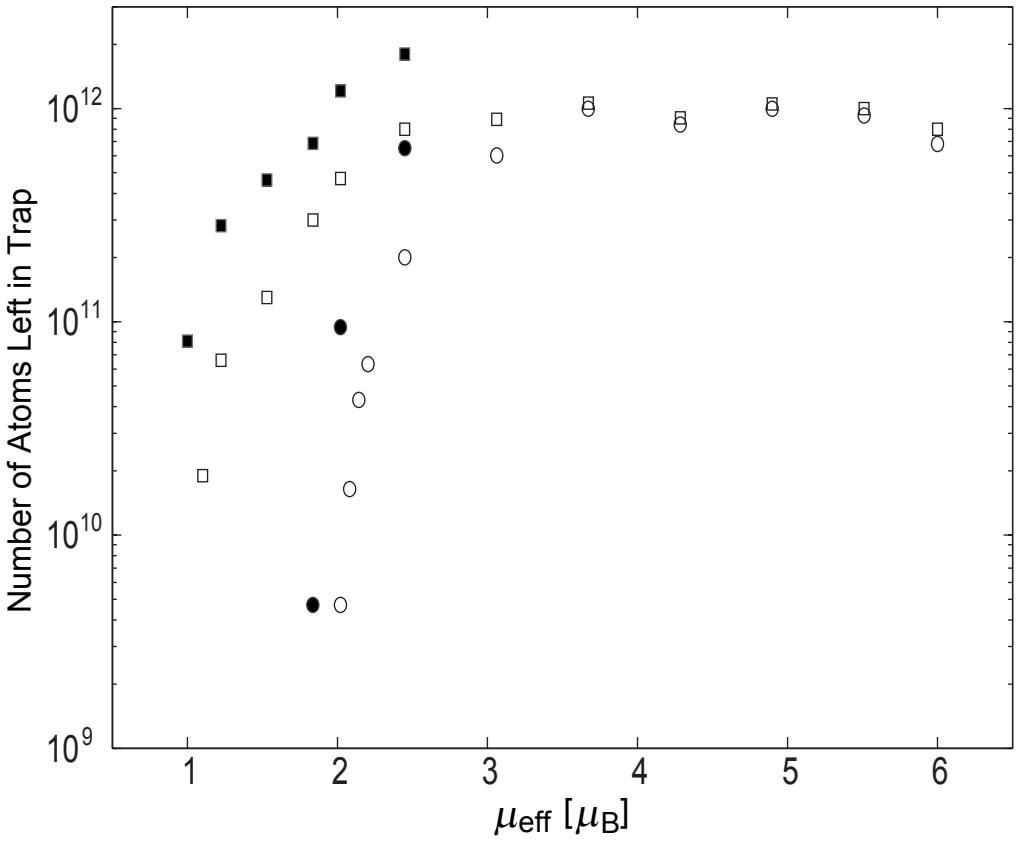

Figure 6.1: Number of atoms left in the trap in the second run (solid points) compared to the first run (open points) at $300ms$ (squares) and $10s$ (circles).

Substrate	Binding Energy (K)	Desorption Time
Graphite	140	$> 10^{100}$ years
Copper (Cu)	60	$> 10^{31}$ years
Aluminum (Al)	44	$> 10^{17}$ years
(solid) H_2	10-20	$0.05ms$ - $23000s$
(solid) Ne	38	7×10^{12} years
(solid) Ar	84	$> 10^{52}$ years
Potassium (K)	36	6×10^{10} years
Lithium (Li)	12	$2.6ms$
Sodium (Na)	6.8	$8 \times 10^{-8}s$
Cesium (Cs)	1.8	$4 \times 10^{-12}s$
^4He	5.2	$3 \times 10^{-9}s$
^3He	~4	$3 \times 10^{-10}s$

Table 6.2: Binding energies and desorption times

Where t_d is the desorption time, and E_b is the binding energy (in Kelvin). The prefactor, τ_0, is related to the oscillation period of an atom in the film and generally taken to be $\sim 10^{-13}s$. Table 6.2 lists various materials along with the binding energy of ^3He to these substances [31] and the solution to eq. 6.1 assuming a cell temperature of $0.5K$.

The exact values in table 6.2 should not be taken too seriously. There is a fair amount of uncertainty in both the binding energy and the value for the prefactor τ_0 in eq. 6.1. The general problem is apparent, however. For the vast majority of common materials that we might use to construct a cell, the desorption time for the first, most tightly bound monolayer is extremely long. There are, however, a few substrates that seem promising. In the previous chapter, we discussed an attempt to coat the cell with solid hydrogen. This proved not to be helpful in dealing with the film. Several of the alkali metals, however, have an even weaker affinity for helium

than does hydrogen. Cesium would be the best choice as far as binding energy is concerned, but it is extremely reactive and difficult to work with.

Instead, we will attempt to coat the cell with sodium. Sodium is also quite reactive (though not so much as cesium) so it is not trivial to apply a film of the pure metal to the cell. We are, however, in a convenient position to do an in-situ deposition of the film once the cell has been sealed, evacuated, and the experiment cooled down. For the second run of the experiment, a lump of sodium metal was placed into the cell. We were going to do this anyway, regardless of the film issue in the hopes of trapping Na. To place a sodium film onto the wall of the cell, we can continuously ablate the sodium sample with the cell filled with a high density of buffer gas. The buffer gas is necessary so that the sodium vapor produced from the ablation will diffuse throughout the cell volume to create a coating on all parts of the cell. Given the production rate for Na from previous ablation experiments in our lab, we expect to be able to create a film of many monolayers by ablating for a period of several hours.

The window in the cell presents a special challenge. Obviously, the window must remain transparent despite the coating in order allow spectroscopy of the trapped sample. Fortunately, a several monolayer thick film can be created without significantly affecting the windows ability to transmit light [64].

6.4 Conclusions and Future Directions

Despite the problems caused by the film, the first run of the experiment was very successful. We were able to demonstrate the basic proof of principle behind a completely new atom/molecule trapping apparatus. We were able to show that adequate vacuum could be achieved in this apparatus to ensure thermal isolation of the sample and to perform evaporative cooling. We were also able to push the limits of buffer gas loading to efficiently trap and thermally isolate species with magnetic moments down to $3\mu_B$ and with less efficiency down to $2\mu_B$. In addition, we showed that a vastly simpler (^4He based) apparatus could be used in working with high magnetic moment species, and we gained valuable insight on what improvements are necessary to extend the limits on buffer gas loading down to $1\mu_B$ species.

During the second run of the experiment, we were able to make marginal improvements in the base temperature of the cell that allowed for more efficient trapping and thermal isolation of ~$2\mu_B$ species. Further improvements should be possible by redesigning the cell and valve shaft to better deal with the heat load on the experiment. If these improvements prove insufficient to allow for the efficient trapping and thermal isolation of $1\mu_B$ species, then a dilution refrigerator could be incorporated to lower the loading temperature further. Another possible avenue to pursue is the construction of a Nb_3Sn superconducting trap. Potentially, this could result in a trapping field ~ 50% greater than what is possible using NbTi.

By implementing one or more of these changes, we expect soon to be able to reach our goal of extending buffer gas loading to $1\mu_B$ species and thus provide a "universal" trapping apparatus for a wealth of paramagnetic atoms and molecules. Extending buffer gas loading to lower magnetic moment species is particularly interesting as it pertains to the production of quantum degenerate gases. So far, the vast majority of experiments on degenerate atoms have used the $1\mu_B$ alkali metals. In addition, metastable helium ($2\mu_B$) has been bose-condensed [65] [66]. Buffer gas loading allows for the trapping of much larger samples than does laser cooling, and offers the promise of producing quantum degenerate samples with orders of magnitude more atoms than can be produced using optical techniques.

For the second run of the experiment, several additional species were placed in the trap along with Cr to study a wide range of collisional physics. Atomic manganese was trapped for the first time, and spin relaxation rates amongst the different hyperfine states have been measured. These will be compared to the rates for similar processes in ^{53}Cr and atomic europium. In addittion, the rates for zeeman state changing collisions between helium atoms and atomic hafnium have been measured. These will be compared to the rates for similair processes in titanium, scandium, and various other "shaped" atoms (that do not have S state ground states) such as the rare earth elements. Copper, rhenium, sodium, and molecular CaF were also placed in the cell during the second run of the experiment, and are actively being investigated at the time of the writing of this thesis

Appendix A
He Films

In this appendix, we consider the role that the helium film adsorbed on the walls of the trapping chamber plays in modifying the buffer gas density during the pump-out. If the film were not present, the buffer gas density would fall simply do to the loss of atoms through the valve aperture as per eq. A.1[36].

$$\dot{n}_{He} = -\frac{n_{He}}{\tau} \tag{A.1}$$

With the film, however, there are two additional processes to consider. First, atoms that desorb from the film provide a flux of atoms into the trapping chamber. Second, atoms in the gas phase in the trapping chamber may be adsorbed into the film. These processes (shown schematically in fig. 6.2) result in a differential equation for the buffer gas density in the trapping chamber.

$$\dot{n}_{He} = -\frac{n_{He}}{\tau} + \dot{n}_d - \dot{n}_a \tag{A.2}$$

The rate that atoms are adsorbed into the film is simply equal to the flux of atoms striking the surface times the cell surface area times the probability that an atom striking the surface will stick.

---

[36] For simplicity, we'll neglect the small difference in the pumping speed in the molecular regime versus that in the viscous regime.

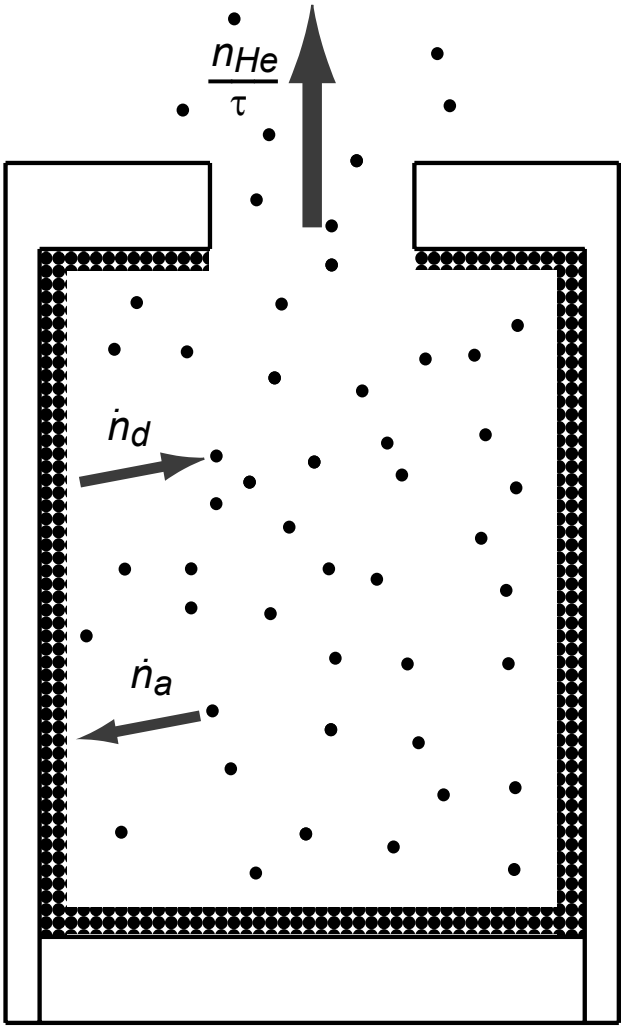

Figure 6.2: Illustration of the three processes effecting the buffer gas density in the trapping chamber. Atoms are lost through the valve aperture at a rate, n_{He}/τ. In the absence of a film, this would be the only process present. With the film, there is an additional source of atoms into the chamber, $\dot{n}_d$, due to atoms desorbing from the film as well as an additional loss process, $\dot{n}_a$, due to adsorption of atoms into the film.

$$\dot{N_a} = flux \times area \times \text{sticking probability} \tag{A.3}$$

and,

$$\dot{n_a} = flux \times \frac{area}{V} \times \text{sticking probability} \tag{A.4}$$

where V is the volume of the chamber.

The flux to the surface is given by the familiar expression [39]:

$$flux = \frac{1}{4} n_{He} v_{av} \tag{A.5}$$

Where v_{av} is the average velocity given by:

$$v_{av} = \sqrt{\frac{8 k_B T}{\pi m}} \tag{A.6}$$

According to the ideal gas law:

$$n_{He} = \frac{P}{k_B T} \tag{A.7}$$

Combining eqs. A.3 - A.7, yields for the adsorption process:

$$\dot{n_a} = n_{He} \frac{A}{V} f \sqrt{\frac{k_B T}{2\pi m}} \tag{A.8}$$

Where A and V are the surface area and volume of the chamber, and f, is the sticking probability (generally ~ 0.75 for helium on solid surfaces [67]). Now, to find the desorption rate, we use the fact that in equilibrium, the rate of desorption from

and adsorption into the film are identical. The resulting pressure above the film (in equilibrium) is simply equal to the vapor pressure. In other words,

$$\dot{n_d} = n_{sat}\frac{A}{V}f\sqrt{\frac{k_BT}{2\pi m}} = P(d)\cdot\frac{Af}{V}\sqrt{\frac{1}{2\pi k_BTm}} \tag{A.9}$$

Here, P, is the vapor pressure above the film which depends on the film thickness, d, according to the FHH expression [39]:

$$P_{sat}(d) = P_0\exp(\frac{-1}{T}\frac{\alpha}{d^3}) \tag{A.10}$$

Where P_0 is the saturated vapor pressure and α is the van der Waals coefficient. For helium, bound to G-10, α is approximately $1900K\mathring{A}^3$ [31]. As we saw in ch. 5, the exact value for α is not very important so long as the first monolayer is bound tightly. The binding energy for an atom to the surface[37] is equal to α/d^3. Because the binding energy is a strong function of the separation and because the vapor pressure has a strong (exponential) dependence on the binding energy, the vapor pressure (and thus the desorption rate) is very strongly dependent on the film thickness. As noted earlier, the desorption rate initially is quite high (when the film is thick) and falls eventually to something quite low (when the film is thin).

Combining eqs. A.9, and A.10 gives an expression for the desorption rate:

---

[37] For two atoms in free space, the van der Waals interaction is proportional to $1/r^6$. The dependence of the van der Waals interaction for an atom and a surface on the third power of the distance separating them results from the integration of the $1/r^6$potential over the three dimensions of the bulk surface. For an atom interacting with an infinite line for example, the van derWaals interaction would be proportional to $1/r^5$ while for an atom above an infinite sheet (with infinitesimal thickness) the interaction would go like $1/r^4$.

$$\dot{n_d} = P_0 \exp(\frac{-1}{T}\frac{\alpha}{d^3}) \cdot \frac{Af}{V}\sqrt{\frac{1}{2\pi k_B T m}} \tag{A.11}$$

If we combine eqs. A.2, A.8, and A.11 and rearrange terms a bit, we have for the total change in density in the trapping chamber:

$$\dot{n}_{He} = \frac{n_{He}}{\tau} + \frac{Af}{V}\left[P_0 \exp(\frac{-1}{T}\frac{\alpha}{d^3})\frac{1}{k_B T} - n_{He}\right] \tag{A.12}$$

Because eq. A.12 depends on the film thickness, we need an expression for how the film thickness varies with time. This is easily found since the film thickness changes due to the desorption and adsorption rates which we have already calculated. Specifically,

$$\dot{d} = \frac{d_0}{N_0} V \cdot (\dot{n}_a - \dot{n}_d) \tag{A.13}$$

Where d_0 and N_0 are the thickness of and number of atoms in a monolayer of the film. Plugging in our expressions for $\dot{n}_a$and $\dot{n}_d$ gives:

$$\dot{d} = -\frac{d_0}{N_0} f A \sqrt{\frac{k_B T}{2\pi m}}\left[P_0 \exp(\frac{-1}{T}\frac{\alpha}{d^3})\frac{1}{k_B T} - n_{He}\right] \tag{A.14}$$

Equations A.12 and A.14 are a set of two coupled first order differential equations which are solved numerically to compute the density of gas in the trapping chamber as well as the film thickness (shown for various conditions in figures in ch. 5). Note, for ^3He, the saturated vapor pressure in our temperature range can be approximated as [51]:

$$P_0 = 4.89 \times 10^5 \exp(\frac{-3.93}{T/K}) \ [dyne/cm^2] \tag{A.15}$$

Appendix B
Elastic versus Diffusion Cross Section

When using a particular cross section (to calculate a mean free path for example), it is important to make sure that one understands exactly what process is occurring in the collision. In all of our simulations of trajectories (see ch. 2) we have used the *elastic* collision cross section (taken to be $10^{-14} cm^2$) for a collision between an atom in the trap and a helium atom. During an elastic collision, the total kinetic energy of the trapped atom and helium atom is conserved. The momentum is of course conserved as well. Also, during the collision, the particle's trajectory is altered. We have assumed for our simulations, that the velocity vector is randomized in the CM frame after the collision. This is an approximation since in a real collision, the differential collisional cross section for scattering at a particular angle will depend upon the impact parameter of the collision (as well as the orientation of the particles if the scattering potential is anisotropic). If we consider a wide range of impact parameters, then it probably isn't so bad an approximation to assume that on average, the CM scattering angle is random and isotropic. This assumption greatly simplifies the simulations, of course, as it allows the use of a single total elastic cross section rather than a differential cross section.

Keeping in mind this assumption that the CM velocity is randomized during each elastic collision, is it interesting to consider how the collision appears in the LAB frame. If the trapped particle were much lighter than a helium atom, then a collision

that randomized the velocity of the particle in the CM frame would also randomize the velocity in the LAB frame. In such a collision, the recoil of the (more massive) helium atom is small, and the LAB and CM frames are essentially identical. In buffer gas loading, we are concerned with the opposite extreme. Generally, the mass of the trapped particle is many times greater than the mass of the helium atoms it collides with. As a result, many elastic collisions are necessary to randomize the velocity of a particle in the LAB frame, and a single elastic collision only slightly alters the particle's trajectory.

We can define another cross section (commonly known as the diffusion cross section) which is related to the elastic cross section through the following expression [25].

$$\sigma_d = \int \int \frac{d\sigma}{d\Omega}(1 - \cos\theta) \sin\theta d\theta d\phi \tag{B.1}$$

Where $d\sigma/d\Omega$ is the differential *elastic* scattering cross section, and θ and ϕ are the polar and azimuthal scattering angles in the LAB frame. For isotropic scattering in the CM frame, eq. B.1 gives the cross section for randomization of the particle's velocity in the LAB frame. The ratio σ/σ_d is the number of elastic collisions necessary to randomize the particles velocity in the LAB frame. To evaluate eq. B.1, it is useful to relate the differential scattering cross section in the LAB frame to the differential scattering cross section in the CM frame. This relation is given by [30]

$$\frac{d\sigma}{d\Omega}_{lab} = \frac{d\sigma}{d\Omega}_{CM} \cdot \frac{(x\cos\theta + \sqrt{1 - x^2\sin^2\theta})^2}{\sqrt{1 - x^2\sin^2\theta}} \tag{B.2}$$

Where, as in eq. B.1, θ is the polar scattering angle in the LAB frame and x is the mass ratio, m/m_{He} between the trapped particle and a helium atom. In general, $x > 1$ (assuming the particle is more massive than a helium atom). If we assume isotropic scattering in the CM frame, then we have simply,

$$\frac{d\sigma}{d\Omega}_{CM} = \frac{1}{4\pi}\sigma \tag{B.3}$$

and,

$$\frac{d\sigma}{d\Omega}_{lab} = \frac{1}{4\pi}\sigma \cdot \frac{(x\cos\theta + \sqrt{1 - x^2\sin^2\theta})^2}{\sqrt{1 - x^2\sin^2\theta}} \tag{B.4}$$

Plugging this in to eq. B.1 gives:

$$\sigma_d = \int\int \frac{1}{4\pi}\sigma \cdot \frac{(x\cos\theta + \sqrt{1 - x^2\sin^2\theta})^2}{\sqrt{1 - x^2\sin^2\theta}}(1 - \cos\theta)\sin\theta d\theta d\phi \tag{B.5}$$

For a ^3He buffer gas, $x = m/3$ and eq. B.5 becomes:

$$\sigma_d = \int\int \frac{1}{4\pi}\sigma \cdot \frac{(\frac{m}{3}\cos\theta + \sqrt{1 - (\frac{m}{3})^2\sin^2\theta})^2}{\sqrt{1 - (\frac{m}{3})^2\sin^2\theta}}(1 - \cos\theta)\sin\theta d\theta d\phi \tag{B.6}$$

We can see from the integrand in eq. B.5, that we must restrict our integration over the polar scattering angle, θ, such that $1 - x^2\sin^2\theta < 1$. For $x < 1$ (in other words, for atoms lighter than He), this is always satisfied, and θ can range from 0

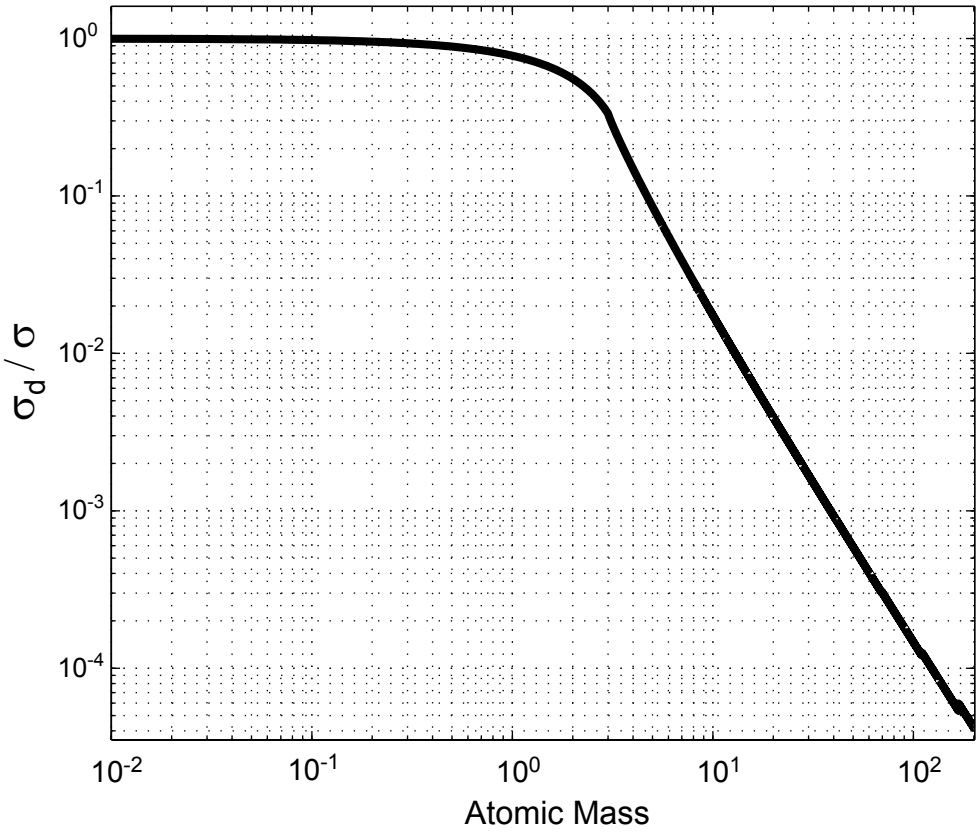

Figure 6.3: Ratio between diffusion and elastic cross section as a function of the mass of the scattered particle. This ratio is determined by numerically integrating eq. B.6.

(forward scattering) to π (backward scattering). If, however, $x > 1$, then there is a maximum scattering angle, $\theta_{\max} = \sin^{-1}(1/x)$. Physically, this means that heavier particles can not be back scattered from the helium atom. If for example the atom has an identical mass to He ($x = 1$), the maximum scattering angle will be ninety degrees. The result of a numeric integration of eq. B.6 is shown in fig. 6.3.

Appendix C
Cooling Power of Refrigerator

The cooling power of a refrigerator that works by pumping to evaporatively cool a liquid is given quite generally by:

$$\dot{Q} = \text{rate of removing atoms } \times \text{ energy removed per atom} \tag{C.1}$$

The energy removed per atom is simply equal to the latent heat of evaporation, while the rate of removing atoms will be equal to the speed of the pump times the vapor pressure above the liquid. The vapor pressure can be related to the temperature and latent heat through the Clausius-Clapeyron equation [15]:

$$P_{vap} \propto \exp(-L/RT) \tag{C.2}$$

Where L is the latent heat (in J/mol), T the temperature (in K) and R the gas constant ($8.3 J/K \cdot mol$).

If we assume the latent heat is roughly independent of temperature, then all of the temperature dependence of the cooling power is contained in the exponential in eq. C.2. Table 6.3 shows the measured cooling power of our ^3He refrigerator at various temperatures.

This data is plotted in fig. 6.4 along with a fit to the function:

$$f = a \cdot \exp(-b/T) \tag{C.3}$$

Temperature (mK)	**Cooling Power (μW)**
295	88.4
333	186
383	502
433	958
500	1930
543	3960
613	7440
660	10300

Table 6.3: Refrigerator cooling power

The best fit yields a value for b of 3.082 which yields for the latent heat of evaporation of ^3He a value of $25.6 J/mol$. This is reasonable given that the latent heat is known to vary over the range $25 - 30 J/mol$ in this temperature range [15].

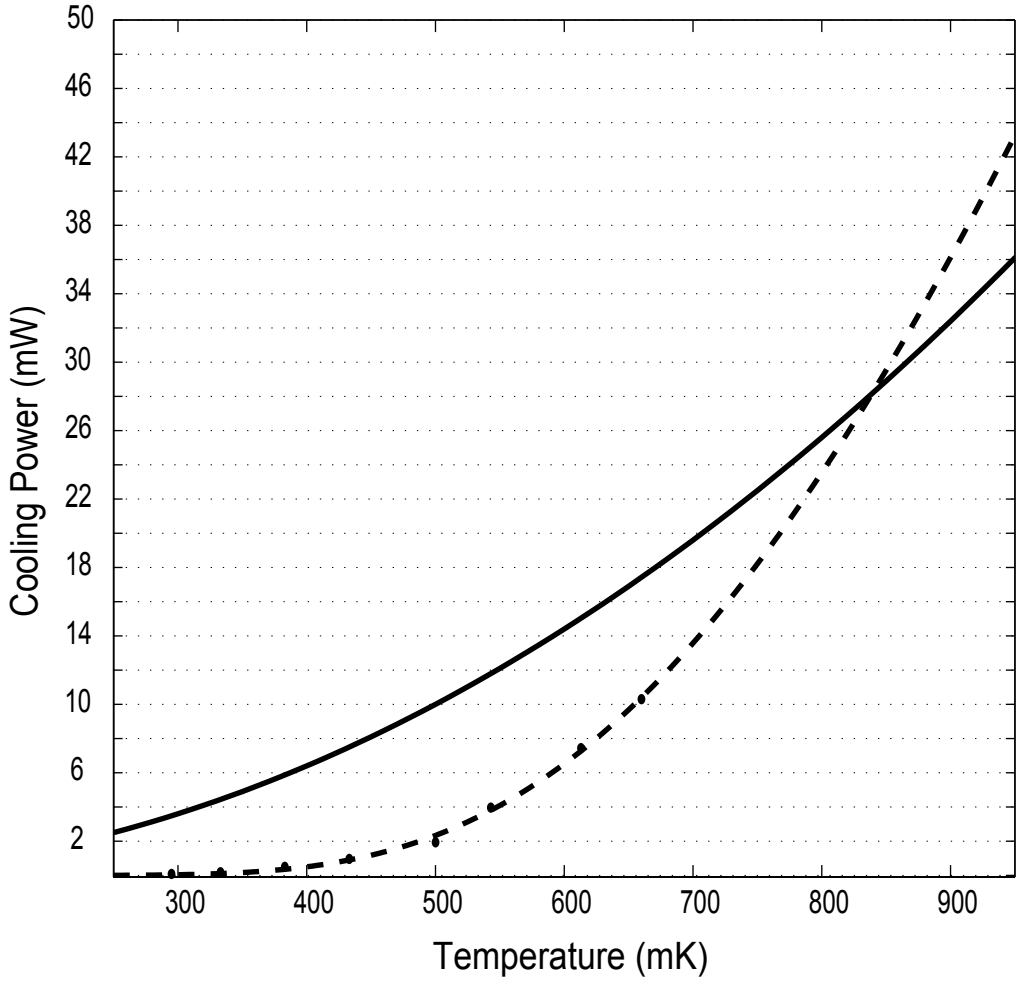

Figure 6.4: Measured cooling power of our ^3He refrigerator as a function of temperature along with fit (dashed line). For comparison, the typical cooling power of a Kelvinox 400 dilution refrigerator is also shown (solid line).

Field (Tesla)	Critical Current (Amps)
9	45
7	140
5	225
3	315

Table 6.4: Short sample critical current of magnet wire.

Appendix D
Critical Current of Magnet

The wire used in our magnet trap is a composite of Cu and NbTi with a copper to superconducting ratio of 1.3 to 1. The role of the copper is to stabilize the wire against a quench (by rapidly conducting heat away from local hot spots) and to dissipate heat in the event of a quench [34]. The wire is type 54S43 (manufactured by Supercon [68]) and is composed of 54 $45\mu m$ NbTi filaments embedded in the copper matrix. The total (uninsulated) wire diameter is 0.020" ($0.051cm$).

To calculate the critical current of the magnet, we first note the short sample critical current of the superconductor measured at different magnetic fields. These values (measured at $T = 4.2K$) are shown in table 6.4. The "load line" of the superconductor determined by these values is plotted in fig. 6.5.

The critical current of the magnet is equal to the value where the maximum field in the magnet is equal to the critical field at the short sample critical current. To find this, we simply take the intersection of the "load line" of the superconductor with the line defined by the maximum field in the magnet as a function of current. This is shown in fig. 6.6.

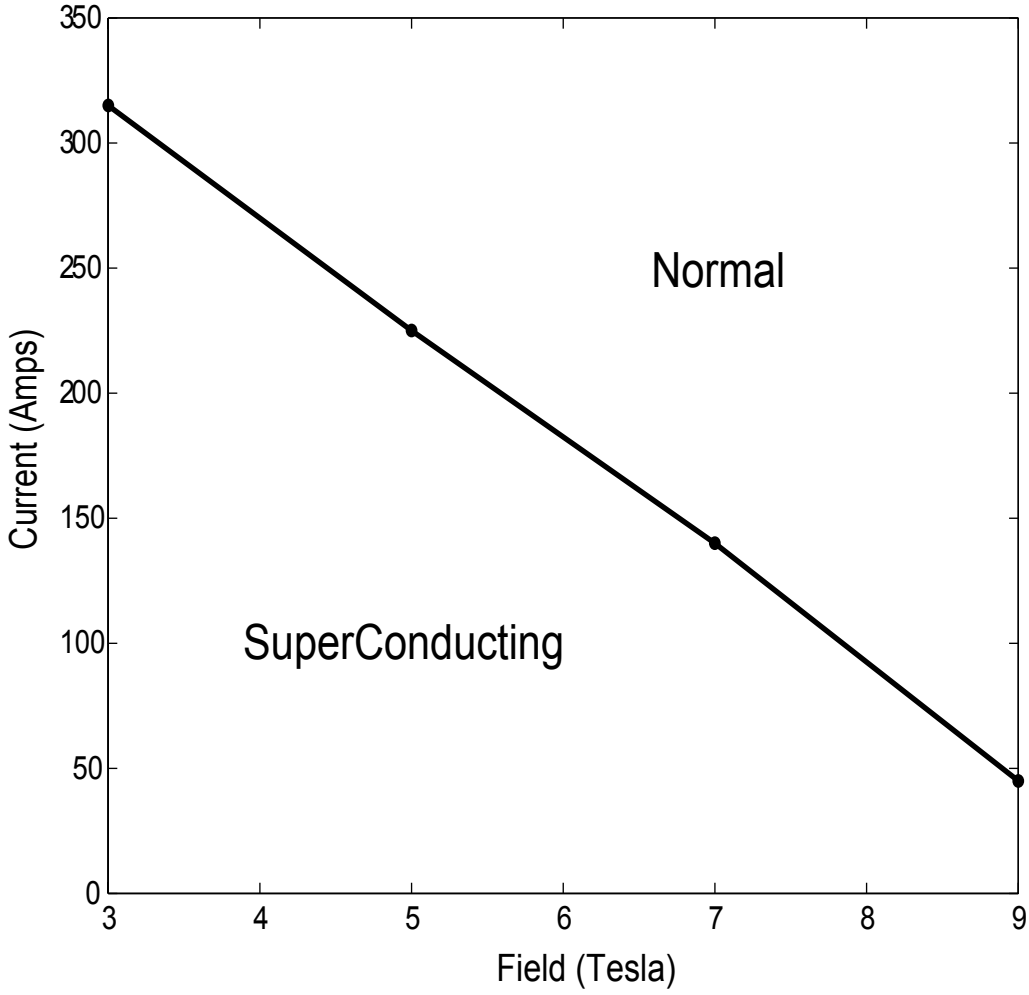

Figure 6.5: Load line for the wire used in our magnetic trap. For currents and fields less than the critical values, the wire is superconducting. For currents and fields above the critical values, the wire is in the normal state.

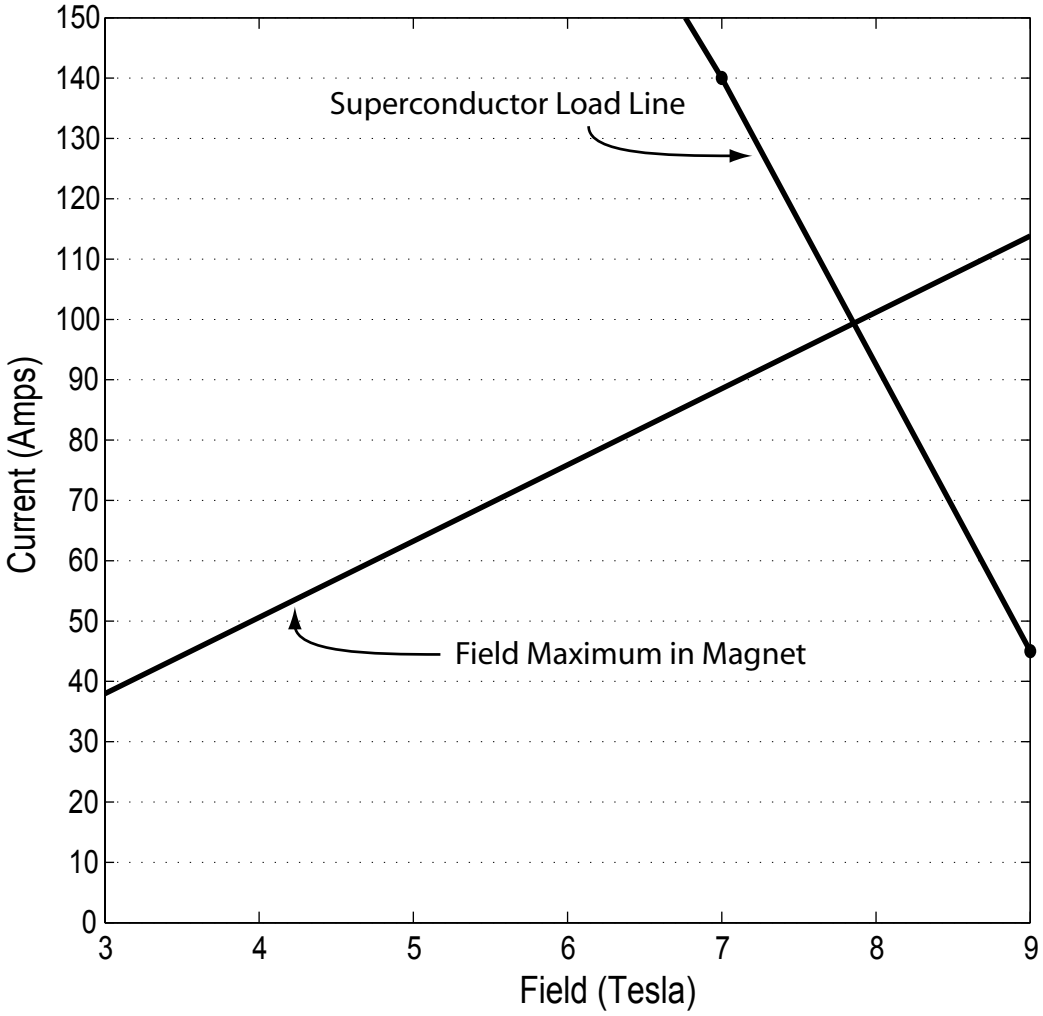

Figure 6.6: Intersection of line defined by the maximum field in the magnet vs. current with the load line of the superconductor. This intersection occurs at a current of ~$100A$ which is the critical current for the magnet.

Bibliography

[1] M. H. Anderson, J. R. Ensher, M. R. Matthews, C. E. Wieman, and E. A. Cornell, "Observation of bose-einstein condensation in a dilute atomic vapor," *Science* **269**, pp. 198–201, 1995.

[2] K. B. Davis, M. O. Mewes, M. R. Andrews, N. J. van Druten, D. S. Durfee, and D. M. Kurn., "Bose-einstein condensation in a gas of sodium atoms," *Physical Review Letters* **75**, pp. 3969–73, 1995.

[3] C. C. Bradley, C. A. Sackett, and R. G. Hulet, "Bose-einstein condensation of lithium," *Physical Review Letters* **78**, pp. 985–89, 1997.

[4] B. DeMarco and D. S. Jin, "Onset of fermi degeneracy in a trapped atomic gas," *Science* **285**, pp. 1703–6, 1999.

[5] Z. Hadzibabic, S. Gupta, C. A. Stan, C. H. Schunck, M. W. Zwierlein, K. Dieckmann, and W. Ketterle, "Fifty-fold improvement in the number of quantum degenerate fermionic atoms," *Physical Review Letters* **91**, p. 160401, 2003.

[6] M. A. et al., "Production and detection of cold antihydrogen atoms," *Science* **419**, pp. 456–459, 2002.

[7] G. G. et al., "Driven production of cold antihydrogen and the first measured distribution of antihydrogen states," *Physical Review Letters* **89**, p. 233401, 2002.

[8] L. S. Brown and G. Gabrielse, "Geonium theory: Physics of a single electron or ion in a penning trap," *Reviews of Modern Physics* **58 no.1**, pp. 233–311, 1986.

[9] P. R. Huffman, C. R. Brome, J. S. Butterworth, K. J. Coakley, M. S. Dewey, S. N. Dzhosyuk, R. Golub, G. L. Greene, K. Habicht, S. K. Lamoreaux, C. E. H. Mattoni, D. N. McKinsey, F. E. Wietfeldt, and J. M. Doyle, "Magnetic trapping of neutrons," *Nature* **403**, pp. 62–64, 2000.

[10] E. L. Raab, M. Prentiss, A. Cable, S. Chu, and D. E. Pritchard, "Trapping of neutral sodium atoms with radiation pressure," *Physical Review Letters* **59**, p. 1987, 1987.

[11] T. Bergeman, G. Erez, and H. J. Metcalf, "Magnetostatic trapping fields for neutral atoms," *Physical Review A* **35 no.4**, pp. 1535–1546, 1987.

[12] C. E. Wieman, D. E. Pritchard, and D. J. Wineland, "Atom cooling, trapping, and quantum manipulation," *Reviews of Modern Physics* **71**, pp. S253–S262, 1999.

[13] W. Petrich, M. H. Anderson, J. R. Ensher, and E. A. Cornell, "Stable, tightly confining magnetic trap for evaporative cooling of neutral atoms," *Physical Review Letters* **74**, p. 3352, 1995.

[14] R. Grimm, M. Weidenmuller, and Y. B. Ovchinnikov, "Optical dipole traps for neutral atoms," *Advances in Atomic, Molecular, and Optical Physics* **42**, pp. 95–170, 2000.

[15] F. Pobell, *Matter and Methods at Low Temperatures*, Springer-Verlag, 1992.

[16] J. M. Doyle, *Energy Distribution Measurement of Magnetically Trapped Spin Polarized Atomic Hydrogen: Evaporative Cooling and Surface Sticking*. PhD thesis, MIT, 1991.

[17] K. Sengstock and W. Ertmer, "Laser manipulation of atoms," *Advances in Atomic, Molecular, and Optical Physics* **35**, pp. 1–44, 1995.

[18] W. Ketterle, K. B. Davis, M. A. Joffe, A. Martin, and D. E. Pritchard, "High densities of cold atoms in a dark spontaneous-force optical trap," *Physical Review Letters* **70**, p. 2253, 1993.

[19] D. G. Fried, *Bose-Einstein Condensation of Atomic Hydrogen*. PhD thesis, MIT, 1999.

[20] J. D. Weinstein, R. deCarvalho, J. Kim, D. Patterson, B. Friedrich, and J. M. Doyle, "Magnetic trapping of atomic chromium," *Physical Review A* **57**, pp. R3173–3175, 1998.

[21] J. Kim, B. Friedrich, D. P. Katz, D. Patterson, J. D. Weinstein, R. deCarvalho, and J. M. Doyle, "Buffer-gas loading and magnetic trapping of atomic europium," *Physical Review Letters* **78**, pp. 3665–3668, 1997.

[22] J. M. Doyle, B. Friedrich, J. Kim, and D. Patterson, "Buffer-gas loading of atoms and molecules into a magnetic trap," *Physical Review A* **52**, pp. R2515–R2518, 1995.

[23] J. Kim, *Buffer-gas Loading and Magnetic Trapping of Atomic Europium*. PhD thesis, Harvard University, 1997.

[24] J. D. Weinstein, *Magnetic Trapping of Atomic Chromium and Molecular Calcium Monohydride*. PhD thesis, Harvard University, 2001.

[25] J. B. Hasted, *Physics of Atomic Collisions*, American Elsevier, second ed., 1972.

[26] F. Reif, *Fundamentals of Statistical and Thermal Physics*, McGraw-Hill Inc., 1965.

[27] N. Ramsey, *Molecular Beams*, Oxford : Clarendon, 1956.

[28] D. J. Griffiths, *Introduction to Electrodynamics*, Prentics Hall, second ed., 1989.

[29] W. Press, S. Teukolsky, W. Vetterling, and B. Flannery, *Numerical Recipes in C*, Cambridge University Press, second ed., 1988.

[30] J. Marion and S. Thornton, *Classical Dynamics of Particles and Systems*, Saunders College Publishing, fourth ed., 1995.

[31] G. Vidali, G. Ihm, H.-Y. Kim, and M. W. Cole, "Potentials of physical adsorption," *Surface Science Reports* **12**, pp. 133–181, 1991.

[32] Janis Research Company, Inc., `http://www.janis.com`.

[33] J. G. E. Harris, R. A. Michniak, S. V. Nguyen, W. C. Campbell, D. Egorov, S. E. Maxwell, L. D. van Buuren, and J. M. Doyle, "Deep superconducting magnetic traps for neutral atoms and molecules," *Review of Scientific Instruments* **75**, pp. 17–23, 2004.

[34] M. N. Wilson, *Superconducting Magnets*, Oxford University Press, 1983.

[35] American Magnetics, Inc., Oak Ridge, TN.

[36] O. Umezawa and K. Ishikawa, "Electrical and thermal conductivities and magnetization of some austenitic steels, titanium and titanium alloys at cryogenic temperatures," *Cryogenics* **32**, pp. 873–880, 1992.

[37] H. E. Boyer and T. L. Gall, eds., *Metals Handbook Desk Edition*, American Society for Metals, 1975.

[38] R. deCarvalho, C. I. Hancox, and J. M. Doyle, "Enhanced inelastic scattering rates of cold atomic chromium," *Journal of the Optical Society of America B* **20 no.5**, p. 1131, 2003.

[39] A. Roth, *Vacuum Technology*, Elsevier Science, third, updated and enlarged ed., 1990.

[40] E. A. Avollone and T. B. III, eds., *Marks' Standard Handbook for Mechanical Engineers*, McGraw-Hill, 10th ed., 1996.

[41] R. P. Reed and A. F. Clark, eds., *Materials at Low Temperatures*, American Society for Metals, 1983.

[42] Precision Cryogenic Systems, Inc., `http://www.precisioncryo.com`.

[43] N. H. Balshaw, *Practical Cryogenics: An introduction to laboratory cryogenics*, Oxford Instruments (UK) Ltd Research Instruments, 1996.

[44] Stycast 2850FT Black epoxy, cured with 24LV catalyst. Emerson & Cuming Inc., http://www.emersoncuming.com.

[45] R. L. Elgin and D. L. Goodstein, "Thermodynamic study of the ^{4}He monolayer adsorbed on grafoil," *Physical Review A* **9**, pp. 2657–2675, 1974.

[46] D. Sedgley, A. Tobin, T. Batzer, and W. Call, "Characterization of charcoals for helium cryopumping in fusion devices," *Journal of Vacuum Science & Technology A (Vacuum, Surfaces, and Films* **5**, pp. 2572–2576, 1987.

[47] I. Ozdemir and D. Perinic, "Helium sticking coefficient on cryopanels coated by activated charcoal," *Journal of Vacuum Science & Technology A (Vacuum, Surfaces, and Films* **16**, pp. 2524–2527, 1997.

[48] P. A. Lessard, "Cryogenic adsorption of noncondensibles in the high-vacuum regime," *Journal of Vacuum Science & Technology A (Vacuum, Surfaces, and Films* **7**, pp. 2373–2376, 1989.

[49] D. S. Greywall, "Thermal-conductivity measurements in liquid ^{4}He below 0.7 K," *Physical Review B* **23**, pp. 2152–2168, 1981.

[50] Stycast 1266 A/B epoxy. Emerson & Cuming Inc.

[51] R. deCarvalho, *Inelastic Scattering of Magnetically Trapped Atomic Chromium*. PhD thesis, Harvard University, 2003.

[52] Continuum Surelite I-10. Continuum. http://www.continuumlasers.com.

[53] Toptica Photonics DL 100 Diode Laser System, http://www.toptica.com/.

[54] Silicon diode thermometer, model DT-470-CU-12A, Lake Shore Cryotronics, `http://www.lakeshore.com/`.

[55] R. J. Knize, Z. Wu, and W. Happer, "Optical pumping and spin exchange in gas cell," *Advances in Atomic, Molecular, and Optical Physics* **24**, pp. 223–267, 1987.

[56] I. F. Silvera and J. T. M. Walraven, "Spin-polarized atomic hydrogen," *Progress in Low Temeprature Physics* **10**, pp. 139–370, 1986.

[57] A. Lagendijk, I. F. Silvera, and B. J. Verhaar, "Spin exchange and dipolar relaxation rates in atomic hydrogen," *Physical Review B* **33**, pp. 626–628, 1986.

[58] A. J. Moerdijk and B. J. Verhaar, "Collisional two- and three-body decay rates of dilute quantum gases at ultralow temperature," *Physical Review A* **53**, pp. R19–R22, 1996.

[59] W. Ketterle and N. V. Druten, "Evaporative cooling of trapped atoms," *Advances in Atomic, Molecular, and Optical Physics* **37**, pp. 181–236, 1996.

[60] R. D. Hight, R. T. Robiscoe, and W. R. Thorson, "Nonadiabatic spin transitions in an inhomogeneous magnetic field," *Physical Review A* **15**, pp. 1079–1087, 1977.

[61] H. M. J. M. Boesten, A. J. Moerdijk, and B. J. Verhaar, "Dipolar decay in two recent bose-einstein condensation experiments," *Physical Review A* **54**, pp. R29–R32, 1996.

[62] J. G. Brisson, *Third sound studies of helium on molecular hydrogen*. PhD thesis, Harvard University, 1990.

[63] R. C. Richardson and E. N. Smith, eds., *Experimental Techniques in Condensed Matter Physics at Low Temperature*, Addison Wesley Longman, Inc., 1988.

[64] J. D. McWhirter, "Extinction coefficient and skin depth of alkali metals from 10 to 1000nm," *Optics and Lasers in Engineering* **28**, pp. 305–309, 1997.

[65] F. S. et al., "Bose-einstein condensation of metastable helium," *Physical Review Letters* **86**, pp. 3459–3462, 2001.

[66] O. S. et al., "Ionization rates in a bose-einstein condensate of metastable helium," *Physical Review Letters* **89**, p. 220406, 2002.

[67] M. Sinvani, M. W. Cole, and D. L. Goodstein, "Sticking probability of ^{4}He on solid surfaces at low temperature," *Physical Review Letters* **51**, pp. 188–192, 1983.

[68] Supercon Inc., 830 Boston Turnpike, Shrewsbury MA, USA.